

Nonlocal damage models for structural integrity analysis

From the Faculty of Mechanical Engineering of the University of Stuttgart for the attainment of the Honour of a Doctorate of Engineering Sciences (Dr.-Ing.):
Treatise Approved

Presented by: Mahendra Kumar Samal, M.Tech., Mumbai, India

Main assessment: Prof. Dr.-Ing. habil. Eberhard Roos
MPA Universität Stuttgart

Second assessment: Prof. Dr.-Ing. Michael M. Resch
High performance computing center (HLRS), Universität Stuttgart

Date of Oral Examination: 6th November 2007

2007

Institut für Materialprüfung Werkstoffkunde und Festigkeitslehre (IMWF)
Universität Stuttgart

Dedicated to my parents and teachers

Acknowledgements

I express my deep sense of gratitude and profound thanks to Professor Dr.Ing. Eberhard Roos and Dr.Ing. Michael Seidenfuss of IMWF, University of Stuttgart for their keen interest and guidance throughout this work. Their constant encouragement and perseverance have always been sources of inspiration to me. I am greatly indebted to Mr. H.S. Kushwaha, Director, Health Safety and Environment Group and Dr. B.K. Dutta, Head, Computational Mechanics Section, Reactor Safety Division, Bhabha Atomic Research Centre, for giving me a chance to work for my doctoral thesis at IMWF, University of Stuttgart and for their invaluable guidance and personal involvement for the successful completion of the thesis. I am grateful to Dr. A.K. Ghosh, Head, Reactor Safety Division for allowing me to carryout my research work at IMWF and for helping me in every possible way. I am thankful to the authorities of Bhabha Atomic Research Centre, Mumbai, India and University of Stuttgart, Germany for giving me necessary permission to pursue my doctoral work at IMWF, University of Stuttgart.

I owe my sincere thanks to several of my colleagues at MPA Universität Stuttgart, especially Dr.Ing. U. Eisele, Dr.Ing. L. Stumpfrock, Dr.Ing. H.P. Seebich, Dip.Ing. Mathias Bauer, Dip.Ing. Roman Kiessling, Dip.Ing. Mathias Buettner for extending all their help and fruitful discussions during my stay at Stuttgart. I would like to thank Ms. Stefanie Bisinger, Ms. Constance Crane and Ms. Elke Kosthaus for their help. I thank my colleague Mr. P.V. Durgaprasad for helping me implement the non-symmetric matrix solver in my finite element program.

I gratefully acknowledge the financial support from German Institute of Aerospace Research (DLR) for my research work at MPA and IMWF, Universität Stuttgart through the Indo-German bilateral project (IND 04/001).

I would like to take this opportunity to thank all my teachers for sharing their knowledge with me and also would like to thank all my friends and well wishers for their help and moral support. I am grateful to the understanding and support of my wife Aspruha and my son Ashutosh. Last but not the least, I dedicate this thesis to my parents and teachers who are my constant source of inspiration.

March 2007

Mahendra Kumar Samal

Contents

Acknowledgements	iii
Abstract	vii
Zusammenfassung	x
Nomenclature	xiii
Chapter 1: Introduction	1
1.1 Safety analysis using continuum damage mechanics	1
1.2 Evolution of nonlocal damage mechanics models	2
1.3 Motivation for the present research	4
1.4 Brief outline of the model developed in this work	8
1.5 Organisation of the thesis	8
Chapter 2: Literature Survey and discussions	10
2.1 Advantages and limitations of conventional fracture mechanics	10
2.2 Crack initiation and growth modelling in fracture mechanics	11
2.3 Constraint based fracture mechanics modelling	13
2.3.1 Crack tip constraint parameter T	13
2.3.2 Crack tip constraint parameter Q	14
2.3.3 Multiaxiality quotient q as a crack tip parameter	15
2.4 Micromechanical models for cleavage fracture (lower shelf)	18
2.4.1 Beremin's model for Cleavage fracture	22
2.4.2 Maximum Likelihood method for determination of Weibull parameters	22
2.5 Micromechanical modelling of ductile crack growth (upper shelf)	25
2.6 Micro-mechanical modeling in the transition regime	30
2.7 Mesh dependency of conventional damage mechanics models and the concept of nonlocal damage mechanics	32
2.8 Nonlocal damage models, state of the art	34
2.9 Integral and gradient enhanced formulations	35
2.10 Concept of nonlocality	37
2.10.1 Explicit gradient approximation for nonlocal damage	38

2.10.2 Implicit gradient approximation for nonlocal damage	39
Chapter 3: Development of a nonlocal damage mechanics model	42
3.1 Coupled equations of equilibrium and diffusion	42
3.2 Development of a nonlocal form of Rousselier's damage model	43
3.3 Kinematic and material constitutive relations	44
3.4 Derivation of stress increment for the non-local model	45
3.5 Evaluation of linearised consistent tangent moduli	48
3.6 Finite Element formulation for the non-local damage model	51
3.7 Derivation of the expression for \dot{f} in terms of $\partial\varepsilon$ and ∂d	52
3.8 Discretization of the weak form of the governing differential equations	53
3.9 Development of a finite element program DEFINE (Damage Evaluation using FINite Elements)	54
Chapter 4: Numerical simulation of ductile crack growth in the upper shelf region	56
4.1 Simulation of material damage in damage mechanics models	56
4.2 Demonstration of mesh independency of results of the new model using a single element (refined gradually)	58
4.3 Analysis of shear band specimen	62
4.4 Analysis of round notched tensile specimens	69
4.5 Analysis of the flat tensile specimen with a hole at the centre	71
4.6 Prediction of size effect for the flat tensile specimens	78
4.7 Analysis of a compact tension specimen	80
4.8 Analysis of a single edge bend specimen	89
4.9 Analysis of a 2T CT specimen	94
4.10 Analysis of a 4T CT specimen	96
4.11 Prediction of geometry effect (effect of specimen size)	99
4.12 Prediction of geometry effect (effect of specimen type)	100
4.13 Prediction of geometry effect (effect of crack depth)	102
4.14 Effect of material symmetry in modeling	104
4.15 Effect of material stress-strain curve	107
4.16 Effect of critical length parameter	110

Chapter 5: Numerical simulation of probability of failure in lower shelf and transition regime	113
5.1 Prediction of probability of cleavage fracture in the transition regime using compact tension specimens (2D plane strain analysis)	114
5.2 Prediction of probability of cleavage fracture in the transition regime using compact tension specimens (3D analysis)	123
5.3 Prediction of probability of cleavage fracture in the transition regime using SEB specimens (3D analysis)	127
5.4 Effect of specimen geometry on prediction of probability of cleavage fracture (CT vs SEB specimen)	129
5.5 Effect of crack depth on prediction of probability of cleavage fracture (deep vs shallow cracked SEB specimens)	130
5.6 Effect of specimen size on prediction of probability of cleavage fracture (1T, 2T and 4T CT specimens)	134
5.7 Effect of specimen thickness on prediction of probability of cleavage fracture (SEB specimens with different thicknesses)	136
5.8 Effect of material stress-strain curve on prediction of probability of cleavage fracture	139
5.9 Effect of crack tip modeling on prediction of probability of cleavage fracture	141
5.10 Effect of characteristics length on prediction of probability of cleavage fracture	143
 Chapter 6: Conclusions, recommendations and scope of future research	145
6.1 Conclusions	145
6.2 Recommendations	147
6.3 Scope for future research	148
 References	149
Appendix A (Rousselier's model)	162
Curriculum Vitae	165

Abstract

The reliable safety assessment of steel components such as pressure vessels, pipe bends and shell-nozzle junctions etc. is of prime interest for the safe operation of plants. It is essential that the assessment be done in a realistic and not too conservative way in order not to impair the economic efficiency too much.

In this context fracture mechanics plays an important role because the load bearing capacity of the components under given loading conditions can be assessed. For such analyses, cracks are assumed to be present in the highest loaded section of the component in order to define a minimum crack length, which must be detected by non-destructive testing methods. However, the fracture mechanics parameters, determined from laboratory scale experiments are not directly transferable to components and hence additional considerations (like constraint effects etc.) need to be taken care of.

Continuum damage mechanics is able to consider these effects inherently by incorporating the features of micro-structural damage evolution into the material models (also called local damage models). These types of models have been highly successful in simulating fracture resistance behaviour of specimens and components of varying geometries, loading and boundary conditions with the same set of material parameters and hence the question of transferability of parameters does not arise. This way, these parameters are truly micro-mechanical properties of the material. However, numerical analyses of ductile fracture process (for strain hardening metallic materials) based on local damage models are often found to depend on the mesh size used (i.e., size of grid for the numerical method, for example, finite element method). Damage tends to localise in only one element layer. As a consequence, increasingly finer discretisation grids can lead to earlier crack initiation and faster crack growth. The reason behind this non-physical behaviour is the loss of ellipticity (non-uniqueness of the solution) of the set of partial differential equations, especially when the softening due to damage dominates over the plastic hardening. Discontinuities may then arise in the displacement solution, which results in a singular damage rate field. Displacement discontinuities and damage rate singularities can be avoided by adding a nonlocal damage term into the constitutive equation of the material model, which carries the material length scale information. With this enhanced continuum description, smooth damage fields are

achieved, in which the localisation of damage is limited to a given length (i.e., characteristics length of the material).

In this work, the Rousselier's damage model has been extended to its nonlocal form using nonlocal damage parameter d as an additional degree of freedom in the finite element model. The evolution of nodal damage of a particular node is related to the nodal damage and the local ductile void volume fraction of the neighbouring nodes (of the finite element model) with the help of a diffusion type equation. This diffusion equation is coupled with the standard stress equilibrium equation of continuum mechanics. A weak form of these coupled equations is developed in order to discretise them in the context of finite element (FE) method. Using standard FE shape functions in the variational equation, the coupled partial differential equations have been converted into the FE algebraic equations. The consistent tangent moduli of the coupled domain have been derived by simultaneously solving the extended material yield function along with the rate equations for the internal variables.

The model has been applied to simulate the load-displacement response and fracture resistance behaviour of different types of specimens in 2-D and 3-D domain made of the reactor pressure vessel steel 22NiMoCr3-7.

In the first part of this work, the deformation and failure behaviour of different types of specimens, such as, notched round tensile specimens, flat tensile specimens (with hole at the specimen center) of different sizes, standard 1T compact tension (CT) and single edge notched bend (SEB) specimens are simulated. The results obtained from the newly developed nonlocal model have been compared with those of the local model and the experiments (carried out at MPA Universität Stuttgart, Germany). In addition, the size and geometry effects have also predicted by the nonlocal model and the results have been compared with those of the experiments. All numerical results obtained with the nonlocal damage model developed in this work are in good agreement with the experimental results.

A further key aspect of this work is prediction of the fracture resistance curve (fracture toughness versus temperature) for the German low alloy pressure vessel steel 22NiMoCr3-7 in the whole transition regime. Effects like purely cleavage fracture at the low end of the regime and ductile crack growth prior to cleavage fracture in the transition temperature region must be taken into account in order to simulate the fracture toughness transition curve accurately. In

order to simulate the experimentally observed behaviour, numerous calculations in the temperature range from -120 deg. C to -20 deg. C have been carried out for specimens with different thickness values and different crack depths. At low temperatures, the stress gradient at the crack tip becomes high and hence a very fine mesh is required to simulate it accurately. However, in order to simulate the preceding stable crack (often very small in size) before cleavage fracture, the mesh independent form of the Rousselier's damage model is necessary.

For the simulation of fracture resistance behaviour of the different types of fracture mechanics specimens in the transition temperature region, the nonlocal mesh independent damage model developed in this work has been coupled with Beremin's model (which enables the prediction of the probability of cleavage fracture). Calculations have been done using

- Beremin's model along with elasto-plastic material model (in which prediction of stable crack growth is not possible) and
- Beremin's model along with nonlocal Rousselier's model (in which prediction of stable crack growth is possible),

assuming constant and temperature independent values for the Weibull parameters (two-parameter Weibull theory).

It was observed that the model without damage is unable to predict the scatter in the fracture behaviour (observed experimentally) especially towards the higher temperature end of the transition region, whereas the combined model with nonlocal damage has been able to predict the scatter very accurately over the whole temperature range. The effects of specimen type, size and geometry on the fracture toughness transition curve have also been captured satisfactorily by the new model.

Keywords: nonlocal model; damage mechanics; Rousselier's model; finite element implementation; ductile-brittle transition; master curve; Beremin's model.

Zusammenfassung

Die zuverlässige sicherheitstechnische Bewertung von Komponenten aus Stahl wie Druckbehälter, Rohre, Abzweige usw. ist für einen sicheren Betrieb von Anlagen essentiell. Dabei ist wichtig, dass die Bewertung realistisch und nicht zu konservativ vorgenommen wird, um die Wirtschaftlichkeit nicht zu sehr zu verschlechtern.

In diesem Zusammenhang spielt die Bruchmechanik eine wichtige Rolle, da mit ihrer Hilfe die Tragfähigkeit rissbehafteter Bauteile unter gegebener Betriebsbeanspruchung analysiert werden kann. Im Allgemeinen werden für diese Analysen Risse im höchstbeanspruchten Querschnitt eines Bauteils postuliert, um eine zerstörungsfrei auffindbare Rissgröße zu definieren. Allerdings sind die an Kleinproben ermittelten Bruchmechanikkennwerte nicht direkt auf Komponenten übertragbar, sondern es sind weiterführende Analysen erforderlich, um z. B. die Mehrachsigkeit des Spannungszustandes mit zu berücksichtigen.

Mit der Schädigungsmechanik ist es möglich, diese Effekte abzubilden. Dies geschieht durch die Berücksichtigung der mikrostrukturellen Schädigungsvorgänge in den Werkstoffmodellen – den sogenannten lokalen Schädigungsmodellen. Diese Modelle werden sehr erfolgreich zur Simulation der duktilen Rissentwicklung in Kleinproben und Komponenten mit unterschiedlichen Geometrien angewendet. Dabei werden für sämtliche Probenformen und -größen dieselben Werkstoffparameter verwendet, ohne dass sich die Frage der Übertragbarkeit stellt.

Die Ergebnisse der lokalen Schädigungsmodelle, die zur numerischen Analyse des Zähbruchs herangezogen werden, sind von der Netzfeinheit des Finite Elemente Modells abhängig. Die Werkstoffschädigung lokalisiert bei den lokalen Schädigungsmodellen in der Regel in einer Elementschicht. Dies hat zur Folge, dass mit feiner werdender Vernetzung des Bauteils die Rissinitiierung früher berechnet und schnelleres Risswachstum ermittelt wird.

Der Grund für dieses Verhalten, welches den physikalischen Prozess fehlerhaft wiedergibt, ist der Verlust der Elliptizität (Eindeutigkeit der Lösung) der partiellen Differentialgleichungen. Dies ist insbesondere der Fall, wenn die Werkstoffentfestigung infolge der Werkstoffschädigung die plastische Werkstoffverfestigung übersteigt. Unstetigkeiten im Verformungsfeld können die Folge sein was zu einem extremen Anstieg der lokalen Schädigung führt. Dies kann vermieden werden, wenn das lokale Schädigungsmodell um einen nichtlokalen Term erweitert wird. Mit dieser erweiterten kontinuumsmechanischen

Formulierung wird eine kontinuierliche Verteilung der Schädigung erreicht, welche die Lokalisierung auf einen vorgegebenen Bereich beschränkt.

In dieser Arbeit wurde das Schädigungsmodell von Rousselier, durch Einführung des nichtlokalen Schädigungsparameter d als zusätzlichen Freiheitsgrad, in eine nichtlokale Form überführt. In dieser nichtlokalen Form wird der Einfluss der Schädigung benachbarter Knoten auf die lokale Schädigung mit einer Diffusionsgleichung beschrieben. Diese Diffusionsgleichung wird mit den Gleichungen zur Beschreibung des mechanischen Verhaltens gekoppelt. Für die Kopplung in einem Finite Elemente Programm wurden die Gleichungen in ihre 'schwache Form' (beschränkte Differenzierbarkeit) überführt. Unter Verwendung der Standard-Formfunktionen der Finiten Elemente Methode wurden die Differentialgleichungen in ein Finite Elemente Programm implementiert. Die Tangentensteifigkeitsmatrix wurde aus der nichtlokal erweiterten Fließfunktion und den Entwicklungsgleichungen für die inneren Variablen abgeleitet.

Das Modell wurde verwendet, um das Verformungsverhalten und die Bruchzähigkeit unterschiedlicher Proben aus dem Werkstoff 22NiMoCr3-7 zwei- und dreidimensional zu simulieren.

In einem ersten Schritt wurde das Verformungsverhalten von gekerbten Rundzugproben, unterschiedlich großen Flachzugproben mit Loch, Standard 1T CT-Proben und SEB-Proben berechnet. Die mit dem nichtlokalen Schädigungsmodell erzielten Ergebnisse wurden anschließend mit den Ergebnissen des lokalen Schädigungsmodells und Versuchen, die an der MPA Universität Stuttgart durchgeführt wurden, verglichen. Zusätzlich wurde der Größen- und Geometrieinfluss mit dem nichtlokalen Modell untersucht. Dabei zeigte sich eine gute Übereinstimmung der numerischen Ergebnisse, die mit dem im Rahmen dieser Arbeit entwickelten nichtlokalen Modell erzielt wurden, mit den experimentellen Werten.

Ein weiterer Hauptaspekt dieser Arbeit ist die Vorhersage der Bruchzähigkeitskurve (Bruchzähigkeit als Funktion der Temperatur) für den Werkstoff 22NiMoCr3-7 im gesamten Übergangsbereich.

Um das Streuband der Bruchzähigkeit, welches im unteren Bereich spröde und im Übergangsbereich sowohl duktil als auch spröde ist, zu simulieren, wurden zahlreiche Berechnungen im Temperaturbereich von -120°C bis -20°C an Proben mit unterschiedlichen Ausgangsrisslängen und Dicken durchgeführt.

Bei tiefen Temperaturen wird der Spannungsgradient an der Rissspitze sehr steil, wodurch ein sehr feines Netz nötig wird, um den Gradienten zu simulieren.

Um das dem Spaltbruch vorangehende, oft sehr kleine duktile Risswachstum zu simulieren, wird zusätzlich die nichtlokale, also die netzunabhängige Formulierung des Rousselier Modells benötigt.

Zur Berechnung der verschiedenen Bruchmechanikproben wurde deshalb das hier entwickelte nichtlokale Rousselier Modell mit dem Beremin Modell (das eine Vorhersage der Spaltbruchwahrscheinlichkeit ermöglicht) gekoppelt. Für einen Vergleich wurden Berechnungen mit einem mit dem Beremin Modell gekoppelten elasto-plastischen Materialmodell (also ohne Berücksichtigung von stabilem Risswachstum) und Berechnungen mit einem mit dem Beremin Modell gekoppelten nichtlokalen Rousselier Modell (also mit Berücksichtigung von stabilem Risswachstum) durchgeführt. Dabei wurden konstante, temperaturunabhängige Weibullparameter (2-parametrische Weibull-Theorie) verwendet.

Es zeigte sich, dass das Modell ohne Berücksichtigung des stabilen Risswachstums nicht in der Lage ist, die experimentelle Streuung im Übergangsbereich zu erfassen, insbesondere bei höheren Temperaturen im oberen Übergangsbereich. Dagegen war es mit dem nichtlokalen schädigungsmechanischen Modell möglich, die Streuung über den gesamten Bereich gut zu beschreiben. Ebenso wurden der Geometrie- und Größeneinfluss auf die Bruchzähigkeit mit dem nichtlokalen Modell gut zu beschreiben.

Nomenclature

a	Crack length
a_0	Initial crack length in fracture mechanics specimens
A, B	Constants for Chu and Needleman's statistical void nucleation model
B	Thickness of fracture mechanics specimens
B_N	Net thickness of fracture mechanics specimens after side grooving
B_u	Derivative of shape function matrix N_u (relating increment of mechanical strain to nodal displacements)
B_d	Derivative of shape function matrix N_d (relating increment of nonlocal damage gradient to nonlocal nodal damage)
c_{length}	Characteristic length parameter in the nonlocal model
$\underline{\underline{C_{ep}}}$	Consistent tangent stiffness matrix relating increment of stress tensor to increment of mechanical strain tensor
$\underline{\underline{C_{ed}}}$	Consistent tangent stiffness matrix relating increment of stress tensor to increment of nonlocal damage
$\underline{\underline{C_{de}}}$	Consistent tangent stiffness matrix relating increment of local void volume fraction to increment of mechanical strain tensor
$\underline{\underline{C_{dd}}}$	Consistent tangent stiffness matrix relating increment of local void volume fraction to increment of nonlocal damage
$\underline{\underline{C_{el}}}$	Elasticity matrix relating increment of stress tensor to increment of elastic part of mechanical strain tensor
d	Nonlocal damage variable
E	Young's modulus of elasticity
f	Ductile void volume fraction (local damage variable)
f^*	Modified void volume fraction introduced by Tvergaard and Needleman in GTN model
f_0	Initial void volume fraction in the material
f_b	Body force vector per unit volume
f_c	Void volume fraction for coalescence of voids
f_f	Final void volume fraction for fracture in the material

f_u^*	Modified void volume fraction at fracture
f_N	Void volume fraction at saturated condition of nucleation
f_N^ε	Void volume fraction at saturated condition of strain controlled nucleation process
f_N^σ	Void volume fraction at saturated condition of stress controlled nucleation process
f_m^{ext}	Nodal force vector corresponding to external mechanical forces
f_m^{int}	Nodal force vector corresponding to internal mechanical forces (due to stresses)
f_d^{ext}	Nodal force vector of external forces corresponding to damage degree of freedom
f_d^{int}	Nodal force vector of internal forces corresponding to damage degree of freedom
\dot{f}_{growth}	Increment in void volume fraction due to growth of voids
$\dot{f}_{nucleation}$	Increment in void volume fraction due to nucleation of voids
g	Yield function of the material ($g = \phi$ for associative plasticity flow rule)
G	Shear modulus or modulus of rigidity
$G(\bar{y}; \bar{x})$	Green's weight function used in the nonlocal model
h^α	Function of internal variables in the porous plasticity model
H^α	Internal variables in the porous plasticity or damage mechanics model
I	Second order unit tensor
J	Rice's J-integral
	Fourth order unit tensor
J'	$J - \frac{1}{3} II$
K	Bulk modulus of material
	Stress intensity factor
K_I	Mode-I stress intensity factor
K_{IC}	Critical stress intensity factor or fracture toughness for onset of unstable fracture in mode-I
K_{JC}	Critical stress intensity factor or fracture toughness for onset of unstable fracture in mode-I (converted from J_c value)
K_{uu}	Part of nonlocal finite element stiffness matrix relating increment of nodal mechanical forces to increment of nodal mechanical displacements
K_{ud}	Part of nonlocal finite element stiffness matrix relating increment of nodal

	mechanical forces to increment of nodal nonlocal damage
K_{du}	Part of nonlocal finite element stiffness matrix relating increment of nodal damage forces to increment of nodal mechanical displacements
K_{dd}	Part of nonlocal finite element stiffness matrix relating increment of nodal damage forces to increment of nodal nonlocal damage
l_0, l_c	Critical length of particle for triggering cleavage fracture
L	Length between supports of the single edge bend (SEB) specimens
m	Shape parameter of Weibull distribution for cleavage fracture toughness in materials
n	Unit normal to the boundary Γ
N_u	Shape function matrix used for interpolation of mechanical displacement within the finite element
N_d	Shape function matrix used for interpolation of nonlocal damage within the finite element
p	Hydrostatic stress or pressure
P_f	Probability of failure (cleavage fracture)
q	von Mises stress
	Multiaxiality quotient or crack tip constraint used as measure of ration of von Mises stress to hydrostatic stress
q_1, q_2, q_3	Constants introduced by Tvergaard and Needleman in GTN model
Q	Crack tip constraint parameter used as a measure of deviation of crack tip stress in a finite body from stresses described by HRR singularity
$R(\varepsilon_{eq})$	Material stress-strain curve as a function of equivalent plastic strain
s_{ij}	Deviatoric part of Cauchy's stress tensor
s_N	Standard deviation of strain for void nucleation
s_N^e	Standard deviation of strain for strain controlled void nucleation process
s_N^σ	Standard deviation of strain for stress controlled void nucleation process
t_s	Surface traction at the boundary
T	Elastic T -stress used as a measure of crack tip constraint in linear elastic material
u	Generalized displacement in the FE formulation
W	Width of fracture mechanics specimens

1T	Standard Fracture mechanics specimens of 1 inch thickness
2T	Fracture mechanics specimens of 2 inch thickness
4T	Fracture mechanics specimens of 4 inch thickness
δ	Variational operator
ε_{ij}	Mechanical strain tensor
ε_{eq}	Equivalent strain
ε_{eq}^p	Equivalent plastic strain
ε_{kk}^p	Hydrostatic part of plastic strain tensor
ε_m	True strain in the material stress-strain curve
ε_N	Mean nucleation strain for strain controlled void nucleation process
$\partial\varepsilon$	Increment in total mechanical strain tensor
$\partial\varepsilon^e$	Increment in elastic part of mechanical strain tensor
$\partial\varepsilon^p$	Increment in plastic part of mechanical strain tensor
κ	Plastic strain hardening parameter
ϕ	Yield potential or function
γ	Modification factor for fracture toughness evaluation of specimens
	Surface energy of the material
Γ_f	Boundary of the domain where mechanical forces are defined
Γ_u	Boundary of the domain where mechanical displacements are defined
Γ_d	Boundary of the domain where boundary conditions for nonlocal damage is defined
η	Factor used for fracture toughness evaluation of specimens from experimental data of area under the load-displacement curve
ν	Poisson's ratio
Ω	Domain in continuum mechanics formulation
$\Psi(\bar{y}; \bar{x})$	Gaussian weight function used in the nonlocal model
σ_{ij}	Cauchy's stress tensor
σ_{eq}	von Mises equivalent stress
σ_{hydro}	Hydrostatic (or mean) stress
σ_N	Mean nucleation stress for stress controlled void nucleation process

σ_w	Weibull stress in Beremin's model for cleavage fracture
σ_I^i	Maximum principal stress over a volume element V_i
σ_{th}	Threshold value of Weibull stress in the three parameter Weibull model
σ_m	True stress in the material stress-strain curve
σ_u	Scaling parameter of Weibull distribution for cleavage fracture toughness in materials
$\Delta\hat{u}$	Increment of FE nodal mechanical displacement vector
$\Delta\hat{d}$	Increment of FE nodal nonlocal damage vector
∇^2	Laplacian operator

Superscripts

T	Transpose of a matrix
\bullet	Increment of a scalar quantity or tensor variable
tr	Elastic predictor part of a tensor

Subscripts

t	Variables at the beginning of the time step t to $t + \Delta t$
$t + \Delta t$	Variables at the end of the time step t to $t + \Delta t$

Abbreviations

ASTM	American society for testing and materials
CMOD	Crack mouth opening displacement
CT	Compact tension specimen
DEFINE	Name of FE code developed in this work (acronym for Damage Evaluation using FINIite Elements)
DOF	Degree of freedom
EPFM	Elasto-plastic fracture mechanics
FE	Finite element
FEM	Finite element method
GTN	Gurson-Tvergaard-Needleman
J-R	J-resistance (fracture resistance)
LEFM	Linear elastic fracture mechanics

PDE	Partial Differential equation
SEB	Single edge (notched) bend specimen
SSY	Small scale yielding
UTS	Ultimate tensile stress
WPS	Warm pre-stressing

Chapter 1

Introduction

Prevention of failure of pressurised and high-energy components and systems made of metallic materials has been an important issue in design of all types of power and process plants. Each individual component of these systems must be dimensioned such that it can resist the forces or moments to which it will be subjected during normal service and upset conditions. Additionally, these should be safe enough during emergency or unforeseen accident conditions such as earthquakes. For standard design purposes, the yield limit is often used as a failure criterion, which means that the component will never undergo permanent (plastic) deformation under design loads. However, when safety and reliability are critical (e.g., in nuclear installations) or when the added weight and cost of over-dimensioning cannot be tolerated (e.g., in design of aircrafts), more accurate predictions are needed for the onset of failure, as well as of the fracture process itself (crack paths, residual strength, remaining service life etc.). These issues have traditionally been addressed using fracture mechanics. For example, in nuclear pressure vessels and pipings, the concept of leak before break design uses the concept of fracture mechanics to prove that the component leaks (which can be detected so that action can be taken for safe shutdown of the plant) before breaking in a catastrophic manner (Roos et al. 1989). Starting from the assumption of an idealised, dominant flaw, fracture mechanics theory provides conditions for the growth of a crack from this flaw (Roos et al. 1991a; Nilsson et al. 1992; Matsubara et al. 2001). Additional criteria have been developed for the crack growth direction, growth rates etc. under monotonically increasing loads (quasi-static), dynamic loads [Zimmermann et al. 1985], constant loads at high temperature (creep), repeated or cyclic loading (fatigue) [Diem et al. 1994] or environmentally assisted loading processes (stress corrosion cracking, hydrogen embrittlement etc.).

1.1 Safety analysis using continuum damage mechanics

The advent of faster computers and the associated computational algorithms have greatly extended the scope of fracture mechanics. Accurate numerical analyses can nowadays be performed for arbitrary geometries and loading conditions. Furthermore, the ability to numerically solve complex mathematical problems has inspired extensions of the classical,

linear theory with nonlinear material behaviour. Under the influence of these developments, a fundamentally different type of modelling has emerged, in which fracture is considered as the ultimate consequence of a material degradation process. Instead of separately defining constitutive relations and a fracture criterion, the loss of mechanical integrity is accounted for in the material constitutive model. Crack initiation and growth then follow naturally (implicitly) from the standard continuum mechanics theory. This theory (called continuum damage mechanics) introduces a set of field or internal variables (damage variables), which explicitly describe the local loss of material integrity or material stress carrying capability. A crack is represented by that part of the material domain in which the damage has become critical, i.e., where the material cannot sustain stress anymore. Redistribution of stresses results in growth of plastic deformation and damage zones in front of the crack tip or the initial critical damage zone.

Unlike fracture mechanics, one does not need to have an initial crack in the model in order to describe the crack initiation and growth processes. The ductile damage models such as those of Rousselier [Rousselier 1987] and Gurson-Tvergaard-Needleman [Gurson 1975,1977; Needleman and Tvergaard 1984; Tvergaard and Needleman 1984] have been widely used for predicting load-deformation and fracture resistance behaviour of different specimens and components (of widely different materials) in literature [Tvergaard 1981; Xia et al. 1995; Xia and Shih 1995a; Brocks et al. 1995; Gao et al. 1998a; Ruggieri et al. 1996; Seidenfuss 1992; Seidenfuss and Roos 2004; Pavankumar et al. 2005]. These coupled models for ductile fracture of materials include the micro-mechanical effects of void nucleation, growth and coalescence of micro-voids in the constitutive equation used for description of the mechanical continuum.

1.2 Evolution of nonlocal damage mechanics models

The models where the evolution of material damage at a point is a function of stress and strain field at the same point are called local models. The disadvantage of these local models lies in use of a constant finite element size (related to characteristic material length which depends upon microstructure and average distance between relevant inclusions and second phase particles) in the fracture zone to simulate the crack initiation and crack growth process when using the finite element method for solving the boundary value problems [Ortiz et al. 1987, Needleman 1988, Needleman and Tvergaard 1994]. There have been efforts by researchers to

remove this problem by development of so-called “nonlocal” damage models [Reusch 2003, Svendsen 1999, Reusch et. el. 2003a,b, Needleman and Tvergaard 1998, Brekelmans and de Vree 1995, de Vree et al. 1995, Ramaswamy and Aravas 1998a,b]. Numerical analyses based on the local damage models depend on the spatial discretisation (i.e., mesh size of the numerical method used). The growth of damage tends to localise in the smallest band that can be captured by the spatial discretisation. As a consequence, increasingly finer discretisation grids can lead to crack initiation earlier in the loading history and to faster crack growth. In the limit of an infinitesimally small spatial resolution, the predicted damage band can have a zero thickness and hence the crack growth becomes instantaneous. This non-physical behaviour is caused by the fact that the localisation of damage in a vanishing volume is no longer consistent with the concept of a continuous damage field, which forms the basis of the local continuum damage mechanics approach.

The origin of the localisation process of damage has been studied by many researchers worldwide (e.g., Needleman 1988, Aifantis 1992, Brekelmans and de Vree 1995, Peerlings et al. 2002 among many others) and different reasons have been attributed for this process. First, the set of partial differential equations, which govern the rate of deformation, may locally lose ellipticity (for statics) and hyperbolicity (for dynamics) at a certain level of accumulated damage (especially when the softening due to damage dominates over the plastic hardening). Discontinuities may then arise in the displacement solution, which result in a singular damage rate. This damage rate singularity in turn leads to the instantaneous initiation of a crack. Second, when a crack has been initiated, either prematurely as a result of displacement discontinuities or because the damage variable has become critical in a stable manner, the damage rate singularity at the crack tip results in instantaneous failure of the material in front of the crack tip. Since the damage rate singularity is preserved as the crack propagates, the remaining cross section is traversed instantaneously.

Displacement discontinuities and damage rate singularities can be avoided by adding nonlocality to the damage model and hence the name nonlocal damage models. In these models, spatially averaged quantities (e.g., strain or damage) are used in the constitutive equations. The enhanced continuum description which is thus obtained results in smooth damage fields, in which the localisation of damage is limited to the length scale introduced by the averaging. As a result, too early initiation of cracks and the non-physical faster crack growth rates are avoided. The other way is to follow an implicit formulation and to introduce

higher order strain or damage gradients into the constitutive equations through another partial differential equation (PDE) along with the standard stress equilibrium PDE of continuum mechanics.

1.3 Motivation for the present research

The present research has two broad objectives, i.e., (a) to develop a model which can predict fracture resistance behaviour of a component without using a constant FE mesh size (this will help to simulate large stress gradients where the stress and strain distribution results are of better accuracy upon mesh refinement) and (b) to simulate very small amounts of crack growth (of the order of 200 micron) when analysing fracture mechanics specimens in the transition temperature regime to predict the probability of cleavage fracture.

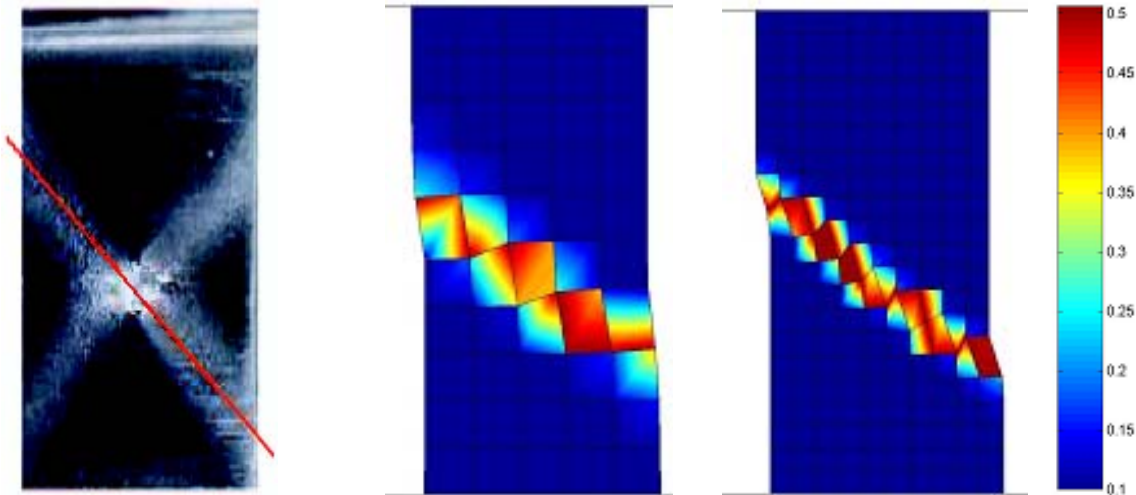


Fig. 1.1(a) Experimentally observed shear band development in a flat tensile sheet

Fig. 1.1(b) Predicted shear band width using 1mm mesh (local damage model), plot of contour material damage

Fig. 1.1(c) Predicted shear band width using 0.5mm mesh (local damage model), plot of contour of material damage

In order to understand the problem associated with the local damage mechanics models, we consider here the example of shear band development in a flat metallic (austenitic steel) sheet loaded in tensile direction. Fig. 1.1(a) shows the shear bands, which develop at local imperfections in the tensile sheet, which are inclined at $\pm 45^\circ$ to the tensile axis. It is known that the width of shear band depends upon the underlying micro-structural features and hence is constant for a given material. In order to simulate the width of shear band using continuum

damage mechanics, let us analyse the specimen using 2D plane strain formulation using two different finite element (FE) mesh sizes (i.e., square elements of 1mm and 0.5mm of element side). Fig. 1.1(b) shows the shear band (zone of contour plot having damage value of 0.5), which is confined to one layer of Gauss points in case of 1mm FE mesh. However, as the mesh size is refined to 0.5mm, the width of shear band narrows down (still confined to one layer of Gauss points). This demonstrates the mesh dependent nature of local damage mechanics results.

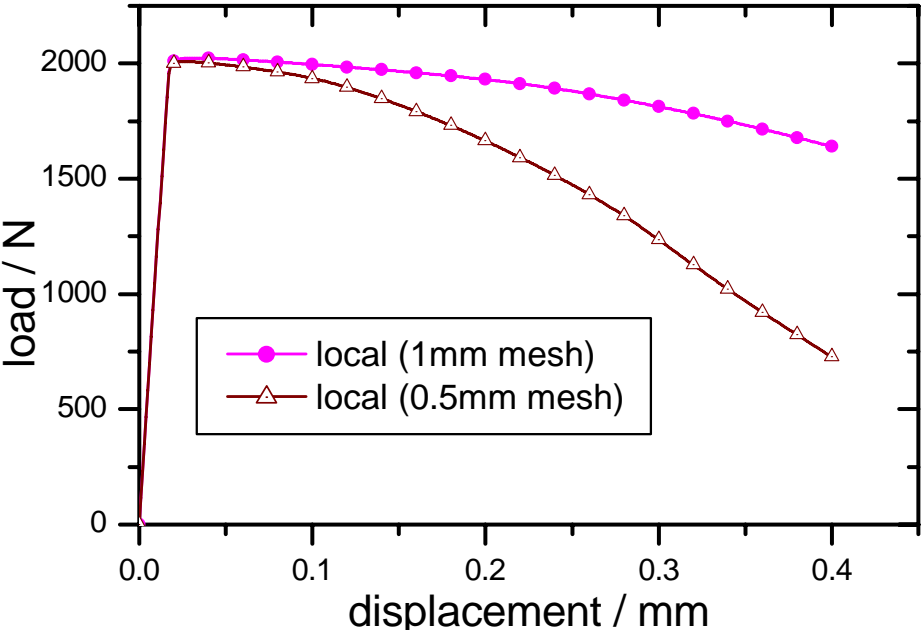


Fig. 1.2 Mesh dependency of load displacement response of the shear band specimen

The above effect is also reflected in the simulation results of the global load-deflection curve of the specimen (Fig. 1.2) where the predicted load carrying capability decreases drastically as the mesh size is refined (which is unrealistic). Hence, in order to predict the accurate response of a specimen or component (when local or conventional damage mechanics approach is used), one has to first determine the size of FE mesh to be used in the damaged zone or region of crack propagation. The same mesh has to be used for analysis of any component of the same material. Hence, the material length scale is incorporated in an explicit way instead of going for modification of the material constitutive equations to take into account of the characteristics length scale of the material in the simulation.

As discussed earlier, the problem of using constant FE mesh size prohibits simulation of large stress gradients where the mesh has to be refined in order to minimise the error associated with

FE computation. This is especially important for simulation of stress-strain behaviour ahead of crack tip when analysis is done in lower shelf and transition temperature regions of a material. As observed from Fig. 1.3, very small amounts of ductile (stable) crack growth were observed before cleavage fracture when carrying out experiments [Eisele et al. 2006] on compact tension (CT) specimens at various temperatures (between -100 and -20 deg. C). Due to these small crack growths, the stress ahead of the crack tip gets redistributed and hence the probability of cleavage fracture (which depends upon the stress state ahead of the crack tip) of CT specimens are largely dependent upon accurate simulation of the stress field and its redistribution due to ductile crack growth. In order to simulate the probability of cleavage fracture in specimens and components, Beremin’s model [Beremin 1983] is widely used where the probability of cleavage fracture depends upon two material properties (i.e., m and σ_u).

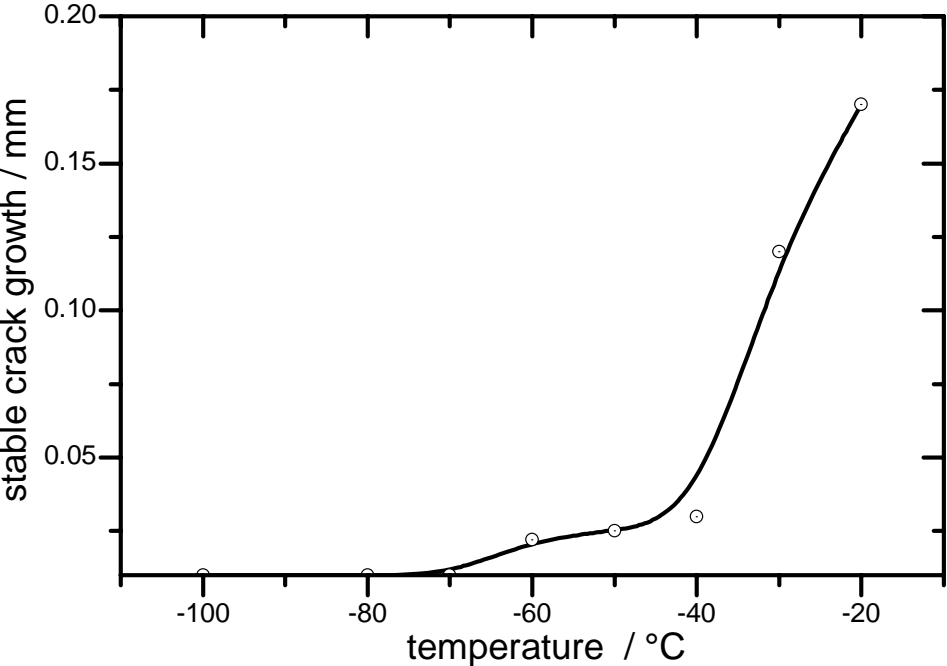


Fig. 1.3 Experimentally measured stable crack growth before cleavage fracture in CT specimens

In order to predict the probability of cleavage fracture in the transition region, one needs to combine Beremin’s model with that of the ductile damage model (i.e., Rousselier or Gurson-Tverggard-Needleman) [Ruggieri and Dodds 1996; Xia and Shih 1996; Xia and Cheng 1997]. However, the conventional (or local) ductile damage model requires use of a constant mesh size (e.g., of the order of 0.2mm), which is too coarse to simulate the stress gradients in the transition region. Hence, the combination of Beremin’s model with local damage models becomes difficult for simulation in the transition temperature region.

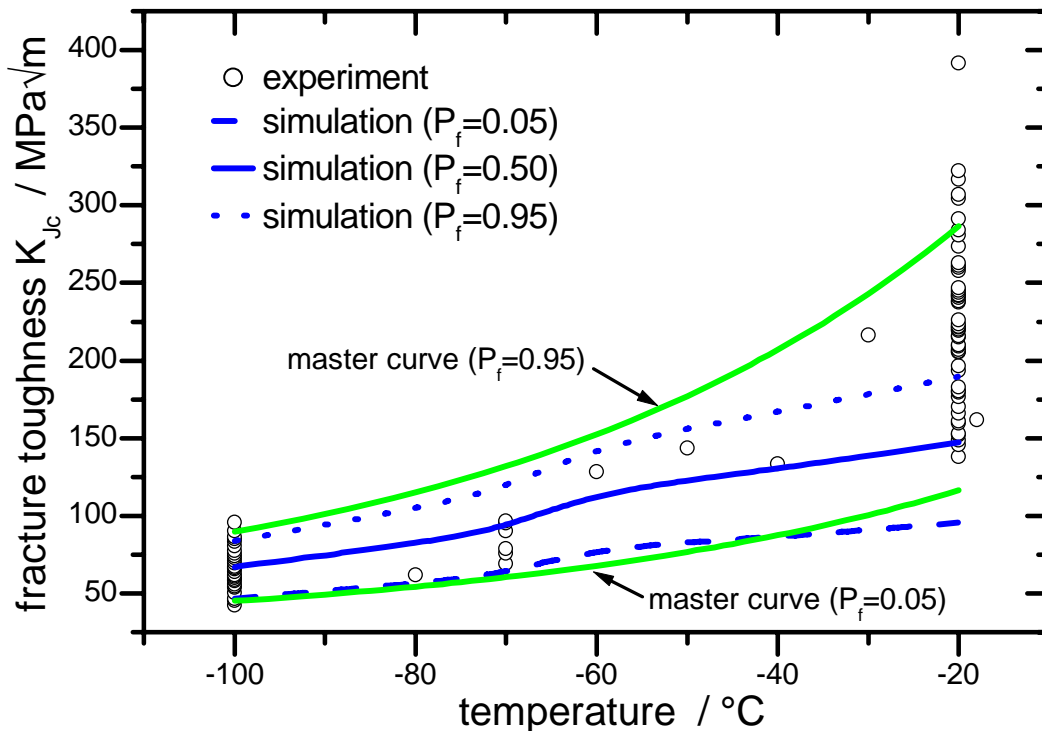


Fig. 1.4 Comparison of scatter band prediction of Beremin's model with experiment

Fig. 1.4 shows the comparison of predicted scatter band in the fracture toughness of a CT specimen with those of experiment [Eisele et al. 2006]. The simulation has been done using elasto-plastic FE analysis [Seebich 2007], where a very fine mesh of 0.02mm (at the crack tip) has been used. Hence, small amounts of crack growth and their corresponding effects on stress redistribution cannot be considered in the present analysis. As seen from Fig. 1.4, the predicted scatter band is in close agreement with those of experiment upto a temperature of approximately -60 deg. C (where the stable crack growth is almost nil). However, the difference between the prediction and the experiment widens once stable crack growth sets in and as expected, predicted results grossly underestimate the experimental scatter.

The inability of the local damage models to use very fine mesh (and hence to simulate very small amounts of crack growth) in the transition regime prevents us from simulating the stress gradients correctly ahead of the crack tip. It may be the reason for the discrepancy between the simulated and experimental cleavage fracture probabilities of standard fracture mechanics specimens when we approach towards the right end of the transition regime. In this work, we investigate the possibility of combining the Rousselier's damage model with the Beremin's model in the transition temperature region, which is the motivation for the present research. In the first phase, the task is to develop a mesh independent damage model and later, the new

model will be used in combination with Beremin's model to predict the probability of cleavage fracture in the transition temperature region.

1.4 Brief outline of the model developed in this work

In this work, a nonlocal description for the evolution of the damage variable d has been derived using an implicit gradient enhancement formulation, which results in a partial differential equation in terms of d and the ductile void volume fraction f . This additional PDE contains diffusion terms with a source term, which depends upon the evolution of the void volume fraction f [Reusch 2003, Reusch et al. 2003a], i.e.,

$$\dot{d} - \dot{f} - C_{length} \nabla^2 \dot{d} = 0 \quad (1.1)$$

When C_{length} is zero, the nonlocal formulation reduces to that of local formulation. The solution of the above PDE (along with the stress equilibrium equation) can be simplified when put into the standard finite element (FE) framework and this necessitates the introduction of an additional degree of freedom (DOF) d in addition to the standard deformation DOFs (i.e., u, v and w). Introduction of an additional damage DOF also necessitates an additional boundary condition for d (often the Neumann boundary condition is used which means that damage flux at the free surface is zero).

The new formulation has been used to predict the load-deformation and fracture resistance behaviour of several specimens using different mesh sizes and the mesh independence nature of the nonlocal solutions have been demonstrated. Later, size and geometry effects on the fracture resistance behaviour of specimens are also predicted using nonlocal damage models. In addition to simulation in the upper shelf, analysis has also been carried out in the lower shelf and transition region to predict the probability of cleavage fracture using different specimens (e.g., CT and single edge bend SEB). The effect of specimen size, geometry, thickness etc. on the probability of cleavage fracture has also been studied.

1.5 Organisation of the thesis

The thesis is organised into six chapters. The first chapter gives an overview of different simulation methods for ductile and cleavage fracture in materials, limitations of continuum

damage mechanics models and discusses the motivations for the current research. The second chapter provides a comprehensive literature survey of the works carried out by various researchers in the fields of constraint based fracture mechanics, continuum damage mechanics and nonlocal damage mechanics respectively. The details of the development of a new nonlocal damage model along with its FE implementation is described in the third chapter. The new FE model has been used to simulate fracture resistance behaviour of different specimens in the upper shelf and study size and geometry effects. The results have been documented in chapter four. The fifth chapter describes the results of simulation of probability of cleavage fracture in the lower shelf and the transition region using various types of specimens. The effect of specimen size and geometry is also discussed. The broad conclusions from the present research along with the scope for future work, is discussed in chapter six.

Chapter 2

Literature Survey and discussions

In this chapter, a detailed review of literature in the field of nonlocal damage mechanics is presented. The disadvantages of conventional fracture mechanics approach are described and hence the need for continuum damage mechanics models is outlined. The important contributions by different researchers in the field of micro-mechanical modelling for ductile and cleavage fracture are described along with their major limitations (e.g., dependence of solutions on numerical grid size and high computational cost etc.). Different approaches (existing in literature) to remove this mesh dependent nature of the solutions are also discussed.

2.1 Advantages and limitations of conventional fracture mechanics

The possibility of a fracture of a reactor pressure vessel has always been considered as a problem of central concern (Roos et al. 1996, 2006) and has indeed been one of the driving forces behind the development of fracture mechanics. Fracture events in other components are also of significant interest although less critical than a pressure vessel failure. As nuclear reactors age, these concerns may increase due to irradiation embrittlement and the possible occurrence of service-induced defects. Although the fracture mechanics methodology has experienced tremendous advance during the last two decades (Kusmaul and Roos 1985; Roos et al. 1985, 2000a, 2001; Kusmaul et al. 1987), still a number of problems remains to be solved. One group of problems falls mainly under the general heading of whether transferability can be relied upon (Roos 1983; Kusmaul et al. 1984; Katzenmeier et al. 1990). The goal of fracture mechanics is to enable predictions of initiation and propagation or growth of existing or postulated cracks of given configurations in structures of arbitrary geometries and boundary conditions. It should be possible to base a prediction on results from experiments performed on specimens of the same material, but with a geometry that differs from the one under consideration (Roos et al. 1991b; Roos and Eisele 1999; Roos and Föhl 1999). It is here to be understood that the environmental conditions such as for instance temperature and the working medium should remain the same.

This concept of transferability of fracture mechanics results is central to the success of fracture mechanics (Roos 1983; Kussmaul et al. 1984; Katzenmeier et al. 1990; Dlouhý and Chlup 2000; Kozák and Dlouhý 2001; Dlouhý et al. 2004). If we can rely on the transferability, results from experiments conducted on small laboratory specimens can be used to predict the fracture behaviour of a large structure for which an assessment is desired. Complicated, occasionally impossible, full scale testing is thus avoided. The load carrying material in a reactor pressure vessel and in several other components is usually a ferritic steel. It is well known that the temperature (in magnitude as well as the gradient form such as thermal shock) has important effects on the fracture behaviour of such materials (Kussmaul et al. 1990; Eisele et al. 1991; Stumpfrock et al. 1993). At high temperatures (upper shelf), crack growth occurs by a ductile mechanism, either through void growth and coalescence or through shear localisation. For these mechanisms, continued crack growth requires increasing loads.

At low temperatures (lower shelf), the fracture mode is cleavage, which is a highly unstable event. In an intermediate temperature region (the transition region), there may be some amount of stable (ductile) crack growth before final fracture by cleavage and hence cleavage and ductile fracture processes are the two competing mechanisms in this temperature region. Characteristic for the loss of stability due to cleavage is that it cannot be explained within the framework of J_R -philosophy based on experimentally measured resistance curves on the macro level, since a change of micro-mechanism occurs and it is also highly statistical in nature. Obviously, both ductile and cleavage micro-mechanisms are operative and competitive. This behaviour is more marked in the upper transition region and has been recognised in a large variety of experiments over the years. While mechanistic explanations of this type of behaviour have been developed, a full understanding of the temperature transition problem is still lacking.

2.2 Crack initiation and growth modelling in fracture mechanics

Depending on the type of problem under consideration, different ways of modelling can be employed. The state of a loaded crack tip in reality is complicated and a detailed modelling of the structure and the processes is in general not possible. Fracture mechanics modelling can be divided into different levels. At the highest level, the crack tip is assumed to be a point and no

special assumptions of the material behaviour apart from those of the matrix material are made. The bulk of current literature in fracture mechanics use the concept of stress intensity factor (K) in LEFM (linear elastic fracture mechanics) and J-integral in EPFM (elasto-plastic fracture mechanics). There are problems of transferability of the parameter from specimens to components when these single parameter approaches are used (Roos et al. 1983, 1987b, 1993, 2000b; Kussmaul et al. 1984). Also, the crack growth cannot be modelled in an implicit way as the material constitutive relations are same as that of a continuum elasto-plastic description. However, for transferability of fracture toughness value (corresponding to crack initiation, i.e., J_i) from specimens to components, the stretch zone width concept has been developed and successfully used by many researchers (Roos et al. 1987a; Eisele and Roos 1991 etc. among others).

If the decohesive processes (crack initiation and growth) are to be modelled explicitly, the simplest way is to use the so-called cohesive zone models (Dugdale 1960; Barenblatt 1962; Sluys 1992; Sluys and de Borst 1994; Simo et al. 1993; Larsson and Runesson 1994; Oliver 1996; Sluys and Berends 1998). Here, it is assumed that the crack surfaces start to separate if some measure of stress or strain exceeds a critical level. Usually this is taken to be the normal stress perpendicular to the prospective crack plane in a mode-I fracture. Behind the front end of the zone, tractions are assumed to act across the partly opened crack surfaces. The constitutive properties of the zone are embodied in a functional relation between these tractions and the crack surface separation. Once this relation has been established, the motion of the front and rear ends of the zone can be calculated and no further fracture criterion is needed.

In certain situations, even the cohesive zone models are not sufficient to describe the crack tip region behaviour (e.g., inability to predict crack growth direction, absence of internal length scale, over-simplified fracture criteria, i.e., based on critical normal stress etc.). Decohesive processes and other forms of damage may occur out of the crack plane whereby some kind of volumetric modelling is necessary. For this purpose, so called damage mechanics constitutive laws have to be used. In addition to the normal constitutive laws, these equations contain state variables that describe the deterioration of the material. Considerable success in modelling ductile fracture processes has been achieved by the use of the two well-known continuum damage mechanics models such as Rousselier's and Gurson-Tvergaard-Needleman's models

[Rousselier 1987, Gurson 1977, Needleman and Tvergaard 1984, Tvergaard and Needleman 1984].

2.3 Constraint based fracture mechanics modelling

In fracture mechanics theories, it is assumed that the state of stress at a point of the crack front can be described by one or few scalar parameters. In the case of linear elastic material behaviour, the fracture mechanics loading of a crack is defined by the stress intensity factor K_I . In the case of nonlinear ductile material behaviour, the J-integral is used to quantify crack tip loading. Both parameters were derived theoretically from a crack in an infinite plane. Appropriate adjustments have to be made to experimentally determine the characteristic values on small-scale specimens. These adjustments are included in appropriate codes and are taken into account with the help of validity limits of the characteristic values determined. For this reason, characteristic values can only be applied to assess fracture mechanics behaviour of a component if the stress state of the specimen and the component are equal. For general use, appropriate criteria need to be determined. This is achieved using an additional parameter quantifying the stress state by multiaxiality or some function of it.

2.3.1 Crack tip constraint parameter T

One of such parameters is the T -stress parameter, first proposed by Williams (1957). It characterizes the difference between the stress state of a finite specimen and the theoretical result of an infinite plate in the case of linear elastic material behaviour and is defined in the following expression.

$$\sigma_{ij} = \frac{K_I}{\sqrt{2\pi r}} f_{ij}(\theta) + T \delta_{1i} \delta_{1j} \quad (2.1)$$

where T is a constant stress parallel to the crack plane. In the case of simple geometries T can be calculated from K_I using the biaxiality ratio β . In the case of complex geometries, numerical methods have to be used. Sometimes, the parameter T is represented in a non-dimensional form by dividing it with the material yield stress σ_y . The parameter T is however limited to linear elastic material behaviour due to its derivation.

In the current methodology of non-linear fracture mechanics, the crack tip loading parameter is the J -integral, which is complemented by some constraint parameter (e.g., q and Q etc.) [Roos et al, 2005]. In numerical evaluation of the J -integral one often employs other formulations such as domain integral and virtual crack extension methods instead of the line integral. Faleskog and Nordlund (1994) compared the different formulations under both proportional and nonproportional loading and found the differences between the methods insignificant.

2.3.2 Crack tip constraint parameter Q

The J -integral, for a stationary crack, is directly related to the magnitude of the HRR singular field [Hutchinson (1968), Rice and Rosengren (1968)]. Except for large deformation effects in the very near tip vicinity, the HRR-singularity prevails in hardening materials. The extent of the singularity region is, however, in many cases too small for a pure one-parameter description. The observation made by O'Dowd and Shih (1991, 1992, 1994) leads to the following approximate and simple form for the stress field σ_{ij} ahead of a crack tip.

$$\sigma_{ij} = (\sigma_{ij})_{SSY} + Q\sigma_y\delta_{ij} \quad (2.2)$$

where $(\sigma_{ij})_{SSY}$ is the stress-field that results from a standard small scale yielding (SSY) analysis and is thus directly related to the J -integral, σ_y denotes the yield stress and Q is the scaled deviation in hydrostatic stress from the SSY-solution. Thus the parameter Q defines the deviation of the current stress state σ_{ij} from a reference solution, e.g. the HRR-field that presumes non-linear elastic material behaviour. The current stress state σ_{ij} is determined using finite element method. The parameter Q is usually determined by the crack opening stress component at a position, which is of the order 2 to 5 times J/σ_y . This position is usually quite near to the crack tip and therefore requires a mesh with very small elements around the crack tip. The local evaluation at the position between 2 to $5J/\sigma_y$ in front of the crack tip supplies a value representing the behaviour of the component. The evaluation position, however, depends on the loading (i.e., J value). Besides the HRR-solution, additional numerical reference solutions simulating small-scale yielding could also be used. Negative values of T and Q parameters indicate loss of constraint at the crack tip. It has been observed by many researchers [Betegon and Hancock (1991), Hancock et al. (1993)] that Q

can be practically uniquely related to the T -stress (the second term of elastic crack tip stress field expansion, i.e., Eq. (2.1)).

2.3.2 Multiaxiality quotient q as a crack tip parameter

The theoretical background of the multiaxiality quotient q is based on the mechanics concept that shear initiates shear fracture and tension initiates cleavage fracture. The representative shear stress for shear fracture can be defined as

$$\tau_r = \sqrt{(J_1^2 - 3J_2)/3} = -\sqrt{-J_2'} \quad (2.3)$$

and the representative tensile stress is the hydrostatic stress defined as

$$\sigma_m = \frac{J_1}{3} \quad (2.4)$$

where $J_1 = \sigma_1 + \sigma_2 + \sigma_3$ is the first invariant of the stress tensor, $J_2 = \sigma_1\sigma_2 + \sigma_2\sigma_3 + \sigma_3\sigma_1$ is the second invariant of the stress tensor and J_2' is the second invariant of the stress deviator.

Using τ_r and σ_m , the multiaxiality quotient q was first defined by Clausmeyer et al. 1991 and it considers the interaction between shear as well as tension initiating shear and cleavage fracture. The multiaxiality quotient q is therefore calculated from the invariants of the stress tensor as

$$q = \frac{\tau_r}{\sigma_m} = \sqrt{3(1 - 3J_2/J_1^2)} = \frac{1}{\sqrt{3}} \frac{\sigma_{eq}}{\sigma_{hydro}} \quad (2.5)$$

where σ_{eq} and σ_{hydro} represent von Mises equivalent stress and mean hydrostatic stress respectively. The parameter q is thus proportional to the ratio of representative shear stress and representative tensile stress. The case of a pure hydrostatic stress state where $\tau_r = 0$ and therefore $q = 0$ indicates the highest possible degree of multiaxiality or constraint for which shear processes are restrained. The quantification of the transition from shear fracture to cleavage fracture is one of the major questions in the safety analysis of components and this is now possible with the help of q .

To predict the different fracture behaviours of specimens and components, it is necessary to determine the change of the multiaxiality quotient in the region ahead of crack tip. The criteria for suppression of plastic flow and hence onset of cleavage fracture is usually defined as the condition when $q < q_c (= 0.27)$ and the criteria for unlimited plasticity is defined when

$q = 0.87$ (Roos et al. 1993). As a result of numerous investigations, a representative range r_i (distance from the crack tip) for analysis of the stress state was derived by Roos et al. 1993. This range is given by either $0 < r_i < 0.3(W - a)$ or $0 < r_i < r(q = 0.87)$, whichever is less. The extensive investigations by Roos et al. 1993 showed that the analysis region r_i has to be transferred from the small specimen to the component in absolute dimensions. Since crack growth is significantly controlled by the multiaxiality of the stress state, quantification of multiaxiality is performed by integration of the multiaxiality quotient over the above-mentioned region r_i ahead of the cracked section (Roos and Eisele 1999, Roos et al 2001). A quantitative statement about the possibility of cleavage fracture or stable crack growth after crack initiation can be expressed as follows. If

$$J > J_i \text{ and } \frac{\int_0^{r_i} q(y) dy}{\int_0^{r_i} q_c dy} \leq 1, \quad (2.6)$$

then brittle fracture can be expected. If

$$J > J_i \text{ and } \frac{\int_0^{r_i} q(y) dy}{\int_0^{r_i} q_c dy} \gg 1, \quad (2.7)$$

then stable crack extension will follow the crack initiation. If

$$J > J_i \text{ and } \frac{\int_0^{r_i} q(y) dy (\text{component})}{\int_0^{r_i} q(y) dy (\text{specimen})} \cong 1, \quad (2.8)$$

then the crack resistance curves of the specimen and the component are comparable. Therefore, similar crack growth in the specimen and in the component can be expected at the same J-integral value. This provides a fracture mechanics assessment concept for a reliable safety analysis of cracked components to be used for all crack sizes. The applicability of the above criteria was extensively studied by Roos et al. 2005 with the help of several experimental and theoretical examples.

For a stationary crack front the J -integral is usually reasonably independent of the integration region if the global loading conditions are reasonably near proportional loading. For a growing crack tip in a material that behaves according to an incremental plastic constitutive law, the loading state is very far from proportional in the crack front region [Nilsson (1992)]. In fact, the order of the singularity for a growing crack in such a material is of such an order that an integration path taken infinitesimally close to the tip would yield a zero value for the J -integral. In order to obtain integration region independent values, the integration path must be taken so remotely from the tip that proportional loading conditions should prevail. The J -integral value evaluated in this way is termed J_F (far-field J).

A common approach is instead to neglect the non-proportionally deforming region and calculate the J -integral assuming the tip has been stationary at its instantaneous position during the loading process. The J -integral value so obtained is termed J_D (deformation theory J). In a numerical investigation by Nilsson (1992) shows that J_D and J_F are approximately equal for two-dimensional problems. Hence, it can be assumed that crack growth along the crack front is governed by

$$J(P, a) = J_R(\Delta a, \beta, Temp) \quad (2.9)$$

where P is measure of applied load, β is some suitable constraint parameter such as q , T , or Q , J_R is the material resistance which is a function of constraint and the crack growth Δa . In fully three-dimensional cases, it is assumed that Eq. (2.9) holds locally at every point along the crack border. The fracture resistance may also depend on the temperature. Conventional fracture mechanics theory does not suggest any way of finding this dependence except for experimental determination. The criterion is also the same for cleavage as well as ductile conditions and hence the distinction between the mechanisms is only given by the value of the material fracture resistance (i.e., J_R curve).

For a propagating crack the constraint factor determination becomes more involved than for stationary crack. Whether the fields in the vicinity of a growing crack in an elastic-plastic material can be written in a form analogous to Eq. (2.2) is not known and it appears uncertain that such an expression should hold. Instead, a constraint parameter Q corresponding to the J_D concept can be considered, i.e., Q is calculated for a stationary crack of the current length subjected to the same loading history. The same type of arguments as for the crack tip

characterising capacity of J -integral was put forward to justify such an approach [Trädegård et al. (1998)]. The characterisation of stationary cracks with J and Q serves reasonably well for growing cracks at least at up to moderately high load levels. The ductile crack initiation (J_i value corresponding to the stretched zone width [Roos et al 1987a, Eisele and Roos 1991]) is relatively insensitive to the constraint level while the J -levels for continued crack growth decrease with increasing Q . It is also not possible to predict the ductile-cleavage transition without resorting to micro-mechanical models. The only way within the conventional type of modelling is the empirical approach, which is to perform experiments under different combinations of J and Q and observe whether cleavage or ductile crack growth results. It was also observed in many experiments carried out by different researchers that the cleavage fracture propensity increases with increasing level of Q .

2.4 Micromechanical models for cleavage fracture (lower shelf)

For initiation of cleavage fracture, several micro-mechanical models have been proposed in literature. Many of these models share the common feature that no modification of the material constitutive laws is performed. It is thus assumed that cleavage fracture occurs before any material degradation due to void growth etc. has taken place [true only in pure lower shelf region]. When treating problems of transition from ductile to cleavage fracture, combination of cleavage and degradation models is necessary.

The micro-mechanical model of Ritchie et al. (1973) [RKR or Ritchie-Knott-Rice's model] predicts transgranular cleavage fracture if the maximum principal stress reaches a critical value σ_c at a critical distance r_c ahead of the crack tip. Later, Curry and Knott's model [Curry and Knott (1978,1979)] modified RKR model by stating that cleavage fracture occurs if the maximum principal stress reaches a critical value over a characteristics volume ahead of the crack tip. A model for the effect of constraint can be obtained by applying the RKR criterion to the crack tip stress field according to Eq. (2.2). The ratio between the critical J value in a finite body (where Q is not zero) to the critical J value in an infinite body ($J = J_0$ for a fully constrained body where $Q = 0$) can be written as (Landes 1996, Miranda and Landes 2001)

$$\frac{J}{J_0} = \left(1 - Q \frac{\sigma_y}{\sigma_c}\right)^n \quad (2.10)$$

where η is equal to $n+1$ (n being the hardening exponent in the power hardening law-Hollomon's law) describing the true stress-strain behaviour of the material.

The inherently random nature of cleavage fracture has prompted many developments of statistical models of fracture. Most of these are based on the so-called weakest link assumption, which leads to the following expression for the probability of fracture, i.e.,

$$P_f = 1 - \exp\left(-\int_V g(\sigma_i^i) \frac{dV}{V_{ref}}\right) \quad (2.11)$$

where V is the volume of the plastically deformed zone, V_{ref} is the reference volume which is taken many times as 0.001 mm^3 . The function $g(\sigma_i^i)$ expresses the probability of failure of an infinitesimal volume i (having volume dV) according to the expression

$$dP_f = g(\sigma_i^i) \frac{dV}{V_{ref}} \quad (2.12)$$

where σ_i^i is the maximum principal stress acting at a material point i in the plastically deformed region having volume dV . It is shown by Wallin (1984) that under one-parameter crack tip control (i.e., when constraint effect is not taken into consideration) in terms of K (stress intensity factor) or alternatively J (i.e., J -integral under more widely spread plasticity), the fracture probability can be described by

$$P_f = 1 - \exp\left(-\frac{B}{B_0} \left(\frac{J}{J_0}\right)^2\right) \quad (2.13)$$

or in terms of mode-I stress intensity factor K_I as

$$P_f = 1 - \exp\left(-\frac{B}{B_0} \left(\frac{K_I}{K_0}\right)^4\right) \quad (2.14)$$

These expressions result irrespective of the form of the g -function, provided that the integral in Eq. (2.12) exists.

As we obtain the same expressions for the probability of failure (output) even when different forms of the g -function are used, it is not possible to determine the parameters (input variables) or the form of the function using only a single output. This is equivalent to saying that different combinations of input parameters or different input functions lead to the same output. Some implications of this fact have been discussed by Gao et al. (1998b, 1999) and

they also discuss the problem of estimation of the parameters in the probabilistic assumptions. When the single-parameter (K or J) dominated crack tip field no longer prevails, Eq. (2.13) loses its applicability and the functional form of $g(\sigma_I^i)$ may influence the resulting probability. In most studies, the following form for the g -function is used, i.e.,

$$g(\sigma_I^i) = \left(\frac{\sigma_I^i}{\sigma_u} \right)^m \quad (2.15)$$

where σ_u is called Weibull's scaling parameter and m is called Weibull's shape parameter or Weibull modulus and the theory is called Weibull's two-parameter theory. Later, many researchers argued that there exists a threshold stress σ_{th} , only above which one can expect a finite probability of fracture (however small). This is in contradiction to the two-parameter theory where a finite probability of cleavage fracture is predicted even if the applied maximum principal stress is very small. This new theory expresses the g -function as

$$g(\sigma_I^i) = \left(\frac{\sigma_I^i - \sigma_{th}}{\sigma_u} \right)^m \quad (2.16)$$

and this is known as Weibull's three parameter theory. However, estimating the threshold stress is many times cumbersome and often explaining it in terms of actual experimental observation is not straightforward.

It should be pointed that there is no fundamental basis for the form of Eq. (2.16). It is simply a convenient mathematical expression that can be fitted to the experimental results by varying the material constants. A function based on more fundamental principles is of interest to the researchers. There is for instance some evidence that plastic deformation should in some way influence the propensity for cleavage fracture. Wang (1991) performed calculations for crack tip stress fields controlled by K_I and T stress as the constraint parameter using modified boundary layer (MBL) conditions. The trend of the mean value is very similar to the behaviour of the RKR-model. Since the effect of constraint (measured as T or Q) essentially results in a hydrostatic stress field, the plastic zone is not much affected. The effect of the additional stresses is nearly the same as shifting the threshold stress and thus the same type of distribution as in the one-parameter case results.

A number of investigations show that under one parameter controlled situations, deviations from the theoretical result [Eq. (2.14)] occur. These deviations are most noticeable at low

fracture toughness levels and therefore a lower limit has been suggested. Thus, for instance, Anderson et al. (1994) suggested that

$$P_f = 1 - \exp\left(-\frac{B}{B_0}\left(\frac{K_I - K_{\min}}{K_0 - K_{\min}}\right)^4\right) \quad (2.17)$$

Here K_{\min} is a constant and it has been suggested that it should be assigned the value 20 MPa for ferritic steels. Similar expressions have also been suggested by other authors. It may be noted that Eq. (2.17) is purely empirical and there is no fundamental theory behind the expression. Various explanations have been given as to whether there should exist a definite lower limit value of toughness.

One reason for the existence of a minimum value is that a cleavage event initiated at some point such as an inclusion does not necessarily lead to a total cleavage fracture. The cleavage crack must also be able to propagate through the interface between the inclusion and the matrix and grow further into the matrix material. Narström and Isacson (1999) performed experiments in the upper part of the transition region. They observed that the number of cleavage initiation sites increase with temperature even though the general character of the fracture becomes increasingly ductile, which supports the view that arrest of cleavage attempts is a phenomenon that contributes to the transition behaviour.

Gao et al. (1999) applied the concept of weakest link modelling to 3D cases of plates with semi-elliptic surface cracks found that their model is able to capture constraint effects satisfactorily. In their analysis, they utilised the following version of the weakest link approach, i.e.,

$$P_f = 1 - \exp\left(-\left(\frac{\sigma_w - \sigma_{th}}{\sigma_u - \sigma_{th}}\right)^m\right) \quad (2.18)$$

where σ_{th} is the threshold value of Weibull stress which is constant and the Weibull stress is evaluated using the expression

$$\sigma_w^m = \frac{1}{V} \int_V (\sigma_i^i)^m \frac{dV}{V_{ref}} \quad (2.19)$$

where σ_i^i is the maximum value of principal stress at the material point i having volume dV and σ_u corresponds to the value of Weibull stress for 63.2% of failure probability. Under

two-dimensional plane strain conditions, these expressions reduce to Eq. (2.17) and are thus three-dimensional versions of that expression.

2.4.1 Beremin's model for Cleavage fracture

The cleavage fracture in a material usually originates from the microcracks, which are formed by different mechanisms. The microcracks are formed due to an inhomogeneous distribution of plastic deformation within the grains. It is called slip-initiated cleavage [Beremin (1983), Mudry (1987)]. In mild steels, the cracked grain boundary carbides also originate the microcracks. This occurs when the stress normal to the planes of carbide particles (i.e., weakest planes inside the carbide particles which are susceptible for fracture) is sufficiently high. This critical stress σ_c required for the separation of cleavage facets, can be related to the length l_0 of a microcrack by the relation

$$\sigma_c = \sqrt{\frac{2E\gamma}{\pi(1-\nu^2)l_0}} \quad (2.20)$$

Where E is Young's modulus of elasticity, ν is the poisson's ratio, and γ is the surface energy. The length l_0 is related to the dimensions of the relevant metallurgical features associated with stable microcracks. In mild steel, the grain boundary carbide width is considered as the relevant metallurgical length.

The probability of finding a microcrack of critical length is a function of the volume of material involved. It is very difficult to find out this probability experimentally. In a population of microcracks, the fracture will take place at the site of longest microcrack. Therefore the knowledge of distribution of microcracks is required for the longer ones. Let us assume that the stressed volume can be divided in smaller volumes V_0 . This volume V_0 should be large enough to the extent that the probability of finding a microcrack of reasonable length is not very small and the statistical independence of neighbouring volumes can be assumed. In each volume, the probability of finding a crack of length between l_0 and $l_0 + dl_0$ can be written as

$$P(l_0)dl_0 = \frac{\alpha}{l_0^\beta} dl_0 \quad (2.21)$$

where α and β are material constants for a particular value of V_0 . Hence in a given volume where the maximum principal stress level is σ_i^i , the probability of failure is expressed as

$$P(\sigma_i^i) = \int_{l_0^c}^{\infty} P(l_0) dl_0 = \left[\frac{\alpha}{(1-\beta)} \cdot \frac{1}{l_0^{\beta-1}} \right]_{l_0^c}^{\infty} = \frac{\alpha}{(\beta-1)} \cdot \frac{1}{l_0^{c(\beta-1)}} \quad (2.22)$$

where l_0^c is given by Eq. (2.20) as

$$l_0^c = \frac{2E\gamma}{\pi(1-\nu^2)(\sigma_i^i)^2} \quad (2.23)$$

Substituting Eq. (2.23) into Eq. (2.22), we obtain

$$P(\sigma_i^i) = \left(\frac{\sigma_i^i}{\sigma_u} \right)^m \quad (2.24)$$

where $m = 2\beta - 2$ and $\sigma_u^m = \frac{(\beta-1)(2E\gamma)^{(\beta-1)}}{\alpha \cdot \pi^{\beta-1} \cdot (1-\nu^2)^{\beta-1}}$, σ_u turns out to be a material constant almost

independent of temperature if it is assumed that γ does not change with temperature. The stressed region of the specimen is divided into n volumes of V_i each which are subjected to a quasi-homogeneous stress state σ_i (the maximum principal stress in the volume i). This implies that the stress variation in V_i is small which is reasonable if V_i is chosen small

enough. The failure probability of the volume V_i is expressed as $P(\sigma_i^i) = \left(\frac{\sigma_i^i}{\sigma_u} \right)^m$. The cumulative probability of failure for the entire specimen or component is written as

$$P_R = 1 - \prod_{i=1}^n [1 - P(\sigma_i^i)] \quad (2.25)$$

Since $P(\sigma_i^i)$ is small, one can write the following relation

$$\ln(1 - P_R) = \sum_{i=1}^n \ln[1 - P(\sigma_i^i)] \approx \sum_{i=1}^n -P(\sigma_i^i) \quad (2.26)$$

In order to determine the failure probability for homogeneously stressed specimens, let us assume a constant maximum principal stress σ_I over the whole volume and hence Eq. (2.26) can be written as

$$\ln(1 - P_R) = -\frac{V}{V_0} \left(\frac{\sigma_I}{\sigma_u} \right)^m \quad (2.27)$$

which is one form of Weibull expression. The average stress at rupture $\langle \sigma_R \rangle$ can be written as

$$\langle \sigma_R \rangle = \sigma_u \left(\frac{V_0}{V} \right)^{1/m} \left(\frac{1}{m} \right)! \quad (2.28)$$

It may be noted that m and σ_u are the two parameters required for determination of probability of failure of the entire specimen or component. However, V_0 must be of the order of ten grains, i.e. small enough to neglect stress gradients in V_0 and large enough to assume statistical independence of the individual volumes. If very small stress gradients are present in the specimen, then V_0 can be arbitrarily chosen. Usually V_0 is chosen as a cubic volume containing about 8 grains of the material, i.e. $100 \times 100 \times 100 \text{ } \mu\text{m}^3$.

For non-homogeneously stressed specimens, Eq. (2.24) is used for calculating failure probability. Substituting Eq. (2.24) into Eq. (2.26), we obtain

$$\ln(1 - P_R) = \sum_{i=1}^n -P(\sigma_i^i) = - \sum_{i=1}^n \left(\frac{\sigma_i^i}{\sigma_u} \right)^m \frac{V_i}{V_0} = \left[- \left(\frac{\sigma_w}{\sigma_u} \right)^m \right] \quad (2.29)$$

where V_i is the volume of the i^{th} element experiencing the maximum principal stress σ_i^i and σ_w is called the Weibull stress. Eq. (2.29) can be rearranged to express the probability of failure (P_R or P_f) for the non-homogeneously stressed specimen as

$$P_f = 1 - \exp \left[- \left(\frac{\sigma_w}{\sigma_u} \right)^m \right] \quad (2.30)$$

The expression for the Weibull stress σ_w can be obtained from Eq. (2.29) as

$$\sigma_w = \sqrt[m]{\sum_{i=1}^n (\sigma_i^i)^m \frac{V_i}{V_0}} \quad (2.31)$$

2.4.2 Maximum Likelihood method for determination of Weibull parameters

In this approach, the values of the two parameters m and σ_u are required to be determined such that they are most likely to describe the experimental data [Khalili and Kromp (1991)]. The probability that, for an estimated set of Weibull parameters, the experimental results would have occurred, should be maximized. This is equal to the probability that all σ_i^i values occur simultaneously which is given by the product of all the fracture probabilities, i.e.,

$f_N = f(\sigma_1^1) \cdot f(\sigma_1^2) \dots f(\sigma_1^N)$. This is defined as the maximum likelihood function F_L , which can be written as

$$F_L = \prod_{i=1}^N f(\sigma_{w_i}) \quad (2.32)$$

In order to maximize the likelihood function F_L , the partial derivatives of the function with respect to m and σ_u are set to zero. Since taking the derivatives of a sum is easier than that of a product, the derivation is done on $\ln F_L$ and it can be written as

$$\ln F_L = N \cdot \ln\left(\frac{m}{\sigma_u}\right) + \sum_{i=1}^N \ln\left(\frac{\sigma_{w_i}}{\sigma_u}\right)^{m-1} - \sum_{i=1}^N \ln\left(\frac{\sigma_{w_i}}{\sigma_u}\right)^m \quad (2.33)$$

Using the condition that $\frac{\partial \ln F_L}{\partial \sigma_u} = 0$, we obtain

$$\sigma_u = \sqrt[m]{\frac{1}{N} \sum_{i=1}^N (\sigma_{w_i})^m} \quad (2.34)$$

Upon using the other condition, i.e., $\frac{\partial \ln F_L}{\partial m} = 0$, we obtain

$$\frac{N}{m} + \sum_{i=1}^N \ln(\sigma_{w_i}) - \sum_{i=1}^N \ln \sigma_u - \left[\frac{\sum_{i=1}^N (\sigma_{w_i})^m \cdot \ln(\sigma_{w_i})}{(\sigma_u)^m} - \frac{\left\{ \sum_{i=1}^N (\sigma_{w_i})^m \right\} \cdot \ln \sigma_u}{(\sigma_u)^m} \right] = 0 \quad (2.35)$$

Substituting Eq. (2.34) into Eq. (2.35), we obtain

$$\frac{N}{m} + \sum_{i=1}^N \ln(\sigma_{w_i}) - N \cdot \frac{\sum_{i=1}^N (\sigma_{w_i})^m \cdot \ln(\sigma_{w_i})}{\sum_{i=1}^N (\sigma_{w_i})^m} = 0 \quad (2.36)$$

Equation (2.36) is nonlinear and has to be solved by an iterative process.

2.5 Micromechanical modelling of ductile crack growth (upper shelf)

Ductile crack growth in steels proceeds by one of two mechanisms (i.e., void nucleation, growth and coalescence and shear localisation). The first one, which dominates at least in modelling, is when the crack grows through void nucleation, growth and subsequent coalescence [Xia and Shih 1995b]. The second one is shear localisation of plastic flow as observed in deformation of thin metal sheets. The first mechanism is typical for materials with

a high degree of hardening, while the latter occurs for high strength materials with a low degree of hardening.

The bulk of micro-mechanical modelling approaches deal with the first type of mechanism and there is very little concern for modelling the second mechanism of ductile crack growth. The shear localisation process is also dependent on void formation in the material but of another size scale and in other directions than the void growth and coalescence mechanism (Tvergaard 1981). When considering crack growth due to the void mechanism it unrealistic to perform full calculations with the voids explicitly modelled. Instead, homogenised models, also called continuum damage constitutive relations are used. A variety of such laws exist in the literature. They do not differ very much and the mostly used models are Rousselier's and Gurson-Tvergaard-Needleman's (GTN) models [Rousselier (1987), Gurson (1977), Needleman and Tvergaard (1984), Tvergaard and Needleman (1984)]. The yield condition for the Rousselier model is written as

$$\phi = \frac{\sigma_{eq}}{1-f} + D\sigma_k f \exp\left(\frac{\sigma_{hydro}}{(1-f)\sigma_k}\right) - R(\varepsilon_{eq}) = 0 \quad (2.37)$$

where σ_{eq} is the von-Mises equivalent stress, D and σ_k are Rousselier's constants, σ_{hydro} is the mean hydrostatic stress, f is the void volume fraction (which is a measure of ductile damage, $f = 0$ corresponds to defect-free material whereas $f = 1$ corresponds to completely damaged material, a crack) and $R(\varepsilon_{eq})$ is the material stress-strain curve, which is a function of equivalent plastic strain ε_{eq} . The details of the development of the model from principles of thermodynamics are given in Appendix-A.

The yield condition for the GTN model is written as

$$\phi = \frac{\sigma_{eq}^2}{\sigma_m^2} + 2q_1 f^* \cosh\left(q_2 \frac{3}{2} \frac{\sigma_{hydro}}{\sigma_m}\right) - 1 - q_3 f^{*2} = 0 \quad (2.38)$$

where σ_m is the true stress in the matrix material which is a function of equivalent plastic strain ε_{eq} in the matrix material (i.e., the material stress-strain curve), q_1 , q_2 and q_3 are the constants introduced by Tvergaard and Needleman (1984) in order to simulate the observed experimental fracture behaviour in many different materials more accurately.

The function f^* , called modified void volume fraction was also introduced by Tvergaard and Needleman (1984) and the modified void volume fraction f^* is related to the actual void volume fraction f through the relationship

$$f^* = \begin{cases} f & \text{if } f \leq f_c \\ f_c + \frac{f_u^* - f_c}{f_f - f_c} (f - f_c) & \text{if } f > f_c \end{cases} \quad (2.39)$$

where f_c is the critical void volume fraction (signifying void coalescence) and f_f is the actual void volume fraction at final fracture and f_u^* is the modified void volume fraction at fracture (usually $f_u^* = \frac{1}{q_1}$).

These yield functions are also valid for an isotropically strain hardening material when the yield stress of the matrix material is replaced by the current flow stress (which is a function of equivalent plastic strain). It can also be easily modified to take into account the kinematic hardening behaviour as observed in low-cycle fatigue loadings. The constants q_1 , q_2 and q_3 depend upon the material. A calibration method for q_1 , q_2 and q_3 for a strain hardening material has been developed and described by Faleskog et al. (1998) by comparing the response of a GTN-cell with an equivalent cell containing one explicitly modelled void. The plastic strain increment follows from the Prandtl-Reuss flow rule and is written as

$$\dot{\epsilon}_{ij}^p = \frac{1}{\kappa} \frac{\partial \phi}{\partial \sigma_{ij}} \frac{\partial \phi}{\partial \sigma_{kl}} \dot{\sigma}_{kl} \quad (2.40)$$

where $\dot{\sigma}_{kl}$ is the Jaumann rate of the Cauchy stress and κ is the hardening parameter. The void growth rate is obtained using the plastic incompressibility condition of the matrix material as

$$\dot{f} = (1-f) \dot{\epsilon}_{kk}^p \quad (2.41)$$

The voids quantified by f are either initially present or nucleated by the deformation process. In the latter case, some void nucleation law has to be specified. Chu and Needleman (1980) proposed the following law for calculating increment of void volume fraction, which tells that the increase in void volume fraction f is due to void growth and void nucleation processes. Hence, it includes the growth law, i.e., Eq.(2.41) and a strain controlled void nucleation mechanism (also a stress-controlled mechanism if it is favourable in the material) which is described as

$$\dot{f} = (1-f)\dot{\varepsilon}_{kk}^p + A\dot{\varepsilon}_{eq}^p + B(\dot{\sigma}_{eq} + \dot{\sigma}_{hydro}) \quad (2.42)$$

where the constants A and B for strain-controlled nucleation are written as

$$A = \frac{f_N^\varepsilon}{\sqrt{2\pi}s_N^\varepsilon} \exp\left(-\frac{1}{2}\left(\frac{\varepsilon_{eq}^p - \varepsilon_N}{s_N^\varepsilon}\right)^2\right), \quad B = 0 \text{ for } \dot{\varepsilon}_{eq}^p > 0 \quad (2.43)$$

and for stress-controlled nucleation

$$A = 0, \quad B = \frac{f_N^\sigma}{\sqrt{2\pi}s_N^\sigma} \exp\left(-\frac{1}{2}\left(\frac{\sigma_{eq} + \sigma_{hydro} - \sigma_N}{s_N^\sigma}\right)^2\right) \text{ for } \dot{\sigma}_{eq} + \dot{\sigma}_{hydro} > 0 \quad (2.44)$$

where f_N^ε and f_N^σ are the values of void volume fractions of void nucleating particles at mean nucleation strain and stresses ε_N and σ_N respectively. s_N^ε and s_N^σ are standard deviations of equivalent plastic strain and sum of equivalent and hydrostatic stress respectively responsible for nucleation assuming a Gaussian distribution. The superscripts ε and σ denote the strain- and stress-controlled nucleation respectively. In this way a number of additional constants is introduced which increases the possibility of fitting the model to data, but on the other hand complicates the parameter identification process. When f is equal to $1/q_1$, the material loses its load bearing capacity.

One fundamental problem with the classical or local Rousselier and GTN-law is that the damage parameter (at the crack tip) approaches the critical value at any finite load when we evaluate the damage parameter very near to the crack tip (i.e., the length of the crack tip finite element tending towards zero). This means that crack growth would commence immediately upon any load application, however small. The only way to mitigate this problem is to introduce a characteristic length in some way. Preferably, this should be done by modification of the material constitutive law introducing the characteristic length parameter. However, a far more common way is to limit the strain levels by letting the elements in a finite element mesh to have a certain size (related to material length scale). The size of the elements in the crack tip vicinity is thus equivalent to a constitutive assumption. This fact seems to have escaped some of the investigators in this area.

Before applying the local models to simulate crack growth in experiments, the initial task is to determine the parameter f_0 (initial volume fraction of relevant inclusions which form voids upon onset of plastic deformation either by debonding from the matrix or particle fracture) and

l_c (characteristic length parameter which is of the order of mean distance between relevant inclusions). The parameters f_0 and l_c are considered as free parameters to be determined from optimization of numerical simulation results (e.g., point of drastic load drop before final fracture in case of notched tensile specimens or fracture resistance curve in case of fracture mechanics specimens) with those of experiment. These parameters are however to be kept fixed (once estimated) for further analysis of different cases of a specific material.

Gao et al (1998a) applied this type of analysis to both nominally two-dimensional tests as well as to the tests with surface cracks performed by Faleskog et al. 1991, Faleskog 1994, Faleskog 1995. The crack propagation results in all the considered cases were well predicted by the local damage model, however the model was less accurate in predicting the onset of ductile crack growth (i.e., crack initiation). Several similar analyses of experiments have been performed (e.g., Rousselier 1987, 2001; Bilby et al 1993, Kussmaul et al. 1995; Brocks et al 1995; Pitard-Bouet et al. 1999). As mentioned earlier, the parameters f_0 and l_c were determined from experiments (preferably a fracture mechanics experiment). It may also be noted that the computational problems associated with the damage based modelling are not trivial. Gullerud et al. (2000) has suggested a number of options in order to obtain reliable results. Among other things they derive the requirements on the load step length.

One major advantage of micro-mechanical modelling (or continuum damage mechanics) when used for prediction of ductile crack growth is that there is no longer any need to use crack growth criteria like Eq. (2.9) and possible constraint effects are automatically accounted for. It should, however, be realised that the outlined scheme is still an over-simplified model. Much research is currently performed to increase the precision and applicability of the damage modelling. It may of course be questioned whether ductile crack growth theory needs to be developed much further. The currently used models provide an accuracy that from a safety point is probably quite sufficient for the problem of ductile crack growth.

The real challenge to micro-mechanical modelling is to predict the transition phenomenon of fracture toughness as discussed below. This rather satisfactory state of affairs for modelling of ductile crack growth applies to the mode-I situation. Mixed mode cases have not been investigated to same degree of understanding as that of mode-I fracture. Experimental studies indicate that the shear localisation mechanism becomes increasingly important, as the amounts

of modes other than mode-I are present. It is likely that the micro-mechanical methods developed for ductile crack growth of the type described above may also be used with success for other crack growth mechanisms. Inter-granular fracture is often regarded as a quasi-brittle process. Fracture in these cases develops as decohesion of relatively weak material along the grain boundaries [Sluys (1992); Sluys and de Borst (1994); Oliver (1996); Sluys and Berends (1998)]. This may be a highly ductile process while the grains themselves experience little plastic deformation. In fact, the cohesive zone models or cell models of the type described can presumably be used provided that the material behaviour of the grain boundaries is well modelled.

2.6 Micro-mechanical modelling in the transition regime

A main feature of ferritic steels is that they exhibit a transition from ductile to cleavage behaviour as the environmental temperature is lowered and/or the applied loading rate is increased. It has also been realised since long that the transition is also dependent of the geometry of the body. In general small specimens have a ductile behaviour while the large structure may fracture in a cleavage mode at the same temperature. Thus tests, which usually are performed on small specimens, may be misleading.

All models of the transition phenomenon are based on the idea of competing mechanisms of ductile and cleavage fracture. Thus both the cleavage and the ductile processes are modelled and the critical event is determined by the mechanism that is most favourable under the actual conditions. Most success has been achieved about the influence of geometry on the transition behaviour at a constant temperature. A simple model can be obtained as follows. Assume that ductile initiation occurs when the J -level reaches J_c^{duct} and that cleavage fracture follows Eq. (2.10). Then cleavage is expected to occur if (Landes 1996, Miranda and Landes 2001)

$$\frac{J_c^{duct}}{J_0} = \left(1 - Q \frac{\sigma_y}{\sigma_c} \right)^\eta \quad (2.45)$$

In this relation the geometry effect enters through Q and clearly increasing values of this parameter promote cleavage fracture. A more realistic model of the same problem (incorporating ductile growth before a possible cleavage fracture) can be obtained by combining the continuum damage mechanics models discussed above with the weakest link modelling according to Eq. (2.11). This is the topic treated by Xia and Shih (1996) among

others. These studies generally show that the probability of cleavage fracture increases with crack growth. The quantitative predictions are however difficult to verify by experiments, since a large amount of tests is usually needed to support probabilistic statements.

While the geometry effects can be successfully modelled, the effect of temperature is still insufficiently understood. The models that are found in literature basically ascribe the problem of temperature transition to a decrease of the yield stress (with increasing temperature). This is clearly not adequate since the change of yield stress is generally too small to furnish an explanation. The temperature transition occurs over a relatively narrow temperature interval. Conventional constitutive properties do not change appreciably over this temperature interval nor does the structure of material, i.e., grain size, inclusion density etc. It thus remains to understand which changes in the material behaviour are responsible for the transition behaviour. Since the transition is strain rate sensitive it is likely that these changes are to be found in materials response to the loading rate. While purely empirical methods to describe the transition through the so-called master curve are successful, insignificant steps have been taken in order to understand why there is such a transition behaviour common to most ferritic steels. The remarkable fact that it is indeed possible to construct a master curve, should tell us a lot about the causes of the transition behaviour.

In the application of fracture mechanics to nuclear technology, there are further problem areas in addition to basic ones outlined here. In connection with certain types of accidental conditions, the possible benefits of so-called warm pre-stressing (WPS) have received much attention in the past. By the term WPS, it is meant that the loading of the cracked structure at a high temperature may enhance its fracture properties at a lower temperature to some extent. This effect is a consequence of the introduction of residual stresses, crack tip blunting and local hardening of the material etc. At the other hand, it can also be envisioned that ductile damage can be initiated in the crack tip region at the high warm loading level, which may counteract the positive effects of the residual stresses. Micro-mechanical modelling can be used here in determining the limits of the WPS argument. Likewise, micro-mechanical modelling can be used to assess the probability of a cleavage fracture at the lower temperature. Presumably, the methods of micro-mechanical modelling as sketched above can be used for this purpose with the additional difficulty to determine the material response at different temperatures.

Repeated load applications up to near critical levels (i.e., initiation level for ductile growth) where material damage occurs and accumulates with the load cycles is a topic that has not been very much studied. It borders on the research of fatigue problems, but for such high load levels the mechanisms are more like those of ductile crack growth than those typical of fatigue crack growth. Kaiser (1983) considered crack growth due to cyclic loading in this regime by use of conventional non-linear fracture mechanics. Again micro-mechanical modelling could be an attractive way of approaching the problems. The main challenge in this respect seems to be the formulation of laws for development of plastic deformation and damage under cyclic loading. While conventional fracture mechanics is capable of predicting crack growth behaviour if sufficient experimental observations are available, micro-mechanical modeling can both increase the accuracy of these predictions and model phenomena that are inaccessible by the conventional theory such as the ductile-cleavage temperature transition and it may serve as a tool by which more simplified engineering methods can be validated.

2.7 Mesh dependency of conventional damage mechanics models and the concept of nonlocal damage mechanics

The very fact that damage mechanics models use a continuous representation of cracks renders them particularly suitable for numerical simulations. Damage formulations can be fitted into nonlinear finite element algorithms and implemented in simulation codes with relative ease and they do not rely on the special discretisation and remeshing techniques used in numerical fracture mechanics. It is an essential requirement of finite element formulations that the approximate solutions provided by them converge to the actual solution of the boundary value problem when the discretisation is refined.

In the early 1980s, however, it was found that finite element solutions of softening damage [Breklemans et al. (1992)] and plasticity problems do not seem to converge upon mesh refinement [e.g., Pietruszczak and Mróz (1981); Bažant et al. (1984); Schreyer and Chen (1986)]. As a matter of fact, they do converge to a solution, but this solution is physically meaningless. Accordingly, the mesh sensitivity of the analyses is not caused by the numerical methods which are used, but by the fact that the underlying continuum model does not properly describe the physical phenomena that take place [Bažant et al. (1984); Triantafyllidis and Aifantis (1986); de Borst et al. (1993)].

The failure of continuum damage models in describing the fracture processes can be understood if one realises that the concept of a continuous damage variable presumes a certain local homogeneity (i.e., at least smoothness of the micro-structural damage distribution). But the continuum models based on this concept allow for discontinuous solutions, in which the development of damage localises in a surface while the surrounding material remains unaffected. This localisation of damage is in contradiction with the supposed smoothness of the damage field and thus affects the physical relevance of the model. Two possible ways out of this conflict present themselves: either the smoothness requirement must somehow be eased, or the continuum formulation must be modified in such a way that a larger degree of smoothness is ensured.

The cohesive zone models of Dugdale (1960) and Barenblatt (1962) and the fictitious crack model proposed by Hillerborg et al. (1976) can be considered as examples of the first category. They assume that the nonlinearity is concentrated in a plane in front of the actual, discrete crack. The faces of this fictitious crack can still transfer stresses, with a magnitude, which is a function of their separation. More recent studies have shown how such functions can be derived from continuum models [Sluys (1992); Sluys and de Borst (1994); Simo et al. (1993); Larsson and Runesson (1994); Oliver (1996); Sluys and Berends (1998)]. It may be noted that, the above approach is also closely related to nonlinear fracture mechanics, since it assumes a discrete crack.

The second strategy concentrates on preventing the so-called pathological localisation of damage and deformation. Stability and bifurcation analyses of plasticity and damage formulations have provided a reasonable understanding of the origins of the behaviour and the conditions under which it occurs [Hill (1962); Rudnicki and Rice (1975); Pijaudier-Cabot and Huerta (1991); Pijaudier-Cabot and Benallal (1993); Huerta and Pijaudier-Cabot (1994); Wang 1997; Peerlings et al. (1998b)]. A range of extensions to the conventional damage and plasticity models have been proposed in order to regularise the localisation of deformation [de Borst et al. (1993)]. Among them, the most promising is perhaps the class of nonlocal and gradient models. Both approaches introduce spatial interaction terms in the constitutive model, either using integral (nonlocal) relations [Bažant et al. (1984); Pijaudier-Cabot and Bažant (1987); Tvergaard and Needleman (1995)] or gradients of some constitutive variable [Aifantis (1984); Coleman and Hodgdon (1985); Lasry and Belytschko (1988); Mühlhaus and Aifantis (1991); de Borst and Mühlhaus (1992); Geers et al. (1998)]. The additional terms have a

smoothing effect on the deformation (and damage) fields, and thus preclude localisation in a plane. From a physical standpoint, the presence of spatial interactions can be motivated by microstructural considerations for some classes of materials [e.g., Aifantis (1984); Bažant (1991); Fleck and Hutchinson (1993); Geers (1997)]. Cosserat continua introduce micro-rotations as degrees of freedom, in addition to the conventional displacements. Gradients of these rotations give rise to micro-couples, which appear in the moment of momentum equations. The interaction between these rotational balances and the conventional, translational balances prevents the concentration of deformations in a surface. However, a mode-II component is needed in the deformation field in order to activate this mechanism. As a consequence, pathological localization may still occur in problems, which are dominated by mode-I loading.

2.8 Nonlocal damage models, state of the art

In recent years intensive research has been performed on the numerical modelling of failure phenomena in many engineering materials. One field of interest is the characteristic softening response that ductile materials exhibit in shear-dominated forming processes and other processes where ductile (stable) crack growth occurs by the microscopic processes of void nucleation, growth and coalescence. These processes are often accompanied by the localisation of deformation into a narrow zone of material (formation of shear band) or ductile damage zones of characteristic length scales. The main focus of this work is the incorporation of ductile damage into the material constitutive equations, which falls into the category of porous plasticity or material softening models and remove the mesh dependent nature of the models through incorporation of the concept of nonlocality.

For material softening (continuum damage mechanics) models, the numerical solution that is obtained from finite element analyses employing standard continuum elasto-plasticity (where a local description of the softening material is used) reveals a pathological dependence on the direction and the fineness of the finite element mesh (Pijaudier-Cabot et al. 1988). For these models, the solutions show no convergence to physically meaningful values upon mesh refinement. This problem is now well known by researchers worldwide and it has been shown that it is not purely of a numerical kind. The mesh-dependence nature of the solutions is due to the consequence of the ill-posedness of the underlying mathematical problem, i.e., the partial

differential equation (PDE) governing the boundary value problem (BVP) loses ellipticity in statics or hyperbolicity in dynamics. At the onset of softening, this change (loss of ellipticity or hyperbolicity) allows discontinuities in the strain distribution to appear and all deformation tends to localise into a zone of zero width.

2.9 Integral and gradient enhanced formulations

Different types of models, such as enhanced physical or phenomenological models have been proposed over the years to overcome the deficiency (i.e., loss of ellipticity of the governing PDE), which has led to various numerical solution strategies. An overview of these methods is given in de Borst et al. (1993). Among these, the higher-order continuum based models are probably best motivated from both the physical and the computational point of view (Aifantis 1987,1992). A common feature of the higher-order formulations is the incorporation of an intrinsic length scale, which is related to the microstructure and the failure mechanisms during plastic slip (e.g., granular deformations, inter-granular cleavage, dislocation dynamics, void nucleation, growth and coalescence, etc.). Examples of the experimental validation and determination of such a length scale for plasticity, crystal plasticity and damage mechanics can be found in Stölken and Evans (1998); Shu and Barlow (2000) and Geers et al. (1999) respectively. Nonlocal plasticity models [Strömberg and Ristinmaa (1996); Nilsson (1998)] incorporate a nonlocal quantity that is defined as the spatially weighted average of the corresponding local field quantity over a finite volume surrounding the point under consideration. Commonly, the nonlocal quantity is computed with an integral format, in which the associated intrinsic length scale influences the weight amplitude in the vicinity of a material point. Gradient-enhanced plasticity formulations [e.g., de Borst and Mühlhaus (1992)] avoid this integral format by approximating the nonlocal kernel with a Taylor series expansion, which yields a differential format. These gradient formulations are in fact higher order extensions of the local plasticity theory.

One subclass of the gradient-enhanced formulations is based on the direct use of higher-order gradient terms of a local quantity in the constitutive framework. They are therefore referred to as explicit formulations. This method involves the use of a plastic yield function (e.g., von-Mises) to which the Laplacian of an equivalent plastic strain measure is added [Mühlhaus and Aifantis (1991); de Borst and Mühlhaus (1992)]. This method has also been analyzed

thoroughly from a numerical point of view by Pamin (1994). The proposed method is based on a numerically rather expensive C^1 -continuous two-field interpolation or a C^0 -continuous three-field formulation.

With the work of Pamin (1994), considerable progress has been made in restoring the well-posedness of the BVP. Nevertheless, several problems have still remained. The adopted softening relation is only characteristic for the evolution of the local yield stress and the total gradient-enhanced yield stress may behave quite differently, which makes it difficult to model complete failure in a physically relevant way (i.e., convergence to an infinite strain in the presence of material separation). Numerical problems have also been reported when the total gradient-enhanced yield strength approaches zero (e.g., in case of porous plasticity models due to the evolution of ductile damage or void volume fraction). The most severe inconvenience resides in the fact that the gradient-enhanced consistency condition, which is solved as an additional partial differential equation (PDE), is only valid in the plastic domain, and no direct long-range interactions (i.e. at finite distances) with the elastic region exist. As a consequence, the evolving elasto-plastic boundary (EPB) depends on the solution, which complicates the numerical calculations considerably.

In order to circumvent the limitations of the existing explicit gradient regularization for softening plasticity, Meftah et al. (1998) rephrased the problem. They adopted a differential approximation of a nonlocal quantity as an additional PDE. Unlike the consistency condition (which is commonly used within the explicit gradient-enhanced formulations), this additional PDE is defined throughout the entire body, whereas it implicitly incorporates a similar gradient regularization. As a result, this method only requires boundary conditions on the external boundary and not on a moving EPB and it benefits from a straightforward C^0 -continuous two-field interpolation. Nevertheless, several inconveniences (e.g., no complete failure, numerical instabilities etc.) persisted and the numerical solution strategy required rather small loading increments.

A second subclass of the gradient-enhanced methods consists of the so-called implicit approaches. These formulations adopt a differential approximation of a nonlocal variable, which involves the higher-order derivatives of a nonlocal variable rather than of a local field variable, which is the case for the explicit models. Both the explicit and implicit gradient

approximations can be easily derived from the nonlocal integral format [Peerlings et al. (1996)]. For the implicit case, the resulting relation is a PDE of the Helmholtz type, from which the nonlocal quantity is solved in a coupled fashion with the equilibrium equation. Similar to the formulation of Meftah et al. (1998), this necessitates only boundary conditions on the external boundary and not on the moving EPB. The dependence of the yield function on the nonlocal field ensures the gradient regularization in an implicit manner. Moreover, the true nonlocal character of the implicit gradient-enhancement enables long-range interactions into the elastic region. Although these approaches have already been successfully applied to damage mechanics for quasi-brittle materials (Peerlings et al. 1996,1998a), the application to elasto-plasticity and ductile damage mechanics has not been satisfactory yet, which is precisely the subject of the current research. In this work, the gradient enhancement formulation is coupled to the constitutive equation through incorporation of ductile damage as a nonlocal variable. The evolution of nonlocal ductile damage is governed by a diffusion type PDE and it is in turn dependent on the local ductile damage variable (i.e., void volume fraction, which is treated as an internal variable in continuum damage mechanics formulations).

2.10 Concept of nonlocality

In order to fully understand the consequences of and the differences between the various gradient approximations of the nonlocal kernel, the definition of a nonlocal quantity, commonly used in various integral nonlocal formulations [e.g., Pijaudier-Cabot and Bažant (1987); Strömberg and Ristinmaa (1996)] is described here in brief. Here, the nonlocal field variable is taken as the ductile void volume fraction (i.e., d) instead of the equivalent plastic strain used in literature for nonlocal plasticity models (i.e., without the effect of ductile damage on material stiffness). The nonlocal variable in a material point \bar{x} , i.e. the nonlocal void volume fraction d , is mathematically defined as a weighted average of the local void volume fraction f in a domain Ω , i.e.,

$$d(\bar{x}) = \frac{1}{\Psi(\bar{x})} \int_{\Omega} \Psi(\bar{y}; \bar{x}) f(\bar{y}) d\Omega(\bar{y}) \quad (2.46)$$

where \bar{y} is the position vector of the infinitesimally small volume $d\Omega$ and $\Psi(\bar{y}; \bar{x})$ is the Gaussian weight function given by

$$\Psi(\bar{y}; \bar{x}) = \frac{1}{8\pi^{3/2}l^3} \exp\left(-\frac{|\bar{x} - \bar{y}|^2}{4l^2}\right) \quad (2.47)$$

The length parameter l determines the size of the volume, which effectively contributes to the nonlocal quantity and is related to the scale of the microstructure. The above integral nonlocal kernel holds the property that the local continuum is retrieved if $l \rightarrow 0$. The nonlocal void volume fraction equals the local void volume fraction for homogeneous strain states, since a normalising factor $\Psi(\bar{x})$ is used and given as

$$\Psi(\bar{x}) = \int_{\Omega} \Psi(\bar{y}; \bar{x}) d\Omega \quad (2.48)$$

2.10.1 Explicit gradient approximation for nonlocal damage

From the integral format Equation (2.46), a relation of d in terms of gradients of f can be derived making use of the following Taylor series expansion, i.e.,

$$\begin{aligned} f(\bar{y}) &= f(\bar{x}) + \frac{\partial f}{\partial x_i}(y_i - x_i) + \frac{1}{2!} \frac{\partial^2 f}{\partial x_i \partial x_j}(y_i - x_i)(y_j - x_j) \\ &+ \frac{1}{3!} \frac{\partial^3 f}{\partial x_i \partial x_j \partial x_k}(y_i - x_i)(y_j - x_j)(y_k - x_k) \\ &+ \frac{1}{4!} \frac{\partial^4 f}{\partial x_i \partial x_j \partial x_k \partial x_l}(y_i - x_i)(y_j - x_j)(y_k - x_k)(y_l - x_l) \end{aligned} \quad (2.49)$$

where Einstein's summation convention applies to the repeated indices. Substitution of Eq.(2.49) into Eq.(2.46) yields

$$d(\bar{x}) = f(\bar{x}) + c_1(l) \nabla^2 f(\bar{x}) + c_2(l) \nabla^4 f(\bar{x}) + \dots \quad (2.50)$$

where the Laplacian operator is defined by $\nabla^2 = \sum_i \frac{\partial^2}{\partial x_i^2}$ and $\nabla^{2n} = (\nabla^2)^n$. The gradient parameters $c_1(l)$ and $c_2(l)$ have the dimensions of length to an even power and that the odd derivatives vanish due to the isotropy of the Gaussian weight function of Eq (2.47). The importance of the Laplacian term for restoring the well-posedness of the mathematical problem in case of localisation has been shown both computationally and analytically by Askes (2000) and Wang (1997). Other gradient formulations, on the contrary [e.g., Zbib and Aifantis (1992); Aifantis (1999)], are constructed on the basis of first order gradients, which may be relevant when dealing with size-effects in hardening plasticity.

Finally, it is rather straightforward to approximate the nonlocal kernel by disregarding terms of order four and higher, which results in the following explicit gradient approximation

$$d(\bar{x}) = f(\bar{x}) + c_1(l) \nabla^2 f(\bar{x}) \quad (2.51)$$

The gradient approximation of Eq. (2.51) is considered explicit in the sense that the (approximated) nonlocal field $d(\bar{x})$ can be directly calculated from the local field $f(\bar{x})$. This approximation preserves some of the properties of the integral format, i.e., the local field is recovered if either $c_1(l) \rightarrow 0$ when $l \rightarrow 0$ or if homogeneous strain fields are considered.

Although the length parameter $c_1(l)$ governs the intensity of the spatial interactions, the explicit gradient approximation is only weakly nonlocal (interactions limited to an infinitesimal neighbourhood), as shown in Peerlings et al. (2001).

2.10.2 Implicit gradient approximation for nonlocal damage

The weakly nonlocal character of the explicit gradient approximation [Eq. (2.51)] can be improved by taking into account more higher-order derivatives of the local quantity in Eq. (2.50). However, from a computational point of view, this is not favourable. Alternatively, the explicit approximation can be improved upon in a different fashion according to Peerlings et al. (1996). The Laplacian of Eq. (2.50) can be written as

$$\nabla^2 d(\bar{x}) = \nabla^2 f(\bar{x}) + c_1(l) \nabla^4 f(\bar{x}) + \dots \quad (2.52)$$

Subtracting Eq. (2.52) from $c_1(l) \times$ Eq. (2.50) results in

$$d(\bar{x}) - c_1(l) \nabla^2 d(\bar{x}) = f(\bar{x}) + [c_2(l) - c_1^2(l)] \nabla^4 f(\bar{x}) + \dots \quad (2.53)$$

If all the coefficients of the higher-order terms on the right-hand side, starting with $c_2(l) - c_1^2(l)$ are set zero, the following expression is obtained

$$d(\bar{x}) - c_1(l) \nabla^2 d(\bar{x}) = f(\bar{x}) \quad (2.54)$$

This relation is the implicit gradient formulation of the nonlocal integral equation [i.e., (2.46)], which is a partial differential equation (PDE) in terms of the nonlocal variable $d(\bar{x})$ of the Helmholtz type. It is emphasised that the influence of the higher-order terms on the right-hand side of Eq. (2.53) vanishes since the resulting weighting function satisfies the condition $c_2(l) - c_1^2(l) = 0$. The gradient approximation given by Eq. (2.54), requiring the solution of this PDE, still represents a truly nonlocal variable from a mathematical point of view. In fact,

the solution of the implicit gradient PDE for an arbitrary local field $f(\vec{x})$ can be determined with the method of Green's functions, i.e.,

$$d(\vec{x}) = \int_{\Omega} G(\vec{y}; \vec{x}) f(\vec{y}) d\Omega \quad (2.55)$$

where the Green's function is given as (the distance between two points is represented as $\rho = |\vec{x} - \vec{y}|$)

$$G(\vec{y}; \vec{x}) = \frac{1}{4\pi \rho l^2} \exp\left(-\frac{\rho}{l}\right) \quad (2.56)$$

Although the above expression adopts the Green's function $G(\vec{y}; \vec{x})$ as the weight function instead of the common Gauss function, it has the same format as the definition of a nonlocal quantity for the integral model [Eq. (2.46)]. Hence, from a mathematical point of view, the implicit gradient approximation [Eq. (2.54)] is strongly nonlocal (interactions within a finite neighbourhood). For the Green's weight function, it can be shown that $c_2(l) - c_1^2(l) = 0$ for an arbitrary local field $f(\vec{x})$. Therefore, when equating these coefficients to zero in Eq. (2.53), no higher-order terms are neglected when the Green's function is used as a weight function. Furthermore, the implicit gradient approximation preserves other properties of the integral format i.e., the local field is recovered if either $c_1(l) \rightarrow 0$ when $l \rightarrow 0$ or if homogeneous fields are considered (i.e., $\nabla^2 d(\vec{x}) = 0$).

The implicit gradient approximation of the nonlocal damage variable derived above can be represented as

$$d(\vec{x}) - c_{length} \nabla^2 d(\vec{x}) = f(\vec{x}) \quad (2.57)$$

where c_{length} is the characteristics length of the material and in this way, it has been incorporated into the continuum framework of damage mechanics models. As a result, it is possible to model the microstructural influence on the macroscopic level and restore the well-posedness of the boundary value problem during material softening.

The past decade has provided us with some understanding of the mathematical implications of the nonlocal and gradient enhancement, particularly in avoiding pathological localization. But fundamental questions still remain. For example, the role of the enhancement in crack growth modelling and the associated treatment of boundaries have not yet been fully clarified.

Furthermore, nonlocal and gradient models are known to be closely related, but may nevertheless behave quite differently. In fact, very similar gradient formulations have been observed to lead to remarkably different localization properties. It is therefore believed that these and other issues need to be further resolved in order to fully exploit the potential of nonlocal and gradient formulations.

Chapter 3

Development of a nonlocal damage mechanics model

In this chapter, a nonlocal form of the Rousselier's continuum damage model is developed by coupled solution of the mechanical stress equilibrium equation and the damage equilibrium (diffusion) equation. The damage equilibrium equation is derived using the implicit gradient formulation of the integral type model as discussed in Section 2.10.2. After a brief description of the kinematic and material constitutive relations, the consistent tangent stiffness matrix is derived for the continuum where the primary variables have been taken as displacements and nonlocal damage. Subsequently, a suitable discretization method (here, finite element method) is used to derive the algebraic equations from the weak form of the coupled differential equations.

3.1 Coupled equations of equilibrium and diffusion [in terms of $d(\bar{x})$]

The following set of governing equations (stress equilibrium equation of mechanical continuum and the damage equilibrium equation) is the starting point for implicit gradient enhanced damage mechanics models.

$$\begin{aligned}\nabla \cdot \sigma + f_b &= 0 \\ d - c_{length} \nabla^2 d &= f\end{aligned}\tag{3.1}$$

where σ is the stress tensor and f_b is the body force vector per unit volume. Eq. (3.1) is a combination of stress equilibrium equation of continuum mechanics along with the implicit gradient equation for the nonlocal damage variable d . In addition to the standard boundary conditions (essential and traction boundary conditions), additional boundary conditions are required in order to uniquely compute the solution of the second PDE of Eq. (3.1). The corresponding boundary conditions apply to the external boundary of the domain rather than to the elasto-plastic boundary (EPB), since for the implicit gradient formulation, the solution d is continuous in the entire domain Ω . Hence, the difficulties of applying boundary conditions with respect to the moving EPB (as required for the explicit formulation) are no longer present.

The additional boundary condition specifies either the value of d or its normal derivative, or a linear combination of these quantities. A simple homogeneous Neumann boundary condition has been used here, i.e.,

$$\nabla \vec{d} \cdot \vec{n} = 0 \text{ on external boundary } \Gamma \quad (3.2)$$

where \vec{n} is the unit outward normal to the external boundary Γ . This boundary condition is consistent with the integral Equation (2.46) in the sense that d equals f for homogeneous deformations and for the limiting case of a vanishing length scale l . Furthermore, the solution of Eq. (3.1) in combination with the Neumann boundary condition [Eq. (3.2)] preserves the total amount of damage, i.e.,

$$\int_{\Omega} (d) d\Omega = \int_{\Omega} (f) d\Omega \quad (3.3)$$

Another effect of the Neumann boundary condition is the increased contribution of points to the nonlocal damage when approaching the external boundary, which can be explained by the increased sensitivity of the material towards formation of surface defects.

3.2 Development of a nonlocal form of Rousselier's damage model

The yield potential of the nonlocal form of Rousselier's damage model in terms of the nonlocal damage parameter d (in place of local void volume fraction f) can be written as

$$\phi = \frac{\sigma_{eq}}{1-d} + D\sigma_k d \exp\left(\frac{\sigma_{hydro}}{(1-d)\sigma_k}\right) - R(\varepsilon_{eq}) = 0 \quad (3.4)$$

where σ_{eq} is the von-Mises equivalent stress, D and σ_k are Rousselier's constants, σ_{hydro} is the mean hydrostatic stress and $R(\varepsilon_{eq})$ is the material stress-strain curve, which is a function of equivalent plastic strain ε_{eq} . The weak form of the governing mechanical equilibrium equation and the damage equilibrium equation (3.1) [in incremental form] can be defined for the mechanical continuum as

$$\begin{aligned} \int_{\Omega} \delta u (\nabla \cdot \sigma + f_b) \cdot d\Omega &= 0 \\ \int_{\Omega} \delta \dot{d} (\dot{d} - \dot{f} - C_{length} \nabla^2 \dot{d}) \cdot d\Omega &= 0 \end{aligned} \quad (3.5)$$

where δu represents the variation of the generalized displacement variable, $\delta \dot{d}$ represents variation of the incremental form of nonlocal damage variable, \dot{f} is the increment of the local

damage variable or void volume fraction. Using the standard displacement based finite element (FE) method of discretization of the mechanical continuum and the standard shape functions for a finite element, we can derive the FE equations of a single element as

$$\begin{bmatrix} K_{uu} & K_{ud} \\ K_{du} & K_{dd} \end{bmatrix} \begin{Bmatrix} \Delta \hat{u} \\ \Delta \hat{d} \end{Bmatrix} = \begin{Bmatrix} f_m^{ext} - f_m^{int} \\ -f_d^{int} \end{Bmatrix} \quad (3.6)$$

The element level equations derived so, can be assembled and solved for the global degrees of freedom when we specify the required boundary and loading conditions. K_{uu} is the usual element stiffness matrix of the mechanical continuum, f_m^{ext} is the externally applied mechanical force vector (because of body force, surface traction and point forces), f_m^{int} is the internal mechanical resistance (force vector) due to stress, f_d^{int} is the generalized force due to damage degree of freedom (internal) whereas externally applied generalized force due to damage f_d^{ext} is zero.

It may be noted that the stiffness terms K_{ud} , K_{du} and K_{dd} in the element stiffness matrix, are contributions of the nonlocal model (because of presence of nonlocal damage as an additional primary variable or degree of freedom in the continuum). The details of the procedure for derivation of the finite element equations [i.e., Eq. (3.6)] are described in detail in the following sections.

3.3 Kinematic and material constitutive relations

In the numerical integration of material constitutive equations, we will use the additive decomposition of the strain rate tensor (hypo-elastic formulation), i.e., decomposition of total strain increment into elastic $\Delta \varepsilon^e$ and plastic $\Delta \varepsilon^p$ parts as

$$\Delta \varepsilon = \Delta \varepsilon^e + \Delta \varepsilon^p \quad (3.7)$$

The yield function can be written in terms of mean hydrostatic and deviatoric parts of stress tensor and other field variables as

$$\phi(p, q, H^\alpha, d) = 0 \quad (3.8)$$

where p and q are the hydrostatic pressure and von Mises equivalent stress respectively and are defined as

$$\begin{aligned}
p &= -\frac{1}{3}\sigma : I, \\
q &= \left(\frac{3}{2}s : s \right)^{1/2},
\end{aligned} \tag{3.9}$$

H^α is internal state variable such as hardening, I is the Kronecker-Delta or second order identity tensor, s is the deviatoric part of stress tensor σ . The generalized flow rule for the increment of plastic strain tensor from time t to $t + \Delta t$ can be written as (Aravas 1987)

$$\Delta \varepsilon^p = \frac{1}{3}\Delta \varepsilon_p I + \Delta \varepsilon_q n_{t+\Delta t} \tag{3.10}$$

where $\Delta \varepsilon_p$ and $\Delta \varepsilon_q$ are the hydrostatic and equivalent parts of plastic strain increment and $n_{t+\Delta t}$ is defined in terms of the deviatoric part of the elastic predictor stress s^{tr} and von Mises equivalent stress q^{tr} (corresponding to elastic predictor stress σ^{tr}) as

$$n_{t+\Delta t} = \frac{3s^{tr}}{2q^{tr}} \tag{3.11}$$

The terms $\Delta \varepsilon_p$ and $\Delta \varepsilon_q$ are related though the equation

$$\Delta \varepsilon_p \frac{\partial g}{\partial q} + \Delta \varepsilon_q \frac{\partial g}{\partial p} = 0 \tag{3.12}$$

where g is the plastic potential and for associated plasticity, $g = \phi$. Hence, to calculate the increment in stress tensor, the equations to be solved simultaneously are (3.12), the yield function ϕ , evolution equation for the hydrostatic stress p , von Mises equivalent stress q and the internal variables H^α as described in the next section.

3.4 Derivation of stress increment for the non-local model

The basic equations to be solved simultaneously are (Aravas 1987; Zhang and Niemi 1995)

$$\Delta \varepsilon_p \frac{\partial g}{\partial q} + \Delta \varepsilon_q \frac{\partial g}{\partial p} = 0 \tag{3.13}$$

$$\phi(p, q, H^\alpha, d) = 0 \tag{3.14}$$

$$p = p^{tr} + K\Delta \varepsilon_p \tag{3.15}$$

$$q = q^{tr} - 3G\Delta \varepsilon_q \tag{3.16}$$

$$H^\alpha = h^\alpha(\Delta \varepsilon_p, \Delta \varepsilon_q, p, q, H^\beta) \tag{3.17}$$

where the quantities with superscript 'tr' refers to 'trial' or the elastic predictor part.

Expanding Eq.(3.13) in Taylor's series, we get

$$\begin{aligned} \Delta \varepsilon_p \frac{\partial g}{\partial q} + \Delta \varepsilon_p \left[\frac{\partial^2 g}{\partial p \partial q} \cdot \partial p + \frac{\partial^2 g}{\partial q^2} \cdot \partial q + \sum_{\alpha=1}^n \frac{\partial^2 g}{\partial q \partial H^\alpha} \partial H^\alpha \right] + \partial \Delta \varepsilon_p \frac{\partial g}{\partial q} + \Delta \varepsilon_p \frac{\partial^2 g}{\partial q \partial d} \partial d \\ + \Delta \varepsilon_q \frac{\partial g}{\partial p} + \Delta \varepsilon_q \left[\frac{\partial^2 g}{\partial p^2} \cdot \partial p + \frac{\partial^2 g}{\partial p \partial q} \cdot \partial q + \sum_{\alpha=1}^n \frac{\partial^2 g}{\partial p \partial H^\alpha} \partial H^\alpha \right] + \partial \Delta \varepsilon_q \frac{\partial g}{\partial p} + \Delta \varepsilon_q \frac{\partial^2 g}{\partial p \partial d} \partial d = 0 \end{aligned} \quad (3.18)$$

Differentiating Eq.(3.15) and (3.16), we get

$$\partial p = K \partial \Delta \varepsilon_p \quad (3.19)$$

$$\partial q = -3G \partial \Delta \varepsilon_q \quad (3.20)$$

Differentiating Eq.(3.17) and substituting Eq.(3.19) and (3.20) for ∂p and ∂q , we get

$$\begin{aligned} \partial H^\alpha &= \sum_{\beta=1}^n c_{\alpha\beta} \left[\frac{\partial h^\beta}{\partial \Delta \varepsilon_p} \partial \Delta \varepsilon_p + \frac{\partial h^\beta}{\partial \Delta \varepsilon_q} \partial \Delta \varepsilon_q + \frac{\partial h^\beta}{\partial p} \partial p + \frac{\partial h^\beta}{\partial q} \partial q \right] \\ &= \sum_{\beta=1}^n c_{\alpha\beta} \left[\frac{\partial h^\beta}{\partial \Delta \varepsilon_p} \partial \Delta \varepsilon_p + \frac{\partial h^\beta}{\partial \Delta \varepsilon_q} \partial \Delta \varepsilon_q + \frac{\partial h^\beta}{\partial p} K \partial \Delta \varepsilon_p + \frac{\partial h^\beta}{\partial q} (-3G) \partial \Delta \varepsilon_q \right] \end{aligned} \quad (3.21)$$

where $c_{\alpha\beta} = \left(\delta_{\alpha\beta} - \frac{\partial h^\beta}{\partial H^\alpha} \right)^{-1}$ and $\delta_{\alpha\beta}$ is the Kronecker Delta function.

Inserting Eq. (3.21) for ∂H^α in Eq.(3.18), we get:

$$\begin{aligned} \Delta \varepsilon_p \frac{\partial g}{\partial q} + \Delta \varepsilon_p \left[\frac{\partial^2 g}{\partial p \partial q} \cdot K \cdot \partial \Delta \varepsilon_p + \frac{\partial^2 g}{\partial q^2} \cdot (-3G) \partial \Delta \varepsilon_q \right. \\ \left. + \sum_{\alpha=1}^n \frac{\partial^2 g}{\partial q \partial H^\alpha} \sum_{\beta=1}^n c_{\alpha\beta} \left(\frac{\partial h^\beta}{\partial \Delta \varepsilon_p} \partial \Delta \varepsilon_p + \frac{\partial h^\beta}{\partial \Delta \varepsilon_q} \partial \Delta \varepsilon_q + \frac{\partial h^\beta}{\partial p} K \partial \Delta \varepsilon_p + \frac{\partial h^\beta}{\partial q} (-3G) \partial \Delta \varepsilon_q \right) \right] \\ + \partial \Delta \varepsilon_p \frac{\partial g}{\partial q} + \Delta \varepsilon_p \frac{\partial^2 g}{\partial q \partial d} \partial d \\ + \Delta \varepsilon_q \frac{\partial g}{\partial p} + \Delta \varepsilon_q \left[\frac{\partial^2 g}{\partial p^2} \cdot K \cdot \partial \Delta \varepsilon_p + \frac{\partial^2 g}{\partial p \partial q} \cdot (-3G) \partial \Delta \varepsilon_q \right. \\ \left. + \sum_{\alpha=1}^n \frac{\partial^2 g}{\partial p \partial H^\alpha} \sum_{\beta=1}^n c_{\alpha\beta} \left(\frac{\partial h^\beta}{\partial \Delta \varepsilon_p} \partial \Delta \varepsilon_p + \frac{\partial h^\beta}{\partial \Delta \varepsilon_q} \partial \Delta \varepsilon_q + \frac{\partial h^\beta}{\partial p} K \partial \Delta \varepsilon_p + \frac{\partial h^\beta}{\partial q} (-3G) \partial \Delta \varepsilon_q \right) \right] \\ + \partial \Delta \varepsilon_q \frac{\partial g}{\partial p} + \Delta \varepsilon_q \frac{\partial^2 g}{\partial p \partial d} \partial d = 0 \end{aligned} \quad (3.22)$$

After collecting the terms of $\partial \Delta \varepsilon_p$ and $\partial \Delta \varepsilon_q$ from Eq. (3.22), we can write them as

$$A_{11} \partial \Delta \varepsilon_p + A_{12} \partial \Delta \varepsilon_q = b_1 + c_{d1} \partial d \quad (3.23)$$

where the coefficients are

$$A_{11} = \frac{\partial g}{\partial q} + \Delta \varepsilon_p \left[K \frac{\partial^2 g}{\partial p \partial q} + \sum_{\alpha=1}^n \frac{\partial^2 g}{\partial q \partial H^\alpha} \sum_{\beta=1}^n c_{\alpha\beta} \left(\frac{\partial h^\beta}{\partial \Delta \varepsilon_p} + K \frac{\partial h^\beta}{\partial p} \right) \right] \\ + \Delta \varepsilon_q \left[K \frac{\partial^2 g}{\partial p^2} + \sum_{\alpha=1}^n \frac{\partial^2 g}{\partial p \partial H^\alpha} \sum_{\beta=1}^n c_{\alpha\beta} \left(\frac{\partial h^\beta}{\partial \Delta \varepsilon_p} + K \frac{\partial h^\beta}{\partial p} \right) \right] \quad (3.24)$$

$$A_{12} = \frac{\partial g}{\partial p} + \Delta \varepsilon_p \left[-3G \frac{\partial^2 g}{\partial q^2} + \sum_{\alpha=1}^n \frac{\partial^2 g}{\partial q \partial H^\alpha} \sum_{\beta=1}^n c_{\alpha\beta} \left(\frac{\partial h^\beta}{\partial \Delta \varepsilon_q} - 3G \frac{\partial h^\beta}{\partial q} \right) \right] \\ + \Delta \varepsilon_q \left[-3G \frac{\partial^2 g}{\partial p \partial q} + \sum_{\alpha=1}^n \frac{\partial^2 g}{\partial p \partial H^\alpha} \sum_{\beta=1}^n c_{\alpha\beta} \left(\frac{\partial h^\beta}{\partial \Delta \varepsilon_q} - 3G \frac{\partial h^\beta}{\partial q} \right) \right] \quad (3.25)$$

$$b_1 = - \left(\Delta \varepsilon_p \frac{\partial g}{\partial q} + \Delta \varepsilon_q \frac{\partial g}{\partial p} \right) \quad (3.26)$$

$$c_{d1} = - \left(\Delta \varepsilon_p \frac{\partial^2 g}{\partial q \partial d} + \Delta \varepsilon_q \frac{\partial^2 g}{\partial p \partial d} \right) \quad (3.27)$$

Now, expanding Eq.(3.14) in Taylor's series, we get

$$\phi + \frac{\partial \phi}{\partial p} \partial p + \frac{\partial \phi}{\partial q} \partial q + \frac{\partial \phi}{\partial H^\alpha} \partial H^\alpha + \frac{\partial \phi}{\partial d} \partial d = 0 \quad (3.28)$$

Substituting Eq.(3.19) and (3.20) for ∂p and ∂q and Eq. (3.21) for ∂H^α in Eq.(3.28), we get

$$\phi + \frac{\partial \phi}{\partial p} K \partial \Delta \varepsilon_p + \frac{\partial \phi}{\partial q} (-3G) \partial \Delta \varepsilon_q + \frac{\partial \phi}{\partial d} \partial d \\ + \frac{\partial \phi}{\partial H^\alpha} \sum_{\beta=1}^n c_{\alpha\beta} \left[\frac{\partial h^\beta}{\partial \Delta \varepsilon_p} \partial \Delta \varepsilon_p + \frac{\partial h^\beta}{\partial \Delta \varepsilon_q} \partial \Delta \varepsilon_q + \frac{\partial h^\beta}{\partial p} K \partial \Delta \varepsilon_p + \frac{\partial h^\beta}{\partial q} (-3G) \partial \Delta \varepsilon_q \right] = 0 \quad (3.29)$$

After collecting the terms of $\partial \Delta \varepsilon_p$ and $\partial \Delta \varepsilon_q$ from Eq.(3.29), we can write them as

$$A_{21} \partial \Delta \varepsilon_p + A_{22} \partial \Delta \varepsilon_q = b_2 + c_{d2} \partial d \quad (3.30)$$

where the coefficients are written as

$$A_{21} = K \frac{\partial \phi}{\partial p} + \sum_{\alpha=1}^n \frac{\partial \phi}{\partial H^\alpha} \sum_{\beta=1}^n c_{\alpha\beta} \left(\frac{\partial h^\beta}{\partial \Delta \varepsilon_p} + K \frac{\partial h^\beta}{\partial p} \right) \quad (3.31)$$

$$A_{22} = -3G \frac{\partial \phi}{\partial q} + \sum_{\alpha=1}^n \frac{\partial \phi}{\partial H^\alpha} \sum_{\beta=1}^n c_{\alpha\beta} \left(\frac{\partial h^\beta}{\partial \Delta \varepsilon_q} - 3G \frac{\partial h^\beta}{\partial q} \right) \quad (3.32)$$

$$b_2 = -\phi \quad (3.33)$$

$$c_{d2} = -\frac{\partial \phi}{\partial d} \quad (3.34)$$

Eqs.(3.23) and (3.30) can be solved simultaneously to get the corrections for $\Delta\varepsilon_p$ and $\Delta\varepsilon_q$ (i.e., $\partial\Delta\varepsilon_p$ and $\partial\Delta\varepsilon_q$) and the solutions for $\partial\Delta\varepsilon_p$ and $\partial\Delta\varepsilon_q$ are

$$\partial\Delta\varepsilon_p = m_{pa} + m_{pb}\partial d \quad (3.35)$$

$$\partial\Delta\varepsilon_q = m_{qa} + m_{qb}\partial d \quad (3.36)$$

where m_{pa} , m_{pb} , m_{qa} and m_{qb} can be written as

$$m_{pa} = \frac{(b_1A_{22} - b_2A_{12})}{(A_{11}A_{22} - A_{21}A_{12})} \quad \text{and} \quad m_{pb} = \frac{(c_{d1}A_{22} - c_{d2}A_{12})}{(A_{11}A_{22} - A_{21}A_{12})} \quad (3.37)$$

$$m_{qa} = \frac{(b_2A_{11} - b_1A_{21})}{(A_{11}A_{22} - A_{21}A_{12})} \quad \text{and} \quad m_{qb} = \frac{(c_{d2}A_{11} - c_{d1}A_{21})}{(A_{11}A_{22} - A_{21}A_{12})} \quad (3.38)$$

After evaluating $\partial\Delta\varepsilon_p$ and $\partial\Delta\varepsilon_q$ from Eqs. (3.35) and (3.36), $\Delta\varepsilon_p$ and $\Delta\varepsilon_q$ can be updated as

$$\begin{aligned} \Delta\varepsilon_p &\rightarrow \Delta\varepsilon_p + \partial\Delta\varepsilon_p \\ \Delta\varepsilon_q &\rightarrow \Delta\varepsilon_q + \partial\Delta\varepsilon_q \end{aligned} \quad (3.39)$$

This is done iteratively till we get convergence in the values of $\Delta\varepsilon_p$ and $\Delta\varepsilon_q$. These values of $\Delta\varepsilon_p$ and $\Delta\varepsilon_q$ are substituted in Eqs. (3.15) and (3.16) to evaluate p and q . The new stress tensor is evaluated as

$$\sigma_{t+\Delta t} = \sigma^{tr} - K\Delta\varepsilon_p I - 2G\Delta\varepsilon_q n_{t+\Delta t} \quad (3.40)$$

where $n_{t+\Delta t} = \frac{3}{2} \frac{s^{tr}}{q^{tr}}$, σ^{tr} is the elastic predictor stress and s^{tr} is the stress deviator for σ^{tr} .

3.5 Evaluation of linearised consistent tangent moduli

If we take the variation of Eq. (3.13), we can write it as

$$\begin{aligned} &\left[\frac{\partial^2 g}{\partial p \partial q} \partial p + \frac{\partial^2 g}{\partial q^2} \partial q \right. \\ &\quad \left. + \sum_{\alpha=1}^n \frac{\partial^2 g}{\partial q \partial H^\alpha} \sum_{\beta=1}^n c_{\alpha\beta} \left(\frac{\partial h^\beta}{\partial \Delta\varepsilon_p} \partial\Delta\varepsilon_p + \frac{\partial h^\beta}{\partial \Delta\varepsilon_q} \partial\Delta\varepsilon_q + \frac{\partial h^\beta}{\partial p} \partial p + \frac{\partial h^\beta}{\partial q} \partial q \right) \right] \\ &+ \Delta\varepsilon_p \frac{\partial^2 g}{\partial q \partial d} \partial d \\ &+ \partial\Delta\varepsilon_q \frac{\partial g}{\partial p} + \Delta\varepsilon_q \left[\sum_{\alpha=1}^n \frac{\partial^2 g}{\partial p \partial H^\alpha} \sum_{\beta=1}^n c_{\alpha\beta} \left(\frac{\partial h^\beta}{\partial \Delta\varepsilon_p} \partial\Delta\varepsilon_p + \frac{\partial h^\beta}{\partial \Delta\varepsilon_q} \partial\Delta\varepsilon_q + \frac{\partial h^\beta}{\partial p} \partial p + \frac{\partial h^\beta}{\partial q} \partial q \right) \right] \end{aligned}$$

$$+\Delta\varepsilon_q \left[\frac{\partial^2 g}{\partial p^2} \cdot \partial p + \frac{\partial^2 g}{\partial p \partial q} \partial q \right] + \Delta\varepsilon_q \frac{\partial^2 g}{\partial p \partial d} \partial d = 0 \quad (3.41)$$

Similarly, if we take the variation of Eq. (3.14), we can write it as

$$\begin{aligned} & \frac{\partial \phi}{\partial p} \partial p + \frac{\partial \phi}{\partial q} \partial q + \frac{\partial \phi}{\partial d} \partial d \\ & + \frac{\partial \phi}{\partial H^\alpha} \sum_{\beta=1}^n c_{\alpha\beta} \left[\frac{\partial h^\beta}{\partial \Delta\varepsilon_p} \partial \Delta\varepsilon_p + \frac{\partial h^\beta}{\partial \Delta\varepsilon_q} \partial \Delta\varepsilon_q + \frac{\partial h^\beta}{\partial p} \partial p + \frac{\partial h^\beta}{\partial q} \partial q \right] \end{aligned} \quad (3.42)$$

Now, we take variations of p and q using Eqs. (3.15) and (3.16) and these can be written as

$$\partial p = \partial p^{lr} + K \partial \Delta\varepsilon_p = -KI : \partial \varepsilon + K \partial \Delta\varepsilon_p \quad (3.43)$$

$$\partial q = \partial q^{lr} - 3G \partial \Delta\varepsilon_q = 2Gn : \partial \varepsilon - 3G \partial \Delta\varepsilon_q \quad (3.44)$$

Substituting the expressions for ∂p and ∂q from Eqs. (3.43) and (3.44) into Eqs. (3.41) and (3.42), we get

$$A_{11}^* \partial \Delta\varepsilon_p + A_{12}^* \partial \Delta\varepsilon_q = (B_{11}I + B_{12}n) : \partial \varepsilon + c_{d1} \partial d \quad (3.45)$$

$$A_{21}^* \partial \Delta\varepsilon_p + A_{22}^* \partial \Delta\varepsilon_q = (B_{21}I + B_{22}n) : \partial \varepsilon + c_{d2} \partial d \quad (3.46)$$

where the coefficients can be written as

$$\begin{aligned} A_{11}^* &= \frac{\partial g}{\partial q} + K \left(\Delta\varepsilon_p \frac{\partial^2 g}{\partial p \partial q} + \Delta\varepsilon_q \frac{\partial^2 g}{\partial p^2} \right) \\ &+ \sum_{\alpha=1}^n \left(\Delta\varepsilon_p \frac{\partial^2 g}{\partial q \partial H^\alpha} + \Delta\varepsilon_q \frac{\partial^2 g}{\partial p \partial H^\alpha} \right) \sum_{\beta=1}^n c_{\alpha\beta} \left(\frac{\partial h^\beta}{\partial \Delta\varepsilon_p} + K \frac{\partial h^\beta}{\partial p} \right) \end{aligned} \quad (3.47)$$

$$\begin{aligned} A_{12}^* &= \frac{\partial g}{\partial p} - 3G \left(\Delta\varepsilon_p \frac{\partial^2 g}{\partial q^2} + \Delta\varepsilon_q \frac{\partial^2 g}{\partial p \partial q} \right) \\ &+ \sum_{\alpha=1}^n \left(\Delta\varepsilon_p \frac{\partial^2 g}{\partial q \partial H^\alpha} + \Delta\varepsilon_q \frac{\partial^2 g}{\partial p \partial H^\alpha} \right) \sum_{\beta=1}^n c_{\alpha\beta} \left(\frac{\partial h^\beta}{\partial \Delta\varepsilon_q} - 3G \cdot \frac{\partial h^\beta}{\partial q} \right) \end{aligned} \quad (3.48)$$

$$\begin{aligned} B_{11}^* &= K \left(\Delta\varepsilon_p \frac{\partial^2 g}{\partial p \partial q} + \Delta\varepsilon_q \frac{\partial^2 g}{\partial p^2} \right) \\ &+ K \sum_{\alpha=1}^n \left(\Delta\varepsilon_p \frac{\partial^2 g}{\partial q \partial H^\alpha} + \Delta\varepsilon_q \frac{\partial^2 g}{\partial p \partial H^\alpha} \right) \sum_{\beta=1}^n c_{\alpha\beta} \left(\frac{\partial h^\beta}{\partial p} \right) \end{aligned} \quad (3.49)$$

$$\begin{aligned} B_{12}^* &= -2G \left(\Delta\varepsilon_p \frac{\partial^2 g}{\partial q^2} + \Delta\varepsilon_q \frac{\partial^2 g}{\partial p \partial q} \right) \\ &- 2G \sum_{\alpha=1}^n \left(\Delta\varepsilon_p \frac{\partial^2 g}{\partial q \partial H^\alpha} + \Delta\varepsilon_q \frac{\partial^2 g}{\partial p \partial H^\alpha} \right) \sum_{\beta=1}^n c_{\alpha\beta} \left(\frac{\partial h^\beta}{\partial q} \right) \end{aligned} \quad (3.50)$$

$$A_{21}^* = K \frac{\partial \phi}{\partial p} + \sum_{\alpha=1}^n \frac{\partial \phi}{\partial H^\alpha} \sum_{\beta=1}^n c_{\alpha\beta} \left(\frac{\partial h^\beta}{\partial \Delta \varepsilon_p} + K \frac{\partial h^\beta}{\partial p} \right) \quad (3.51)$$

$$A_{22}^* = -3G \frac{\partial \phi}{\partial q} + \sum_{\alpha=1}^n \frac{\partial \phi}{\partial H^\alpha} \sum_{\beta=1}^n c_{\alpha\beta} \left(\frac{\partial h^\beta}{\partial \Delta \varepsilon_q} - 3G \frac{\partial h^\beta}{\partial q} \right) \quad (3.52)$$

$$B_{21}^* = K \left(\frac{\partial \phi}{\partial p} + \sum_{\alpha=1}^n \frac{\partial \phi}{\partial H^\alpha} \sum_{\beta=1}^n c_{\alpha\beta} \frac{\partial h^\beta}{\partial p} \right) \quad (3.53)$$

$$B_{22}^* = -2G \left(\frac{\partial \phi}{\partial q} + \sum_{\alpha=1}^n \frac{\partial \phi}{\partial H^\alpha} \sum_{\beta=1}^n c_{\alpha\beta} \frac{\partial h^\beta}{\partial q} \right) \quad (3.54)$$

The coefficients c_{d1} and c_{d2} are same as those in Eqs. (3.27) and (3.34) respectively. Now, the solutions for $\partial \Delta \varepsilon_p$ and $\partial \Delta \varepsilon_q$ from Eqs. (3.45) and (3.46) can be written as

$$\partial \Delta \varepsilon_p = (m_{pl} I + m_{pn} n) : \partial \varepsilon + m_{pd} \partial d \quad (3.55)$$

$$\partial \Delta \varepsilon_q = (m_{ql} I + m_{qn} n) : \partial \varepsilon + m_{qd} \partial d \quad (3.56)$$

where the coefficients m_{pl} , m_{pn} , m_{pd} , m_{ql} , m_{qn} and m_{qd} can be written as

$$m_{pl} = \frac{(B_{11} A_{22}^* - B_{21} A_{12}^*)}{(A_{11}^* A_{22}^* - A_{21}^* A_{12}^*)}, \quad m_{pn} = \frac{(B_{12} A_{22}^* - B_{22} A_{12}^*)}{(A_{11}^* A_{22}^* - A_{21}^* A_{12}^*)} \quad \text{and} \quad m_{pd} = \frac{(c_{d1} A_{22}^* - c_{d2} A_{12}^*)}{(A_{11}^* A_{22}^* - A_{21}^* A_{12}^*)} \quad (3.57)$$

$$m_{ql} = \frac{(B_{21} A_{11}^* - B_{11} A_{21}^*)}{(A_{11}^* A_{22}^* - A_{21}^* A_{12}^*)}, \quad m_{qn} = \frac{(B_{22} A_{11}^* - B_{12} A_{21}^*)}{(A_{11}^* A_{22}^* - A_{21}^* A_{12}^*)} \quad \text{and} \quad m_{qd} = \frac{(c_{d2} A_{11}^* - c_{d1} A_{21}^*)}{(A_{11}^* A_{22}^* - A_{21}^* A_{12}^*)} \quad (3.58)$$

Now, taking the variation of Eq. (3.40) for $\sigma_{t+\Delta t}$, we get

$$\partial \sigma = 2G [J' : \partial \varepsilon - \partial \Delta \varepsilon_q n - \Delta \varepsilon_q \partial n] + K [I : \partial \varepsilon - \partial \Delta \varepsilon_p] I \quad (3.59)$$

where J' and ∂n are defined as

$$J' = J - \frac{1}{3} II \quad (3.60)$$

$$\partial n = \frac{3G}{q^{tr}} \left(J' - \frac{2}{3} nn \right) \quad (3.61)$$

where J is the fourth order unit tensor. Substituting Eqs. (3.55), (3.56), (3.60) and (3.61) in Eq. (3.59) and rearranging the terms, we get

$$\partial \sigma = \underline{\underline{C_{ep}}} : \partial \varepsilon + \underline{\underline{C_{ed}}} : \partial d \quad (3.62)$$

After substituting $\Delta \varepsilon_q = -\frac{1}{3G} (q - q^{tr})$, we get the consistent tangent stiffness matrices as

$$\underline{\underline{C}}_{ep} = 2G \frac{q}{q^{tr}} J' + K(1 - m_{pl}) II + \frac{4}{3} G \left(1 - \frac{q}{q^{tr}} - \frac{3}{2} m_{qn} \right) nn - 2Gm_{ql}nI - Km_{pn}In \quad (3.63)$$

$$\underline{\underline{C}}_{ed} = -2Gm_{qd}n - Km_{pd}I \quad (3.64)$$

3.6 Finite Element formulation for the non-local damage model

The partial differential equations for the mechanical continuum to be solved simultaneously are

$$\nabla \cdot \sigma + f_b = 0 \quad (3.65)$$

$$\dot{d} - \dot{f} - C_{length} \nabla^2 d = 0 \quad (3.66)$$

The associated boundary conditions are

$$\sigma \cdot n|_{\Gamma_f} = f_m \quad (3.67)$$

$$u|_{\Gamma_u} = u_0 \quad (3.68)$$

$$\nabla \dot{d} \cdot n|_{\Gamma_d} = 0 \quad (3.69)$$

Eq. (3.67) is the traction or force boundary condition, $n|_{\Gamma_f}$ is the normal to the boundary Γ_f , Eq. (3.68) is the geometric or essential displacement boundary condition, Eq. (3.69) is the Neumann or force boundary condition for the damage degree of freedom and $n|_{\Gamma_d}$ is the normal to the boundary Γ_d of the domain Ω . The weak forms of the Eqs. (3.65) and (3.66) can be written by multiplying it with the weight functions [here, the weight functions are takes as the variations of the generalized primary variables, i.e., variations of displacement for residue of Eq. (3.65) and variation of nonlocal damage for residue of Eq. (3.66)] and integrating the weighted residual over the domain Ω , these can be expressed as

$$\int_{\Omega} \delta u (\nabla \cdot \sigma + f_b) \cdot d\Omega = 0 \quad (3.70)$$

$$\int_{\Omega} \delta \dot{d} (\dot{d} - \dot{f} - C_{length} \nabla^2 \dot{d}) \cdot d\Omega = 0 \quad (3.71)$$

Using the Gauss's divergence theorem, Eqs. (3.70) and (3.71) can be simplified as

$$\int_{\Omega} \delta (\nabla u) \sigma \cdot d\Omega = \int_{\Omega} \delta u \cdot f_b \cdot d\Omega + \int_{\Gamma} \delta u \cdot t_s \cdot d\Gamma \quad (3.72)$$

$$\int_{\Omega} \delta \dot{d} \dot{d} \cdot d\Omega + \int_{\Omega} \delta \dot{d} (-\dot{f}) \cdot d\Omega + \int_{\Omega} \delta (\nabla \dot{d}) C_{length} (\nabla \dot{d}) \cdot d\Omega = 0 \quad (3.73)$$

where t_s is the surface traction and is given as $t_s = \sigma \cdot n|_{\Gamma_f}$ (Cauchy's traction law).

3.7 Derivation of the expression for \dot{f} in terms of $\partial\varepsilon$ and ∂d

The increase in void volume fraction during plastic deformation in the ductile fracture process can be written as

$$\dot{f} = \dot{f}_{growth} + \dot{f}_{nucleation} = (1-f)\partial\varepsilon^p I + A(\varepsilon_m)\dot{\varepsilon}_m \quad (3.74)$$

where $\partial\varepsilon^p$ is the change in plastic strain tensor ε^p , I is the tensor equivalent to Kronecker-Delta, $\dot{\varepsilon}_m$ is the increment of strain in the matrix ε_m and A is void nucleation constant. Again, we know that the increase in equivalent plastic strain of the matrix material $\dot{\varepsilon}_m$ can be written as

$$\dot{\varepsilon}_m = \frac{\sigma : \partial\varepsilon^p}{(1-f)\sigma_m} \quad (3.75)$$

where σ_m is the equivalent stress or current flow stress of the matrix material. We can write the increment of plastic strain tensor $\partial\varepsilon^p$ in terms of total strain increment $\partial\varepsilon$ and damage increment ∂d as

$$\partial\varepsilon^p = (\partial\varepsilon - \partial\varepsilon^e) = \left(\partial\varepsilon - \underline{\underline{C}}_{el}^{-1} : \partial\sigma \right) \quad (3.76)$$

where $\partial\varepsilon$ is the increment in total strain, $\partial\varepsilon^e$ is the increment in elastic part of strain, $\underline{\underline{C}}_{el}$ is the elastic material property matrix. Now, substituting $\partial\sigma$ from Eq. (3.62) in Eq. (3.76), we get

$$\begin{aligned} \partial\varepsilon^p &= (\partial\varepsilon - \partial\varepsilon^e) \\ &= \left(\partial\varepsilon - \underline{\underline{C}}_{el}^{-1} : \left[\underline{\underline{C}}_{ep} : \partial\varepsilon + \underline{\underline{C}}_{ed} : \partial d \right] \right) \\ &= \left(\underline{\underline{J}} - \underline{\underline{C}}_{el}^{-1} : \underline{\underline{C}}_{ep} \right) : \partial\varepsilon - \left(\underline{\underline{C}}_{el}^{-1} : \underline{\underline{C}}_{ed} \right) : \partial d \end{aligned} \quad (3.77)$$

Substituting Eqs. (3.75) and (3.77) in Eq. (3.74), we get the expression for increment of void volume fraction \dot{f} as

$$\begin{aligned} \dot{f} &= (1-f)I : \left(\underline{\underline{J}} - \underline{\underline{C}}_{el}^{-1} : \underline{\underline{C}}_{ep} \right) : \partial\varepsilon - (1-f)I : \left(\underline{\underline{C}}_{el}^{-1} : \underline{\underline{C}}_{ed} \right) : \partial d \\ &+ A(\varepsilon_m) \frac{\sigma}{(1-f)\sigma_m} : \left(\underline{\underline{J}} - \underline{\underline{C}}_{el}^{-1} : \underline{\underline{C}}_{ep} \right) : \partial\varepsilon - A(\varepsilon_m) \frac{\sigma}{(1-f)\sigma_m} : \left(\underline{\underline{C}}_{el}^{-1} : \underline{\underline{C}}_{ed} \right) : \partial d \\ &= \underline{\underline{C}}_{de} : \partial\varepsilon + \underline{\underline{C}}_{dd} : \partial d \end{aligned} \quad (3.78)$$

where the consistent tangent matrices $\underline{\underline{C}}_{de}$ and $\underline{\underline{C}}_{dd}$ are written as

$$\underline{\underline{C}}_{de} = (1-f)I : \left(\underline{\underline{J}} - \underline{\underline{C}}_{el}^{-1} : \underline{\underline{C}}_{ep} \right) + A(\varepsilon_m) \frac{\sigma}{(1-f)\sigma_m} : \left(\underline{\underline{J}} - \underline{\underline{C}}_{el}^{-1} : \underline{\underline{C}}_{ep} \right) \quad (3.79)$$

$$\underline{\underline{C}}_{dd} = -(1-f)I : \left(\underline{\underline{C}}_{el}^{-1} : \underline{\underline{C}}_{ed} \right) - A(\varepsilon_m) \frac{\sigma}{(1-f)\sigma_m} : \left(\underline{\underline{C}}_{el}^{-1} : \underline{\underline{C}}_{ed} \right) \quad (3.80)$$

3.8 Discretization of the weak form of the governing differential equations

The generalised displacement and damage vectors at any material point inside the finite element is written in terms of the generalized nodal variables (\hat{u} and \hat{d}) as

$$u = N_u \hat{u}, \quad \nabla u = \varepsilon = B_u \hat{u} \quad (3.81)$$

$$\dot{d} = N_d \hat{d}, \quad \nabla \dot{d} = B_d \hat{d} \quad (3.82)$$

where N_u and N_d are the shape function matrices for the displacement and nonlocal damage variable, B_u and B_d are matrices containing the derivatives of the shape function N_u and N_d respectively. Substituting the expressions for $u, \nabla u, \dot{d}$ and $\nabla \dot{d}$ from Eqs. (3.81) and (3.82) in the incremental form of Eq. (3.72) [using Eq. (3.62) for $\partial \sigma$] and Eq. (3.73) [note that Eq. (3.73) is already in incremental form] and substituting expression for \dot{f} from Eq. (3.78), we get

$$\delta(\Delta \hat{u})^T \left[\left(\int_{\Omega} B_u^T \underline{\underline{C}}_{ep} B_u \cdot d\Omega \right) \Delta \hat{u} + \left(\int_{\Omega} B_u^T \underline{\underline{C}}_{ed} N_d \cdot d\Omega \right) \hat{d} - \int_{\Omega} N_u^T f_b d\Omega - \int_{\Gamma} N_u^T t_s d\Gamma \right] = 0 \quad (3.83)$$

$$\delta \hat{d}^T \left[\left(\int_{\Omega} N_d^T N_d \cdot d\Omega \right) \hat{d} - \left(\int_{\Omega} N_d^T \underline{\underline{C}}_{de} B_u \cdot d\Omega \right) \hat{u} - \left(\int_{\Omega} N_d^T \underline{\underline{C}}_{dd} N_d \cdot d\Omega \right) \hat{d} + \left(\int_{\Omega} B_d^T C_{length} B_d \cdot d\Omega \right) \hat{d} \right] = 0 \quad (3.84)$$

For arbitrary value of $\delta(\Delta \hat{u})^T$ and $\delta \hat{d}^T$, the terms inside the brackets of Eqs. (3.83) and (3.84) should be zero and hence these equations reduce to the set of finite element algebraic equations, which can be written in convenient (matrix) form as

$$\begin{bmatrix} K_{uu} & K_{ud} \\ K_{du} & K_{dd} \end{bmatrix} \begin{Bmatrix} \Delta \hat{u} \\ \Delta \hat{d} \end{Bmatrix} = \begin{Bmatrix} f_m^{ext} - f_m^{int} \\ -f_d^{int} \end{Bmatrix} \quad (3.85)$$

where the matrices and the force vectors can be written as

$$\begin{aligned}
K_{uu} &= \int_{\Omega} B_u^T \underline{\underline{C_{ep}}} B_u \cdot d\Omega \\
K_{ud} &= \int_{\Omega} B_u^T \underline{\underline{C_{ed}}} N_d \cdot d\Omega \\
K_{du} &= - \int_{\Omega} N_d^T \underline{\underline{C_{de}}} B_u \cdot d\Omega \\
K_{dd} &= \int_{\Omega} N_d^T N_d \cdot d\Omega - \int_{\Omega} N_d^T \underline{\underline{C_{dd}}} N_d \cdot d\Omega + \int_{\Omega} B_d^T C_{length} B_d \cdot d\Omega \\
f_m^{ext} &= \int_{\Omega} N_u^T f_b \cdot d\Omega + \int_{\Gamma} N_u^T t_s \cdot d\Gamma \\
f_m^{int} &= \int_{\Omega} B_u^T \sigma_i \cdot d\Omega \\
f_d^{int} &= \int_{\Omega} N_d^T \dot{d}_i \cdot d\Omega - \int_{\Omega} N_d^T \dot{f}_i \cdot d\Omega + \int_{\Omega} B_d^T C_{length} \nabla \dot{d}_i \cdot d\Omega
\end{aligned} \tag{3.86}$$

where the subscript 'i' refers to the quantities at the end of previous iteration step of the incremental nonlinear finite element analysis. It may be observed from the FE Eq. (3.85) that the stiffness matrix of the finite element contains coupled terms corresponding to displacement and damage degrees of freedom. The matrix K_{uu} represents the conventional stiffness of the finite element where damage degree of freedom is not considered in the analysis and it represents the mechanical stiffness, which corresponds to the relationship of the to nodal mechanical forces and nodal displacement vectors. Similarly, K_{ud} represents the matrix, which produces nodal damage vector corresponding to applied mechanical force vector. The matrix K_{du} produces nodal displacement vector corresponding to applied damage force vector and K_{dd} produces nodal damage vector corresponding to applied damage force vector respectively.

3.9 Development of a finite element program DEFINE (Damage Evaluation using FINite Elements)

Based on the finite element formulation developed in the previous section, a FE code (acronym DEFINE) has been written using fortran 90. It may be noted that Eq. (3.85) and hence the global stiffness matrix is in general non-symmetric. Hence, a non-symmetric sparse matrix solver has been used in the code. The code incorporates plane strain and axisymmetric finite elements in 2D and 3D elements for 3D continuum. Isoparametric elements (4-noded and 8-noded quadrilateral in 2D, 8-noded and 20-noded brick elements in 3D) are used for

simulation. The shape functions used for the elements can be found in standard FE textbooks (e.g. Bathe 1995) and hence are not discussed here.

Updated Lagrangian formulation has been used, where all the variables are referred to the configuration at time t , i.e. the updated configuration of the body. In the equilibrium equation, the stress (second Piola-Kirchoff stress tensor) and strain (Green-Lagrange strain tensor) measures are (as defined in the large strain FE analysis) from the configuration at time t to the configuration at time $t + \Delta t$ and referred to the configuration at time t . Standard nonlinear element stiffness matrices (corresponding to geometric nonlinearity and effect of stress stiffening) corresponding to updated Lagrangian formulation has been added to the linear stiffness matrix (derived in the previous section) in order to obtain overall stiffness matrix for the element (Bathe 1995). Full integration scheme is used for Gaussian quadrature for evaluation of stiffness matrices. The code has been verified by solving problems from literature and then comparing the results with available solutions.

In the next chapter, numerical results are presented for several problems involving prediction of load-deformation and fracture resistance behaviour of different specimens. The aim is to demonstrate the mesh independent nature of the solutions obtained using nonlocal damage models. Initially, a single element in 2D axisymmetric mode has been analysed to obtain its load-displacement response and the change in load-displacement response is studied upon subsequent refining of the FE mesh. Once the mesh independency has been demonstrated, analysis has been extended to other types of specimens.

Chapter 4

Numerical simulation of ductile crack growth in the upper shelf region

For safety analysis of engineering components in the upper shelf temperature region of the material, ductile fracture resistance curve is an important tool. As has been previously discussed, continuum damage mechanics models are able to simulate the ductile crack initiation and crack growth processes using only a set of material properties and a critical length parameter as FE mesh size. In the newly developed nonlocal form of the Rousselier's damage model, the material characteristics length parameter is incorporated into the material constitutive equation. In this chapter, the newly developed model is used to simulate the fracture resistance behaviour of different types of specimens at room temperature (using different FE mesh sizes to study the mesh independent nature of solutions of the nonlocal model). Before describing the numerical results of the specimens for which experiments have been conducted by Eisele et al 2006 at MPA Universität Stuttgart, the FE code DEFINE is verified by analysis of a cylindrical specimen of 2mm length and 2mm diameter using 2D axisymmetric assumption using different FE mesh sizes.

4.1 Simulation of material damage in damage mechanics models

In damage mechanics models for ductile fracture, the damage state of the material is defined in terms of the ductile void volume fraction f . As these are coupled (stress and strain affects damage accumulation and vice versa) and porous plasticity models, the void volume fraction starts accumulating in the material once there is plastic deformation due to loading. Theoretically, the state of the material point with $f = 0$ refers to damage free material and $f = 1$ refers to the completely damaged materials and hence a crack (having no stress carrying capability). However in actual materials, the void volume fraction f evolves (through nucleation of new voids and growth of existing voids) from the initial void volume fraction f_0 in the material (volume fraction of relevant inclusions or void nucleation sites) with increasing plastic strain and at a certain value of void volume fraction (i.e., f_c), the material stress carrying capability reduces drastically and this simulates damage of the material point and

hence formation of the crack. This parameter f_c (called void volume fraction at coalescence) is a material property and is usually determined by comparing the numerical simulation results of drastic load drop in a round tensile specimen with that of experiment. For many of the engineering materials (e.g., mainly steels), this value is often used as 0.05. The value of initial void volume fraction f_0 is material parameter and is usually determined from microscopic quantification of relevant inclusions (i.e., manganese sulphides in case of low alloy steels), which can lead to void formation with plastic straining of the matrix. Many times, these are also determined numerically by fitting numerical simulation results with those of experiments (mostly in round tensile specimens). In our work, we have studied the fracture resistance behaviour of the German low alloy steel 22NiMOCr3-7 and the initial void volume fraction has been taken as 0.0003 (Krieg and Seidenfuss 2003, Seidenfuss and Roos 2005, Seebich 2007).

In this work, we have also used $f_c = 0.05$ for all our numerical simulations with damage mechanics models. In order to simulate the complete loss of stress carrying capability of the material point when the void volume fraction reaches f_c , the stiffness of the said material point (Gauss point in FE simulation) is assigned a small value. However, numerical convergence problems usually appear for the FE simulation and the alternate way is to reduce the Gauss point stiffness gradually in an indirect manner by accelerating the void volume fraction with the help of f^* in place of f as described in Eq.(2.39). In the numerical simulations carried out in this work, the acceleration factor for both the local and nonlocal model has been taken as 3. In nonlocal models, there is an additional material parameter (i.e., the characteristics length parameter C_{length}) and it is determined by comparing the experimentally measured J-resistance curve of a compact tension specimen with the numerical simulation curve. Analysis is carried out with various values of C_{length} . The value of C_{length} that is selected as the material parameter corresponds to the simulation, which describes the experiment satisfactorily. It was also shown by Reusch et al. (2003a) that $C_{length} \approx \frac{l_c^2}{4}$ where l_c is the characteristics length for the material and it represents the mean distance between relevant inclusions of the material. For the material under consideration here (i.e., 22NiMoCr3-7), the characteristics length l_c has been determined as 0.4 (Seebich 2007) and the C_{length} parameter has been chosen as 0.05 as this value of C_{length} simulates the fracture

resistance behaviour of the fracture mechanics specimens satisfactorily when compared with the experimental fracture resistance curve.

4.2 Demonstration of mesh independency of the results of the new model by analysis of a cylindrical specimen with different mesh sizes

To demonstrate that the finite element results converge as the mesh size is reduced in case of the new nonlocal formulation, analysis has been carried out for a cylindrical specimen of 2mm length and 2mm diameter. Analysis has been done using 2D axisymmetric finite element meshes of different sizes. Initially, 1mm x 1mm mesh is used in the analysis and it is subsequently refined. The cylindrical specimen along with the loading and symmetric boundary conditions is shown in Fig. 4.1(a).

Table-4.1: Parameters of the nonlocal damage model used for analysis of the cylindrical specimen (2D axisymmetric model)

Model parameters	D	σ_k (MPa)	f_0	f_c	f_f	C_{length}	E (GPa)	ν
Value	2	445	0.002	0.05	0.3	0.5	210	0.3

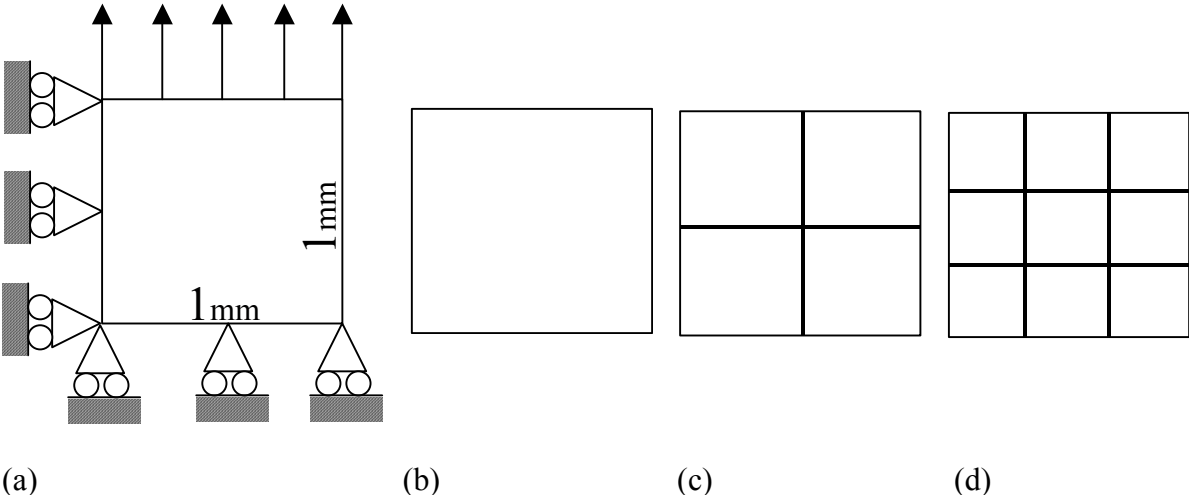


Fig. 4.1: (a) Geometry and symmetric boundary conditions for the axisymmetric round tensile specimen; (b) 1x1 FE mesh; (c) 2x2 FE mesh; (d) 3x3 FE mesh

The parameters of Rousselier damage mechanics model along with the critical length parameter C_{length} used in the analysis are shown in Table-4.1. The FE mesh of the single element (1x1 mesh) used in the analysis is shown in Figs. 4.1(b). The single element has been refined gradually into a 2x2 and 3x3 mesh as shown in Figs. 4.1(c-d). Eight-noded isoparametric 2D axisymmetric elements have been used. A little imperfection has been provided at the bottom right end in order to simulate necking. The applied displacement (at the top loading edge) and diametral contraction (bottom right corner) have been plotted against reaction load. The Young's modulus (E) of the material is taken as 210Gpa and Poisson's ratio (ν) as 0.3. The material stress-strain curve used in the analysis is shown in Fig. 4.2.

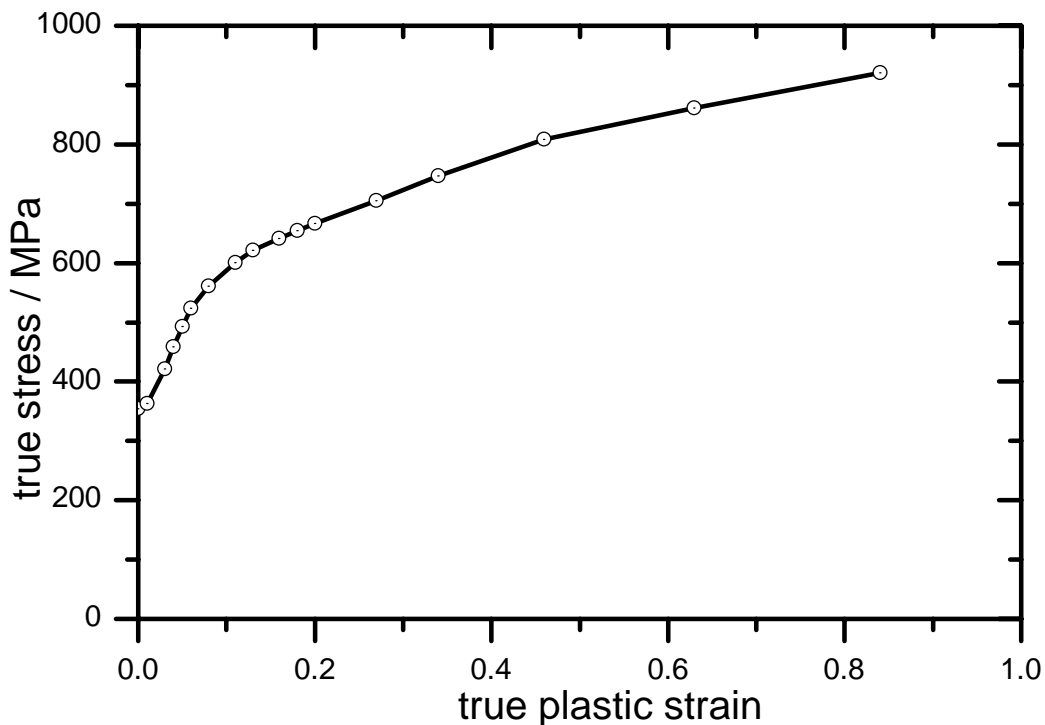


Fig. 4.2: True stress vs true strain curve of the material used in analysis of the round tensile specimen

Three different types of analyses have been carried out (i.e., elasto-plastic, local damage model, nonlocal damage model) in order to illustrate the differences among these approaches. Elasto-plastic analysis ($f_0 = 0$, 1x1 mesh) doesn't consider the effect of ductile damage f (void volume fraction) on material stress carrying capability and hence it cannot simulate the drastic load drop phenomenon before fracture of the tensile specimen [Fig. 4.3, 4.4]. However, when the damage mechanics analysis (local model, $C_{length} = 0$) is used, there is a

drastic reduction in load carrying capacity of the specimen when f approaches critical value (i.e., f_c) at a Gauss point as shown in the load-displacement and load-diametral contraction response of the tensile specimen in Fig. 4.3 and 4.4. Analysis of the same single element (1x1) mesh has also been carried out using the newly developed nonlocal model with a characteristics length parameter of $C_{length} = 0.5$. For this value of C_{length} , the load-displacement and load-diametral contraction results of the tensile specimen are nearly the same for both the local and nonlocal damage models [Figs. 4.3 and 4.4].

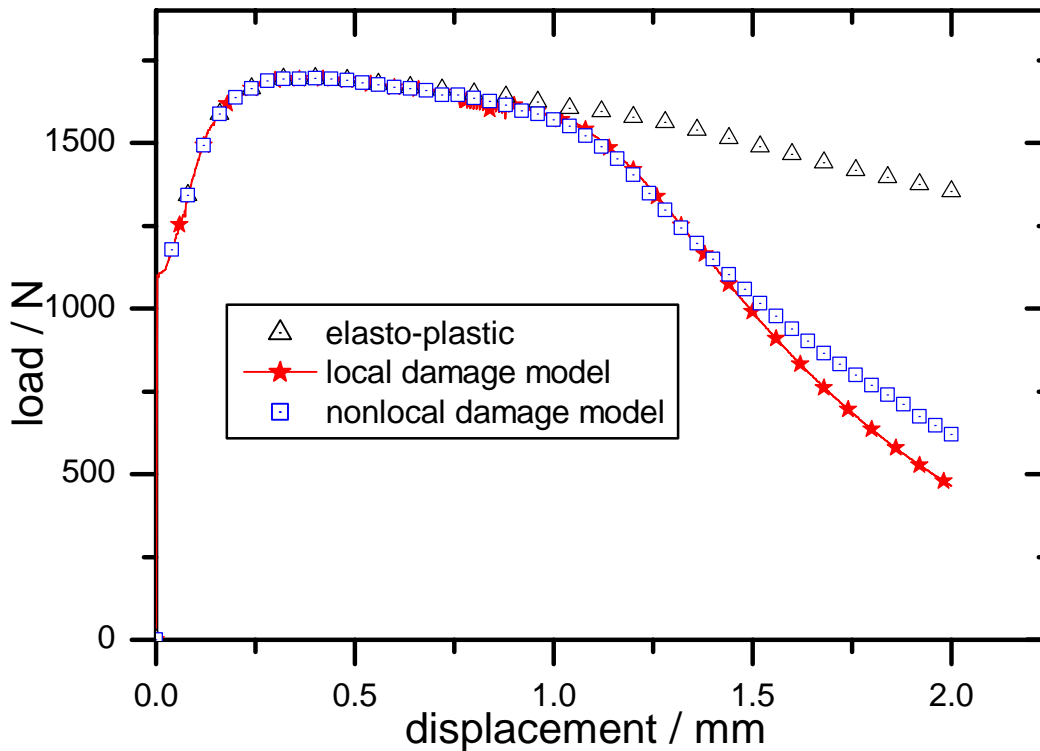


Fig. 4.3: Comparison of load-displacement response of the round tensile specimen analyzed using different models (1x1 mesh)

In order to study the effect of mesh size on the load-displacement and the load-diametral contraction response of the tensile specimen, the 1x1 mesh has been refined progressively to a 2x2 and 3x3 mesh. Fig. 4.5 and 4.6 show the comparison of load-displacement and load-diametral contraction response of the specimen using both local ($C_{length} = 0$) and nonlocal ($C_{length} = 0.5$) models for the three different FE mesh sizes. It can be seen that the responses of the local model are highly mesh dependent (i.e., load reduces quickly as mesh size is refined) whereas the responses of the nonlocal model are mesh independent. This simple example demonstrates the mesh independent nature of the newly developed nonlocal Rousselier's model, which has been applied to other types of examples in subsequent sections.

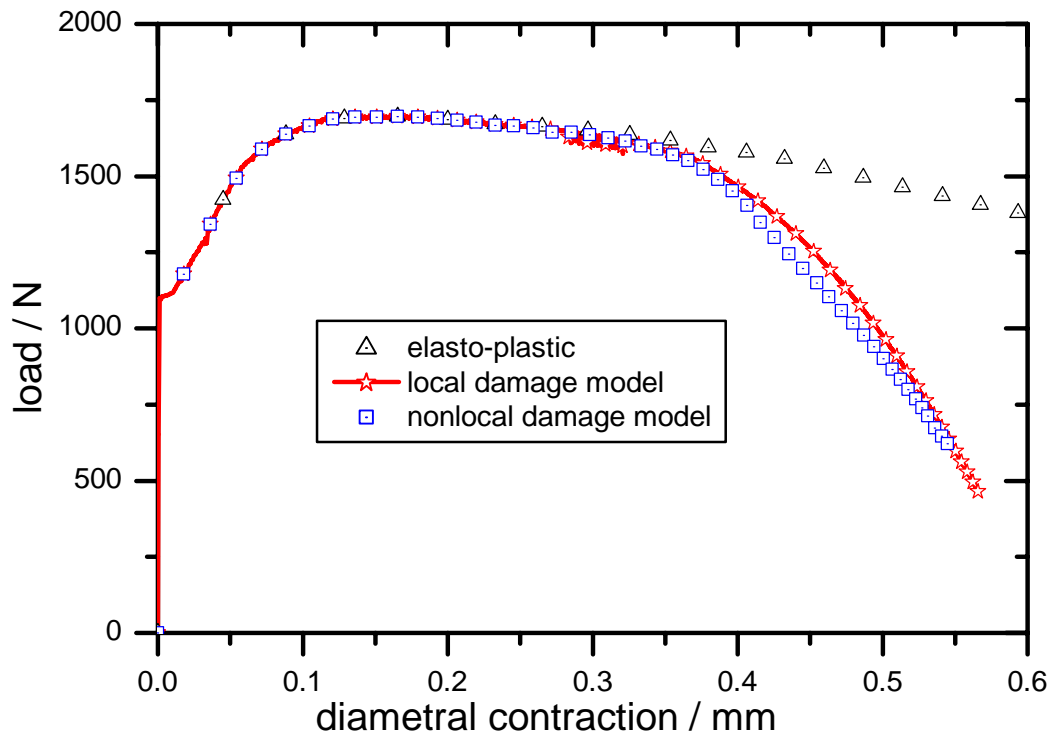


Fig. 4.4: Comparison of load-diametral contraction response of the round tensile specimen analyzed using different models (1x1 mesh)

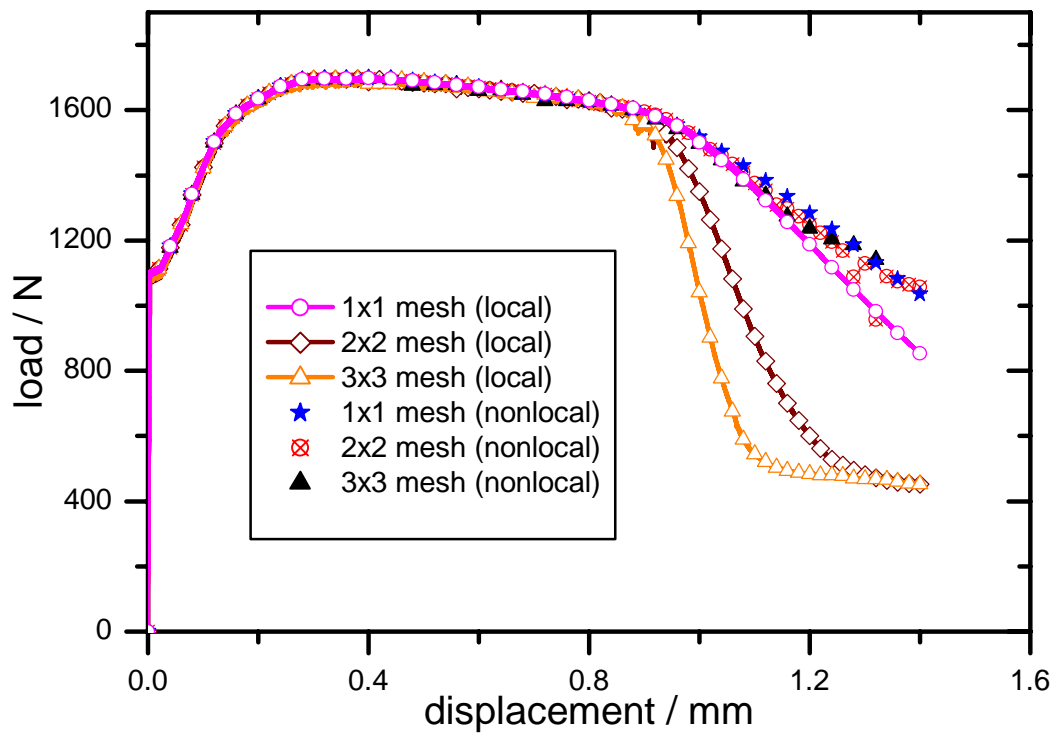


Fig. 4.5: Comparison of load-displacement response of the round tensile specimen analyzed with different mesh sizes

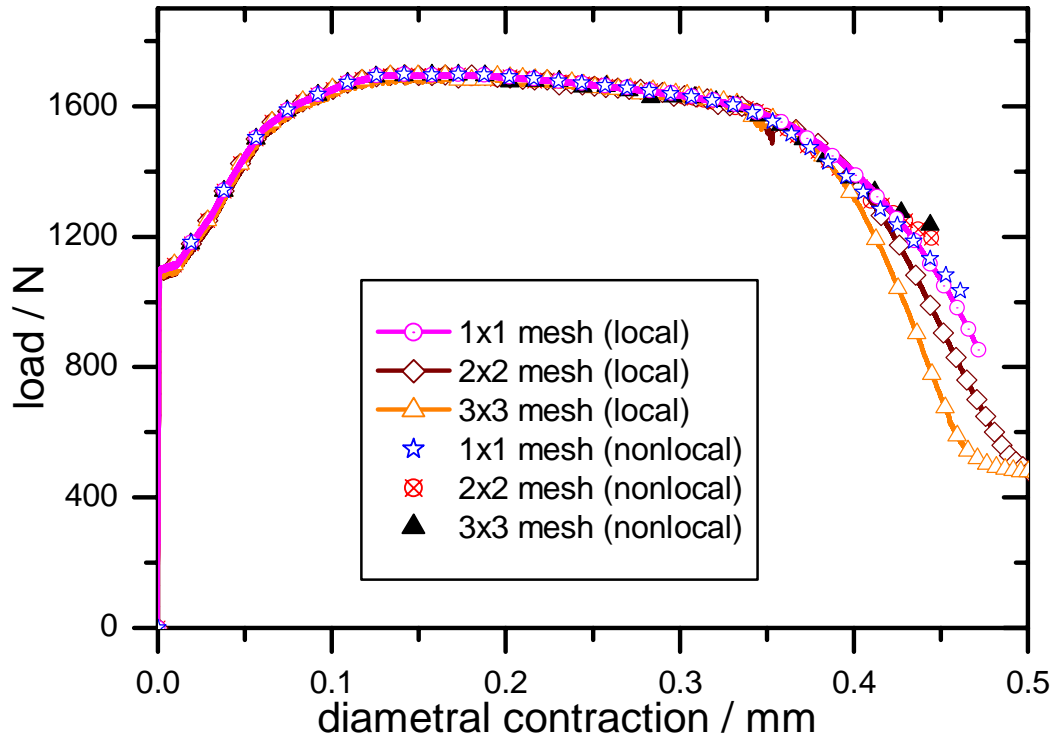


Fig. 4.6: Comparison of load-diametral contraction response of the round tensile specimen analyzed with different mesh sizes

4.3 Analysis of shear band specimen

We consider the analysis of a shear band specimen (flat tensile specimen of 5mm width and 10mm length) to study the development of width of shear band. Here, a 2-D plane strain analysis (with 8-noded isoparametric quadrilateral elements) has been used. The geometry and boundary conditions of the shear band (flat tensile) specimen are shown in Fig. 4.7. An initial imperfection (slightly high value of the initial void volume fraction f_0 , i.e., 0.005) has been used at the marked location in Fig. 4.7 (in order to initiate the shear band at that point). Three different mesh sizes (square elements of 1.0mm, 0.5mm and 0.33mm side lengths) have been used in the analysis. The material stress-strain curve used in the analysis is shown in Fig. 4.8 for this elastic-perfectly plastic material. Other material properties are shown in Table-4.2.

Table-4.2: Parameters of the nonlocal damage model used for analysis of the shear band specimen

Model parameters	D	σ_k (MPa)	f_0	f_c	f_f	C_{length}	E (GPa)	ν
Value	2	445	0.002	0.05	0.3	0.05	210	0.3

The characteristic length parameter used here is 0.05. An interesting feature of this specimen is the development of shear band. Because of tensile loading in the flat specimen, we know that shear bands (zones of shear localisation where damage accumulation occurs subsequently) develop at $\pm 45^\circ$ to the tensile axis and as it is an instability, it can develop anywhere along the length of the specimen. In order to study it numerically, a slightly high value of initial void volume fraction has been used at the location of imperfection.

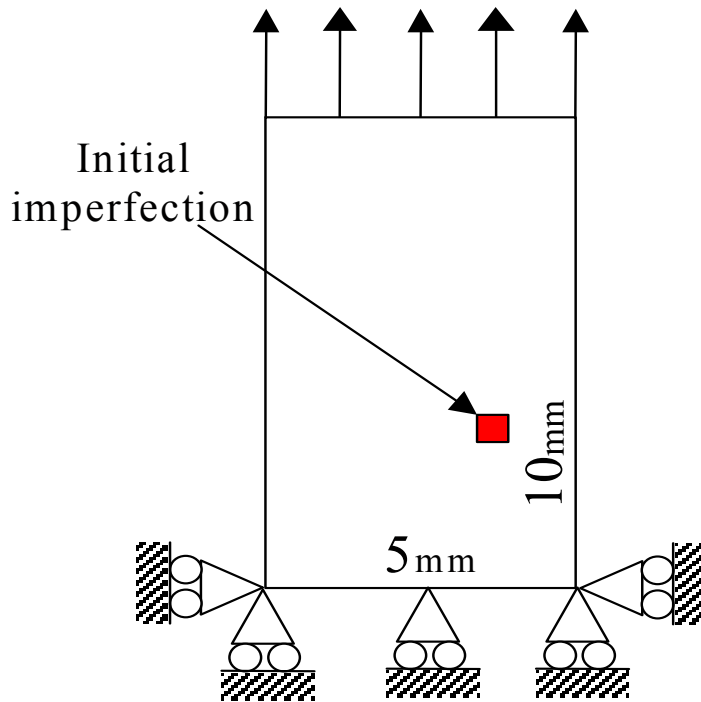


Fig. 4.7: Schematic figure of the flat tensile specimen used to study shear band formation

It is well known that the width of shear band depends upon the mean distance between relevant inclusions and second phase particles and hence it is a material property. Fig. 4.9-11 show the widths of shear band (the shear band region is represented by the region within the contour plot of damage with the value of damage as 0.5) in the FE meshes of three of different mesh sizes (1mm, 0.5mm and 0.33mm) predicted by the local damage model of Rousselier. It can be observed that shear band localises to one element layer in case of 1mm mesh. However, as the mesh size is refined, it still localises in one element layer. In other words, as the element size is refined, the actual width of shear band predicted by the local model reduces with mesh refinement. This is in contradiction to the observed experimental behaviour, where the width of shear band is constant. The above mesh dependent nature of the prediction for width of shear band can be removed by the use of nonlocal damage model as discussed in the following text.

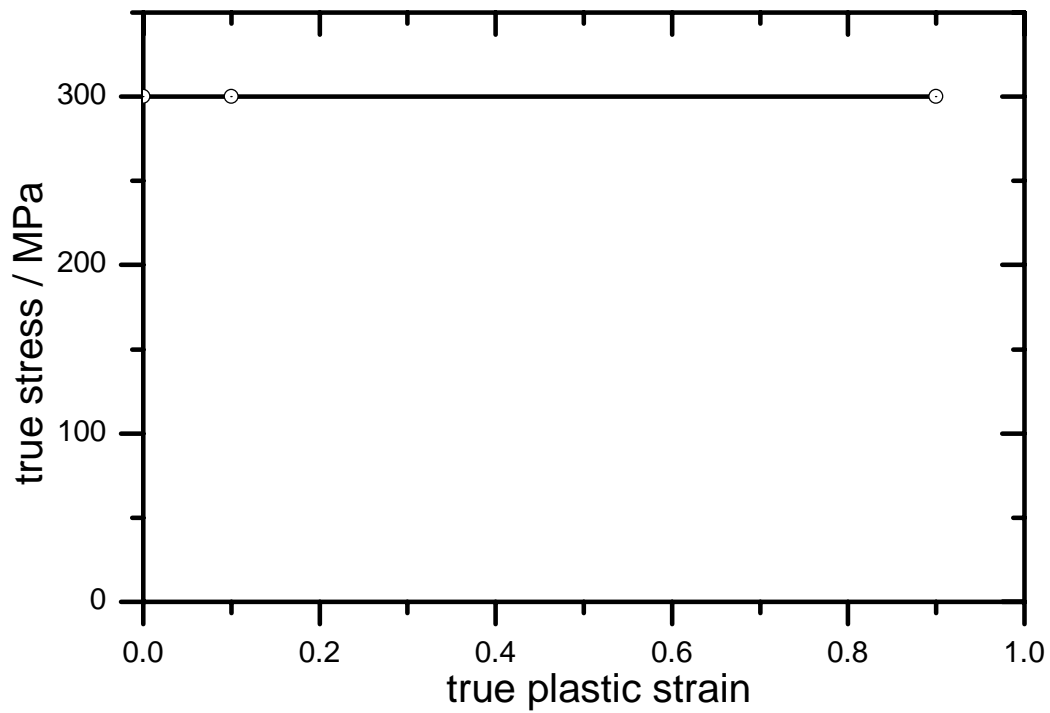


Fig. 4.8: True stress vs true strain curve of the material of the shear band specimen

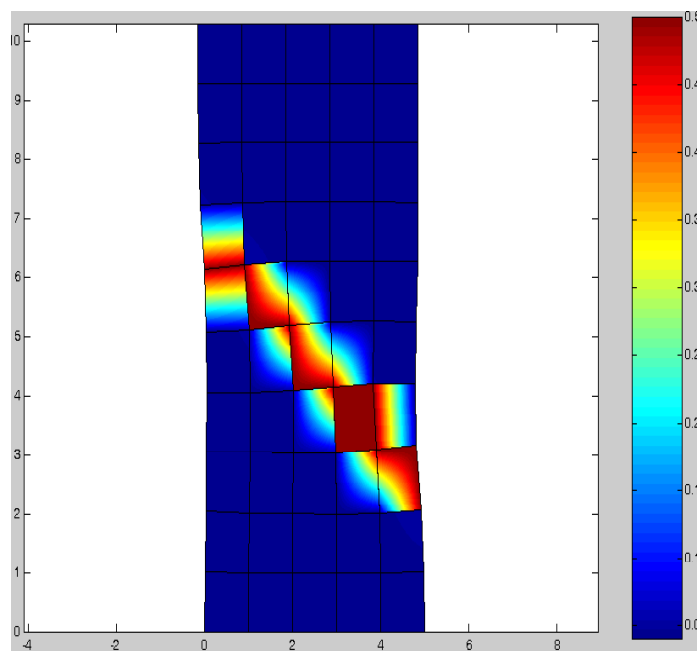


Fig. 4.9: Shear band development in the flat tensile specimen for 1mm FE mesh size (local model), contour plot of damage

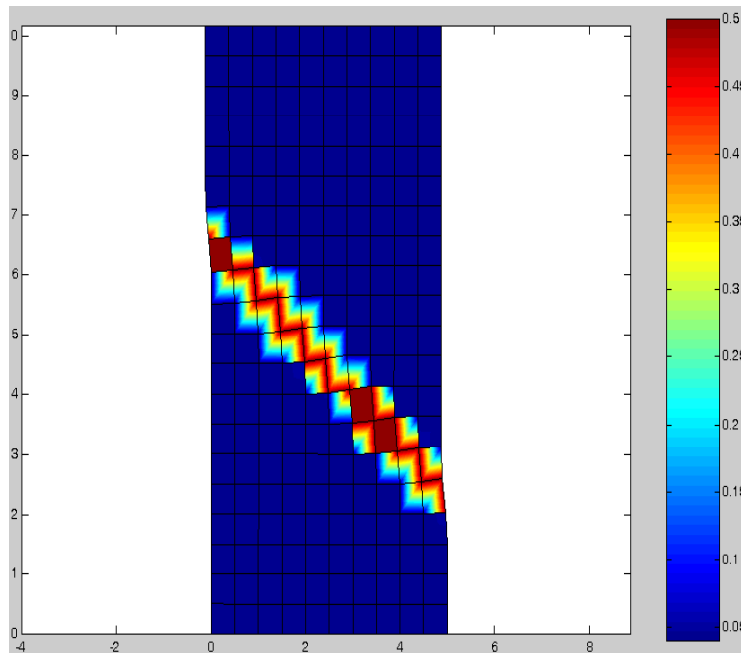


Fig. 4.10: Shear band development in the flat tensile specimen for 0.5mm FE mesh size (local model), contour plot of damage

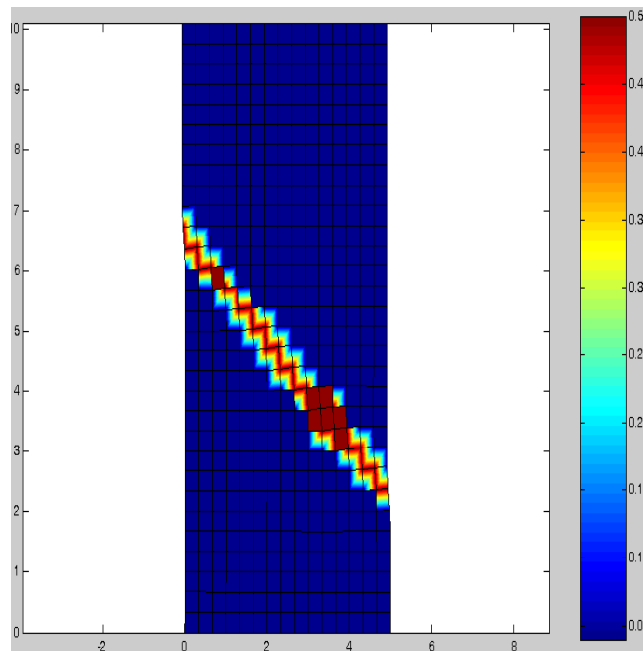


Fig. 4.11: Shear band development in the flat tensile specimen for 0.33mm FE mesh size (local model), contour plot of damage

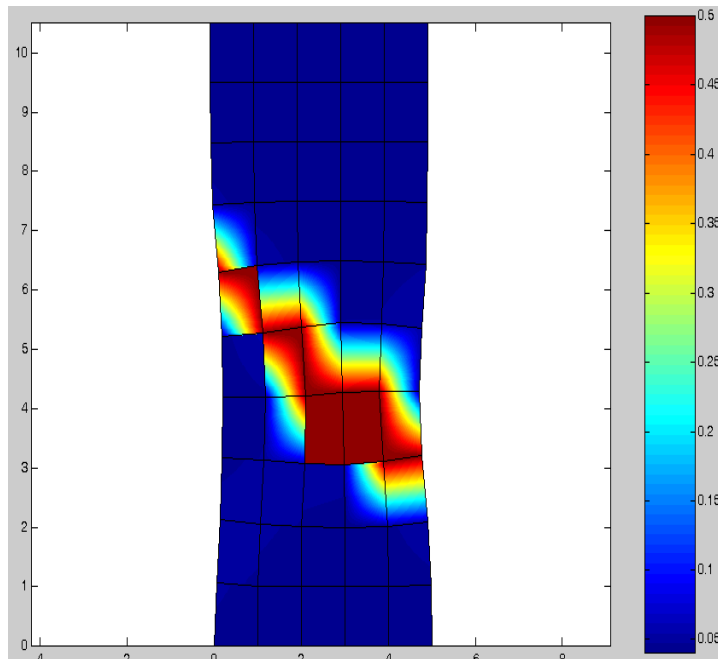


Fig. 4.12: Shear band development in the flat tensile specimen for 1mm FE mesh size (nonlocal model), contour plot of damage

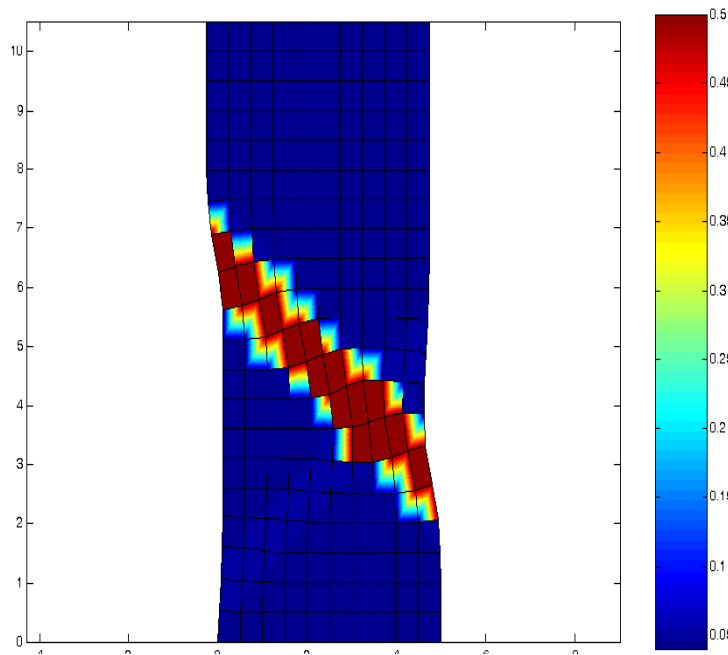


Fig. 4.13: Shear band development in the flat tensile specimen for 0.5mm FE mesh size (nonlocal model), contour plot of damage

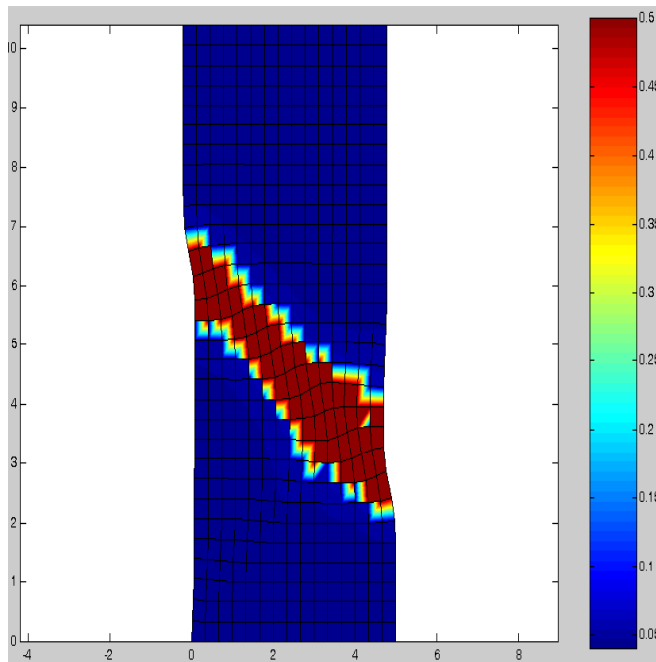


Fig. 4.14: Shear band development in the flat tensile specimen for 0.33mm FE mesh size (nonlocal model), contour plot of damage

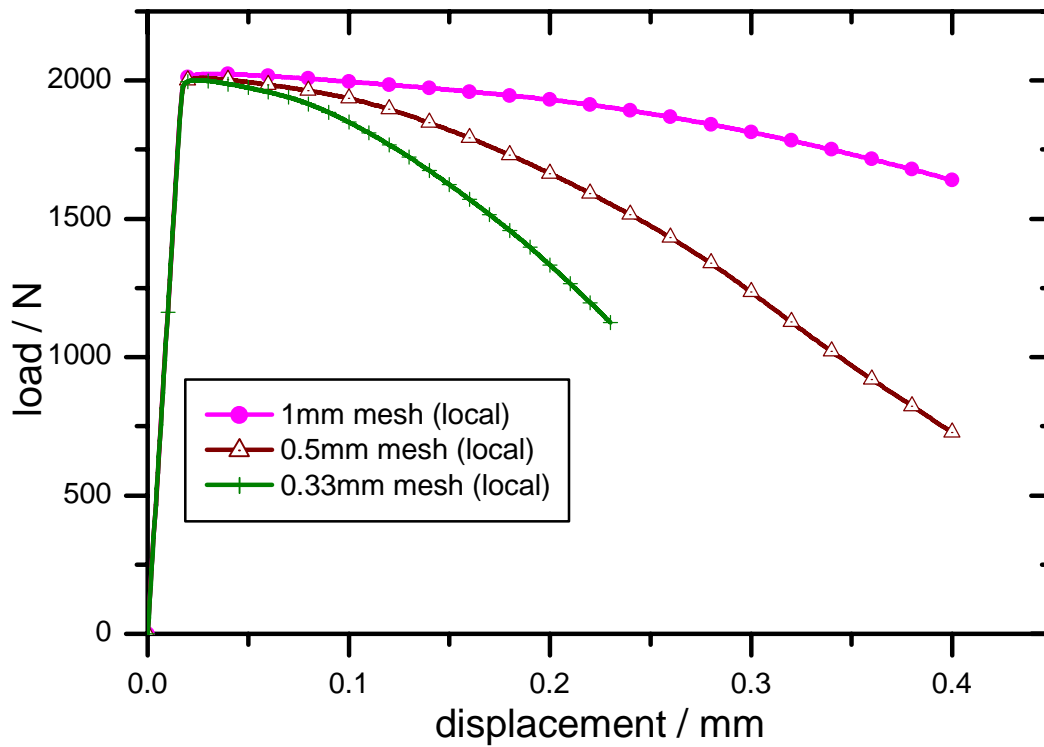


Fig. 4.15: Load-displacement response of the flat tensile specimen for different mesh sizes (local model)

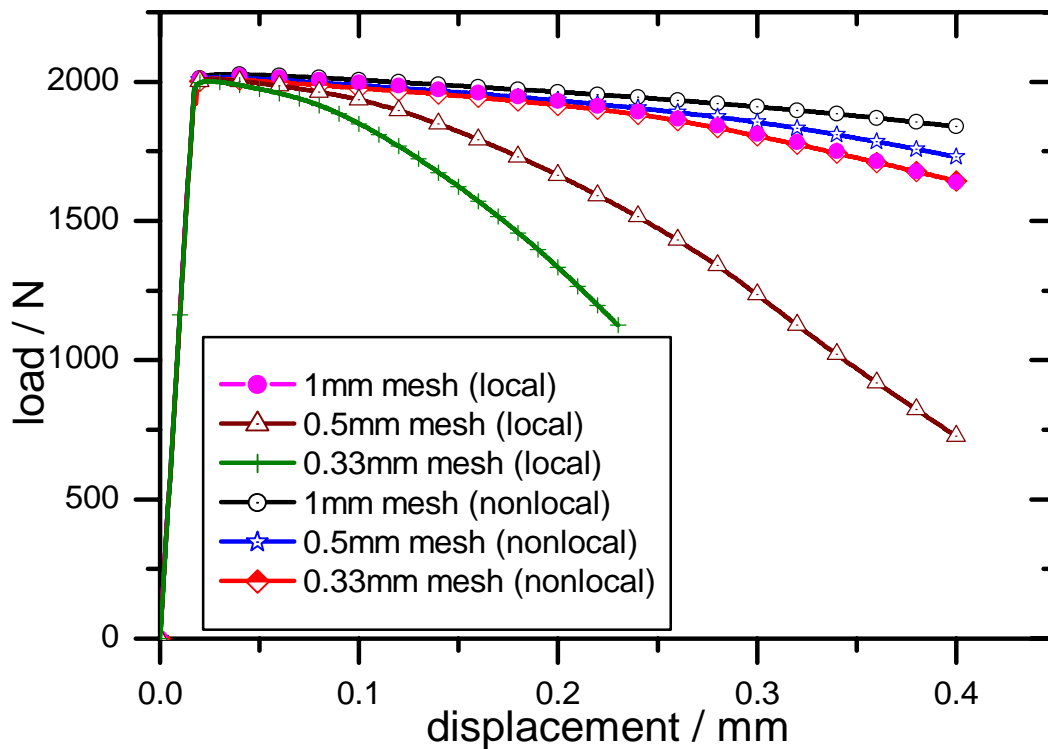


Fig. 4.16: Load-displacement response of the flat tensile specimen for different mesh sizes (local vs nonlocal model)

Fig. 4.12-14 show the predicted width of shear band of the flat tensile specimen for three different mesh sizes (1mm, 0.5mm and 0.33mm) when nonlocal form of the Rousselier model is used. It can be observed that the shear band is localised to a single element layer in case of 1mm mesh, 2-element layers in case of 0.5mm mesh and 3-element layers in case of 0.33 mesh of the nonlocal model. Hence, the width of the shear band can be evaluated and it comes out to be almost constant which again demonstrates the mesh independent nature of solution of the nonlocal model.

The effect of development of the width of shear band also gets reflected on the load-response behaviour of the shear band specimen. When the shear band narrows down with mesh refinement, the load also drops quickly with respect to end displacement. Hence, the local model predicts lower and lower load-displacement responses, as the mesh size is refined [Fig. 4.15] whereas the responses predicted by the nonlocal model are almost mesh-independent [Fig. 4.16]. It is because of the constant width of shear band predicted by the nonlocal model.

4.4 Analysis of round notched tensile specimens

Round-notched tensile specimens are widely used geometries to study the effect of geometry of notch (and hence stress multiaxiality) on the load-response curve of the specimen. In this work, such a specimen was simulated in order to study the effect of FE mesh size on the results of analysis with both local and nonlocal models. The specimen geometry is shown in Fig. 4.17(a). The dimensions of the specimen are given as: $d = 20\text{mm}$, $D = 16\text{mm}$, $R = 2\text{mm}$ and 120mm gauge length. Due to symmetry, half of the specimen has been modeled and then axisymmetric modeling is used. 8-noded isoparametric quadrilateral elements of 2D axisymmetric formulation has been used in the FE mesh. Fig. 4.17(b) and (c) show two different meshes of 0.44 and 0.22mm size (near the notch region) respectively used in the FE analysis. The material of the specimen is 22NiMoCr3-7 and the true stress-strain curve of the material (at room temperature) used in the analysis is shown in Fig. 4.18 (taken from Krieg and Seidenfuss 2003).

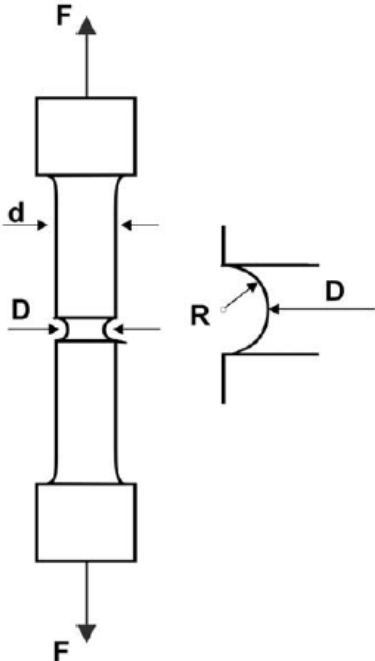


Fig. 4.17(a): Geometry of the round notched tensile specimen

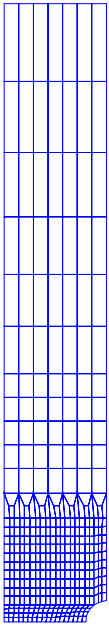


Fig. 4.17(b): FE mesh of round notched tensile specimen (0.44mm mesh near the notched region)

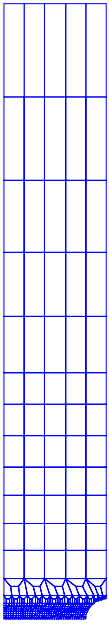


Fig. 4.17(c): FE mesh of round notched tensile specimen (0.22mm mesh near the notched region)

Table-4.3: Parameters of the nonlocal damage model for the material 22NiMoCr3-7

Model parameters	D	σ_k (MPa)	f_0	f_c	f_f	C_{length}	E (GPa)	ν
Value	2	445	0.0003	0.05	0.3	0.05	210	0.3

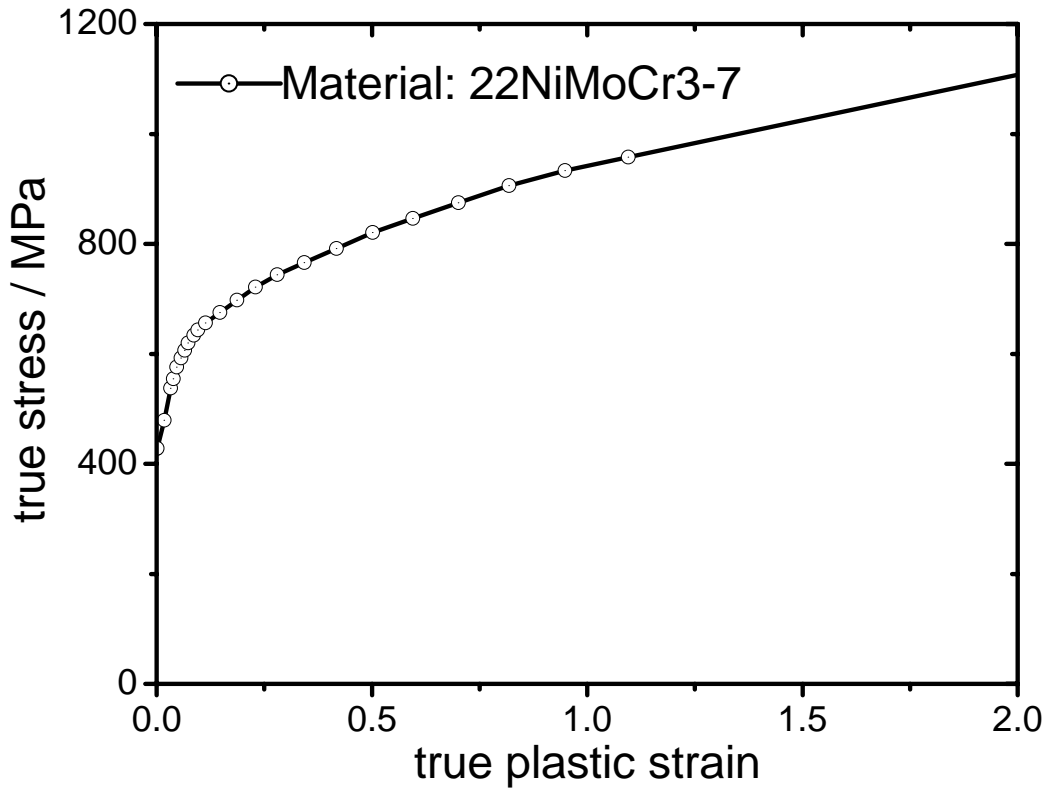


Fig. 4.18: True stress vs true strain curve of the material 22NiMoCr3-7 at room temperature

Other material parameters are given in Table-4.3. Fig. 4.19 shows the results of analysis using two different mesh sizes of 0.44 and 0.22mm (near the notched region where crack initiation and propagation occurs). As can be taken from Fig. 4.19, the local model predicts an early load drop (due to crack development at the center of the specimen before final rupture) when the mesh size is decreased from 0.44mm to 0.22mm. However, the load-diametral contraction response of the specimen predicted by the nonlocal model is almost independent of the mesh size as can be seen from Fig. 4.19.

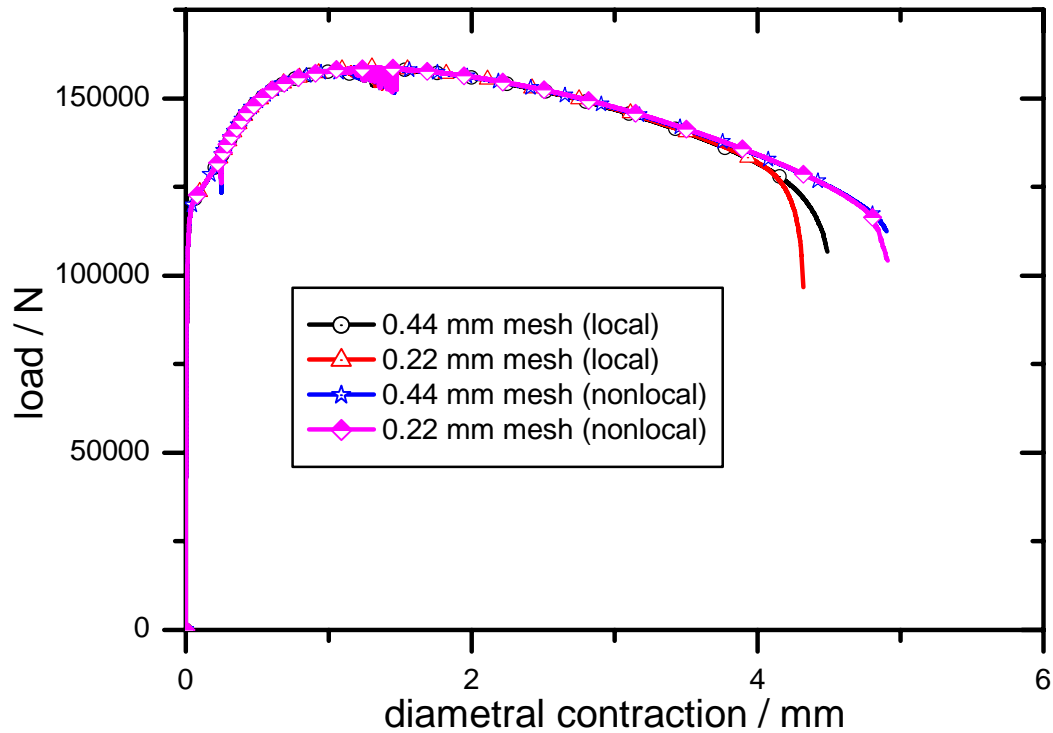


Fig. 4.19: Load-diametral contraction response of the round notched tensile specimen (local vs nonlocal model predictions)

4.5 Analysis of the flat tensile specimen with a hole at the center (LISSAC: Krieg and Seidenfuss 2003)

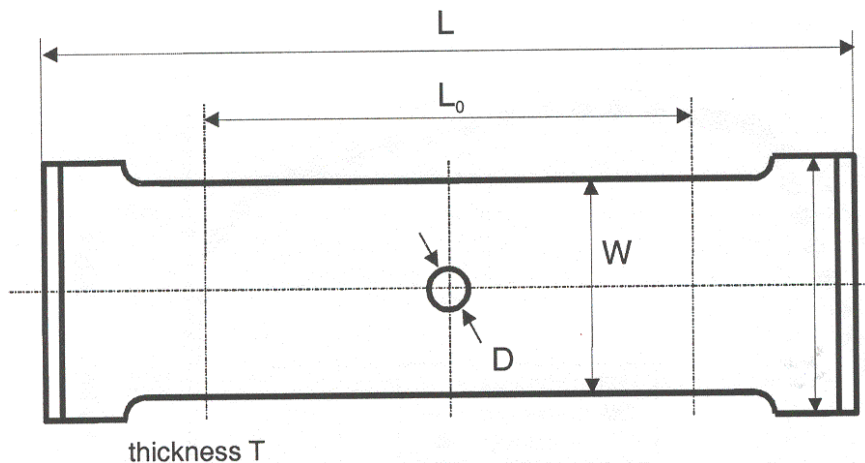


Fig. 4.20: Schematic diagram of the flat tensile specimen with hole at the center

In an effort to establish a limit value of local strain (for failure or crack initiation), which can be used for design of different components, a detailed experimental and analytical program was undertaken [i.e., LISSAC: Krieg and Seidenfuss 2003]. Here, effect of specimen size, type, thickness, crack depth, temperature etc. were varied in order to study the effect of all

these parameters on the limiting value of strain. Several experiments were carried under this program and one such specimen has been used in this section for analysis with damage mechanics models.

The specimen shown in Fig. 4.20 is a flat tensile specimen with a hole at the centre with dimensions $D = 2\text{mm}$, $W = 5D = 10\text{mm}$, $L_0 = 12D = 24\text{mm}$, thickness $T = 2D = 4\text{mm}$. This is the smallest specimen among a series of specimens with thickness ranging from 4 to 200mm (the other dimensions of the specimen are proportional to thickness and the proportions are same as that of the specimen with 4mm thickness). Though the specimen thickness is small compared to other dimensions of the specimen, 2D plane strain analysis has been carried out in order to simulate the load-response behaviour of the specimen using both Rousselier's local and nonlocal damage mechanics models.

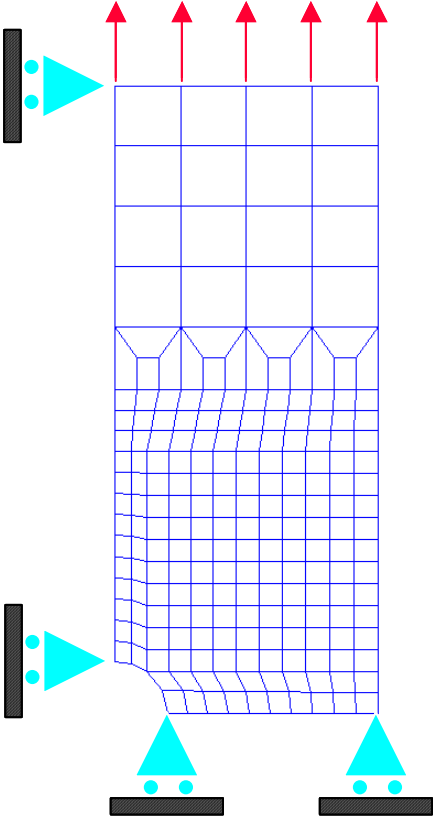


Fig. 4.21: FE mesh of the flat tensile specimen with hole (one-fourth of the specimen with symmetric boundary conditions), mesh size: 0.4mm along the crack path

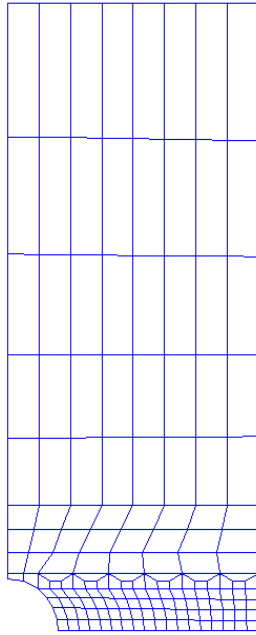


Fig. 4.22: FE mesh of the flat tensile specimen with hole, mesh size: 0.2mm along the crack path

Due to symmetry, one fourth of the specimen has been analyzed. The FE mesh of one-fourth of the specimen along with the boundary and displacement loading conditions are shown in Fig. 4.21. Figs. 4.21-23 show FE meshes with three different mesh sizes of 0.4mm, 0.2mm and 0.1mm near the hole region (and in direction of crack propagation) which has been used in the analysis. In order to understand the effect of mesh size on the crack or damage zone development in the flat tensile specimen, the damage zones (damage zones within the contour plot is represented by damage values of 0.5) have been plotted for the three different mesh sizes in Figs. 4.24-26 for the local model.

Fig. 4.24 shows that damage zone (after substantial load drop due to crack growth) is confined only to one Gauss point layer (approximately half the element height) at the center of the specimen for the 0.4mm mesh, For the 0.2 and 0.1mm meshes also, the damage zone is spread over one Gauss point layer or half the element height [Fig. 4.25-26]. However, the element sizes are small for 0.2 and 0.1mm FE meshes and hence the actual damage zone height gets reduced with mesh refinement for the local model.

When the same FE meshes are used in the nonlocal model, we obtain the damage zone height as one Gauss point layer (or half the element height) for 0.4mm mesh, 1 element height for

0.2mm mesh and approximately 1.5-element height for 0.1mm mesh [Figs. 4.27-29]. When the actual element heights are used for calculation of damage zone height, it turns out to be approximately constant for all the three different FE mesh sizes. Hence, the damage zone height results predicted by nonlocal models are mesh independent as opposed to local models.

The effect of damage zone height also gets reflected in the load-displacement response of the flat tensile specimen. For comparison of responses of different sizes of specimens, the load-displacement response curve has been normalized and plotted as nominal stress vs %age hole opening in Fig. 4.30. The results of the elasto-plastic analysis (no damage) has also been plotted in Fig. 4.30 in order to show the effect of rapid load drop in case of damage mechanics analysis. It can be observed that local model predicts early load-drop when the mesh size is refined from 0.4mm to 0.2mm and 0.1mm, whereas the response curves of the nonlocal model are nearly the same for all the three different mesh sizes. This demonstrates the mesh independent nature of the nonlocal analysis results.

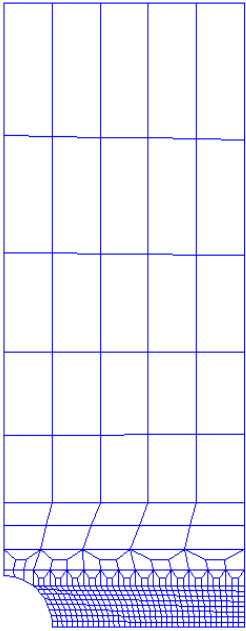


Fig. 4.23: FE mesh of the flat tensile specimen with hole, mesh size: 0.1mm along the crack path

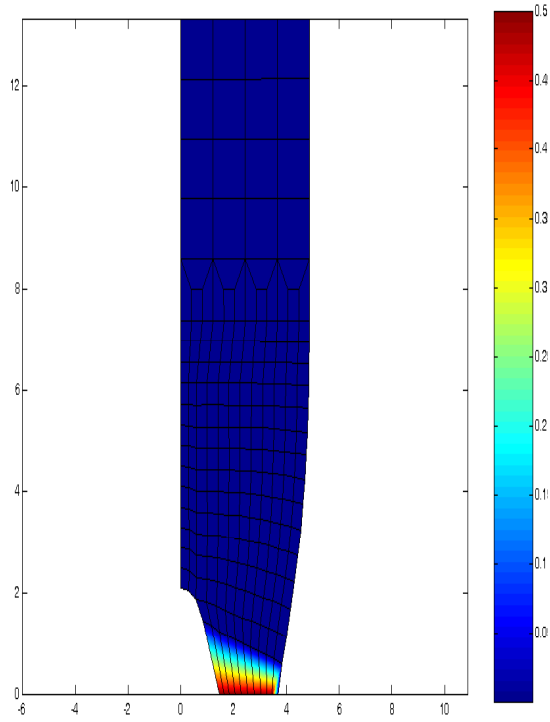


Fig. 4.24: Damage zone predicted for the flat tensile specimen with hole at center (0.4mm mesh, local model), contour plot of damage

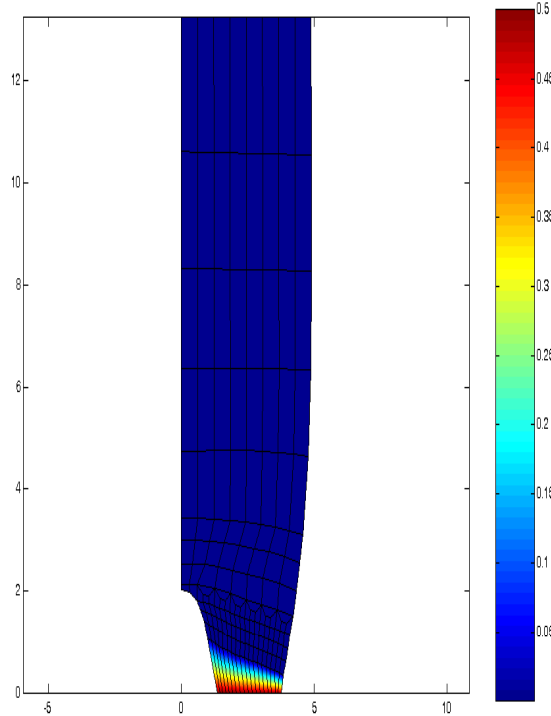


Fig. 4.25: Damage zone predicted for the flat tensile specimen with hole at center (0.2mm mesh, local model), contour plot of damage

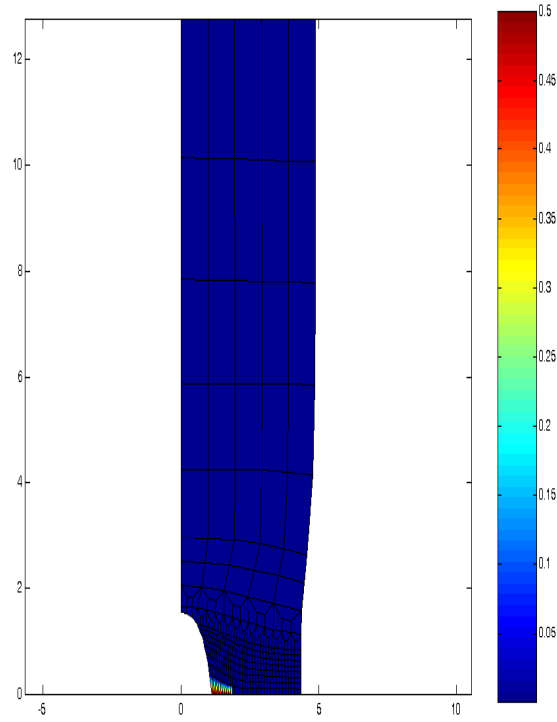


Fig. 4.26: Damage zone predicted for the flat tensile specimen with hole at center (0.1mm mesh, local model), contour plot of damage

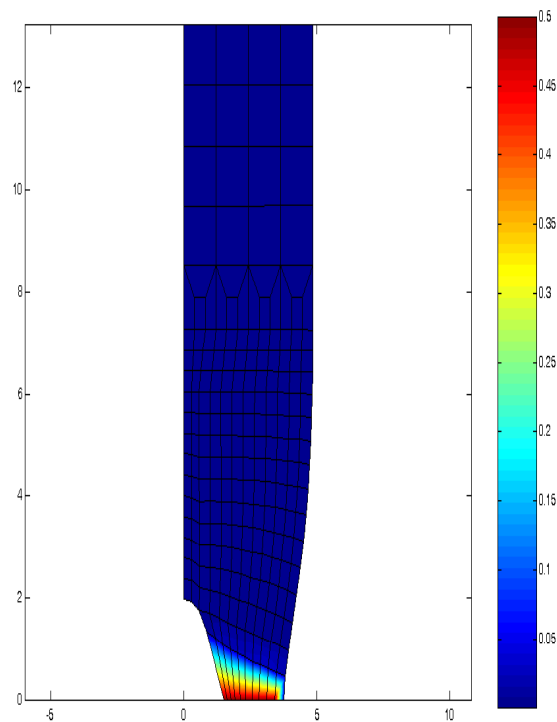


Fig. 4.27: Damage zone predicted for the flat tensile specimen with hole at center (0.4mm mesh, nonlocal model), contour plot of damage

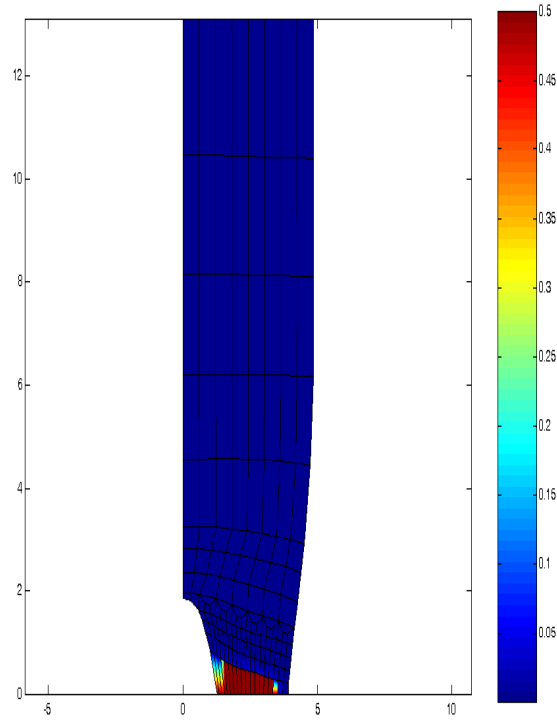


Fig. 4.28: Damage zone predicted for the flat tensile specimen with hole at center (0.2mm mesh, nonlocal model), contour plot of damage

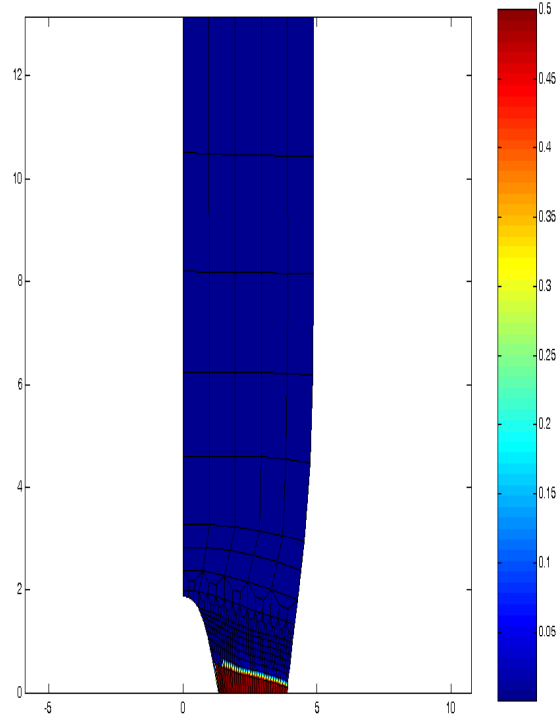


Fig. 4.29: Damage zone predicted for the flat tensile specimen with hole at center (0.1mm mesh, nonlocal model), contour plot of damage

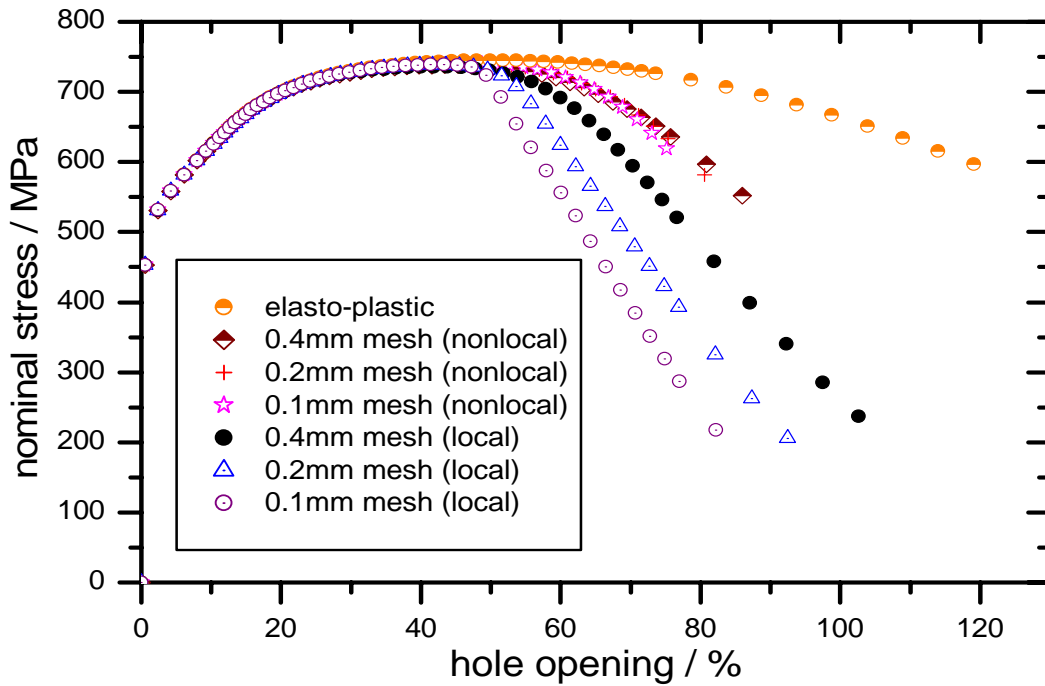


Fig. 4.30: Nominal stress vs %age hole opening response of the flat tensile specimen with hole at the center (local vs nonlocal model with different mesh sizes)

4.6 Prediction of size effect for the flat tensile specimens (LISSAC specimens: Krieg and Seidenfuss 2003)

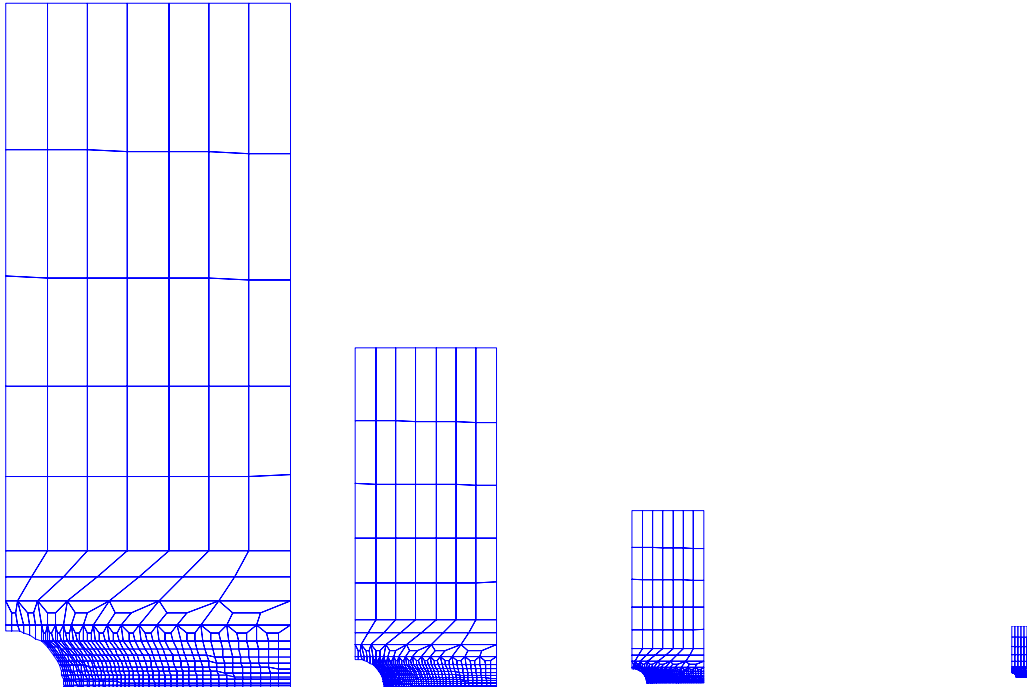


Fig. 4.31(a): FE mesh for the flat tensile specimen with hole (40mm hole diameter)

Fig. 4.31(b): FE mesh for the flat tensile specimen with hole (20mm hole diameter)

Fig. 4.31(c): FE mesh for the flat tensile specimen with hole (10mm hole diameter)

Fig. 4.31(d): FE mesh for the flat tensile specimen with hole (2mm hole diameter)

In the previous section, the effect of FE mesh size on the normalized load-displacement response of the LISSAC flat tensile specimen (with hole at the centre) predicted by both local and nonlocal models was studied and it was demonstrated that results are independent of mesh sizes when mesh is refined. Hence, one should be able to predict the size effect in these specimens using the same mesh design. Hence, a FE mesh was designed for the specimen with 80mm thickness, 40mm hole diameter and 200 mm width. A mesh size of 0.7mm was used near the notch region [Fig. 4.31(a)]. The same mesh was squeezed proportionally to make FE mesh for the specimens with 20mm hole diameter (0.35mm mesh in notch region), 10mm hole diameter (0.175mm mesh in notch region) and 2mm hole diameter (0.035mm mesh in notch region) as shown in Figs. 4.31(b-d). The aim is to predict the %age of hole diameter at which rapid load drop occurs due to crack development (from the hole of the specimen) and how does it get affected because of specimen size.

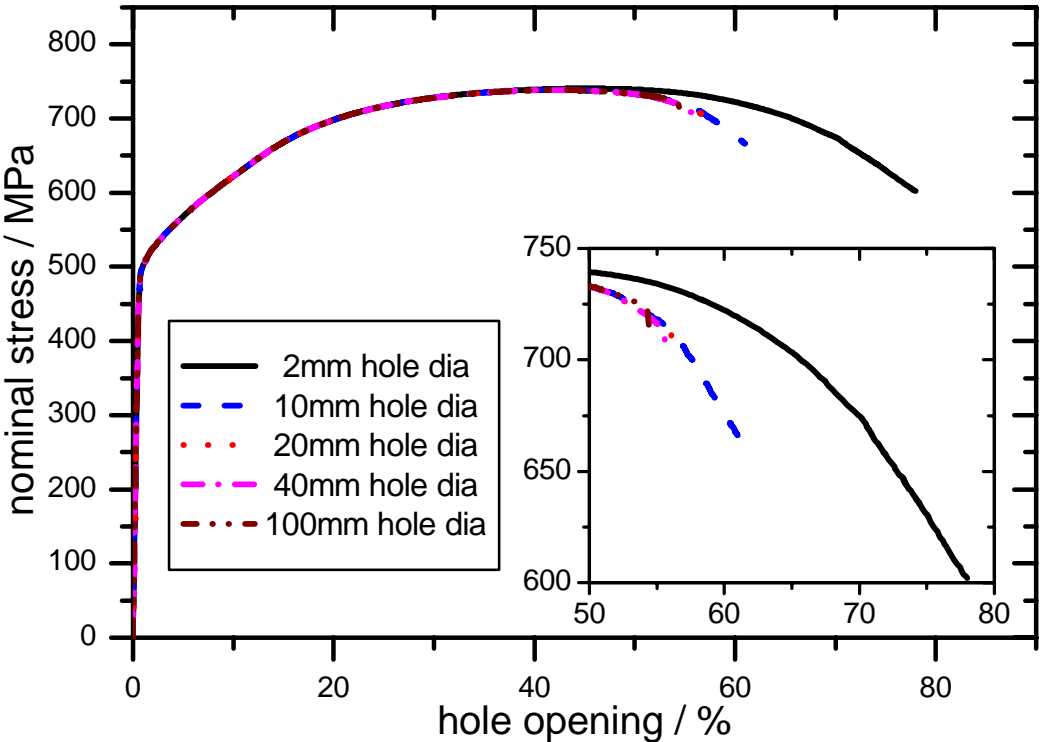


Fig. 4.32: Effect of specimen size on nominal stress vs %age hole opening behaviour (nonlocal model)

Analysis was done using the nonlocal model. 8-noded quadrilateral elements in 2D plane strain were used in the analysis. As can be seen from Fig. 4.32, the smallest specimen shows the highest %age hole diameter at which rapid load drop occurs and this value becomes smaller and smaller from specimens with larger size. The effect is more pronounced between the specimen of 2mm and 10mm hole diameter and subsequently, the effect of specimen size

on %age hole diameter at failure is less. This is similar to the experimentally observed behaviour (Krieg and Seidenfuss 2003) where the dependence of fracture strain on specimen size is exponential in nature, i.e., at the lower end of size, the effect is more and when the sizes are large, the effect is less. Hence, the mesh independent nonlocal model has been able to simulate the size effect in flat tensile specimens using the same mesh design (though the finite elements have different sizes for different specimens).

4.7 Analysis of a compact tension specimen

Having studied the mesh independent nature of solutions of the nonlocal Rousselier's model, we proceed to evaluate fracture resistance behaviour of materials using standard fracture mechanics specimens and study how FE mesh affects the fracture resistance behaviour. Analysis of standard fracture mechanics specimens is of considerable importance to evaluate fracture resistance behaviour of different materials. In this context, the damage mechanics analysis of a 1T CT specimen [with 20% side groove] is presented. Here, a 2-D plane strain analysis (with 8-noded isoparametric quadrilateral elements) has been used. The geometry of the specimen is shown in Fig. 4.33. The dimensions are: $W = 50\text{mm}$, $B = 25\text{mm}$, $B_n = 20\text{mm}$, Height = 60mm. The initial crack to width ratio is $a_0/W = 0.522$. Hence, it is deep cracked specimen according to ASTM standard. Due to symmetry, only half of the specimen has been analysed. Experiments on the CT specimen have been carried out at MPA Universität Stuttgart, Germany (Eisele et al. 2006) at various temperatures starting from -150 deg. C to room temperature (also upto very high temperatures for the creep range, but these results are not discussed here).

The material of the CT specimen is a low alloy German pressure vessel steel (22NiMoCr3-7). The material stress-strain curve used in this analysis is the same as that of Fig. 4.18. Other material properties used in the analysis are given in Table-4.3. The finite element meshes of the CT specimen are shown in Figs. 4.34-37(a) along with their enlarged view near the crack tip [Figs. 4.34-37(b)] for four different mesh sizes of 0.4mm, 0.2mm, 0.1mm and 0.02mm near the crack tip. These four different mesh sizes have been used to study the mesh dependent behaviour of both local and nonlocal damage models.

The damage profile at the end of 3mm crack growth simulation is an important parameter to observe the difference in the results of the two types of models. Fig. 4.38 shows the damage

zone (damage zone is represented by damage value of 0.5 within the contour plot) predicted by the local model for the 0.4mm mesh size. The damage zone is along one row of Gauss points of the bottom layer of elements ahead of crack tip (initially the crack runs in the top row of Gauss points and then switches to the bottom row). As the mesh size is refined, the element size becomes smaller and smaller (0.2mm and 0.1mm mesh). In case of local model, the damage zone is still confined to the bottom single layer of elements (one Gauss point row) and hence the damage zone size predicted becomes narrower as the mesh is refined (Fig. 4.39-40) and hence the results are mesh dependent.

The damage zone for the 0.4mm mesh is shown in Fig. 4.41 for the nonlocal simulation. Here, nearly one and a half layer of elements is damaged and the damage zone is uniform. When the mesh size is refined to 0.2mm, nearly 3mm layer of elements are damaged. For 0.1mm mesh, a zone of 6 layers of elements is damaged [Fig. 4.42-43]. Hence, the damage zone spreads over a layer, which more or less remains uniform even though we refine the size of FE mesh. Analysis has been carried out even for a very small mesh size of 0.02mm near crack tip which is required to analyse high stress gradients when the CT specimens are tested at lower temperatures in the transitions regime (where stress redistribution becomes difficult because of more constraint). For this analysis, the damage is spread over all the elements in the fine mesh zone as shown in Fig. 4.44(a-b)]. However, because of extreme small element size and damage development, the strain developed in the elements (in the fine mesh region) becomes very high and the elements become too much distorted and hence, there is convergence problem in the numerical simulation.

The above problem (in the use of extremely small mesh size) may be removed by either the use of large strain formulations of Eterovic and Bathe (1990) [i.e., Updated Lagrangian Hencky formulation] where a multiplicative decomposition of deformation gradient is used [instead of additive decomposition of strain tensor] or by Arbitrary Lagrangian Eulerian (ALE) formulation or by the use of element extinction techniques, which is a scope of future research. Nevertheless, the load-displacement response and fracture resistance behaviour of the CT specimen has been studied upto a crack growth of 0.7mm (for the FE mesh with 0.02mm element size) and the mesh independent nature of the solutions have been demonstrated as will be seen in the following discussion.

This important characteristic of the nonlocal model (i.e., damage zone width is independent of mesh size) also helps it to predict the global load-displacement response and J-resistance behaviour of the CT specimen, which become independent of mesh size. Fig. 4.45 shows load-CMOD (crack mouth opening displacement) results of the CT specimen obtained using the local model for 3 different mesh sizes (i.e., 0.4, 0.2 and 0.1mm respectively). The load-CMOD response for the 0.4mm mesh compares well with that of experimental result (the maximum load of analysis is slightly higher as the analysis is with 2D plane strain assumption). However, as the mesh size is refined, the local model predicts faster crack growth and hence lower load-CMOD response. The same trend is observed in the J-resistance behaviour also (Fig. 4.47). It may be noted that the experimental results referred here are taken from Eisele et al. 2006.

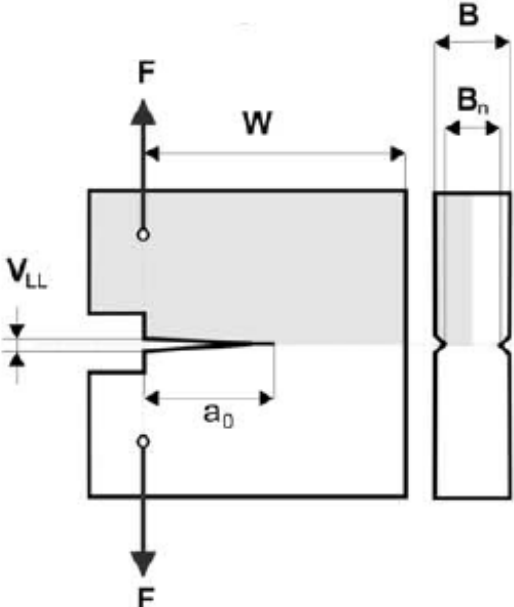


Fig. 4.33: Geometry of the compact tension specimen with loading configuration

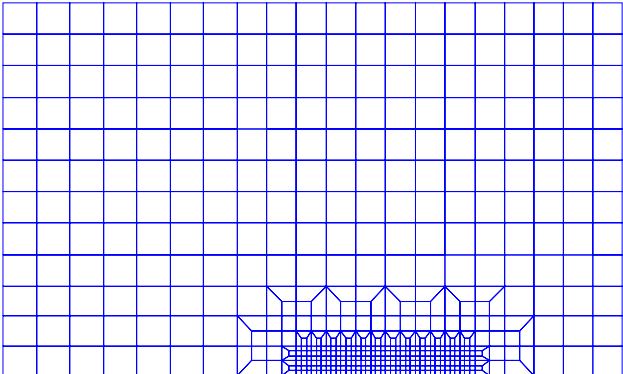


Fig. 4.34(a): FE mesh of CT specimen (0.4mm mesh near crack tip)

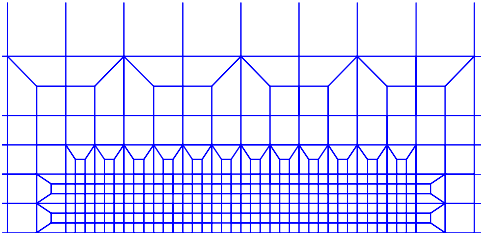


Fig. 4.34(b): Enlarged view Fig. 4.34(a) near crack tip

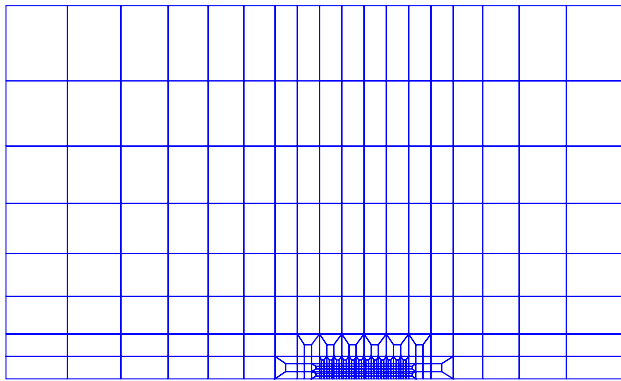


Fig. 4.35(a): FE mesh of CT specimen (0.2mm mesh near crack tip)

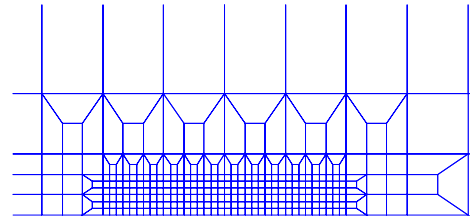


Fig. 4.35(b): Enlarged view Fig. 4.35(a) near crack tip

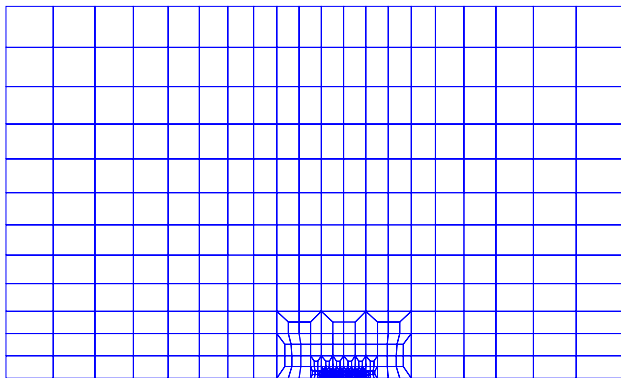


Fig. 4.36(a): FE mesh of CT specimen (0.1mm mesh near crack tip)

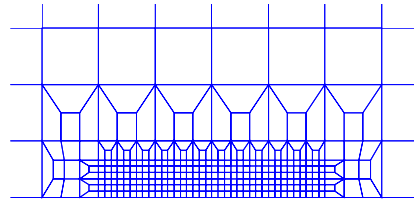


Fig. 4.36(b): Enlarged view Fig. 4.36(a) near crack tip

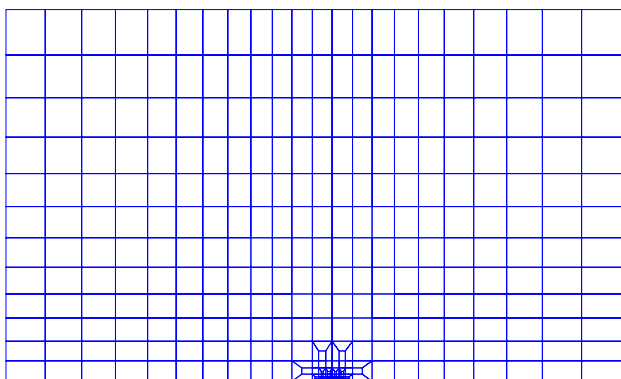


Fig. 4.37(a): FE mesh of CT specimen (0.02mm mesh near crack tip)

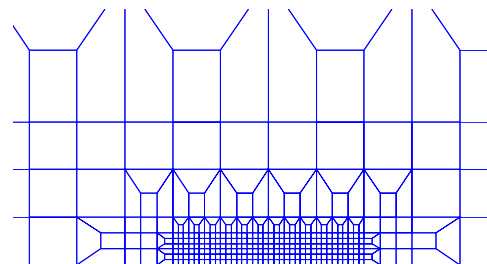


Fig. 4.37(b): Enlarged view Fig. 4.36(a) near crack tip

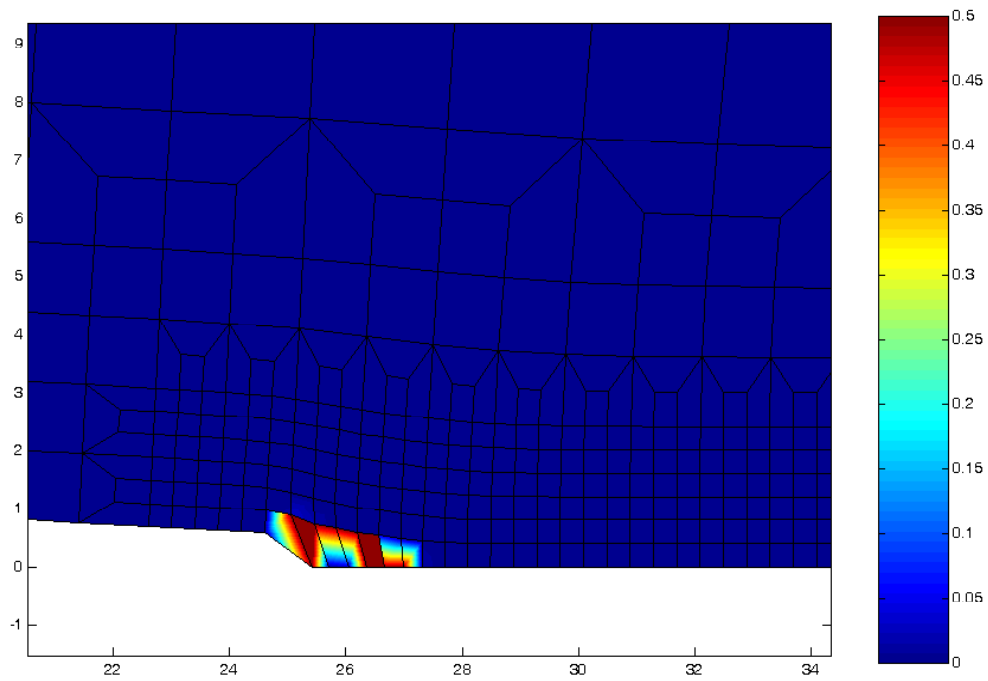


Fig. 4.38: Damage zone near crack tip for CT specimen with 0.4mm mesh (local model), contour plot of damage

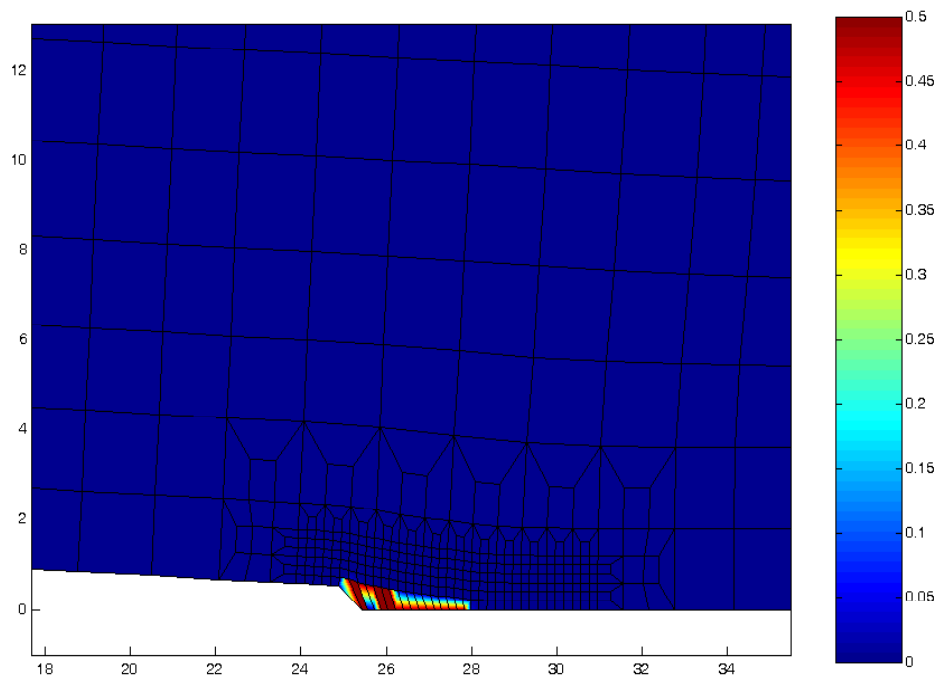


Fig. 4.39: Damage zone near crack tip for CT specimen with 0.2mm mesh (local model), contour plot of damage

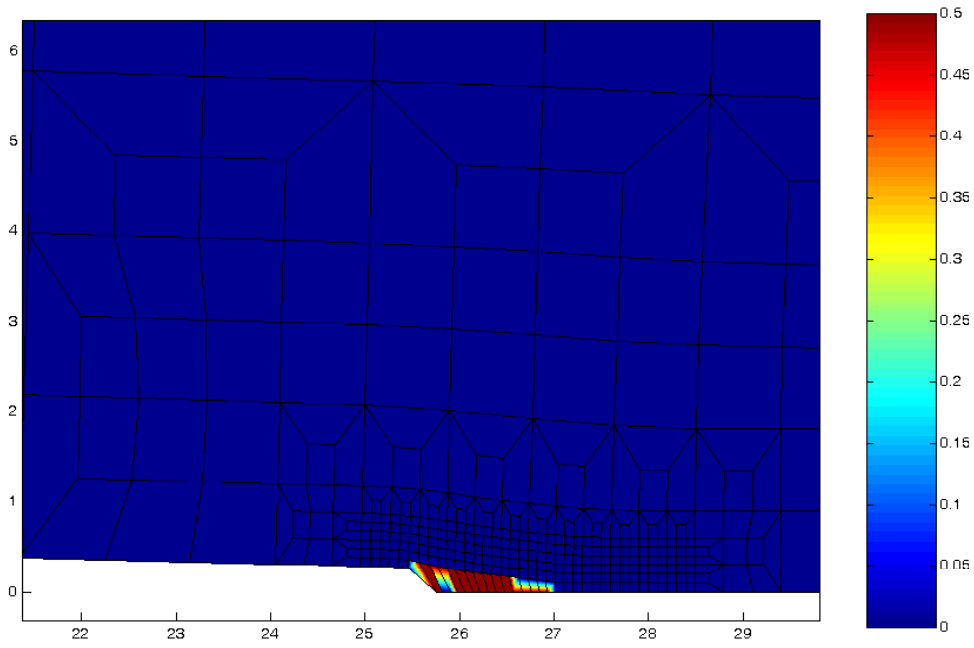


Fig. 4.40: Damage zone near crack tip for CT specimen with 0.1mm mesh (local model), contour plot of damage

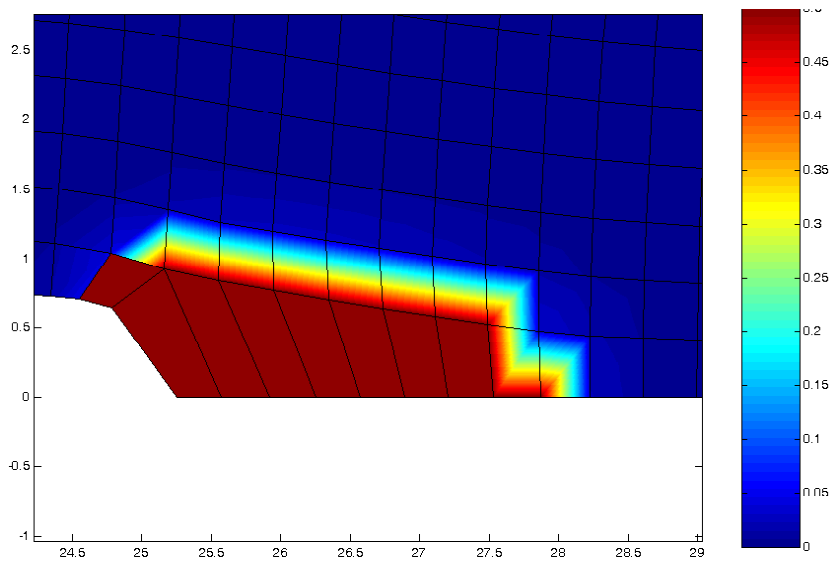


Fig. 4.41: Damage zone near crack tip for CT specimen with 0.4mm mesh (nonlocal model), contour plot of damage

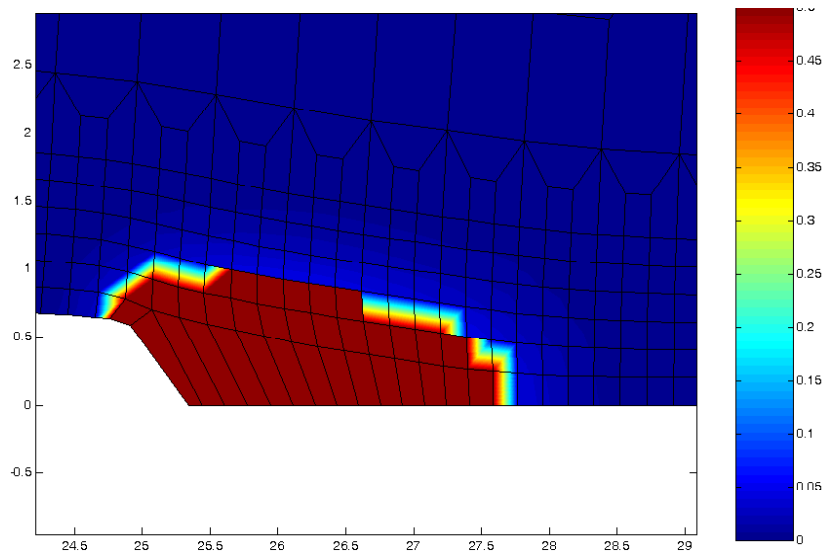


Fig. 4.42: Damage zone near crack tip for CT specimen with 0.2mm mesh (nonlocal model), contour plot of damage

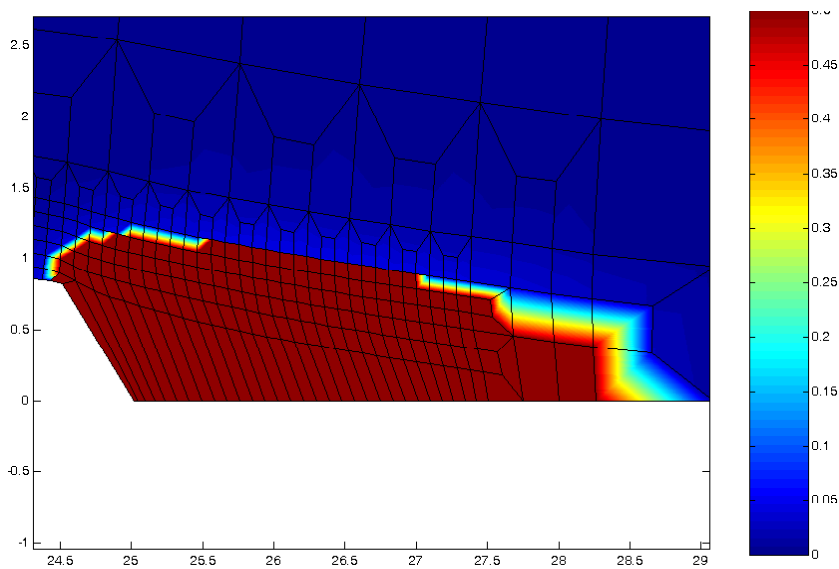


Fig. 4.43: Damage zone near crack tip for CT specimen with 0.1mm mesh (nonlocal model), contour plot of damage

In case of the nonlocal model, the load-CMOD and the J-resistance curves match very well with those of experiment for the three different mesh sizes (Figs. 4.46 and 4.48) and there is very little difference among the results of different mesh sizes (i.e., 0.4, 0.2, 0.1 and 0.02mm). Hence, the mesh independent nature of the nonlocal model is demonstrated for the fracture mechanics specimen. It may be noted that the J-integral has been calculated from the area under the load-displacement curve using ASTM η and γ factors as followed for the standard CT specimen test during the experimental J-resistance curve evaluation. For calculating the

crack growth during numerical simulation, a crack growth of one-third (as 3x3 or full Gauss point integration scheme has been used here) of the element size is assumed when a Gauss point is completely damaged due to growth of local void volume fraction f . By summing the crack growth of all the elements ahead of crack tip (with increase of CMOD), the total crack extension at any time during loading of CT specimen is calculated.

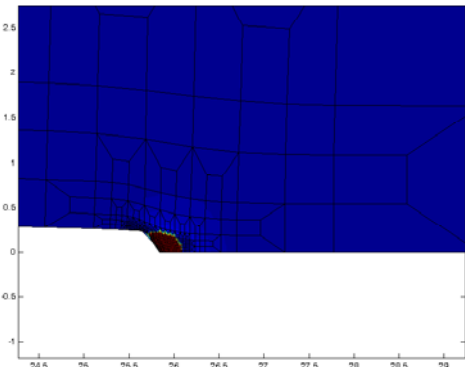


Fig. 4.44(a): Damage zone near crack tip for CT specimen with 0.02mm mesh (nonlocal model), contour plot of damage

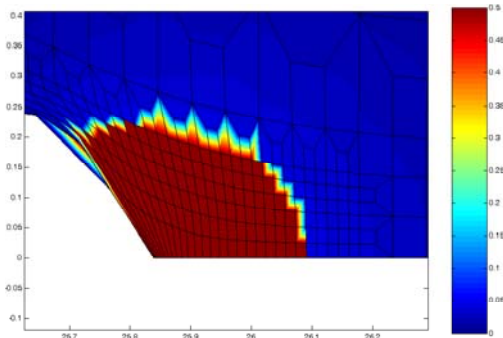


Fig. 4.44(b): Enlarged view of Fig. 44(a) near crack tip, contour plot of damage

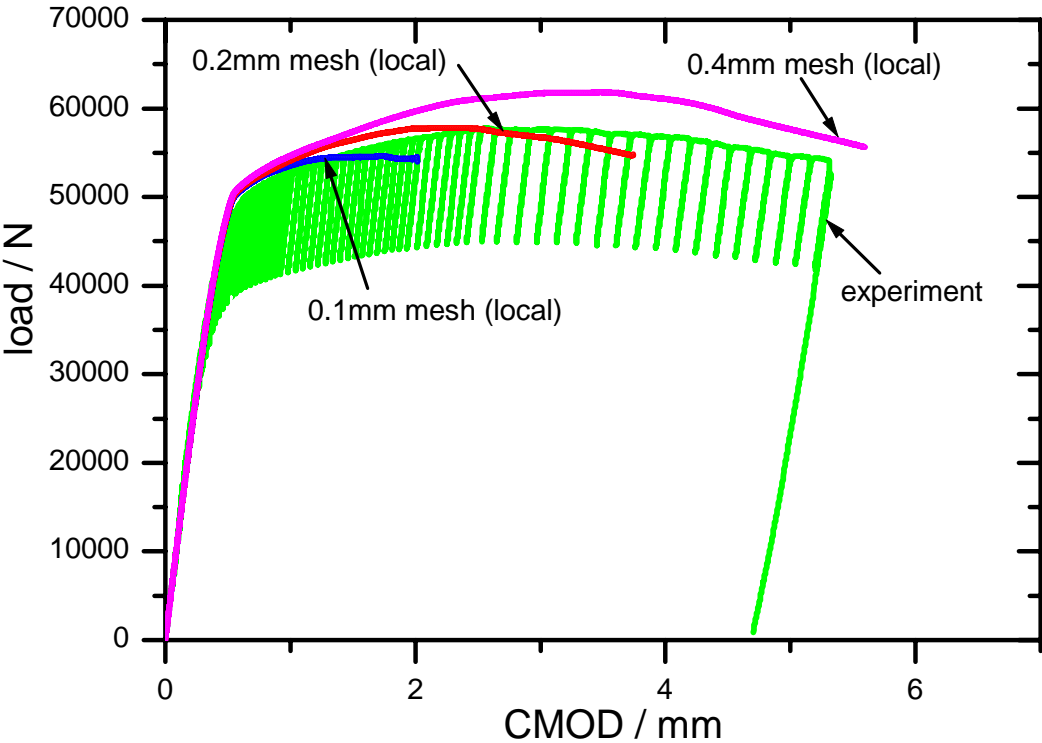


Fig. 4.45: Load-CMOD response of the 1T CT specimen for different FE mesh sizes (local model)

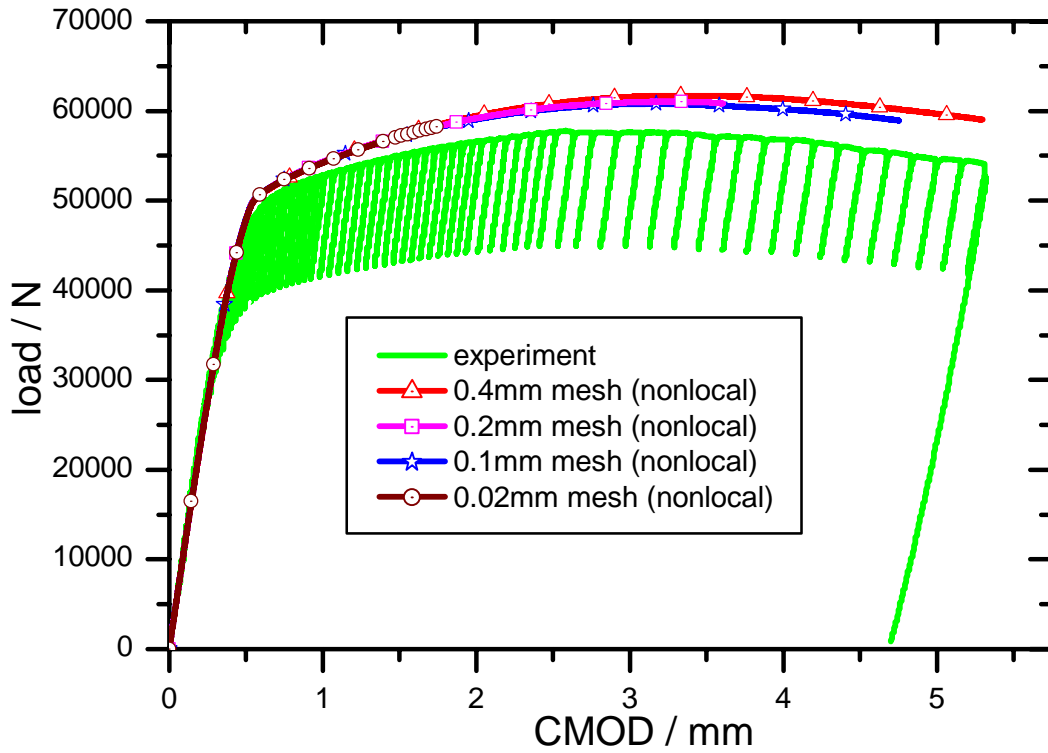


Fig. 4.46: Load-CMOD response of the 1T CT specimen for different FE mesh sizes (nonlocal model)

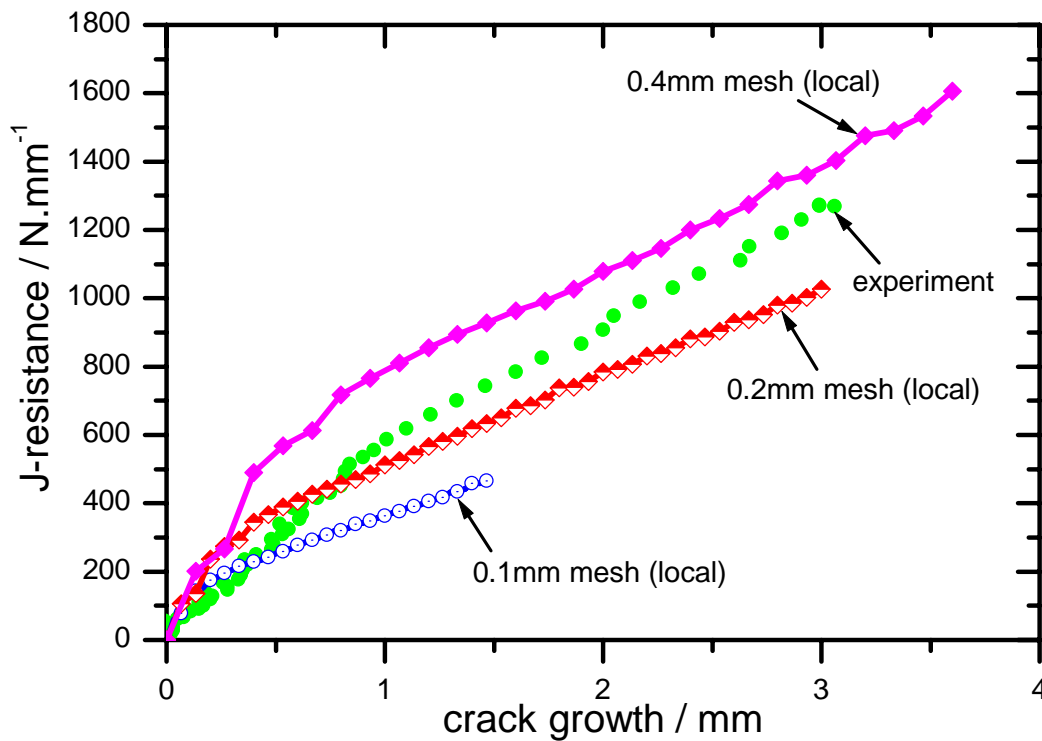


Fig. 4.47: J-resistance behaviour of the 1T CT specimen with crack growth for different FE mesh sizes (local model)

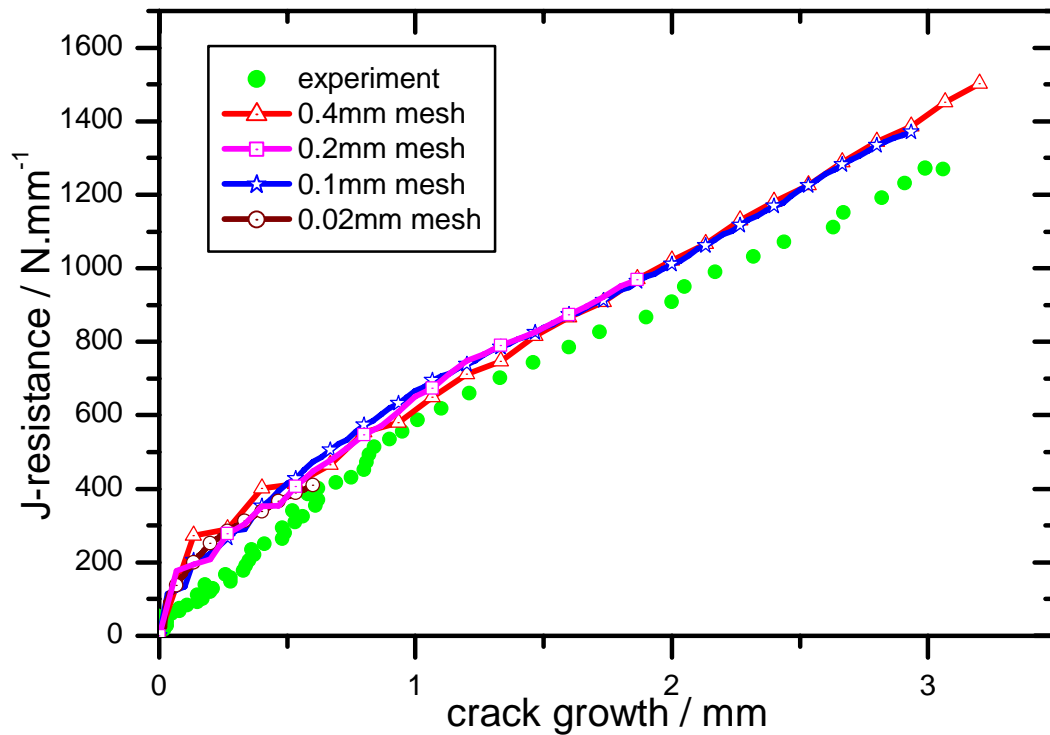


Fig. 4.48: J-resistance behaviour of the 1T CT specimen with crack growth for different FE mesh sizes (nonlocal model)

4.8 Analysis of a single edge notched bend (SEB) specimen

Having demonstrated the mesh independent nature of the load-CMOD and fracture resistance behaviour of the 1T compact tension specimen with the help of nonlocal models, we need to see if the same observation holds for other types of specimens where geometry and loading conditions are different. It may be noted that a dominant tensile mode of loading occurs ahead of crack tip for the CT specimen whereas bending mode is dominant in case of SEB (Single edge notched bend) specimen when loaded in three-point bending as shown in Fig. 4.49. Hence, the standard 1T SEB specimen was chosen for analysis using nonlocal models to determine the load-CMOD and J-resistance behaviour.

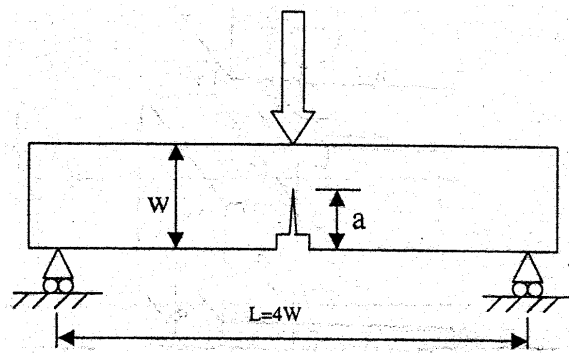


Fig. 4.49: Geometry of the single edge (notched) bend SEB specimen

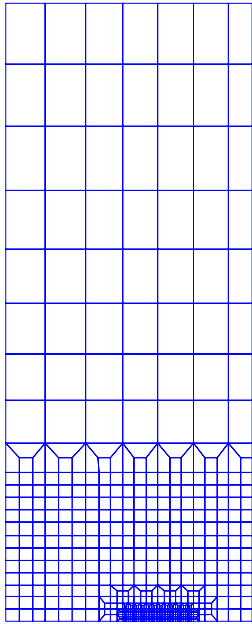


Fig. 4.50(a): FE mesh of the 1T SEB specimen (0.4mm mesh near crack tip)

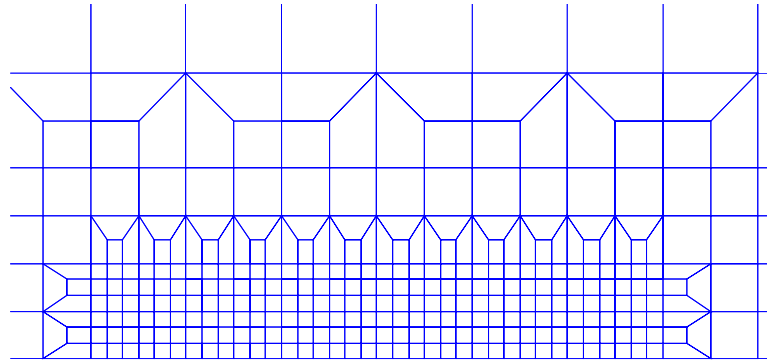


Fig. 4.50(b): Enlarged view of Fig. 4.50(a) near the crack tip

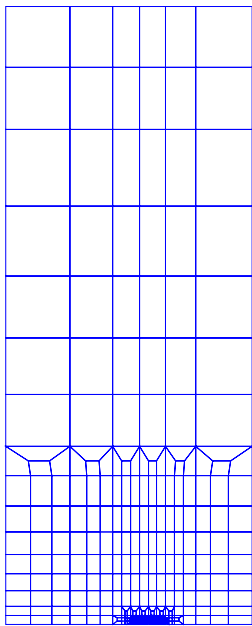


Fig. 4.51(a): FE mesh of the 1T SEB specimen (0.2mm mesh near crack tip)

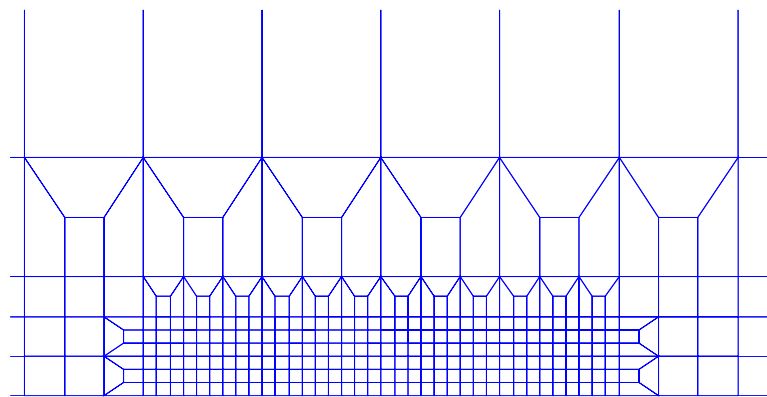


Fig. 4.51(b): Enlarged view of Fig. 4.51(a) near the crack tip

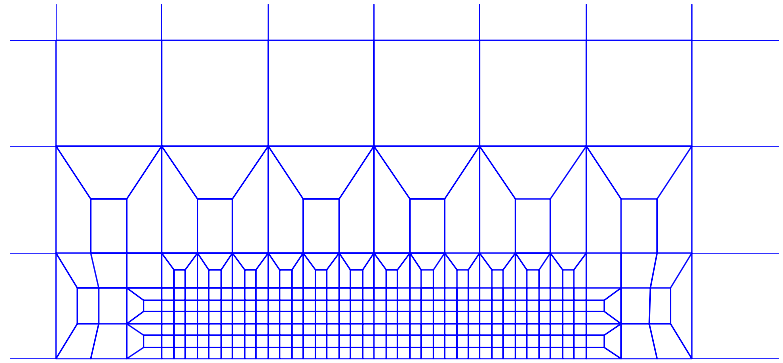
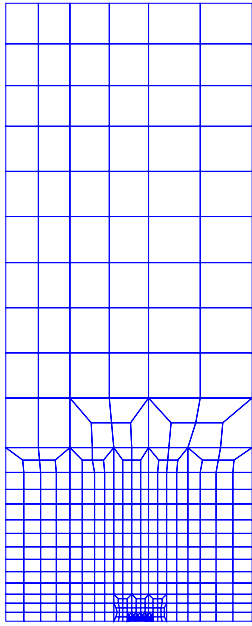


Fig. 4.52(a): FE mesh of the 1T SEB specimen (0.1mm mesh near crack tip)
 Fig. 4.52(b): Enlarged view of Fig. 4.52(a) near the crack tip

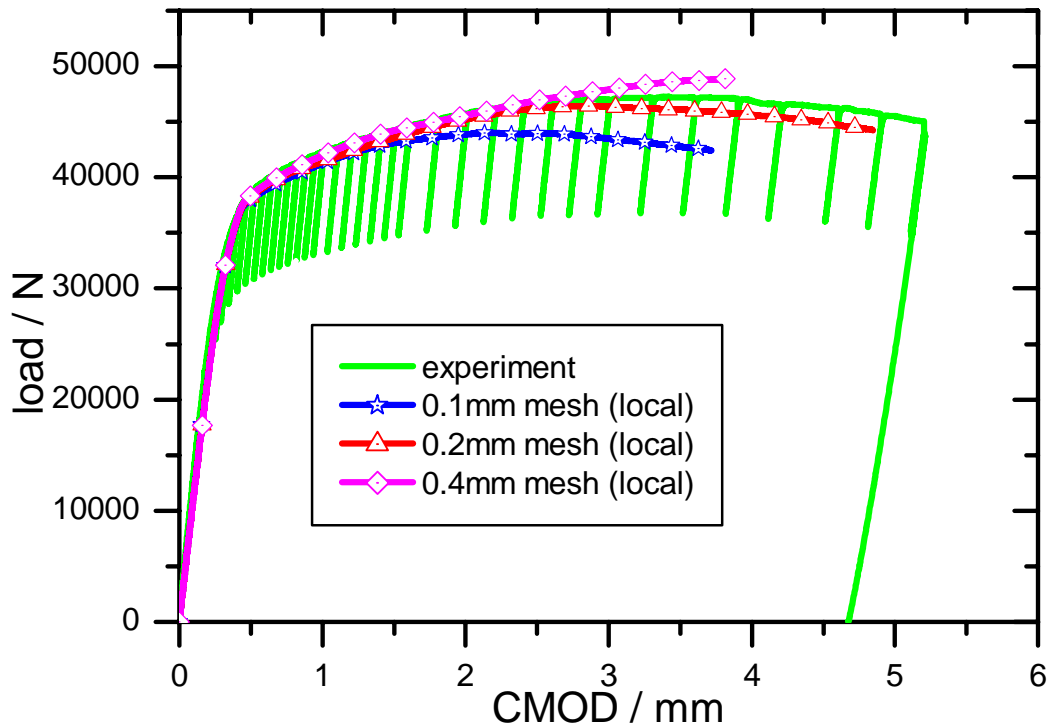


Fig. 4.53: Load-CMOD behaviour of 1T SEB specimen for different FE mesh sizes (local model)

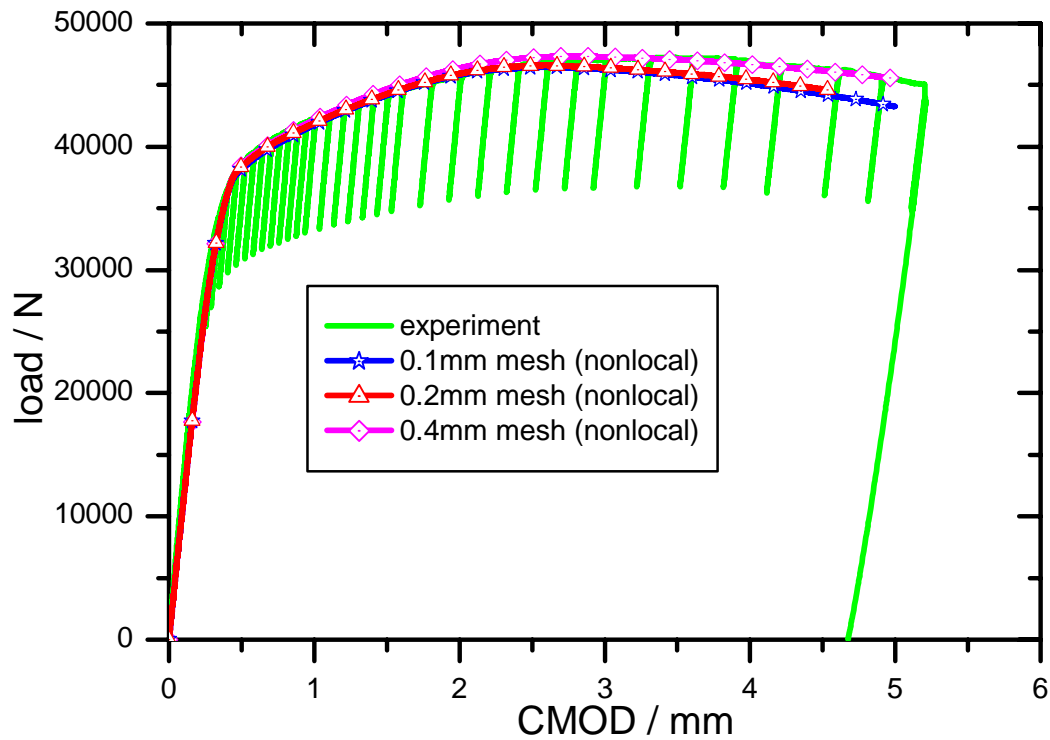


Fig. 4.54: Load-CMOD behaviour of 1T SEB specimen for different FE mesh sizes (nonlocal model)

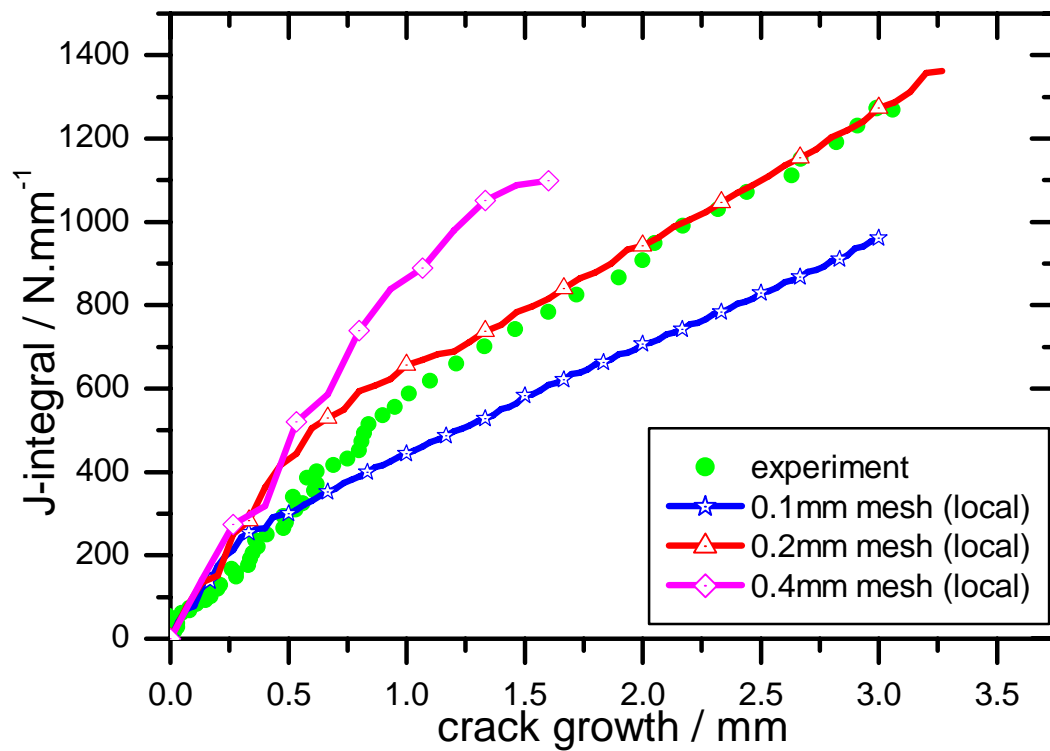


Fig. 4.55: J-resistance behaviour of the 1T SEB specimen with crack growth for different FE mesh sizes (local model)

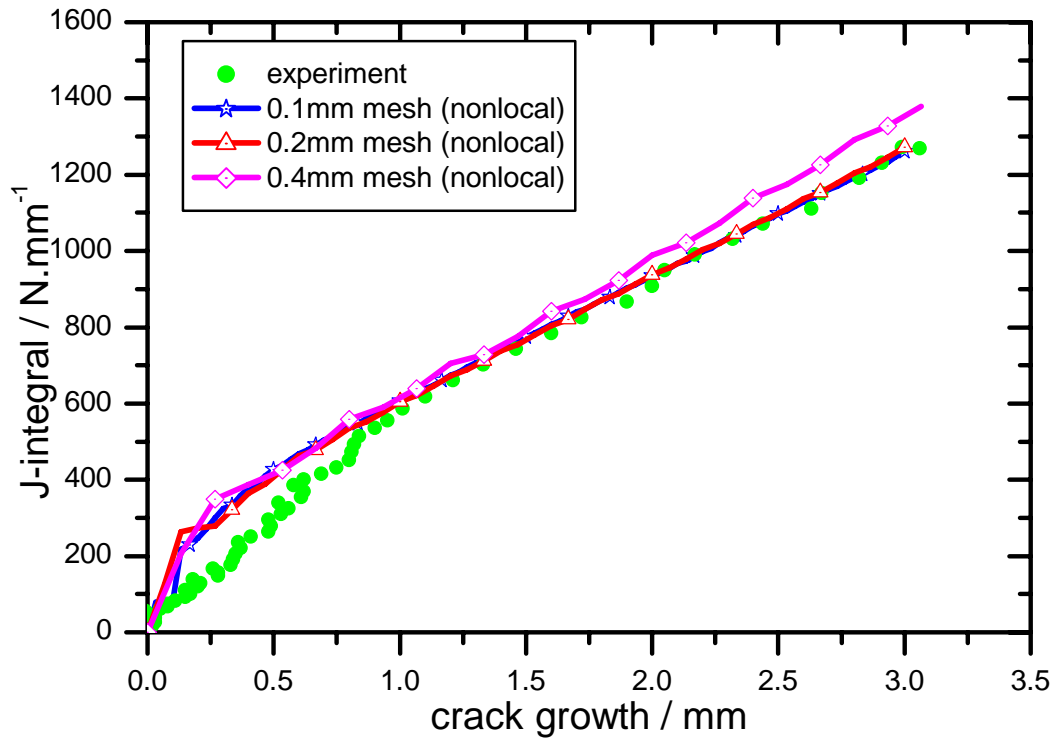


Fig. 4.56: J-resistance behaviour of the 1T SEB specimen with crack growth for different FE mesh sizes (nonlocal model)

The geometry of the specimen with loading arrangement is shown in Fig. 4.49. The dimensions of the specimen are: $W = 50\text{mm}$, $L = 4W = 200\text{mm}$, thickness = 25mm with an initial crack depth to width ratio as $a_0/W = 0.522$ and it is 20% side-grooved. Similar to the 1T CT specimen, a 2D plane strain analysis has been done for this SEB specimen and 8-noded quadrilateral elements have been used. Due to symmetry, only half of the specimen has been analyzed. Three different mesh sizes (0.4, 0.2 and 0.1mm respectively near the crack tip) have been used in the analysis in order to study the mesh independent behaviour of local and nonlocal models. The FE meshes along with their enlarged views near the crack tip are shown in Figs. 4.50-52 for 0.4, 0.2 and 0.1mm meshes respectively. The results of local and nonlocal analysis (with different mesh sizes near the crack tip) have also been compared with those of experiment (experimental results are taken from Eisele et al. 2006).

It may be noted that the method of crack growth and J-integral calculation is same as that followed for the CT specimen except the fact that different values of η and γ factors (suitable for SEB specimen according to ASTM standard) are used. The load-CMOD results of the local analysis using three different mesh sizes are shown in Fig. 4.53. It is evident that the local model predicts faster crack growth when the mesh size is refined and hence the load goes

down quickly with CMOD for smaller mesh sizes. However, for the nonlocal model, the load-CMOD results converge to a solution when mesh size is refined [Fig. 4.54]. The above effect is also reflected in the J-resistance curve where the results of local model [Fig. 4.55] are highly mesh dependent, whereas the J-resistance curves predicted by nonlocal analysis almost remain same with respect to mesh size.

4.9 Analysis of 2T CT specimen

In this section, the effect of specimen size on the fracture resistance behaviour of the CT specimen has been studied. For this purpose, analysis has been done for the 2T CT specimen (all the dimensions are twice those of 1T CT) in 2D plane strain. The element types and material properties remain unchanged. Experiments have been conducted at MPA, Stuttgart and the results of analysis have been compared with those of experiment. Fig. 4.57 shows the comparison of load-CMOD response of the 2T CT specimen for three different mesh sizes (0.4, 0.2 and 0.1mm respectively near the crack tip) when the local model is used. Fig. 4.58 shows the same response for analysis using nonlocal model. Again, the load-CMOD responses of the 2T specimen have been proved to be mesh independent in case of nonlocal model whereas the local model results are mesh-dependent as expected.

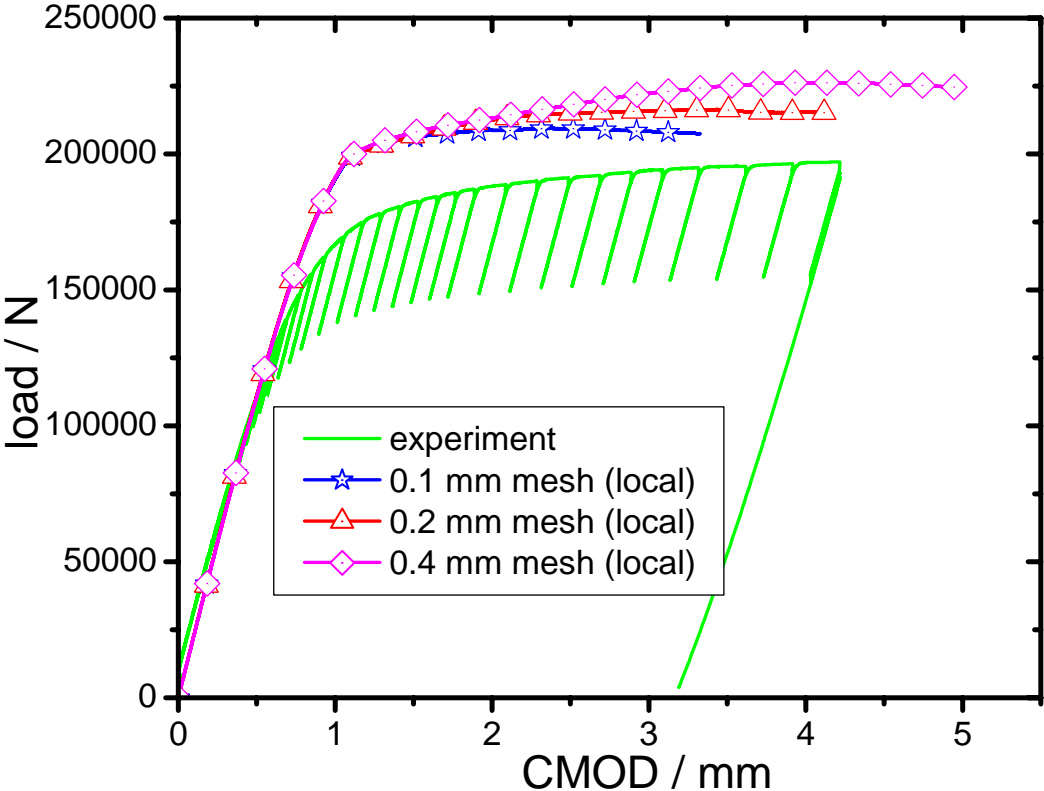


Fig. 4.57: Load-CMOD behaviour of 2T CT specimen for different FE mesh sizes (local model)

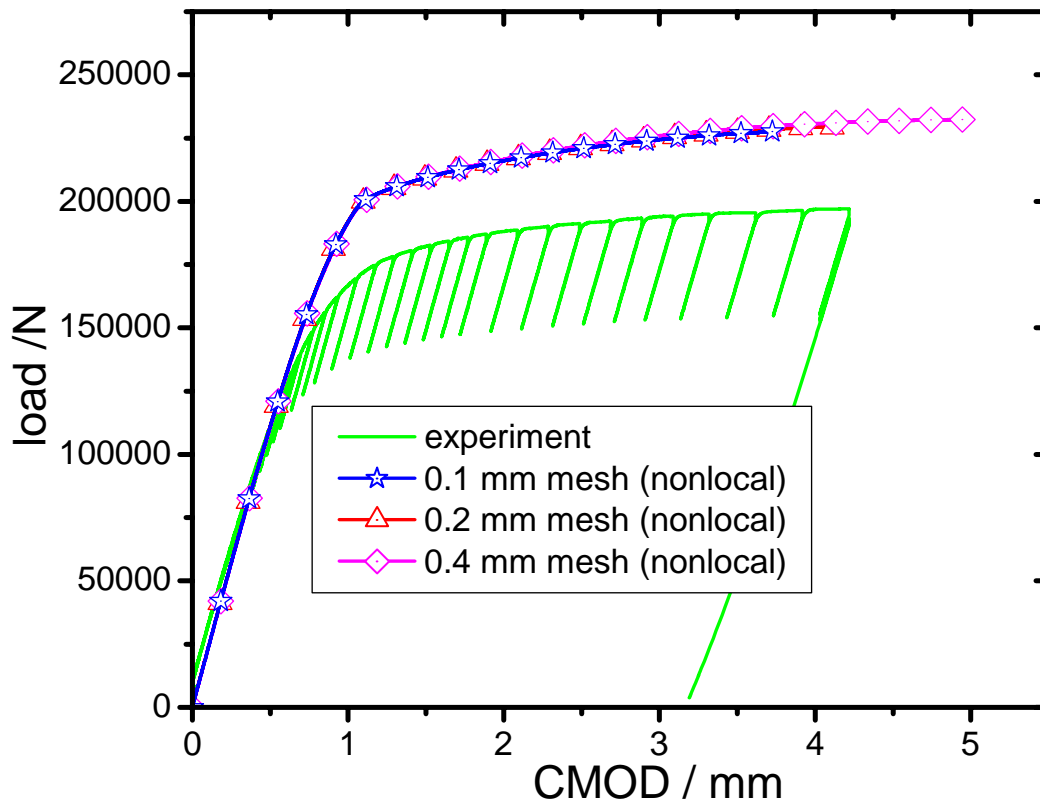


Fig. 4.58: Load-CMOD behaviour of 2T CT specimen for different FE mesh sizes (nonlocal model)

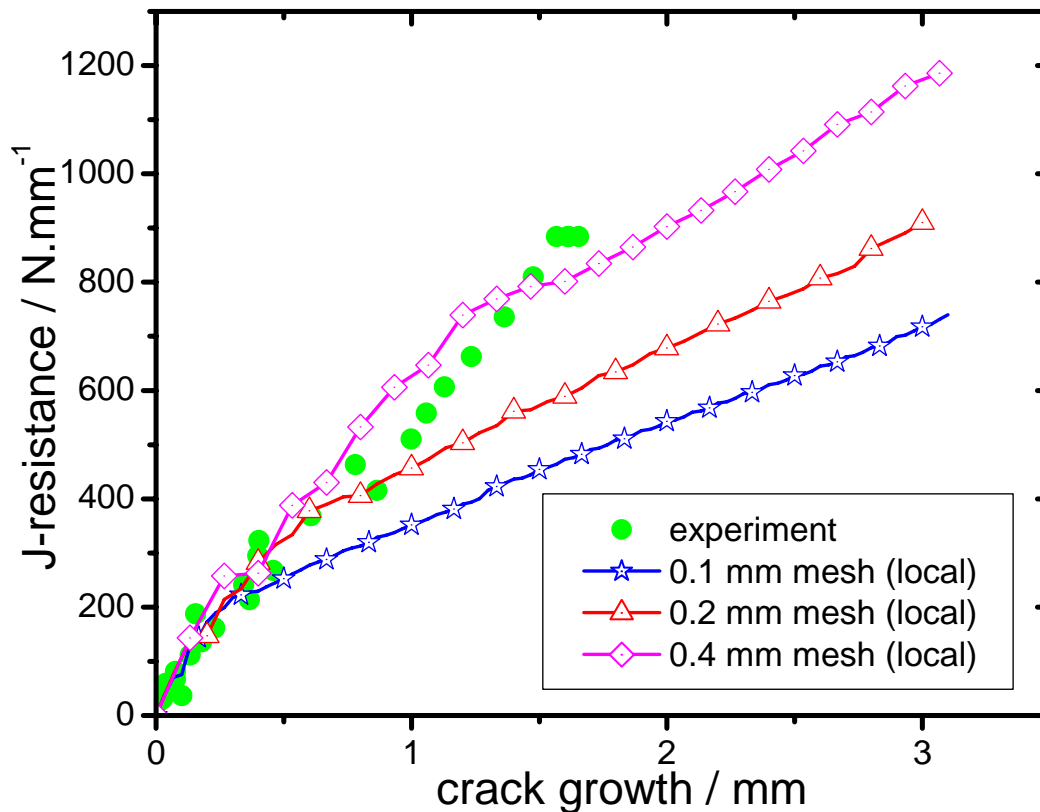


Fig. 4.59: J-resistance behaviour of the 2T CT specimen with crack growth for different FE mesh sizes (local model)

Similar observations hold true for the J-resistance behavior also [Figs. 4.59 for local model, 4.60 for nonlocal model]. It may be noted that the predicted load-CMOD results are higher because of 2D plane strain assumption (3D analysis will be able to predict accurate load carrying capacity of the specimen). However, the predicted J-resistance curve is very close to that of experiment.

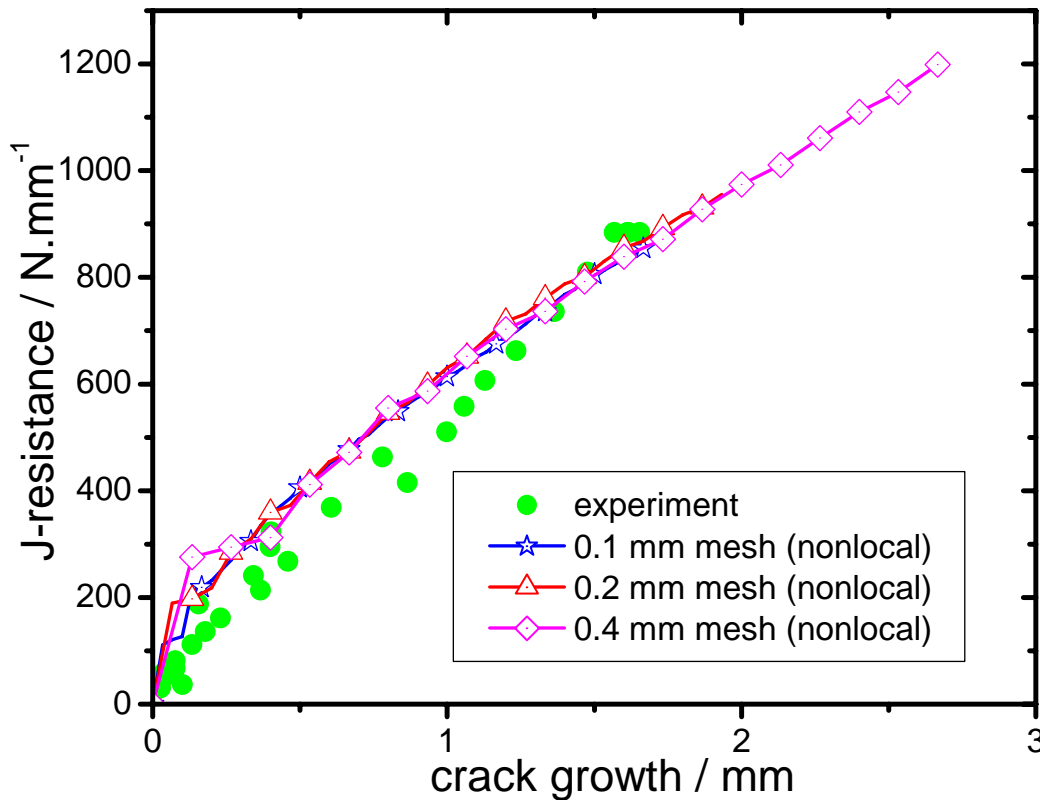


Fig. 4.60: J-resistance behaviour of the 2T CT specimen with crack growth for different FE mesh sizes (nonlocal model)

4.10 Analysis of 4T CT specimen

In this section, the effect of specimen size on the fracture resistance behaviour of the CT specimen has been studied with the help of 4T CT specimen (all the dimensions are four-times those of 1T CT) in 2D plane strain. The element types and material properties remain unchanged. Fig. 4.61 shows the comparison of load-CMOD response of the 4T CT specimen for three different mesh sizes (0.4, 0.2 and 0.1mm respectively near the crack tip) when the local model is used. Fig. 4.62 shows the same response for analysis using nonlocal model. Again, the load-CMOD responses of the 4T specimen have been proved to be mesh independent in case of nonlocal model whereas the local model results are mesh dependent as

expected. Similar observations hold true for the J-resistance behavior also [Figs. 4.63 for local model, 4.64 for nonlocal model].

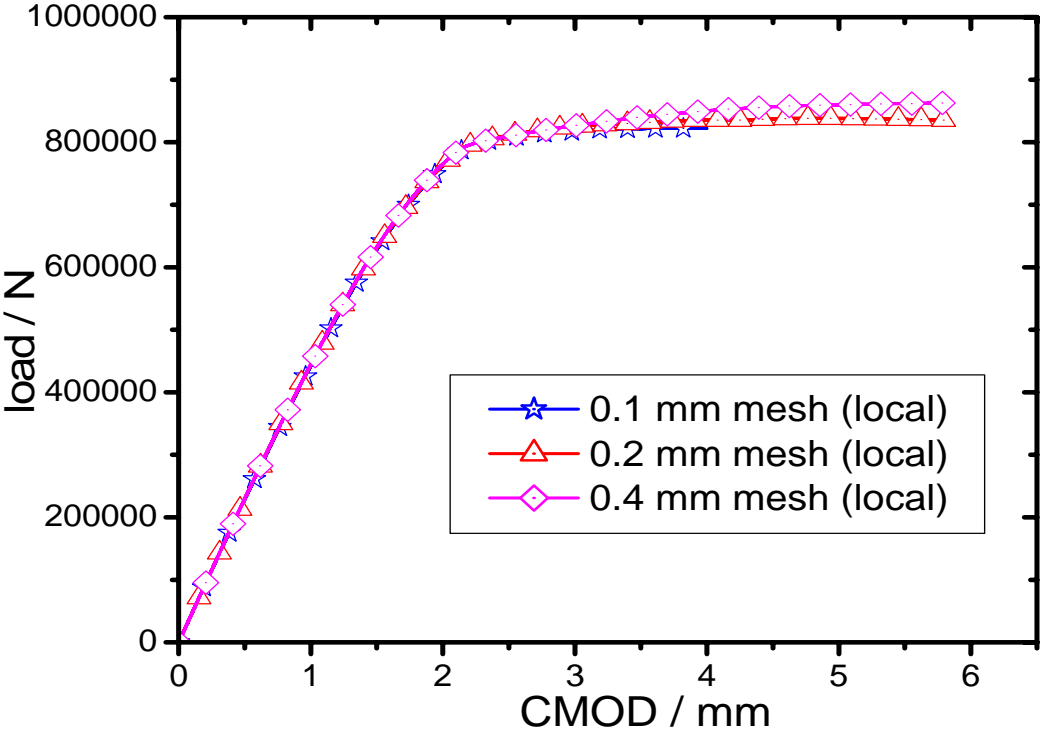


Fig. 4.61: Load-CMOD behaviour of 4T CT specimen for different FE mesh sizes (local model)

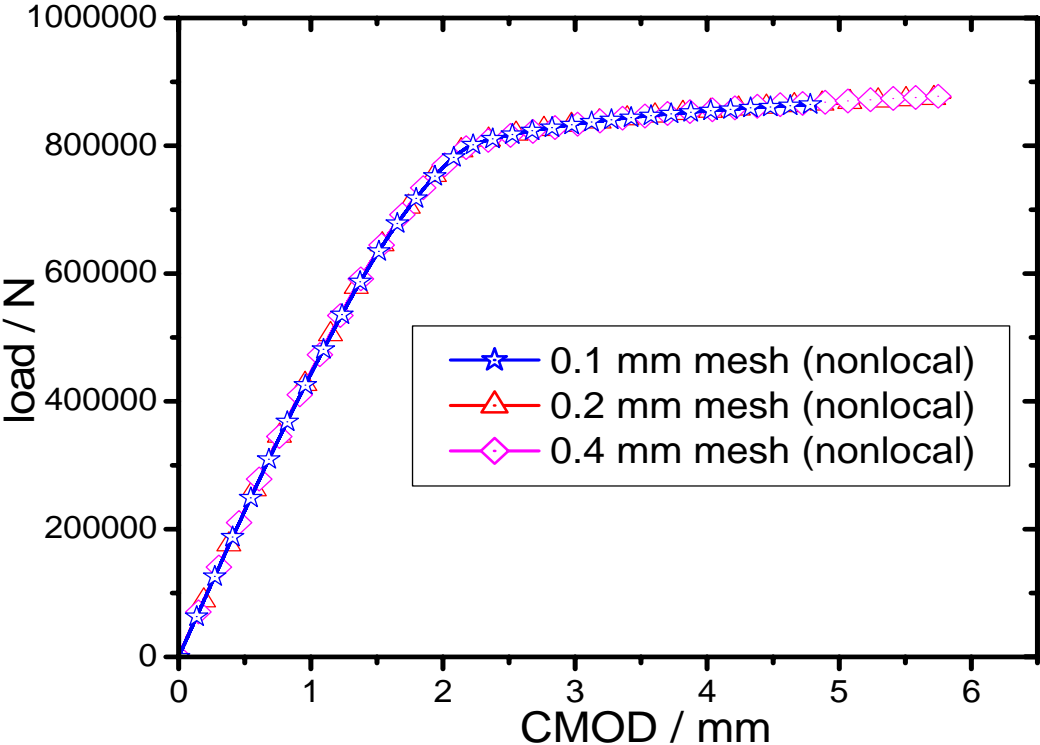


Fig. 4.62: Load-CMOD behaviour of 4T CT specimen for different FE mesh sizes (nonlocal model)

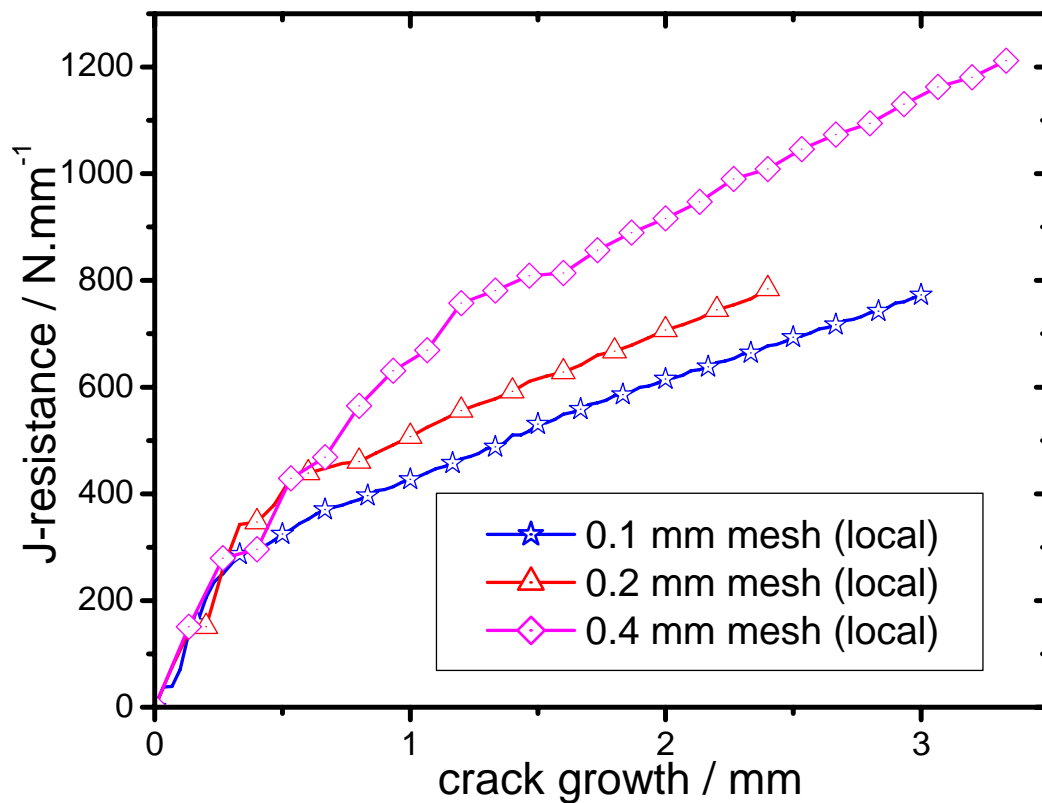


Fig. 4.63: J-resistance behaviour of the 4T CT specimen with crack growth for different FE mesh sizes (local model)

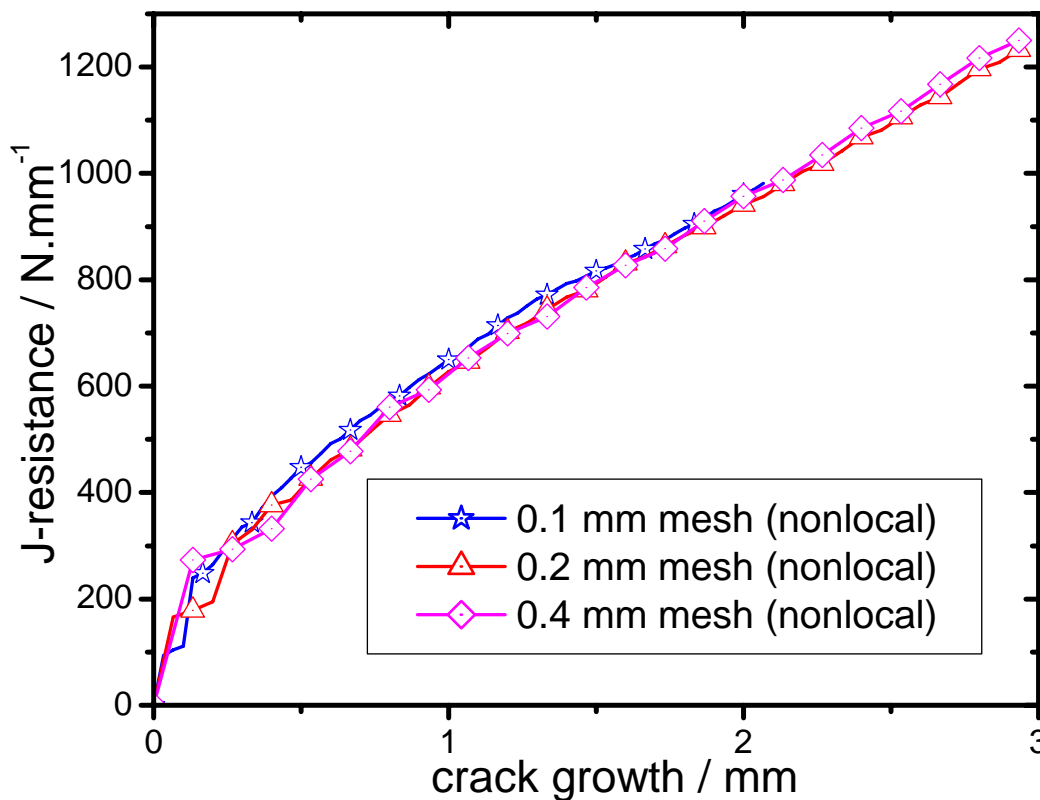


Fig. 4.64: J-resistance behaviour of the 4T CT specimen with crack growth for different FE mesh sizes (nonlocal model)

Comparison of the effects of specimen size on the load-CMOD and fracture resistance behaviour of the CT specimen will be presented in the next section where only the results of the nonlocal (mesh independent) model are presented for all CT specimens (meshed with 0.1mm of element size).

4.11 Prediction of geometry effect (effect of specimen size)

As was discussed in the previous section, the aim here is to see whether nonlocal models will be able to successfully predict the size effects as observed in the experiments. For this purpose, the simulation results of the nonlocal model with 0.1mm mesh (near crack tip) for all the specimens (i.e., 1T, 2T and 4T) has been compared along with the experimental results wherever available. Fig. 4.65 shows the simulated load-CMOD response of all the specimens along with those of experiment. As expected, the load carrying capability of the larger size CT specimens will be higher compared to smaller size specimens [Fig. 4.65].

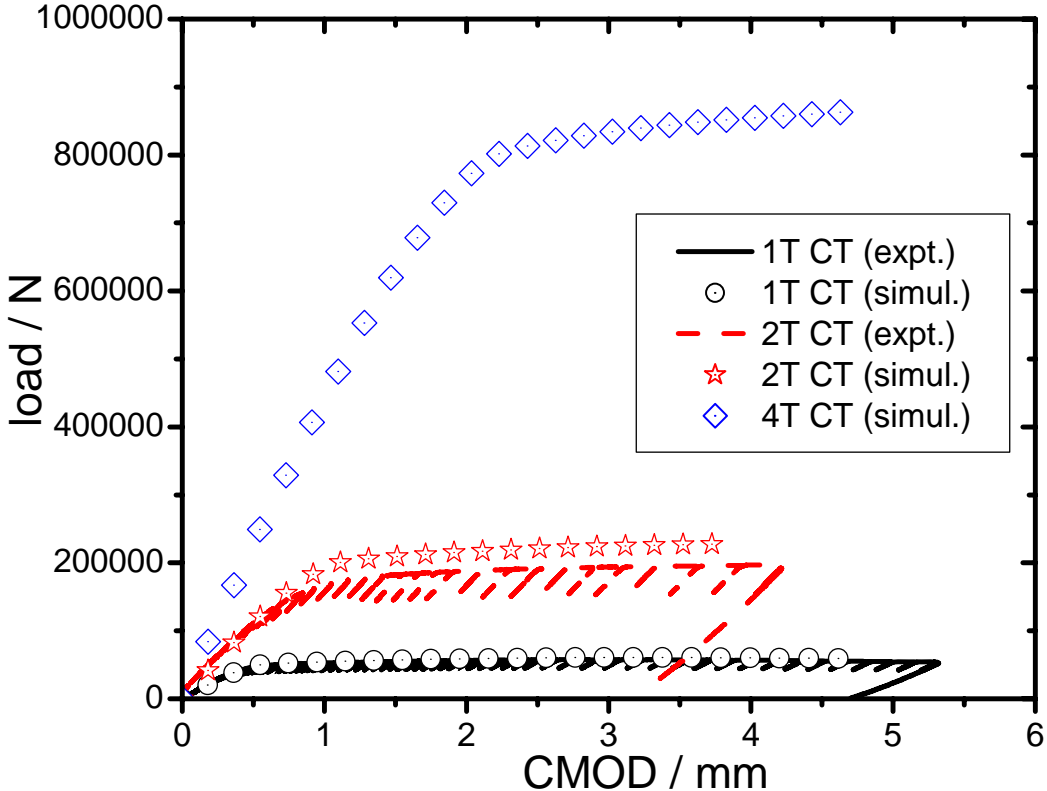


Fig. 4.65: Prediction of geometry effect (effect of specimen size) on load-CMOD response of CT specimen with the help of nonlocal model

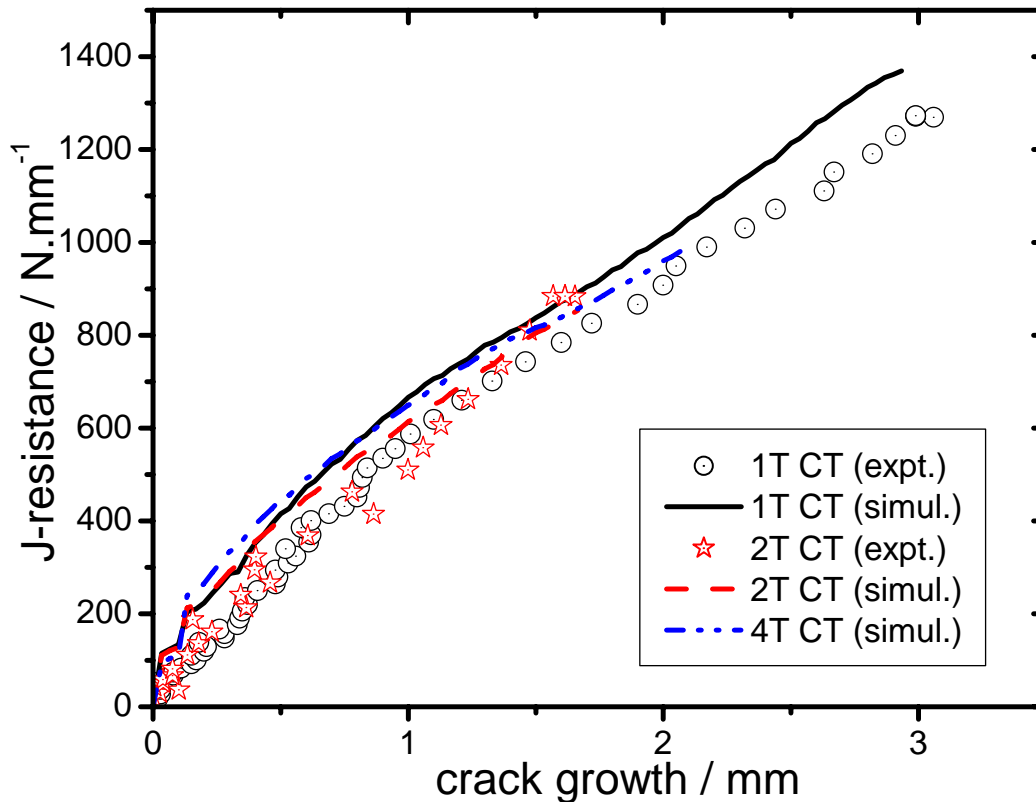


Fig. 4.66: Prediction of geometry effect (effect of specimen size) on J-resistance behaviour of CT specimen with the help of nonlocal model

However, in the J-resistance behaviour prediction, this size effect gets normalized as the J-integral is a measure of energy release rate ahead of crack tip per unit un-cracked ligament area. Instead, the predicted resistance of the larger specimens to crack propagation becomes slightly lower compared to 1T CT specimen [Fig. 4.66]. This effect also gets reflected in the experimental data [Fig. 4.66]. Hence, it can be concluded that the nonlocal models have been able to predict the size effect on the fracture resistance behaviour of specimens in addition to their mesh-independent nature.

4.12 Prediction of geometry effect (effect of specimen type)

In this section, the effect of specimen type on the load-CMOD and fracture resistance behaviour of different types of specimens has been studied with the help of nonlocal models. Similar to the study of size effect, results of two different specimens (i.e., 1T CT and 1T SEB) have been compared when simulated using 2D nonlocal plane strain formulation. The results of analysis using 0.1mm mesh near crack tip have been presented here for comparison.

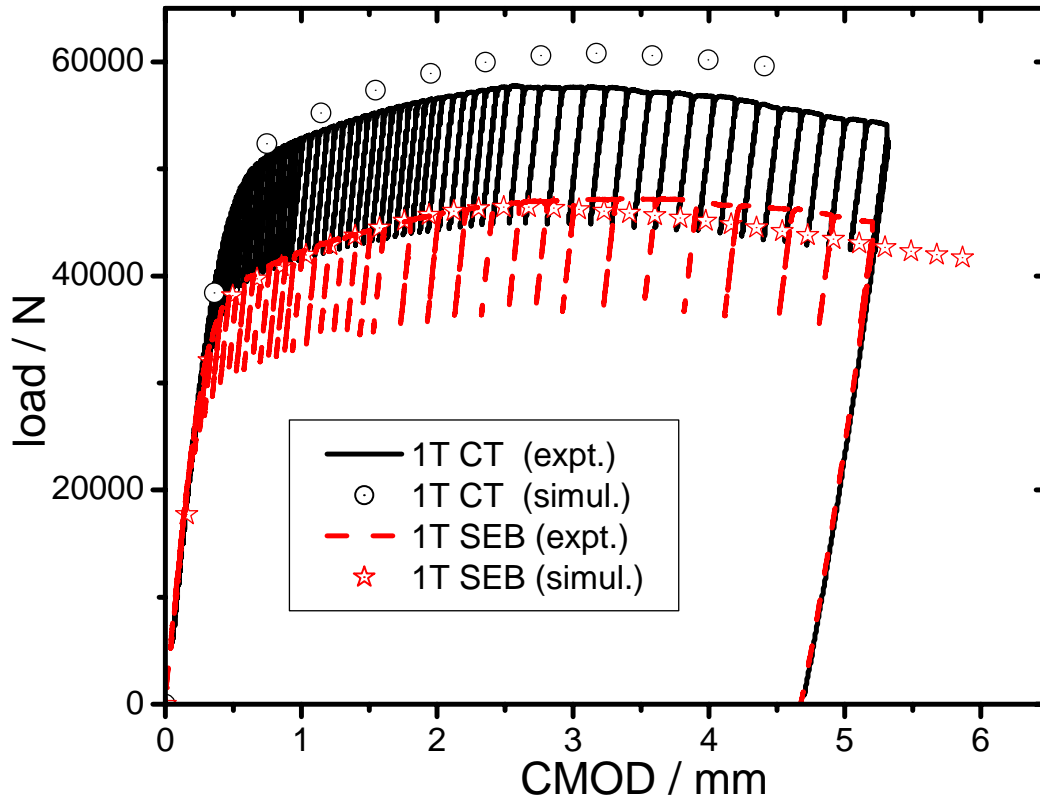


Fig. 4.67: Prediction of geometry effect (effect of specimen type) on load-CMOD response of different specimens with the help of nonlocal model

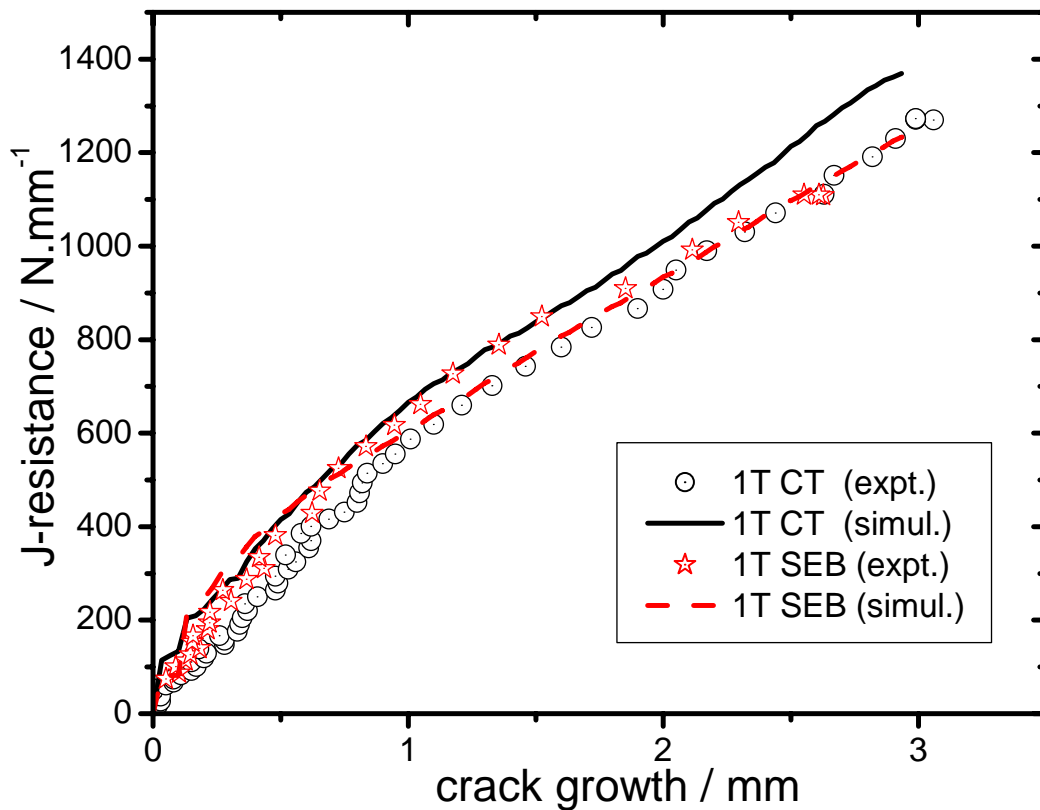


Fig. 4.68: Prediction of geometry effect (effect of specimen type) on J-resistance behaviour of different specimens with the help of nonlocal model

Fig. 4.67 shows the comparison of load-CMOD responses of 1T CT and 1T SEB specimen. As expected, 1T SEB specimen shows a lower load-CMOD behavior as it is loaded dominantly in bending compared to the CT specimen, which is loaded dominantly in tension. The above effect of state of stress ahead of crack tip for the two specimens also gets reflected in their fracture resistance behaviour. Fig. 4.68 shows that the predicted fracture resistance behaviour of the 1T SEB specimen is slightly lower than that of the 1T CT specimen because of dominant bending (and hence more constraint). Similar trend is also observed in case of experimental results.

4.13 Prediction of geometry effect (effect of crack depth)

In this section, the effect of crack depth on the load-CMOD and fracture resistance behaviour of a 1T SEB specimen has been studied with the help of nonlocal models. Two different values of crack sizes have been used (i.e., a deep cracked specimen of $a_0/W = 0.522$ and a shallow cracked specimen of $a_0/W = 0.13$) in the analysis. The FE mesh of the shallow cracked specimen is shown in Fig. 4.69 (a) along with its enlarged view near the crack tip. Fig. 4.70 shows the comparison of predicted load-CMOD responses of deep and shallow cracked 1T SEB specimen along with the experimental results.

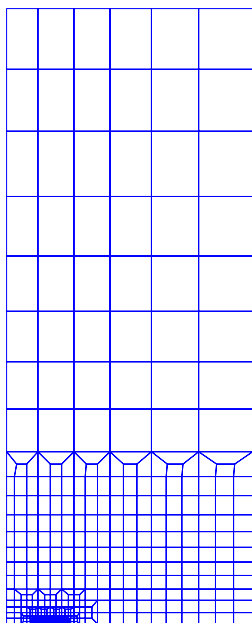


Fig. 4.69(a): FE mesh of the shallow cracked SEB specimen ($a/w = 0.13$)

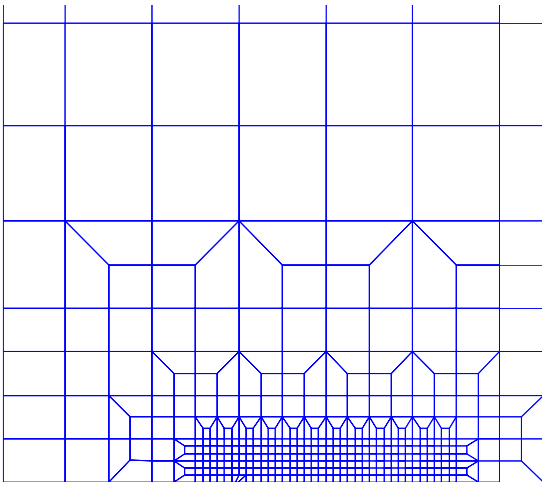


Fig. 4.69(b): Enlarged view of Fig. 4.69(a) near the crack tip

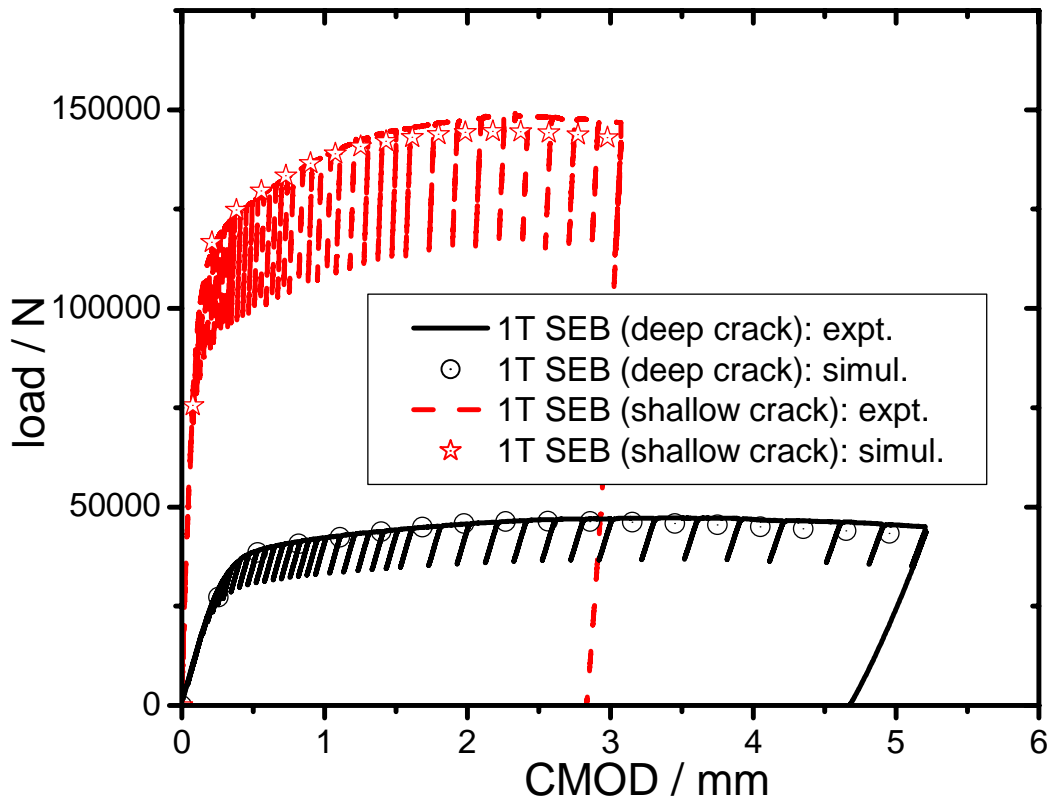


Fig. 4.70: Prediction of effect of crack depth on load-CMOD response of 1T SEB specimen with the help of nonlocal model

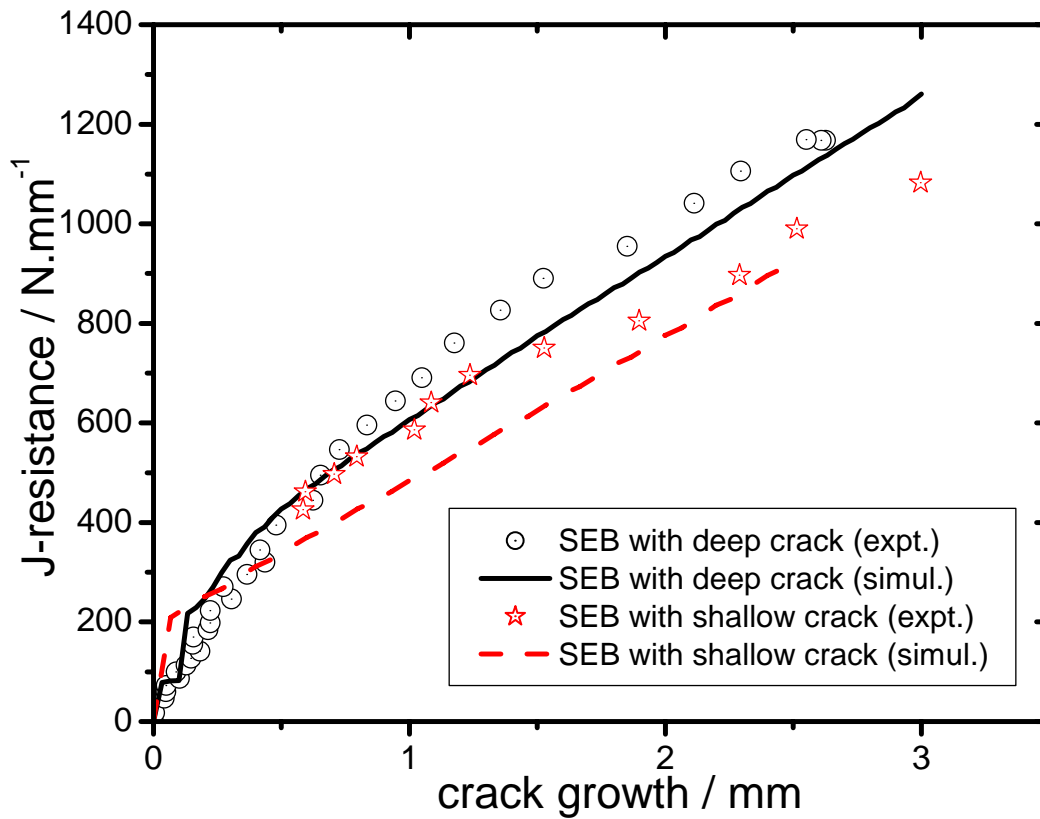


Fig. 4.71: Prediction of effect of crack depth on load-CMOD response of 1T SEB specimen with the help of nonlocal model

The evaluation of η factor is different for deep and shallow cracked specimens. For shallow cracked specimens, the η factor formula of Sreenivasan and Mannan (2000) has been used, whereas for the deep cracked SEB specimen, ASTM formula for η factor is used. The η factor of the shallow cracked SEB specimen is significantly lower than that of the deep cracked SEB specimen and this takes care of the constraint effect in the J-resistance behaviour. As can be seen from Fig. 4.70, the load-response is higher for the shallow cracked specimen compared to the deep specimen. It is because the un-cracked ligament (load-carrying) area is high in case of shallow cracked specimen. However, the fracture resistance behaviour is slightly lower for the shallow cracked specimen compared to the deep cracked specimen and similar trend is observed in the experimental result [Fig. 4.71].

4.14 Effect of material symmetry in modelling

In this section, the effect of symmetric boundary condition on crack path and hence load-displacement response of a flat tensile specimen has been analyzed. As is commonly known, considerations of symmetric conditions existing in geometry, material property, loading and boundary conditions are always exploited in the FE analysis in order to reduce number of degrees of freedom of the model and hence the solution time. However, such approaches can create problems especially when crack growth modeling is considered using local damage model. This problem is discussed here by using the example of the same flat tensile specimen (with hole at the center) as discussed earlier. Exploiting symmetry, we can either use one-half of the specimen as a FE model [Fig. 4.72(a)] or one-fourth of the specimen as a FE model [Fig. 4.72(b)].

The difference between the two models is that crack can initiate and traverse along a path (depending upon the stress and strain distribution during loading) inside the material in case of 4.72(a) whereas crack initiates and propagates along the symmetric plane (bottom layer) in case of 4.72(b). 4.72(b) is the model which is used popularly because of less computational effort. However, crack initiation and propagation can be modeled realistically considering 4.72(a), which has been used for the present study. Also, as will be observed subsequently, one can come across another inconsistency of the local damage model (in addition to the mesh dependent nature) when the mesh shown in Fig. 4.72(a) is used for analysis.

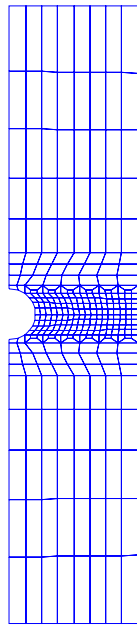


Fig. 4.72(a): FE mesh of half of the flat tensile specimen with hole at the centre



Fig. 4.72(b): FE mesh of one-fourth of the flat tensile specimen with hole at the centre (symmetric boundary condition has been used)



Fig. 4.73(a): Crack propagation in the flat tensile specimen (local model), contour plot damage

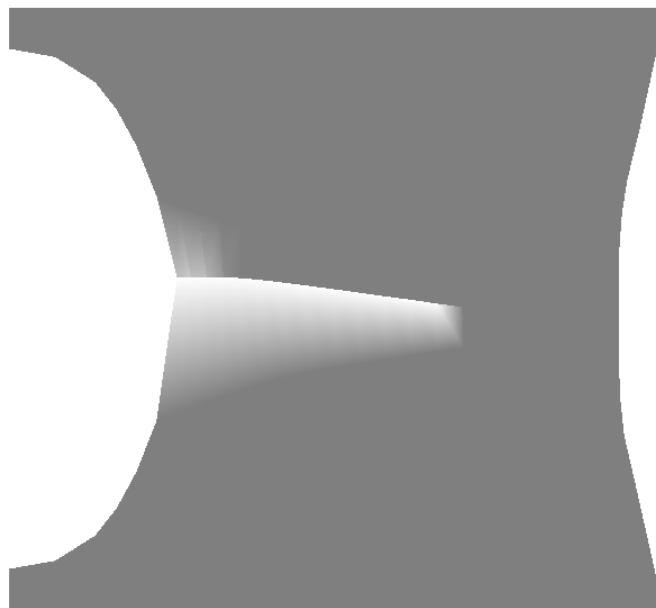


Fig. 4.73(b): Enlarged view of Fig. 4.73(a) near the hole

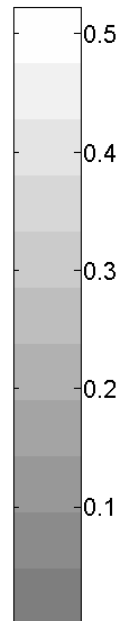




Fig. 4.74(a): Crack propagation in the flat tensile specimen (nonlocal model), contour plot of damage

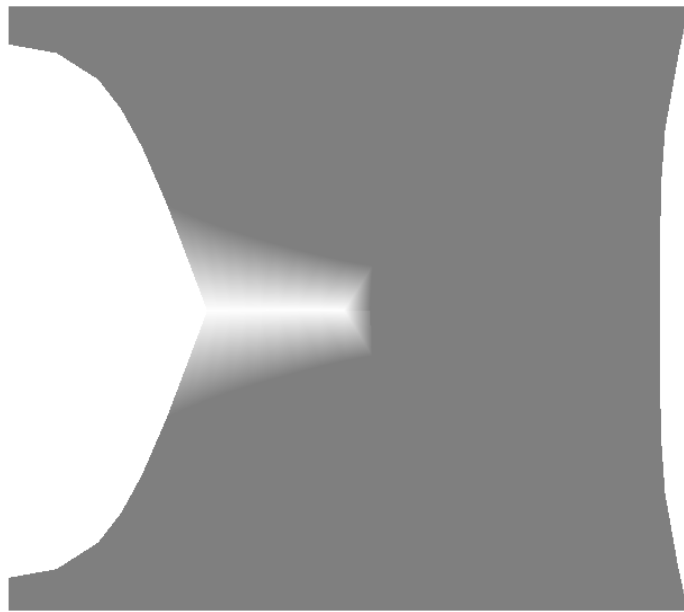


Fig. 4.74(b): Enlarged view of Fig. 4.74(a) near the hole

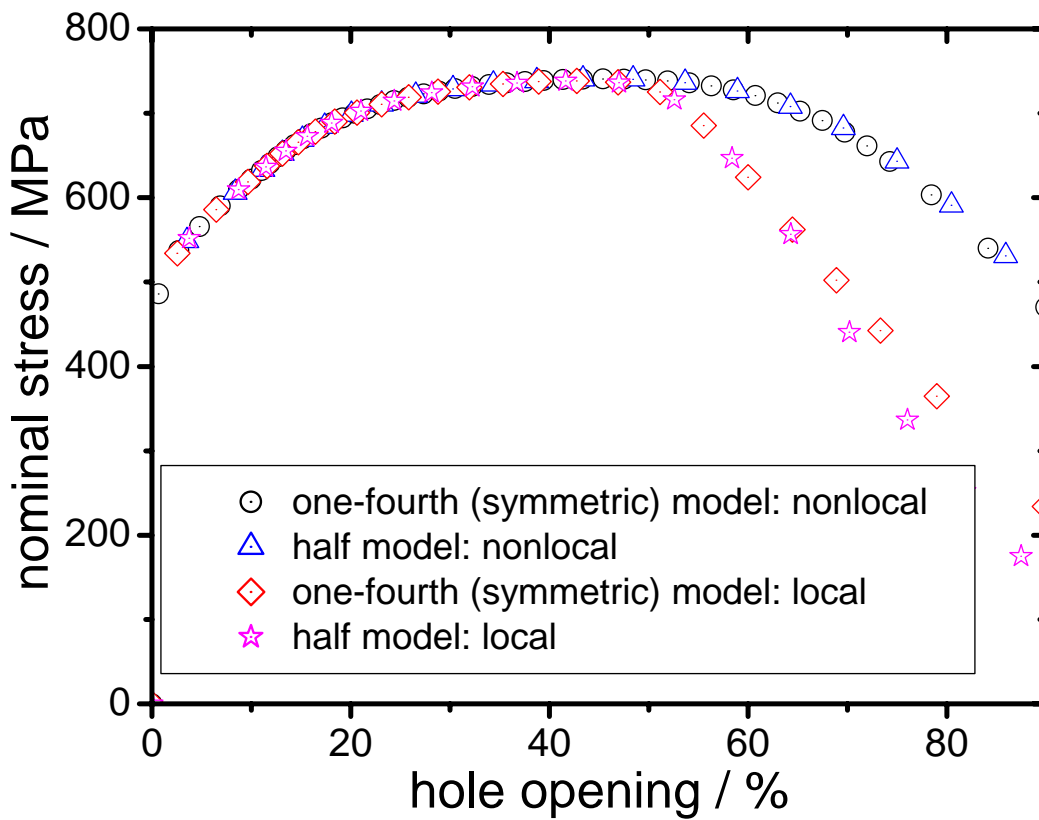
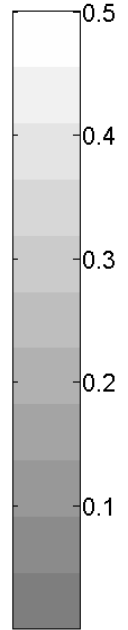


Fig. 4.75: Nominal stress vs %age hole opening behaviour of the flat tensile specimen with hole at centre (effect of symmetric modeling with local and nonlocal models)

For the analysis, the mesh size of 0.2mm has been used for modeling the flat tensile specimen. The damage zone path (it is represented by damage value of 0.5 in the contour plot) is shown in Fig. 4.73(a) [with its enlarged view in Fig. 4.73(b)] for the local model. It can be observed from Fig. 4.73 that though crack initiation occurs on both sides (top and bottom) of the central position of hole, the damage zone finally runs along the bottom element layer in case of the local model. This is a problem of localization of the damage zone where damage is restricted to one element layer. However, the problem is purely symmetric and hence the damage zone should propagate equally on top and bottom layers around the central line of the specimen and this is exactly what happens in case of Fig. 4.74. Hence, nonlocal models not only produce mesh-independent results, they can also model the symmetry condition accurately. This is because of preservice of the elliptical nature of the PDEs by the nonlocal model with mesh refinement, which is not the case for local models.

The effect of preservice of symmetric nature of the solution by the nonlocal models also gets reflected in the nominal stress vs %age hole opening behaviour of the flat tensile specimen. Fig. 4.75 compares the results of analysis of the flat tensile specimen with mesh designs of 4.72(a) [half model] and 4.72(b) [one-fourth model]. As expected the results of nonlocal analysis for the two mesh designs are exactly same whereas the local analysis results depend upon mesh design. Hence, symmetric boundary conditions cannot be properly modeled in local damage mechanics and so one needs to use nonlocal models in order to remove the above inconsistency.

4.15 Effect of material stress-strain curve

In this section, the effect of material stress-strain curve on the load-response and fracture resistance behaviour of a specimen will be discussed. The discussion on the effect of material stress-strain curve stems from the fact that many times the true stress-strain curve beyond the true strain at UTS is obtained by extrapolating the curve before UTS. The extrapolation curve depends upon the number of points (before UTS) that one uses for this purpose and hence many times the effect of multiaxiality is not properly corrected for the true stress-strain curve beyond UTS. The aim is to study the effect of the error in the extrapolated curve on the fracture resistance prediction using nonlocal damage models. For this purpose, two slightly different true stress-strain curves have been used in the analysis as shown in Fig. 4.76. Curve-1 stands for the actual material stress-strain curve for the material 22NiMoCr3-7 that has been

used till now in all the analyses. Curve-2 is the slightly modified true stress-strain curve, which is exactly same upto the UTS and slightly lower (true stress for the modified curve is 10% lower than the true stress of the actual curve for the same value of true plastic strain) than the Curve-1 beyond UTS which reflects the effect of extrapolation on the stress-strain curve.

With these two stress-strain curves in our hand, we have analyzed a 1T CT specimen using nonlocal damage model. The mesh size used near crack tip is 0.1mm. Fig. 4.77 shows the load-CMOD response of the CT specimen for the two stress-strain curves and Fig. 4.78 compares the predicted J-resistance curves. As can be seen from Figs. 4.77 and 4.78, the load-CMOD and J-resistance responses of the CT specimens are almost same for the two stress-strain curves. Hence, it can be concluded that though there can be some uncertainty in the extrapolation method to determine the true stress-strain curve beyond UTS, its effect on the fracture resistance behaviour (at room temperature) is minimal. However, as will be observed for analysis in the ductile to brittle transition temperature region, the probability of brittle fracture can get significantly affected because of slight error in the stress-strain extrapolation especially towards the higher temperature side of the transition temperature region.

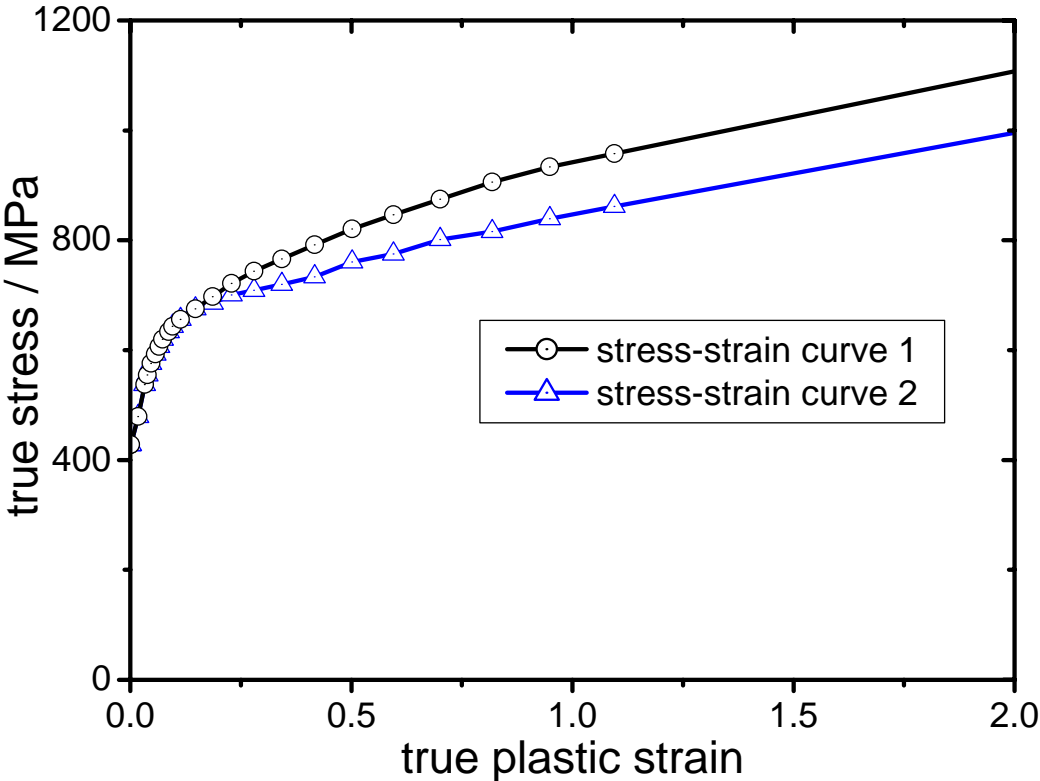


Fig. 4.76: True stress-strain curve of the material 22NiMoCr3-7: curve 1 (actual), curve 2 (modified)

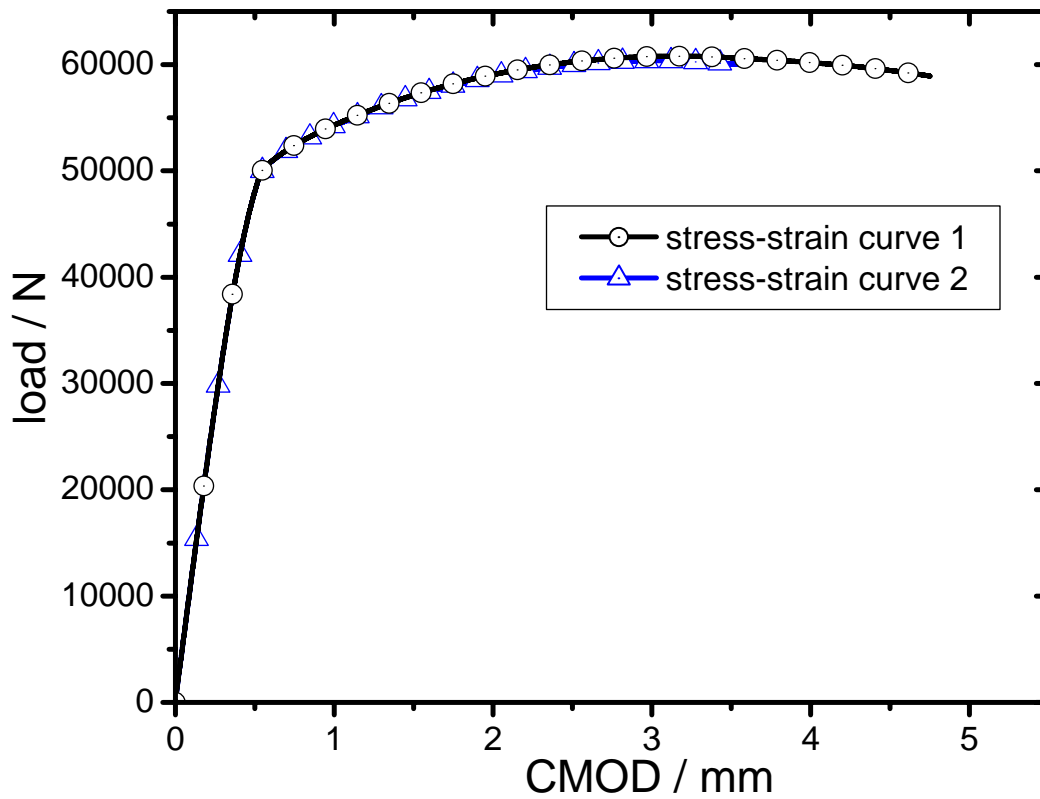


Fig. 4.77: Effect of material stress-strain curve on load-displacement response of the 1T CT specimen (nonlocal model)

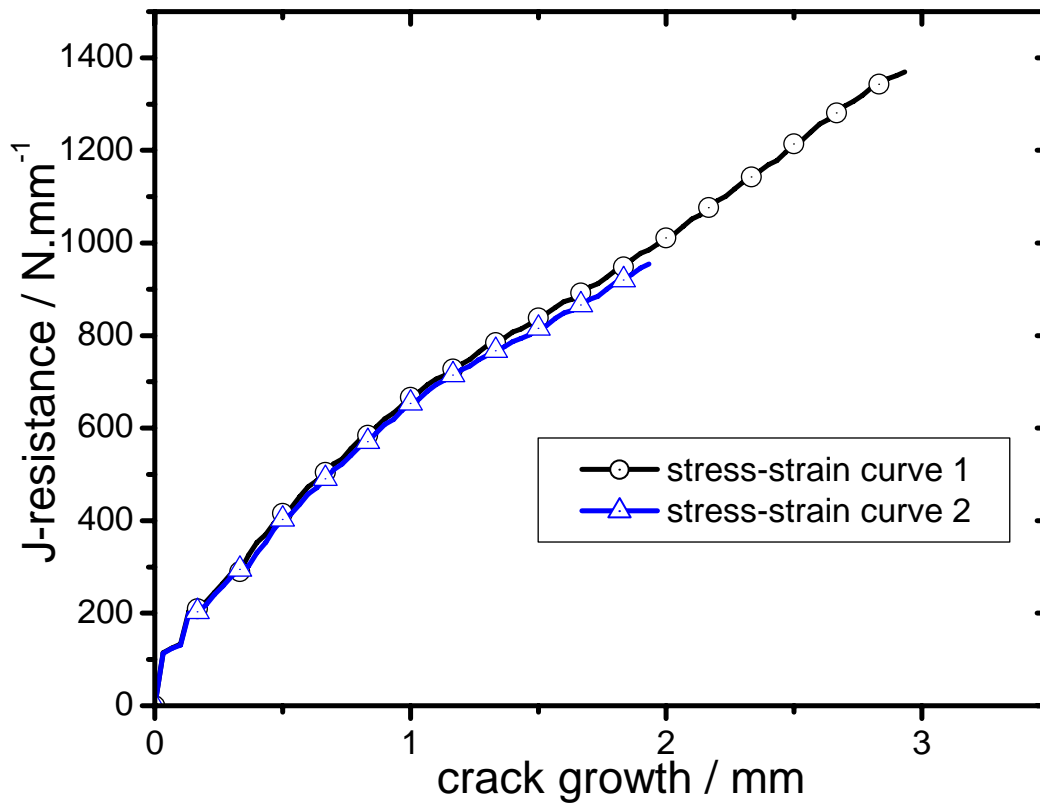


Fig. 4.78: Effect of material stress-strain curve on J-resistance behaviour of the 1T CT specimen (nonlocal model)

4.16 Effect of critical length parameter

As discussed in Chapter-3, introduction of the concept of nonlocality into the material constitutive relation is through the characteristics length parameter C_{length} . Theoretically, The results of the nonlocal model reduces to that of the local model when $C_{length} \rightarrow 0$. The characteristics length parameter C_{length} is used to regularize the development of damage in nonlocal models. If this length cannot be uniquely determined from the microstructure of the material, it must be fitted from experimental results. This can be done indirectly, by relating the internal length scale to the difference between homogeneous and heterogeneous responses [Bažant and Pijaudier-Cabot (1989)] or to size effects [Pijaudier-Cabot (1995), Carmeliet (1996)]. But a more direct and probably more reliable method is to measure the extent of material damage in experiments, for instance by optical deformation measurements [Geers (1997)]. Reusch 2003, Reusch et al. (2003a,b) and Peerlings et al. (2001, 2002) have shown that the characteristics length parameter C_{length} is proportional to $l_c^2/4$ where l_c is the critical or characteristics length of the material (which is of the order of the mean distance between relevant inclusions from which voids can be nucleated and grow further).

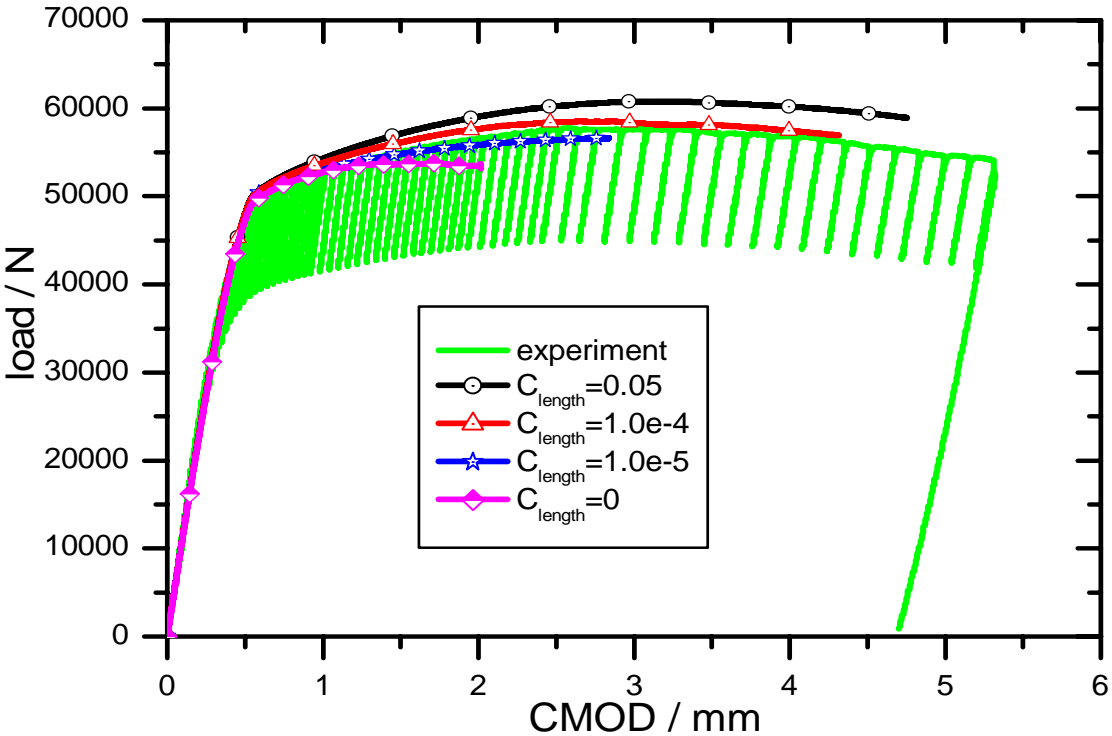


Fig. 4.79: Effect of critical length parameter on load-displacement response of the 1T CT specimen (nonlocal model)

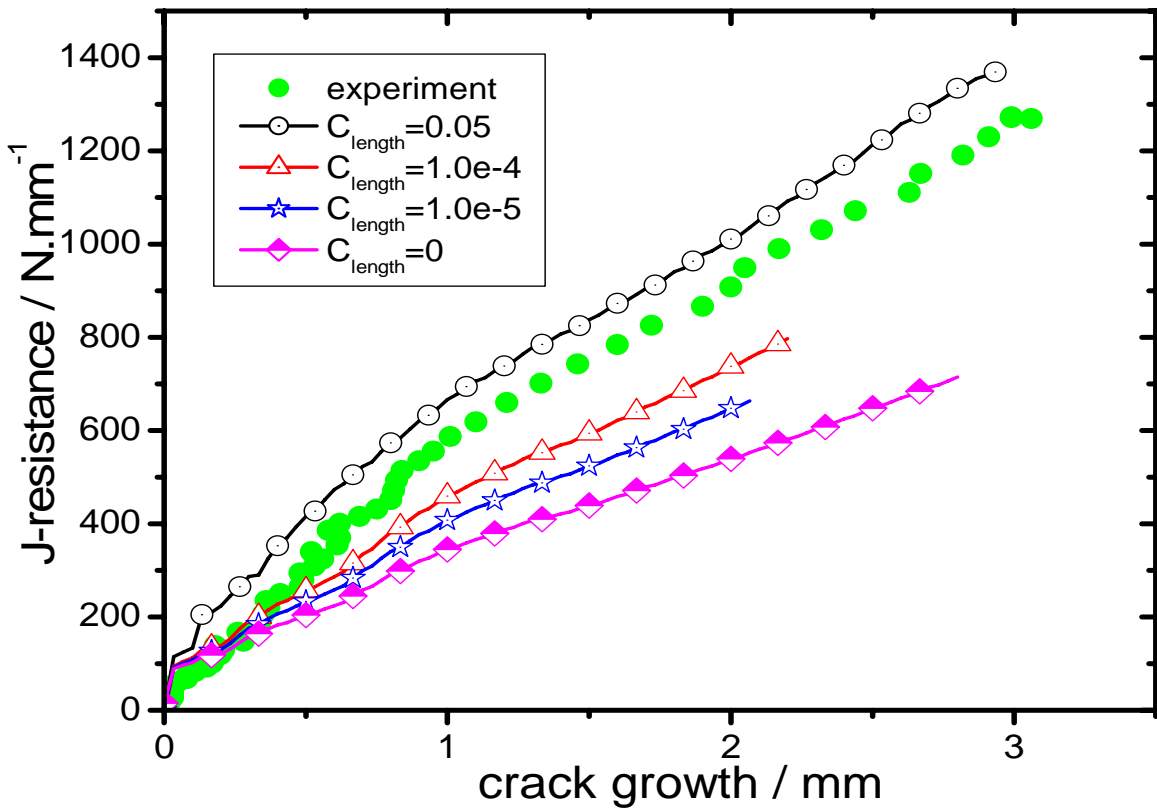


Fig. 4.80: Effect of critical length parameter on J-resistance behaviour of the 1T CT specimen (nonlocal model)

The characteristic length parameter l_c for the material under consideration (i.e., 22NiMoCr3-7), has been determined by Seidenfuss and Roos (2004) as approximately 0.4mm. In order to study the effect of C_{length} on the load-CMOD and fracture resistance behaviour of the 1T CT specimen, analysis has been carried using nonlocal model with different values of C_{length} (i.e., 0, 1.0e-5, 1.0e.4 and 0.05). The FE mesh size of 0.1mm near the crack tip has been used. The predicted load-CMOD response and the J-resistance curve of the CT specimen for different values of C_{length} have been compared with experiments [Fig. 4.79 and 4.80]. As expected, the model predicts faster crack growth with lower values of C_{length} (more towards local behaviour) and hence lower load-CMOD curves. For the C_{length} value of 0.05, the predicted J-resistance curve compares very well with that of experiment and hence it has been selected at the C_{length} value for all the analyses carried out in this work. This value of C_{length} also compares favourably well with the theoretical derivations of Reusch et al. (2003a,b) and Peerlings et al.

(2001, 2002) [i.e., $C_{length} \approx \frac{l_c^2}{4}$].

In this chapter, the ductile crack growth in various components was simulated by the use of both local and nonlocal models. The results of the nonlocal model were proved to be mesh-independent. Having predicted the behaviour of specimens in the upper shelf region successfully, we proceed for simulation of probability of cleavage fracture of fracture mechanics specimens in the lower shelf and transition region in the next chapter.

Chapter 5

Numerical simulation of probability of failure in lower shelf and transition region

In this chapter, the cleavage fracture process in fracture mechanics specimens is modeled using Beremin's model, which uses Weibull statistics and weakest link theory of fracture. The two-parameter Weibull's model with parameters m and σ_u is considered in this work. The theory for Beremin's model is described in the second chapter along with the maximum likelihood method for determination of the Weibull parameters from combined numerical simulation and experiment. The same material (i.e., 22NiMoCr3-7) as studied in fourth chapter is also considered here for numerical simulation in the ductile to brittle transition region. All the referred experiments have been carried out at MPA Universität Stuttgart using different types of fracture mechanics specimens (such as CT and SEB) for the whole transition temperature region (Eisele et al. 2006). A number of specimens were tested at the same temperature (e.g., -100, -60, -20 deg. C etc.) in order to capture the statistical scatter in the cleavage fracture process.

Ductile and cleavage fracture processes are two competing mechanisms in the ductile to brittle transition temperature region of a material. It was experimentally observed that [Fig. 1.3], in the temperature ranges of -100 to -60 deg. C, there is virtually no remarkable stable crack growth in the fracture mechanics specimens before final fracture by cleavage and hence the fracture is nearly pure cleavage. However, at temperature beyond -60 deg. C, there is onset of plastic deformation and hence some stable crack growth, which is of the order of 200 micron at -20 deg. C. The ductile crack growth alters the stress and strain distribution ahead of the crack tip (Eisele et al. 2006) in the specimens and hence it can significantly affect their probability of cleavage fracture in the specimens.

To take into the account of the effect of ductile crack growth and stress redistribution, one needs to combine the ductile damage model with Beremin's model. In this work, Rousselier's model has been combined with Beremin's model to simulate fracture process in the transition region. As discussed earlier, the FE mesh required for local Rousselier's model is too coarse to

capture the large stress gradient ahead of the crack tip at low temperatures and to simulate small amounts of crack growth. In order to circumvent the above problems, the nonlocal form of the Rousselier model has been used here in combination with the Beremin's model as the nonlocal model has the advantage of predicting the ductile crack growth process even if very fine mesh is used. Simulations have been carried out in both 2D and 3D domains and the effects of specimen size and geometry on the ductile to brittle transition curve (for fracture toughness) of the material has been studied.

5.1 Prediction of probability of cleavage fracture in the transition regime using compact tension specimens (2D plane strain analysis)

In this section, we discuss the results of analysis in the transition region using 1T CT specimens (with initial crack to width ratio $a_0/W = 0.522$). 2D plane strain analysis is used for the simulation.

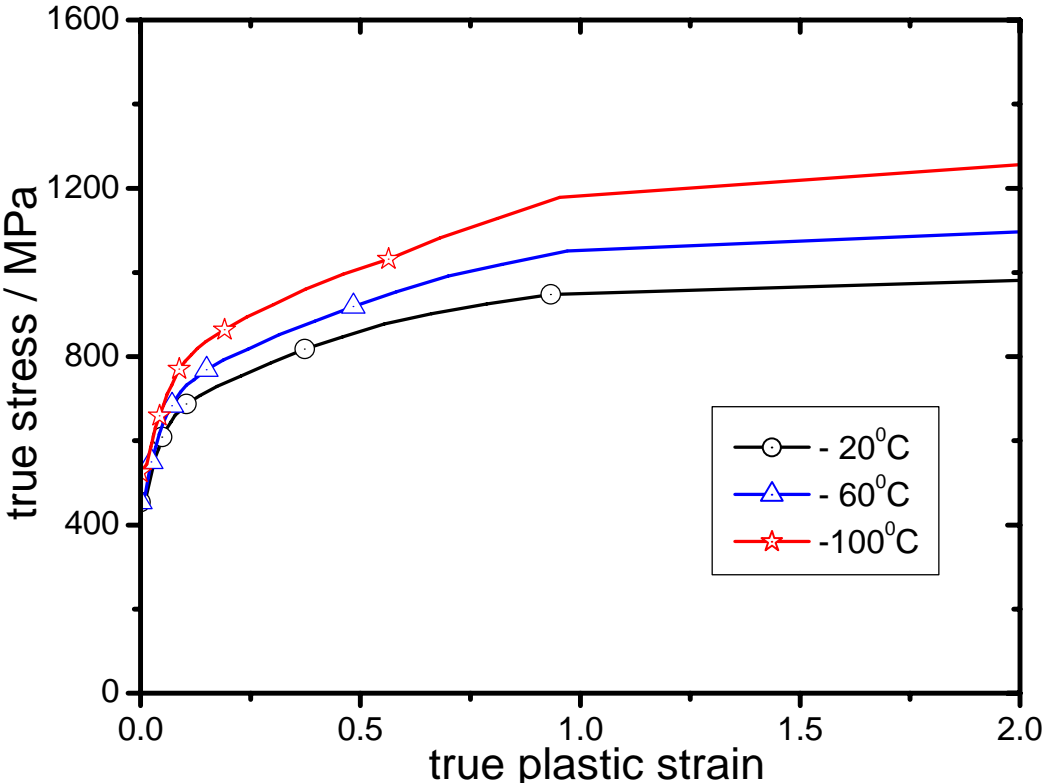


Fig. 5.1: True stress-strain curves of the material 22NiMoCr3-7 at three different temperatures in the transition regime

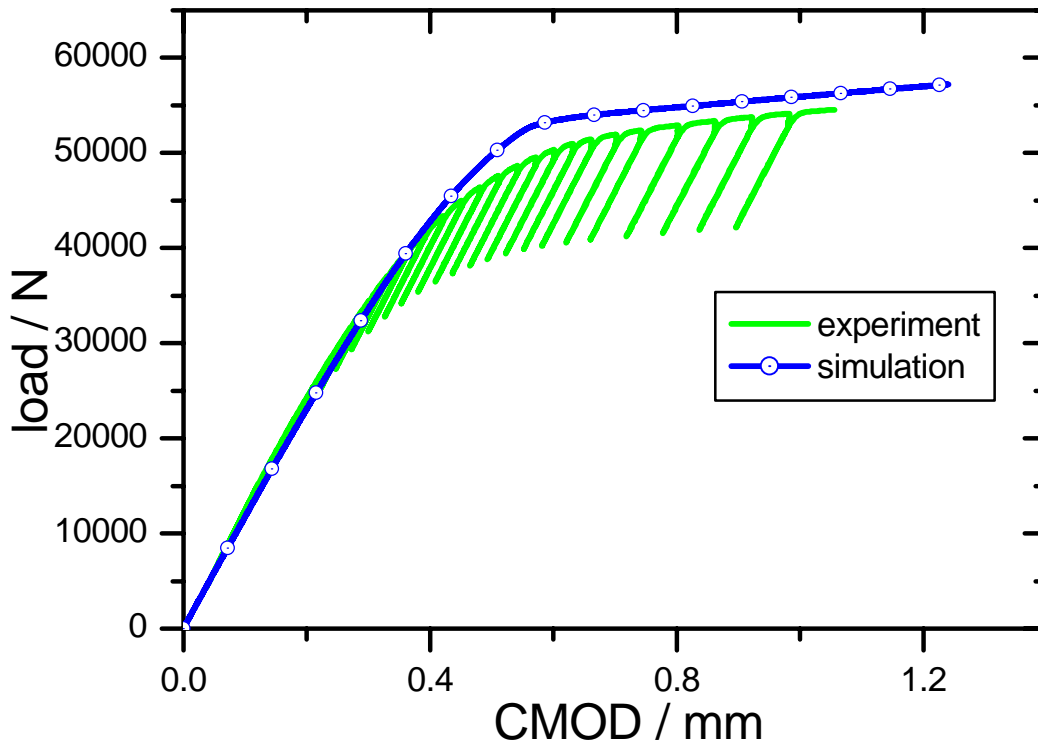


Fig. 5.2: Load-CMOD curve of the 1T CT specimen at -20 deg. C (2D plane strain analysis)

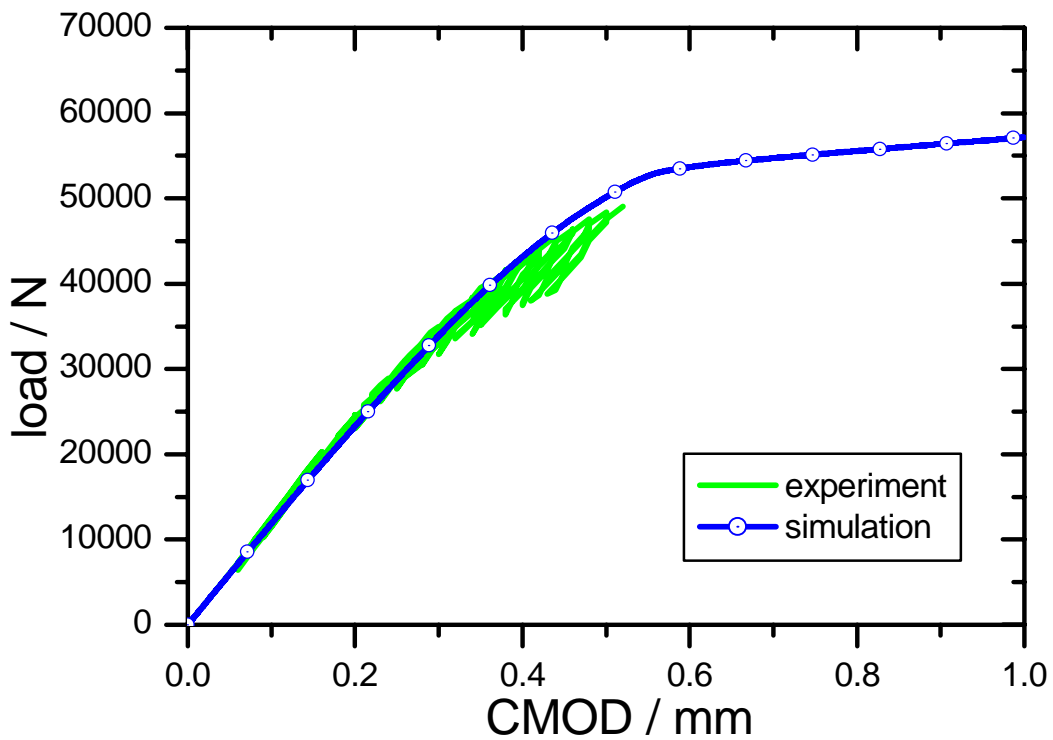


Fig. 5.3: Load-CMOD curve of the 1T CT specimen at -60 deg. C (2D plane strain analysis)

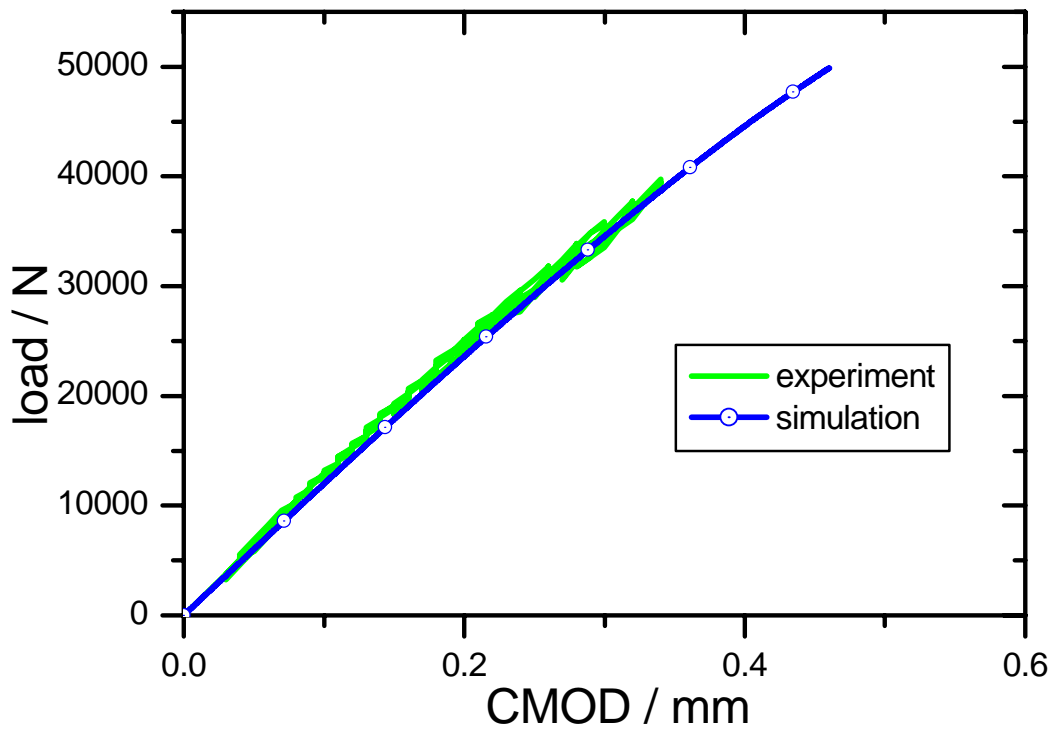


Fig. 5.4: Load-CMOD curve of the 1T CT specimen at -100 deg. C (2D plane strain analysis)

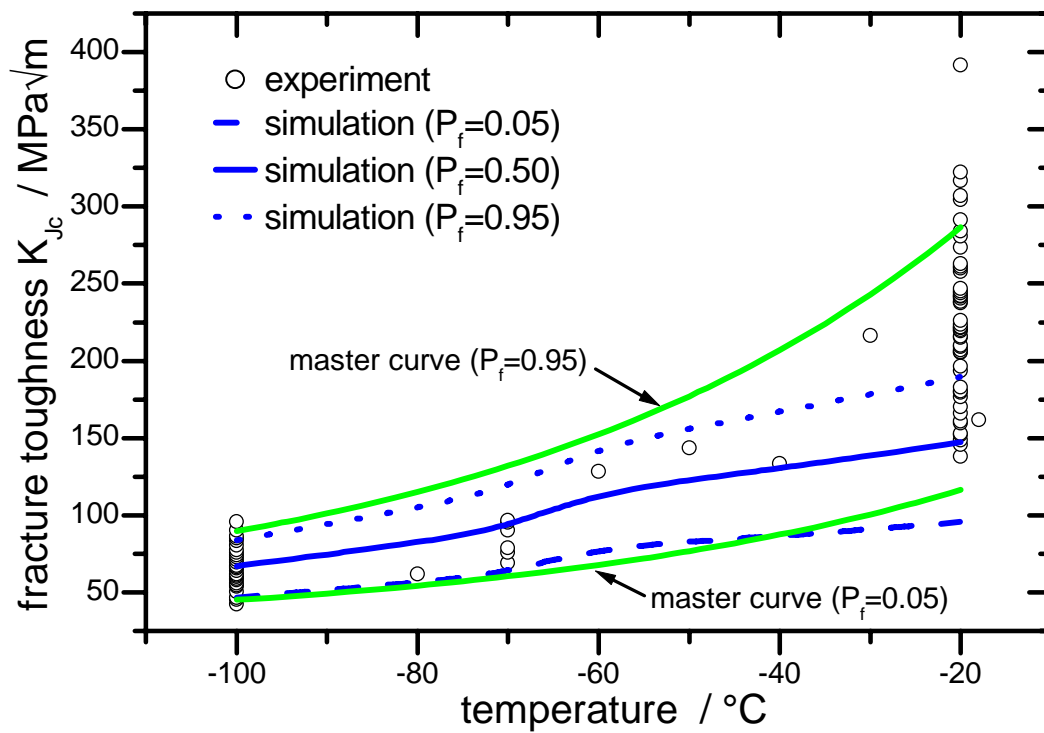


Fig. 5.5: Comparison of simulated (elasto-plastic analysis) scatter of fracture toughness with experiment in the transition temperature region [2D plane strain analysis of 1T CT]

The material stress-strain curves used in the analysis at three different temperatures (i.e., -100, -60 and -20 deg. C) are shown in Fig. 5.1. The FE mesh size used for the CT specimens is 0.02mm ahead of crack tip [Fig. 4.37]. Figs. 5.2-4 show the comparison of load-CMOD results of numerical simulation with those of experiment. The numerical simulation results slightly over-predict the experimental results especially for the temperatures of -20 and -60 deg. C. It is because of the use of plane strain formulation and as will be seen later, the 3D simulation results compare very well with the experimental load-CMOD response of the specimens.

Experiments were conducted on CT specimens and the experimental points of fracture toughness (K_{Jc} , which has been calculated from the critical value of J -integral at unstable fracture, i.e., J_c by using the conversion formula $K = [J.E/(1-\nu^2)]^{1/2}$) at which final fracture (by instability) occurred are plotted with respect to temperature (-100 to -20 deg. C) in Fig. 5.5 (open circles denote experimental points). It can be seen from Fig. 5.5 that the scatter in the experimental fracture toughness is large at -20 deg. C compared to the scatter at -100 deg. C. In order to calculate the probability of cleavage fracture, elasto-plastic analysis was performed initially using CT specimens with a mesh size of 0.02mm at the crack tip [Seebich 2007]. Obviously, crack growth is not simulated in this analysis and hence the predicted probability of cleavage fracture P_f of the Beremin's model (without damage) could not capture the experimental scatter as shown in Fig. 5.5. The solid line in Fig. 5.5 represents the 50% probability of failure ($P_f = 0.50$) curve for fracture toughness with respect to temperature. The dashed curve represents 5% probability of cleavage fracture ($P_f = 0.05$) and the dotted curve correspond to 95% of cleavage fracture probability ($P_f = 0.95$).

The Weibull parameters m and σ_u used in determination of probability of cleavage fracture (using the data of Weibull stress with respect to applied loading) have been taken as 34.8 and 1968 MPa respectively (Seebich 2007) and these are kept constant for the whole temperature range of consideration in the present simulation (i.e., temperature independent Weibull parameters). Fig. 5.5 also shows the prediction of the cleavage fracture probabilities ($P_f = 0.05$ and 0.95) by a simple empirical model of Wallin (1984), popularly known as master curve concept. Master curve is a very popular and simple tool widely used by researchers and designers to design components (against failure by the catastrophic brittle

process) and it has also been incorporated in ASME code as ASME master curve. The master curve equation requires a reference temperature T_0 (signifying ductile to brittle transition temperature) for predicting different probabilities of cleavage fracture and it has been taken here as -68 deg. C (Seebich 2007).

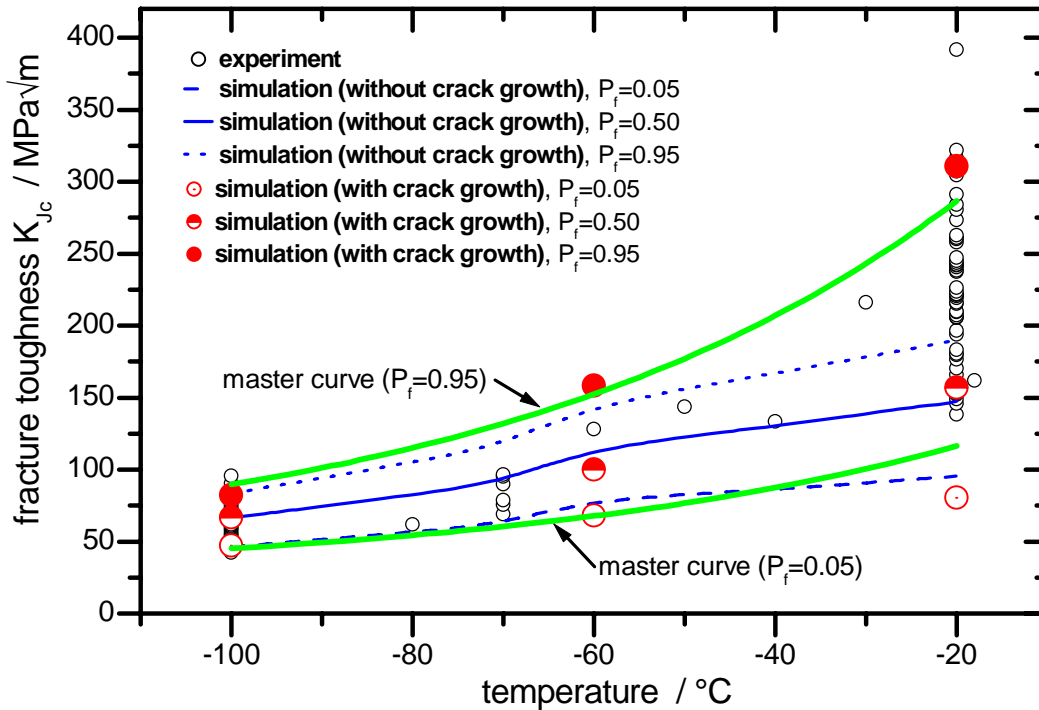


Fig. 5.6: Comparison of simulated (nonlocal damage) scatter of fracture toughness with experiment in the transition temperature region [2D plane strain analysis of 1T CT]

It can be observed (Fig. 5.5) that the master curves for 5% and 95% probabilities of cleavage fracture are able to predict the experimental trend (scatter) very satisfactorily. It may be noted that the Beremin's model (without consideration of material damage) is able to predict very well the scatter in cleavage fracture toughness from -100 to -60 deg. C. It is because, there is actually no significant stable crack growth observed in experiments in this temperature range and hence the stress state ahead of the crack tip (and also the Weibull stress and the probability of cleavage fracture) can be very well described by the elasto-plastic analysis. However, the model grossly underestimates the experimental scatter band towards upper end of the transition region (e.g., -20 deg. C). The reason for the inability of the numerical simulation results in predicting experimental scatter satisfactorily is due to non-consideration of the effect of ductile damage on the stress-strain distribution ahead of the crack tip of the fracture mechanics specimen and hence the aim of the present work is to improve the correspondence

of the simulation results with experiment by consideration of the effect of ductile damage on the Weibull stress.

The above discrepancy (of probability of cleavage fracture) between simulation and experiment has been removed by the use of the nonlocal form of the Rousselier's damage model for calculating stress-strain distribution in the finite element mesh (which is used subsequently to determine the probability of cleavage fracture). Fig. 5.6 shows the comparison of predicted cleavage fracture probability (for fracture toughness) curves (with and without consideration of ductile damage or stable crack growth) with experimental scatter bands of the CT specimen when analysis is done using 2D plane strain assumption. The lines (solid for 50%, dashed for 5% and dotted for 95% probability of cleavage fracture corresponding to fracture toughness) represent simulation results of combined elasto-plastic analysis and Beremin's model (without modeling of stable crack growth) and the dots (open dots for 5%, semi-open dots for 50% and closed dots for 95% probability of cleavage fracture) represent the simulation results using combined nonlocal damage mechanics analysis and Beremin's model. The value of C_{length} parameter for the material has been taken as 0.05 and other model parameters are same as those used in the analysis of fracture resistance behaviour in the upper shelf region. The Weibull parameters m and σ_u used in the determination of probability of cleavage fracture in the combined nonlocal Rousselier and Beremin's model have been taken as 34.6 and 2005 MPa respectively and these are kept constant for the whole temperature range.

It can be observed from Fig. 5.6 that predicted fracture toughness values (corresponding to 5%, 50% and 95% probability of failure) match very well with those of experimental data except the fracture toughness corresponding to 5% probability of failure at -20 deg. C (simulation value is slightly less than that of experiment). The above discrepancy may be due to insufficiency of the modeling process (i.e., use of 2D plane strain assumption in the FE analysis instead of the actual 3D simulation) or may lie in use of improper extrapolated stress-strain curve (beyond UTS of the material). Both these aspects will be discussed in subsequent sections. The master curve has also been plotted in Fig. 5.6 for 5% and 95% probabilities of fracture and the simulation results correspond very well with the scatter band predicted by the master curve except little discrepancy for prediction of 5% probability of fracture at the upper end of the transition region.

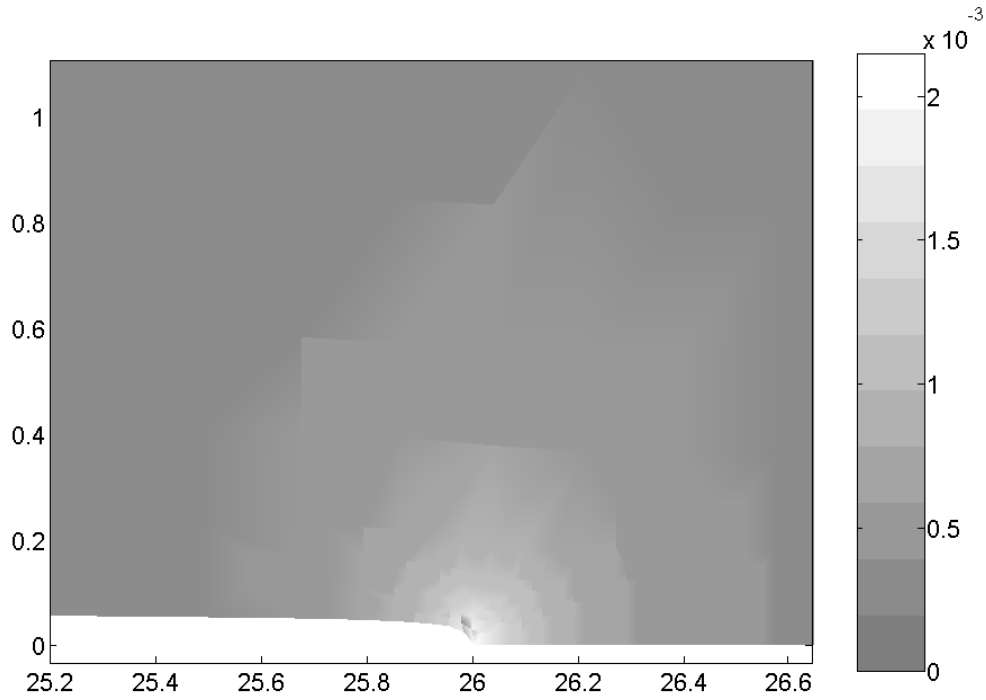


Fig. 5.7: Contour plot of damage at instability near the crack tip of the 1T CT specimen at -100 deg. C (as the critical value of damage is not reached, there is no stable crack growth at instability)

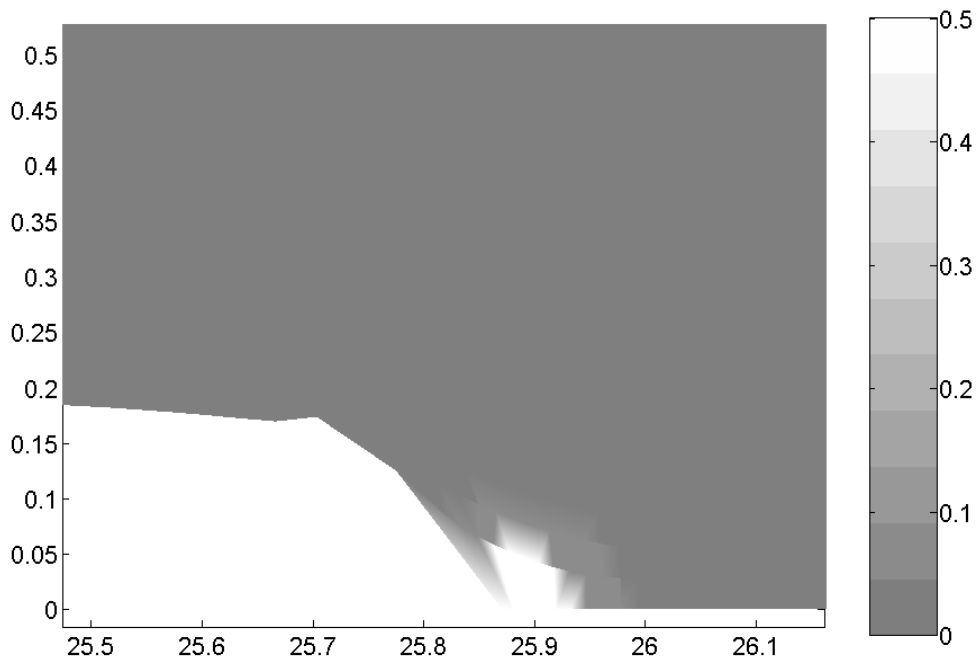


Fig. 5.8: Contour plot of damage at instability near the crack tip of the 1T CT specimen at -60 deg. C (it shows 40 micron of stable crack growth before instability)

As discussed in the previous paragraphs, the predicted probability of cleavage fracture (of the CT specimen) by the combined nonlocal Rousselier and Beremin’s model (in the transition region) correspond very well with the experimental fracture probabilities (when compared to the results of the earlier Beremin’s model coupled with elasto-plastic analysis, Fig. 5.6) and this is due to the ability of the nonlocal model to simulate small amount of stable crack growth. It may be noticed that, for experiments at -100 deg. C (i.e., lower end of the transition region), there is no stable crack growth observed in the CT specimen before the instability and hence the fracture is purely cleavage. The above fact is also observed in the simulation results of the CT specimen at -100 deg. C with the new combined nonlocal Rousselier and Beremin’s model.

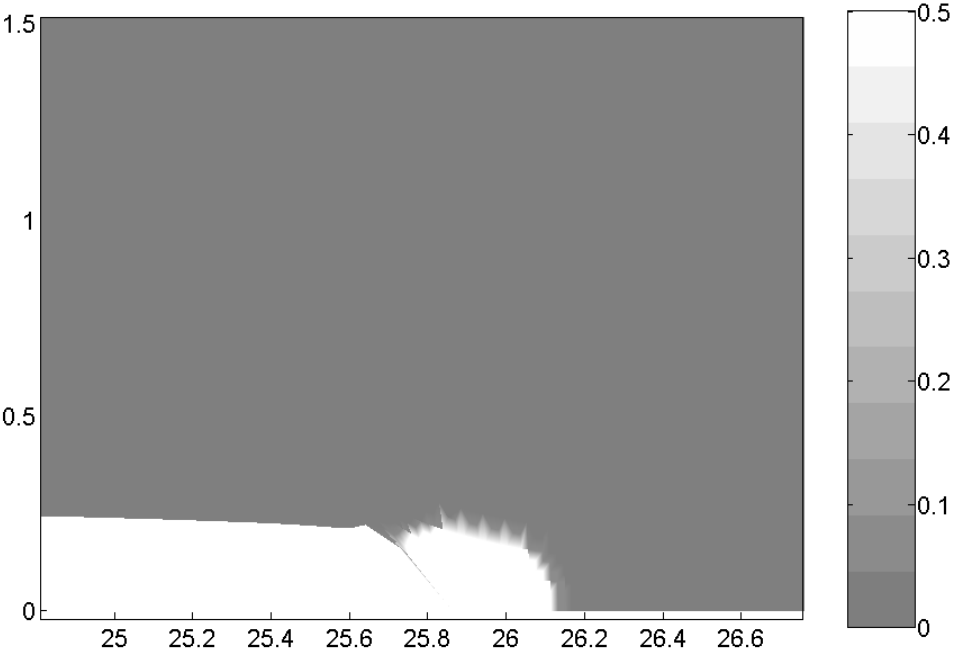


Fig. 5.9: Contour plot of damage at instability near the crack tip of the 1T CT specimen at -20 deg. C (it shows 240 micron of stable crack growth before instability)

Fig. 5.7 shows the contour damage distribution ahead of the crack tip of the CT specimen at -100 deg. C and it can be observed that damage has not reached the critical value of 0.05 and hence there is no stable crack growth before the final unstable fracture by cleavage. However, some amounts of stable crack growth were observed in the simulations of the CT specimen at -60 and -20 deg. C by the new model (Fig. 5.8-9). Fig. 5.8 shows the contour of damage ahead of the crack tip for the simulation of the CT specimen at -60 deg. C and a stable crack growth of approximately 40 micron was calculated (as represented by the zone with damage value of

0.5 in the contour plot) before the instability. The stable crack growth calculated at -20 deg. C by the new model is approximately 240 micron (Fig. 5.9).

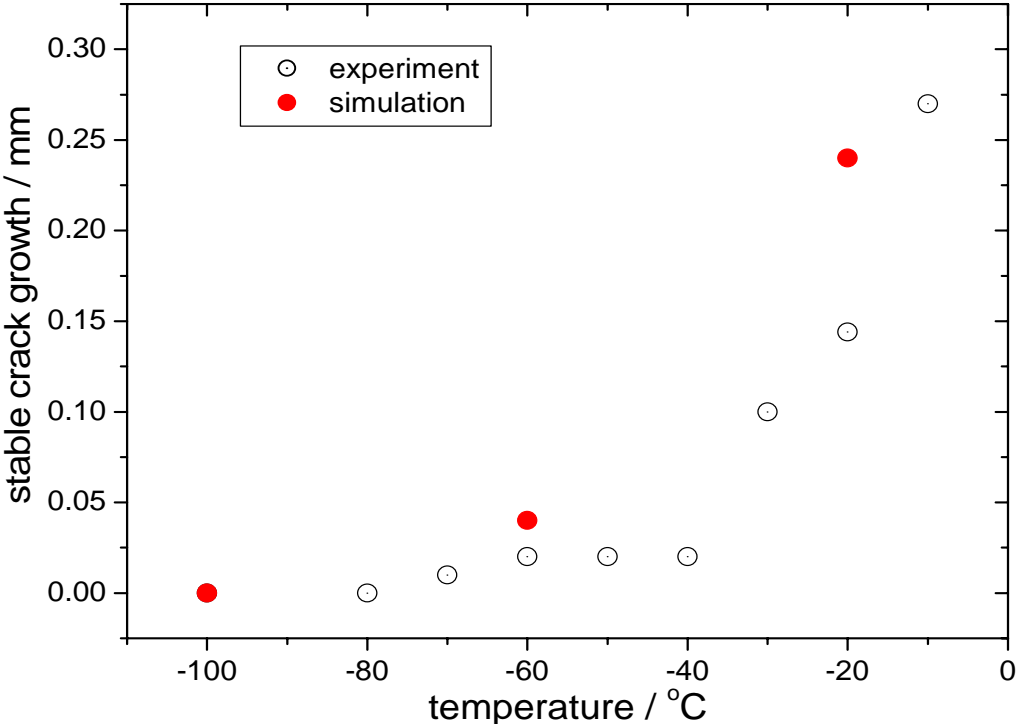


Fig. 5.10: Comparison of calculated and experimental observed stable crack growth at instability of the 1T CT specimen at various temperatures

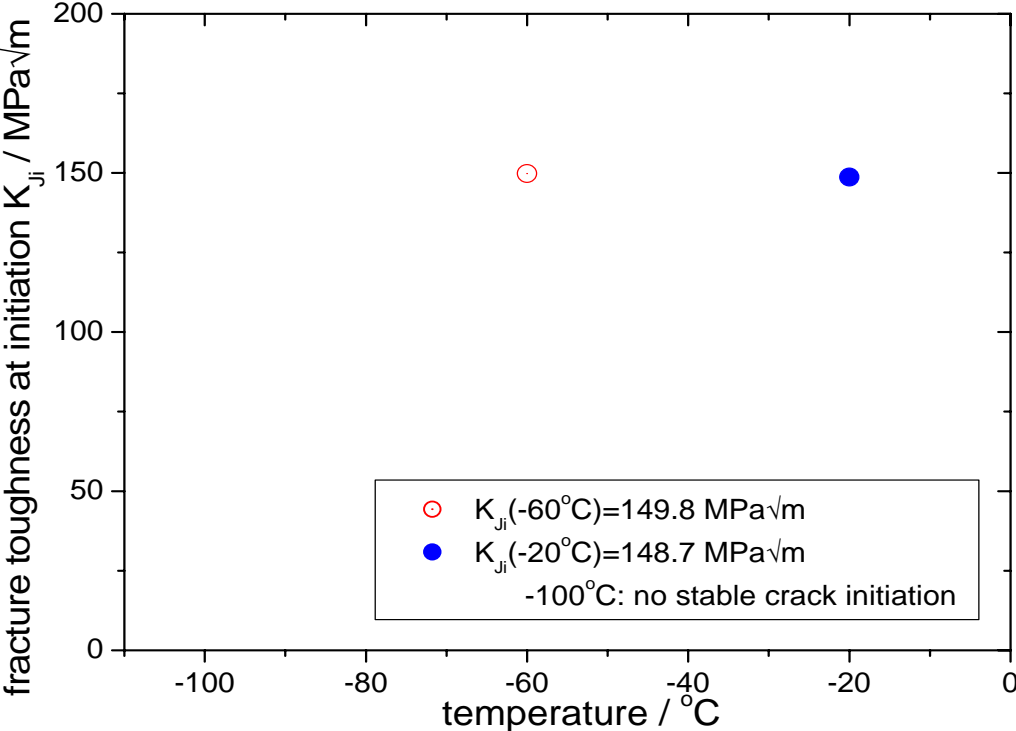


Fig. 5.11: Simulated values of fracture toughness at stable crack initiation of the 1T CT specimen at various temperatures

Fig. 5.10 shows the variation stable crack growth (before instability) with temperature in the transition region for both experiment and simulation. It can be observed that the new combined model is able to simulate the experimentally observed stable crack growth before instability in the whole transition region very satisfactorily. Fig. 5.11 shows the variation of calculated K_{Ji} values (fracture toughness at stable crack initiation converted from J_i values) with temperature. It may be observed that there is no stable crack initiation at -100 deg. C whereas the K_{Ji} values are nearly the same at both the temperatures of -60 and -20 deg. C respectively ($K_{Ji} = 149.8$ MPa at -60 deg. C and $K_{Ji} = 148.7$ MPa at -20 deg. C).

5.2 Prediction of probability of cleavage fracture in the transition regime using compact tension specimens (3D analysis)

As discussed in the previous section, we are able to predict the variation of fracture toughness with respect to temperature in the transition region (-100 to -20 deg. C) of material satisfactorily using 2D plane strain analysis of the CT specimen and a set of temperature independent Weibull material parameters, where the nonlocal damage mechanics model was combined with the Beremin's model to predict the probability of cleavage fracture. However, there were some discrepancies of the results of simulation at the higher end of temperature scale (i.e., -20 deg. C) especially for the 5% fracture probability (P_f) prediction. The effect of modeling on the cleavage fracture probability is investigated here by conducting a 3D analysis of the CT specimen with initial crack to width ratio $a_0/W = 0.522$ (instead of the earlier 2D plane strain analysis).

The FE mesh of the CT specimen along with the enlarged view near the crack tip is shown in Fig. 5.12. Due to symmetry, one-fourth of the CT specimen in 3D domain has been considered. The mesh size ahead of crack tip is 0.05mm x 0.05mm x 1mm (1mm in thickness direction). We have used a coarse mesh of 1mm size in the thickness direction in order to reduce the computational time associated with the 3D simulations. Also, the mesh size is little coarser (0.05mm) in the plane compared to 0.02mm in 2D plane strain analysis. However, it is obvious that the predictions will be better if one can use very small mesh sizes in all the three directions ahead of crack tip.

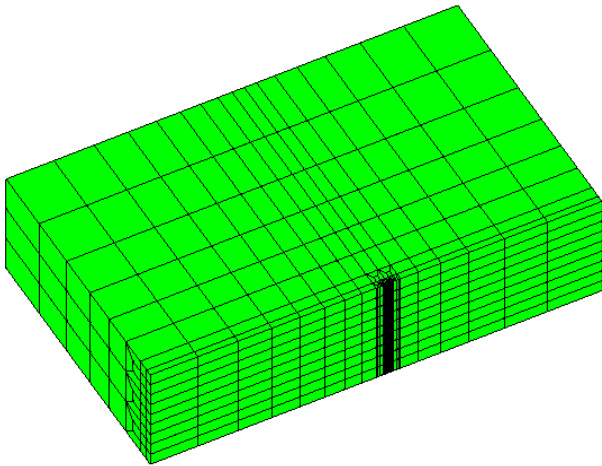


Fig. 5.12(a): 3D FE mesh of the 1T CT specimen

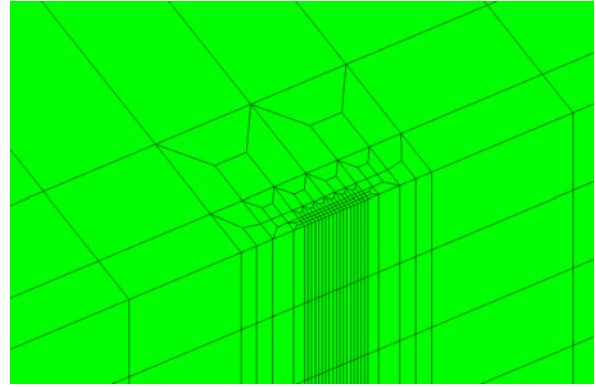


Fig. 5.12(b): Enlarged view of Fig. 5.12(a) near crack tip

Fig. 5.13-15 show the comparison of the predicted load-CMOD responses of the CT specimen with the experimental responses for the three temperatures (i.e., -20, -60 and -100 deg. C respectively). As expected, the 3D simulation results compare very well with those of experiment and hence it is also expected that the predicted fracture toughness vs temperature results (corresponding to different fracture probabilities) will be better for 3D analysis compared to 2D analysis.

Fig. 5.16 shows the variation of fracture toughness (open dots for 5%, semi-open dots for 50% and closed dots for 95% probability of cleavage fracture) with respect to temperature for the 1T CT specimen using nonlocal 3D damage mechanics analysis and it has been compared with the experimental scatter band as well as the results of the elasto-plastic analysis. The Weibull parameters m and σ_u used in the calculation of probability of cleavage fracture in this 3D analysis have been taken as 38 and 2003 MPa respectively. It can be observed that the 3D numerical simulation predict the experimental scatter very well for the whole transition temperature region using a single set of temperature independent Weibull parameters and the results are better when compared to 2D plane strain results [Fig. 5.6]. Master curves corresponding to 5% and 95% failure probabilities are also presented in Fig. 5.16 and it can be observed that the numerical simulations results compare very well with those of master curve predictions (of the fracture toughness scatter band of the specimen) over the whole transition temperature region. It may be noted that though the actual CT specimen (used in the experiments) were side-grooved, we do not model the side-groove in this analysis. Hence, the predicted results may further improve by modeling the side groove as well as the use of a fine mesh in all the directions ahead of the crack tip of the CT specimen.

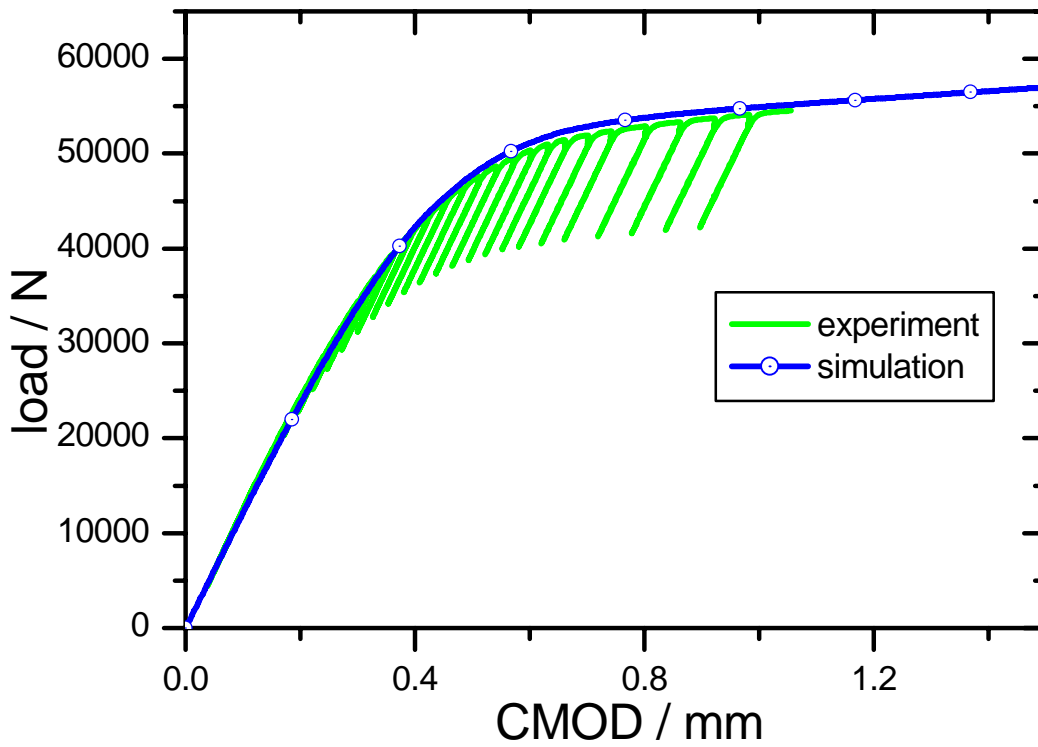


Fig. 5.13: Load-CMOD curve of the 1T CT specimen at -20 deg. C (3D analysis)

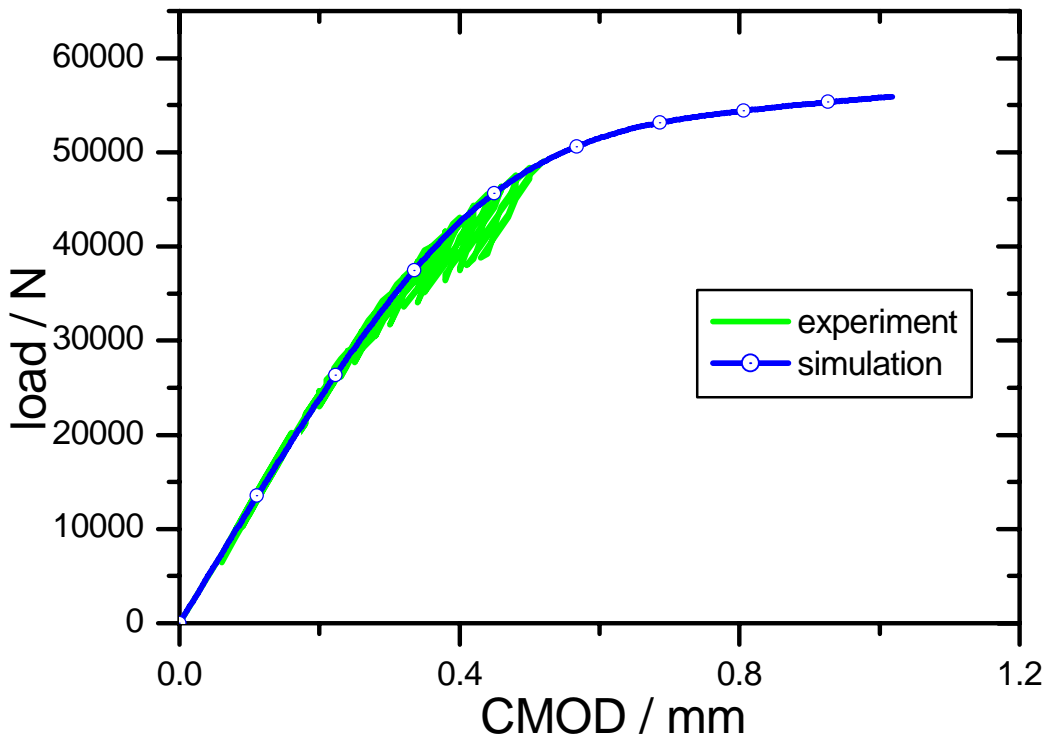


Fig. 5.14: Load-CMOD curve of the 1T CT specimen at -60 deg. C (3D analysis)

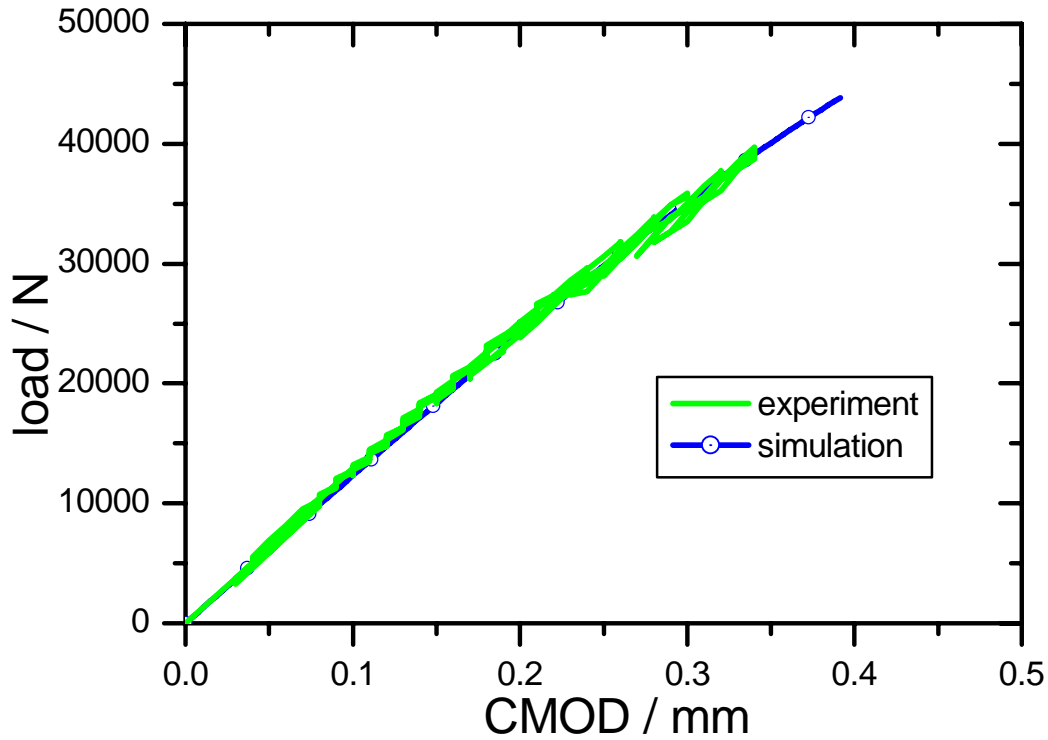


Fig. 5.15: Load-CMOD curve of the 1T CT specimen at -100 deg. C (3D analysis)

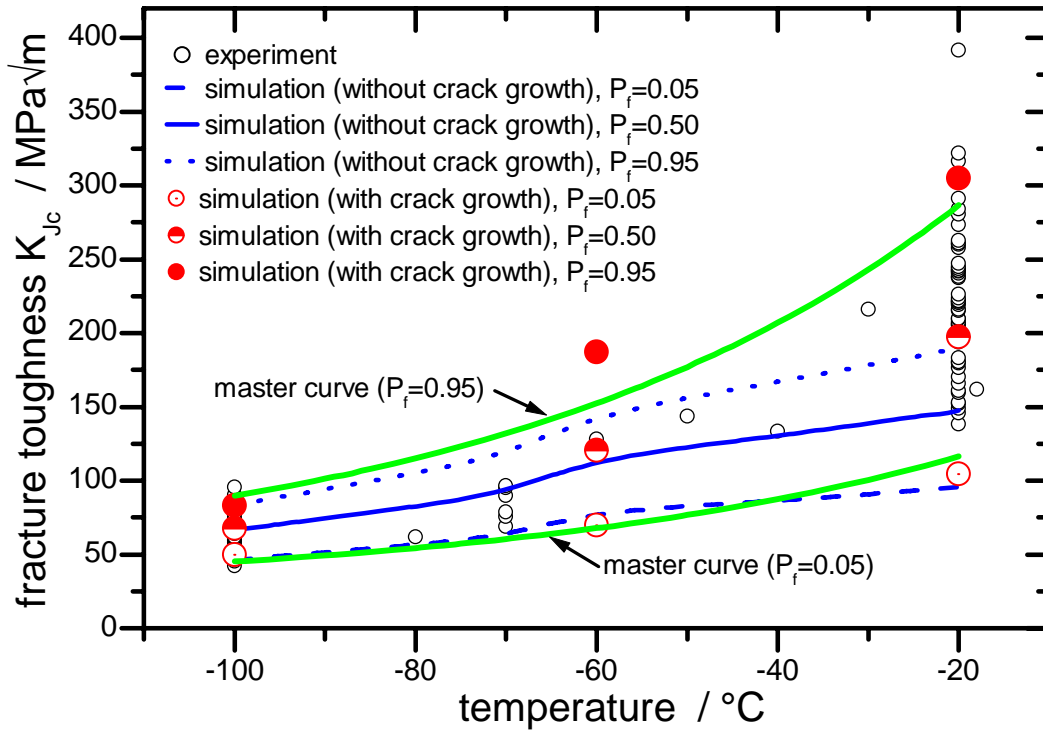


Fig. 5.16: Comparison of simulated (nonlocal damage) scatter of fracture toughness with experiment in the transition temperature region [3D analysis of 1T CT]

5.3 Prediction of probability of cleavage fracture in the transition regime using SEB specimens (3D analysis)

Having used the 1T compact tension specimen for simulation of the ductile to brittle transition curve (fracture toughness vs temperature), we proceed to investigate the effect of specimen geometry and size on the variation of ductile to brittle transition curve of the material. In this section, the standard single edge notched bend (SEB) specimen with initial crack size to width ratio $a_0/W = 0.522$ is used for simulation of the transition curve for fracture toughness. 3D analysis was used with the FE mesh shown in Fig. 5.17(a-b). The size of the elements ahead of the crack tip used here is the same as that used for the CT specimen simulation (i.e., 0.05mm x 0.05 mm x 1mm) and one-fourth of the specimen is simulated taking the symmetry into account.

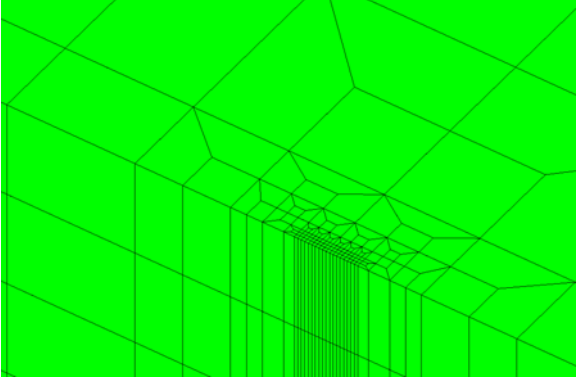
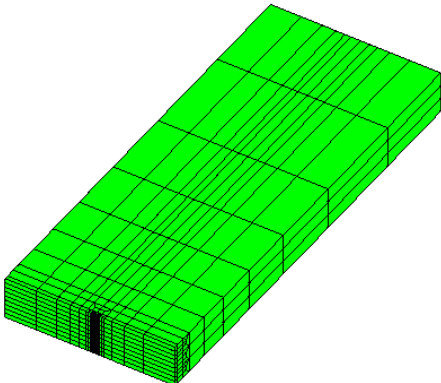


Fig. 5.17(a): 3D FE mesh of the 1T SEB specimen Fig. 5.17(b): Enlarged view of Fig. 5.17(a) near crack tip

Figs. 5.18-19 show the predicted load-CMOD results of the SEB specimen at -20 and -100 deg. C respectively and their comparison with respect to experimental response. It can be observed that the predicted load-CMOD results match very well with those of experiment. Fig. 5.20 shows the variation of predicted fracture toughness of the SEB specimen with respect to temperature corresponding to 5% (open diamond), 50% (semi-open diamond) and 95% (closed diamond) probabilities of cleavage fracture. The experimental points are also plotted as open dots at various temperatures. It can be observed that numerical simulation results are able to successfully predict the observed experimental scatter for the whole transition temperature region of the material.

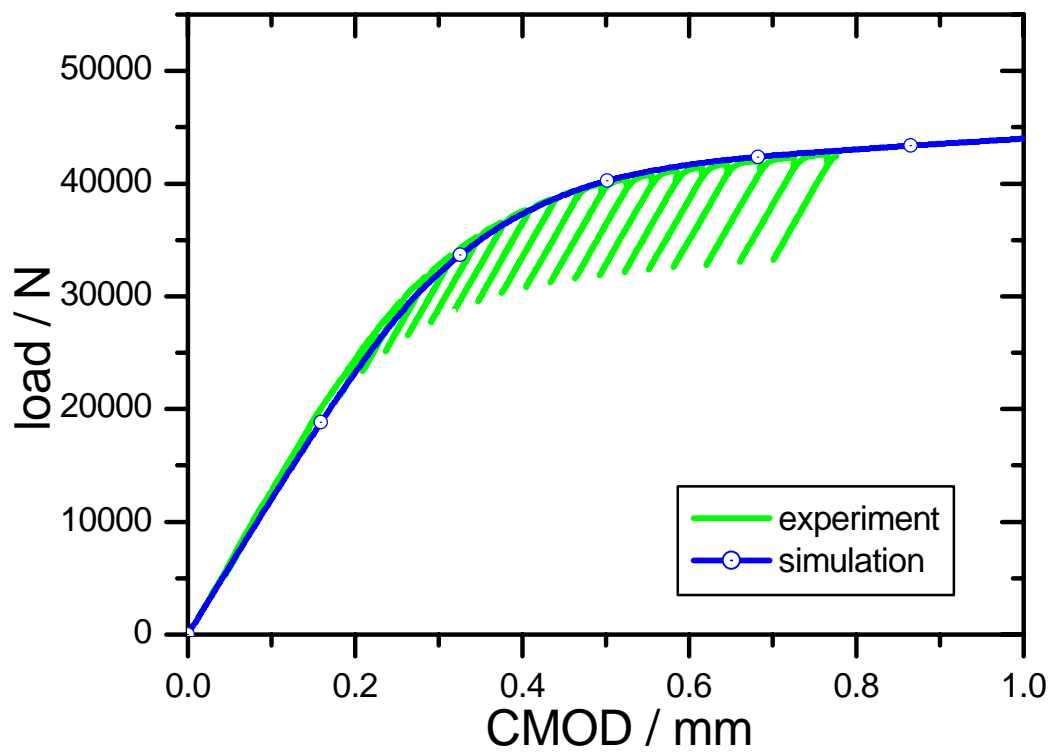


Fig. 5.18: Load-CMOD curve of the 1T SEB specimen at -20 deg. C (3D analysis)

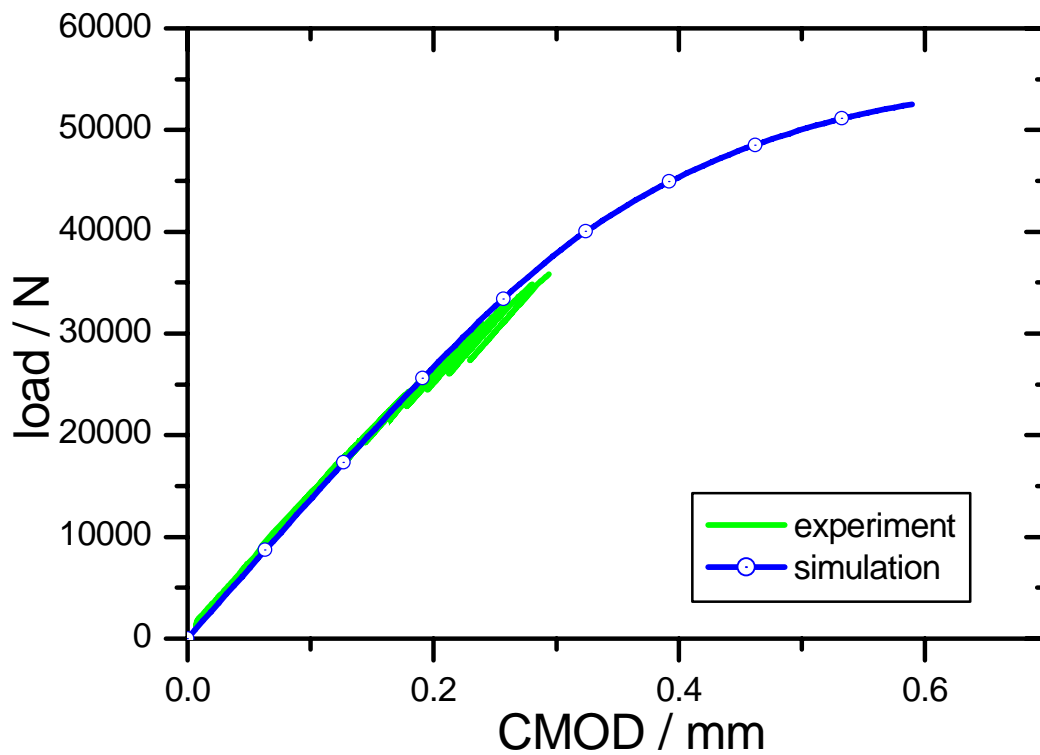


Fig. 5.19: Load-CMOD curve of the 1T SEB specimen at -100 deg. C (3D analysis)

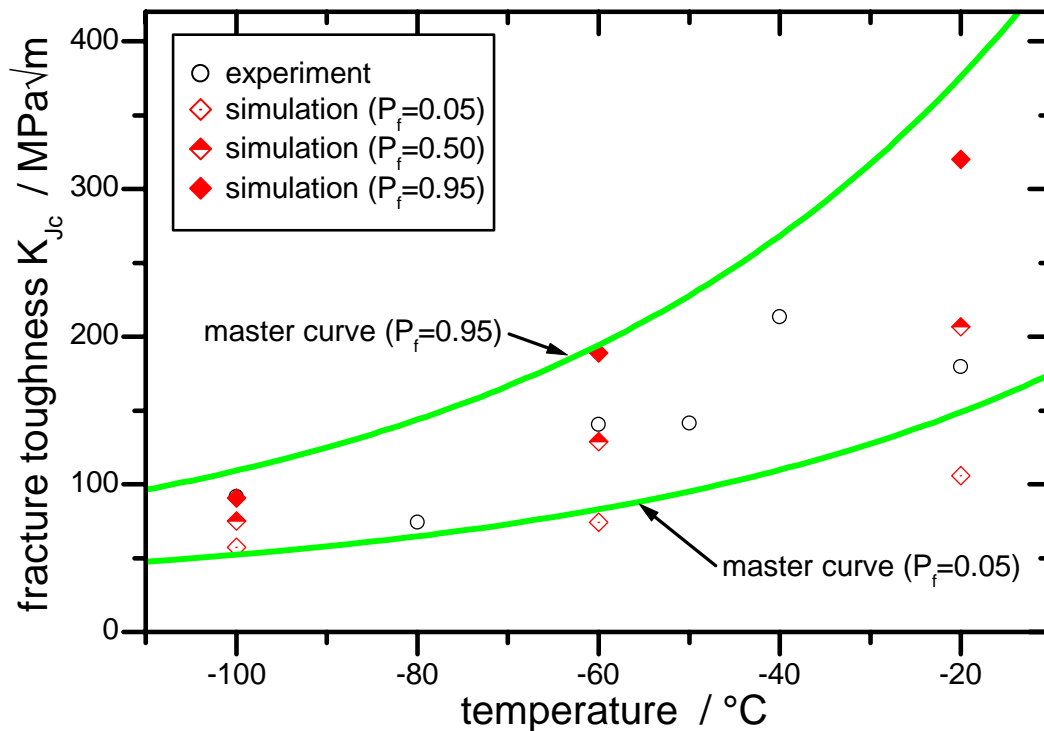


Fig. 5.20: Comparison of simulated (nonlocal damage) scatter of fracture toughness with experiment in the transition temperature region [3D analysis of 1T SEB]

Master curves corresponding to 5% and 95% failure probabilities are also presented in Fig. 5.20 and it can be observed that the numerical simulations results compare very well with those of master curve predictions (of the fracture toughness scatter band of the specimen) over the whole transition temperature region. Having demonstrated the ability of the combined nonlocal damage and Beremin's model to simulate fracture toughness variation with respect to temperature in the whole transition region using CT and SEB specimens, we investigate the ability of the above combined model to predict the effect of specimen size and geometry on the ductile to brittle fracture toughness transition curve.

5.4 Effect of specimen geometry on prediction of probability of cleavage fracture (CT vs SEB specimen)

In this section, the effect of specimen geometry on the fracture toughness vs temperature curve is studied. Fig. 5.21 shows the predicted fracture toughness values (corresponding to different failure probabilities P_f) vs temperature for both 1T CT and 1T SEB specimens (3D analysis). It can be observed that fracture toughness results for SEB specimen are slightly higher compared to CT specimen and the effect is more pronounced in the higher end of temperature.

This may be explained from the fact that the SEB is a low constraint geometry compared to CT because of dominant bending loading and hence the fracture toughness corresponding to different probabilities of cleavage fracture are little higher compared to CT specimen.

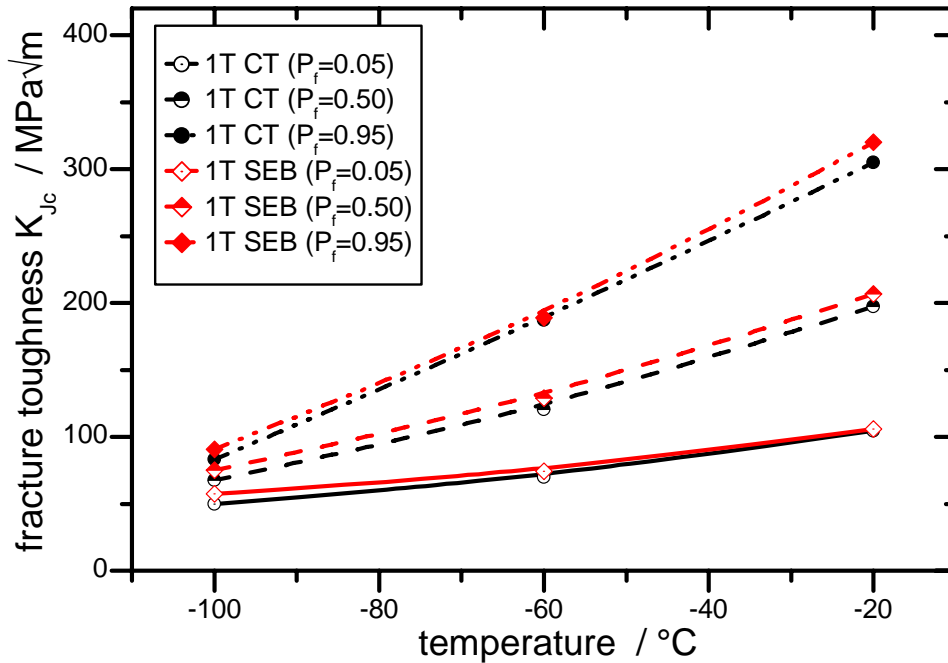


Fig. 5.21: Effect of specimen type on probability of cleavage fracture in the transition temperature region [1T CT vs 1T SEB]

5.5 Effect of crack depth on prediction of probability of cleavage fracture (deep vs shallow cracked SEB specimens)

In this section, the effect of initial crack depth on the fracture toughness vs temperature curve is studied. Two types of specimens (i.e., deep cracked SEB specimen with $a_0/W = 0.522$ and shallow cracked SEB specimen with $a_0/W = 0.13$) have been used in experiment and their 3D numerical simulations have been done using the combined nonlocal damage and Beremin's model. Fig. 5.22 shows the 3D FE mesh of the shallow cracked SEB specimen. The same mesh size and material parameters as discussed earlier for the deep cracked SEB specimen, are also used here.

Figs. 5.23-25 show the comparisons of predicted load-CMOD results of the shallow cracked SEB specimen with respect to experimental results at three different temperatures of -10, -60 and -100 deg. C respectively. It can be observed that the simulated results compare very well

with respect to those of experiment. Fig. 5.26 shows the predicted fracture toughness (corresponding to different failure probabilities P_f) vs temperature results for the shallow cracked SEB specimen. The experimental scatter is also plotted in Fig. 5.26 and the simulated fracture toughness variation (with respect to temperature) compares well with the experimental scatter. Master curves corresponding to 5% and 95% failure probabilities are also presented in Fig. 5.26 and it can be observed that the numerical simulations results compare very well with those of master curve predictions (of the fracture toughness scatter band of the specimen) over the whole transition temperature region. It may be noted that the η factor formula of Sreenivasan and Mannan et al. (2000) for the shallow cracked SEB specimen has been used here for calculation of J -integral which has been later converted to the fracture toughness parameter (K_{JC}).

Fig. 5.27 shows comparison of the predicted fracture toughness vs temperature curves (corresponding to different P_f) between deep and shallow cracked SEB specimens. It can be observed that the fracture toughness results for the shallow cracked SEB specimen are much higher compared to the deep cracked SEB specimen and this effect is more pronounced in the higher end of the temperature of the transition region. This is because of the fact that the shallow cracked SEB specimen has a low constraint field compared to the deep cracked specimen and hence the fracture toughness corresponding to different probabilities of cleavage fracture are higher for the shallow cracked specimen.

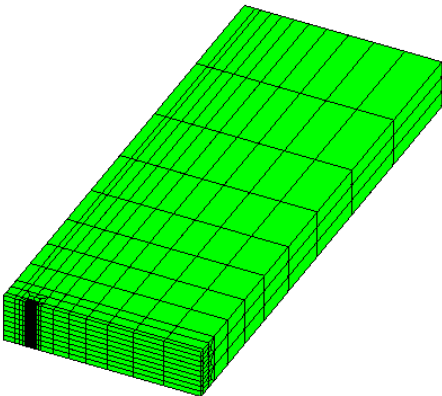


Fig. 5.22(a): 3D FE mesh of the 1T SEB (shallow cracked) specimen

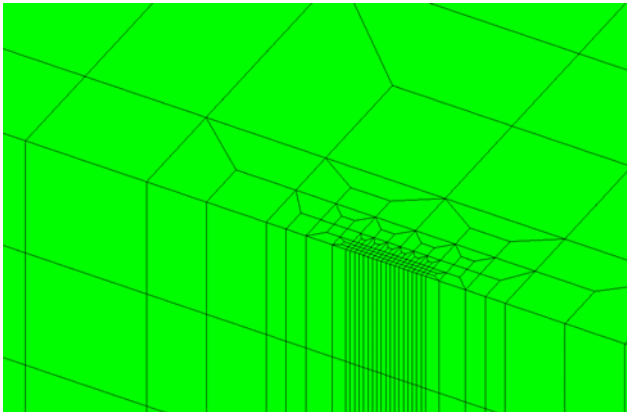


Fig. 5.22(b): Enlarged view of Fig. 5.22(a) near crack tip

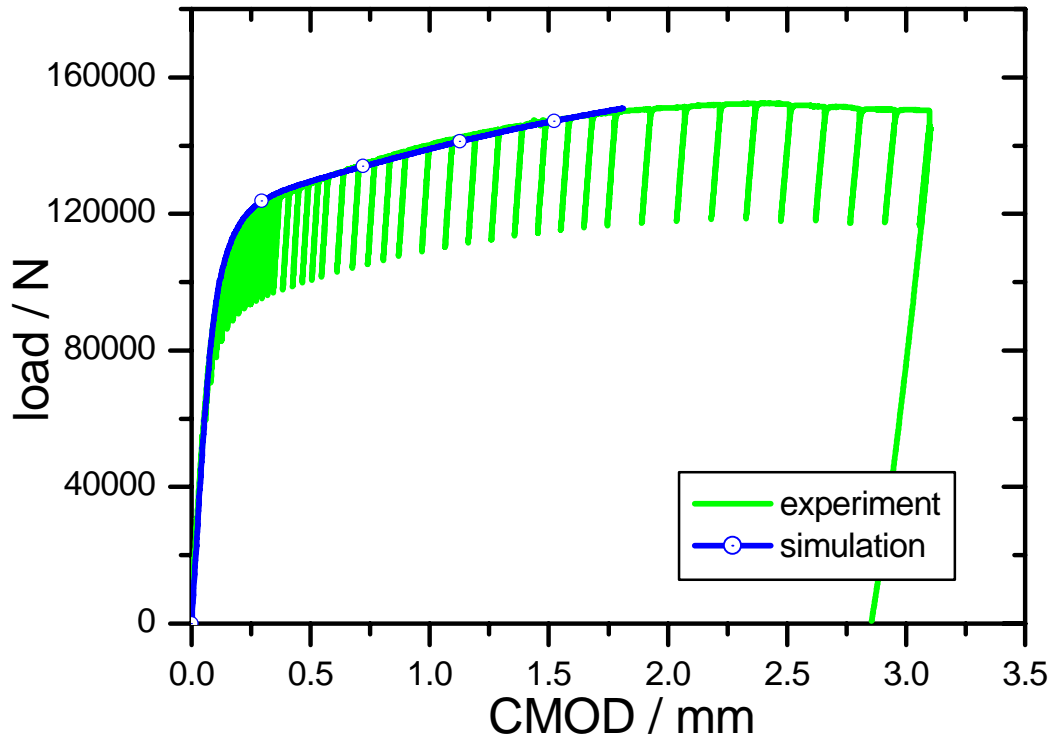


Fig. 5.23: Load-CMOD curve of the 1T SEB (shallow cracked) specimen at -10 deg. C (3D analysis)

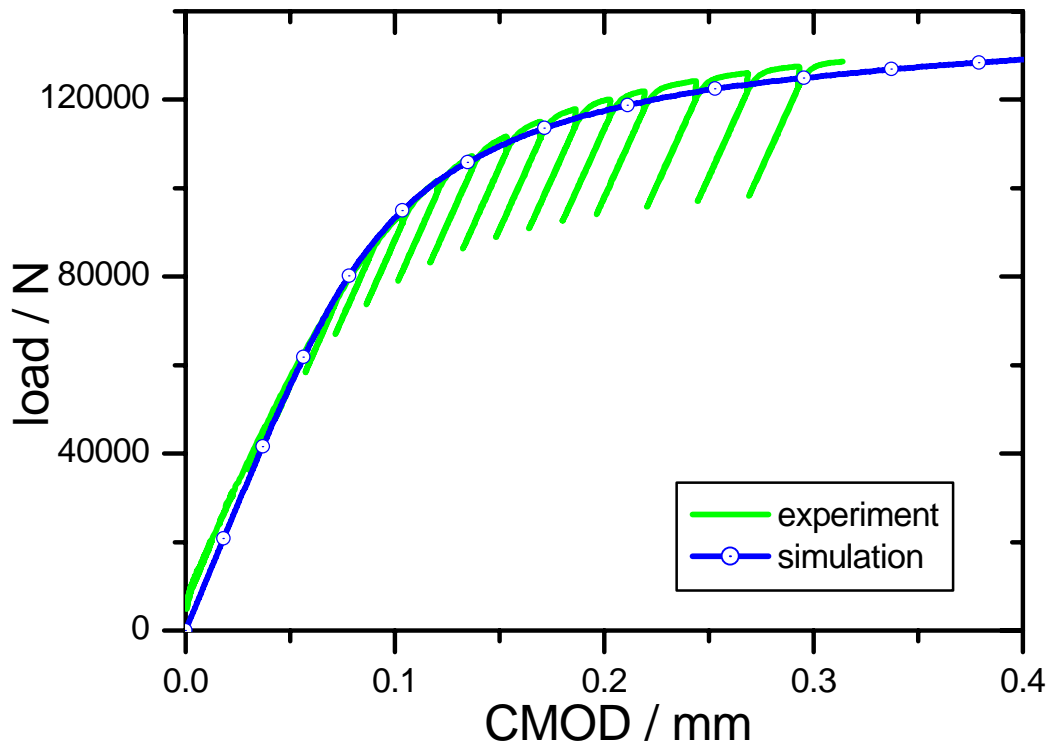


Fig. 5.24: Load-CMOD curve of the 1T SEB (shallow cracked) specimen at -60 deg. C (3D analysis)

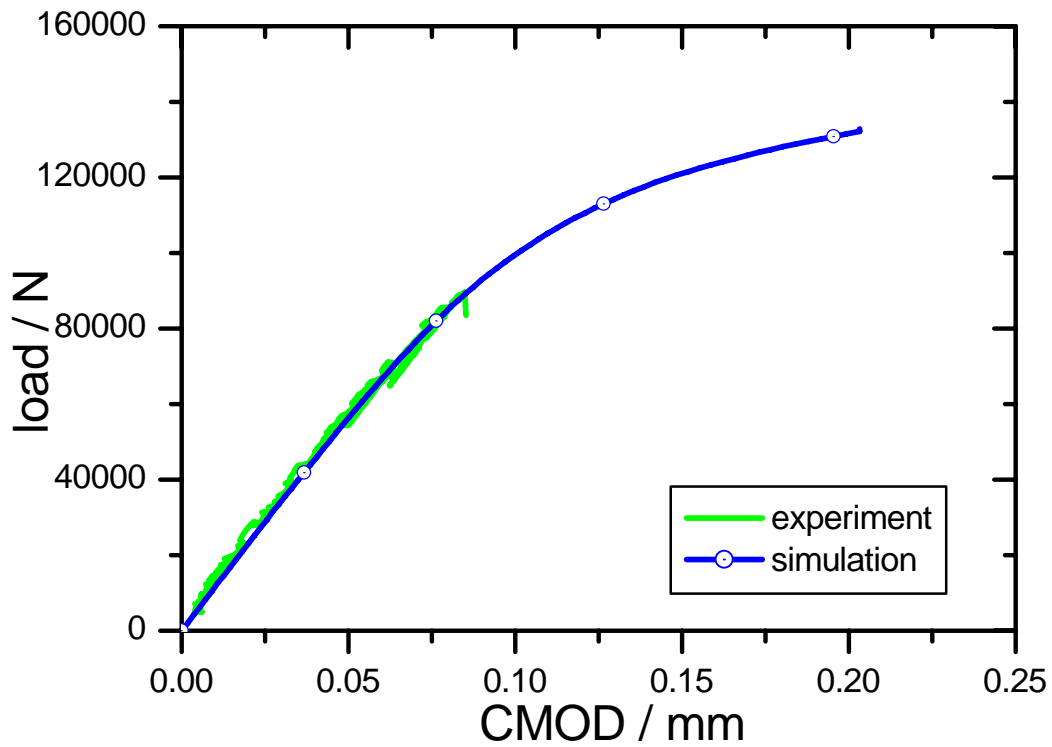


Fig. 5.25: Load-CMOD curve of the 1T SEB (shallow cracked) specimen at -100 deg. C (3D analysis)

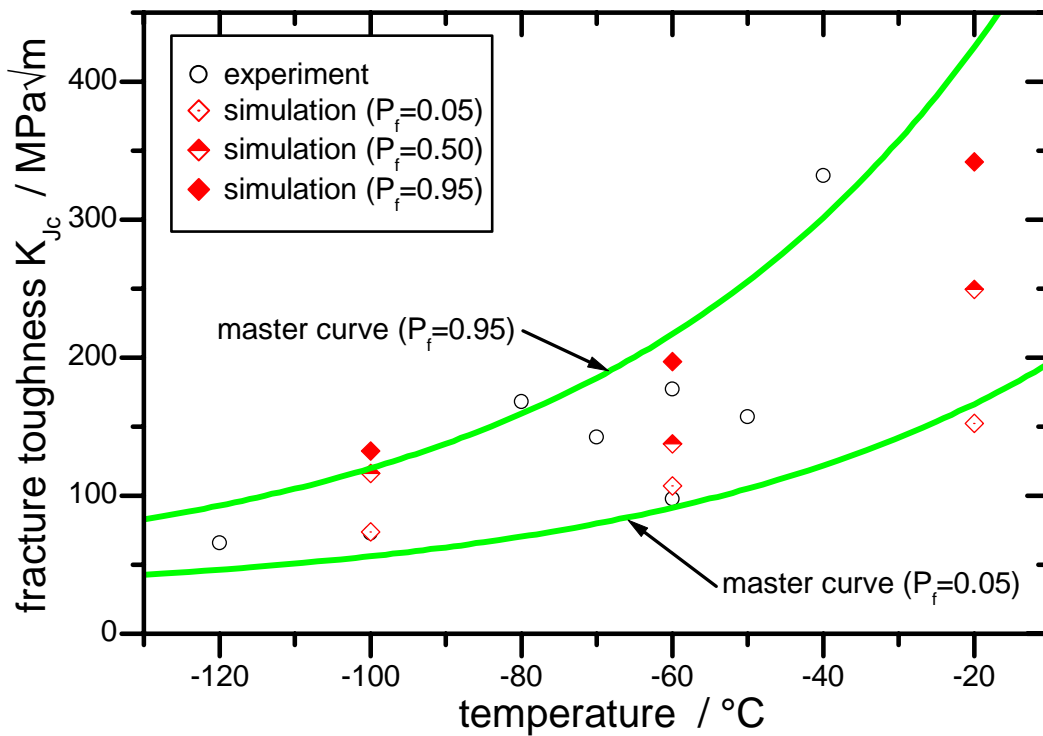


Fig. 5.26: Comparison of simulated (nonlocal damage) scatter of fracture toughness with experiment in the transition temperature region [3D analysis of 1T SEB (shallow crack)]

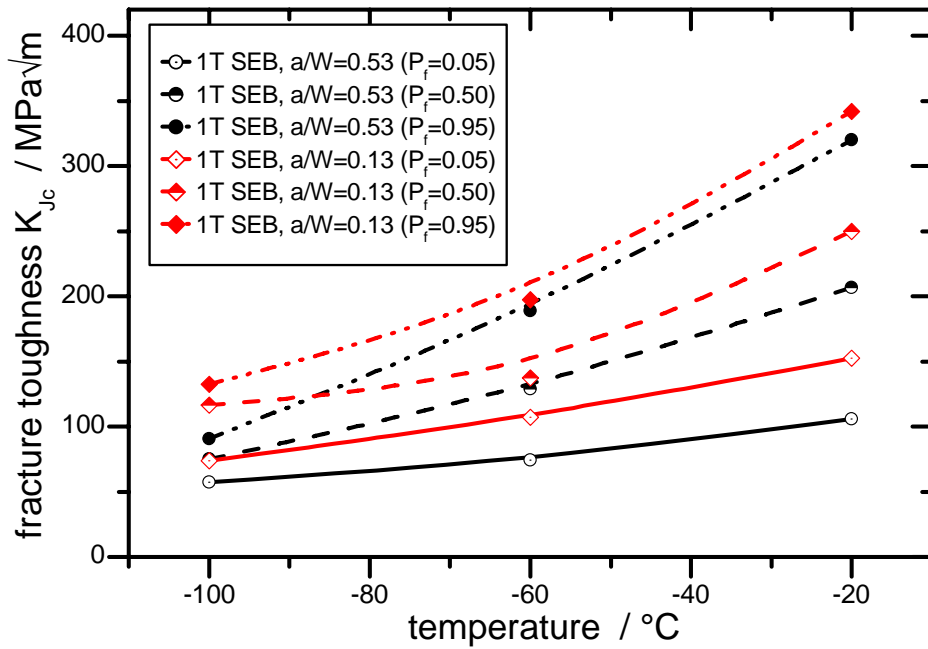


Fig. 5.27: Effect of crack depth on probability of cleavage fracture in the transition temperature region [1T SEB, deep vs shallow crack, 3D analysis]

5.6 Effect of specimen size on prediction of probability of cleavage fracture (1T, 2T and 4T CT specimens)

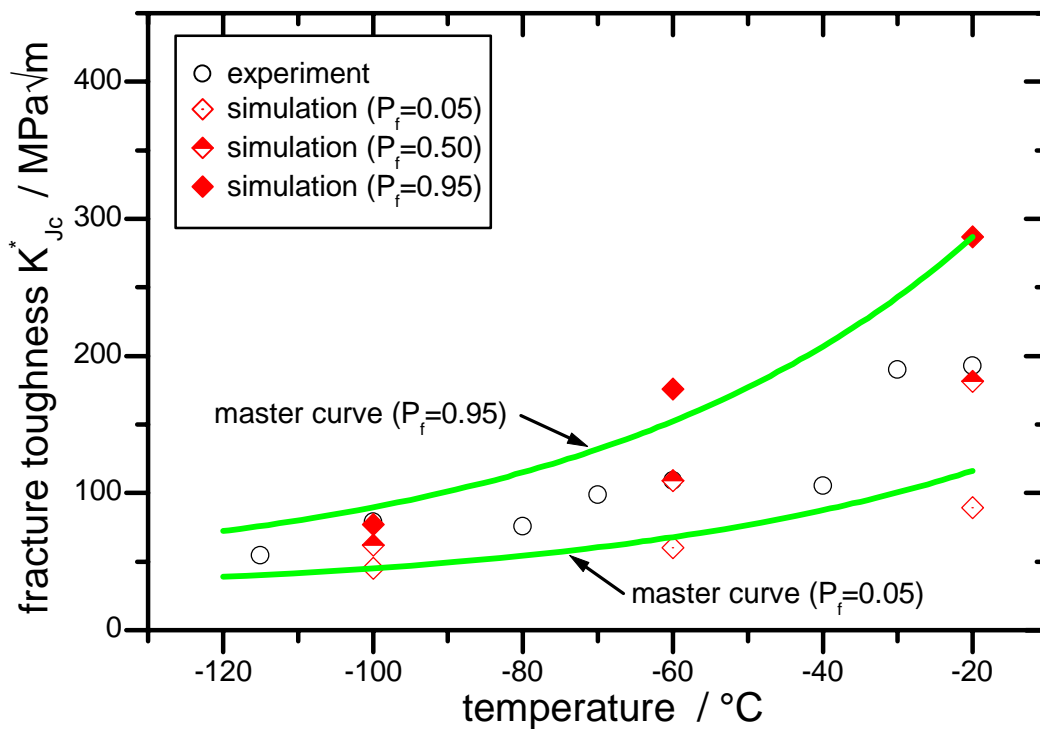


Fig. 5.28: Comparison of simulated (nonlocal damage) scatter of fracture toughness with experiment in the transition temperature region [3D analysis of 2T CT], * stands for the value of K_{Jc} which is not corrected for specimen size effect

In this section, the effect of specimen size on the fracture toughness vs temperature curve of the CT specimen is studied. For this purpose, three different CT specimens (1T, 2T and 4T as discussed in the fourth chapter) have been analyzed in the 3D domain. The results of 1T CT specimen are already presented in section 5.2. In this section, the comparison of simulated scatter in fracture toughness with respect to experiment for the 2T and 4T CT specimen is presented followed by the comparison among themselves.

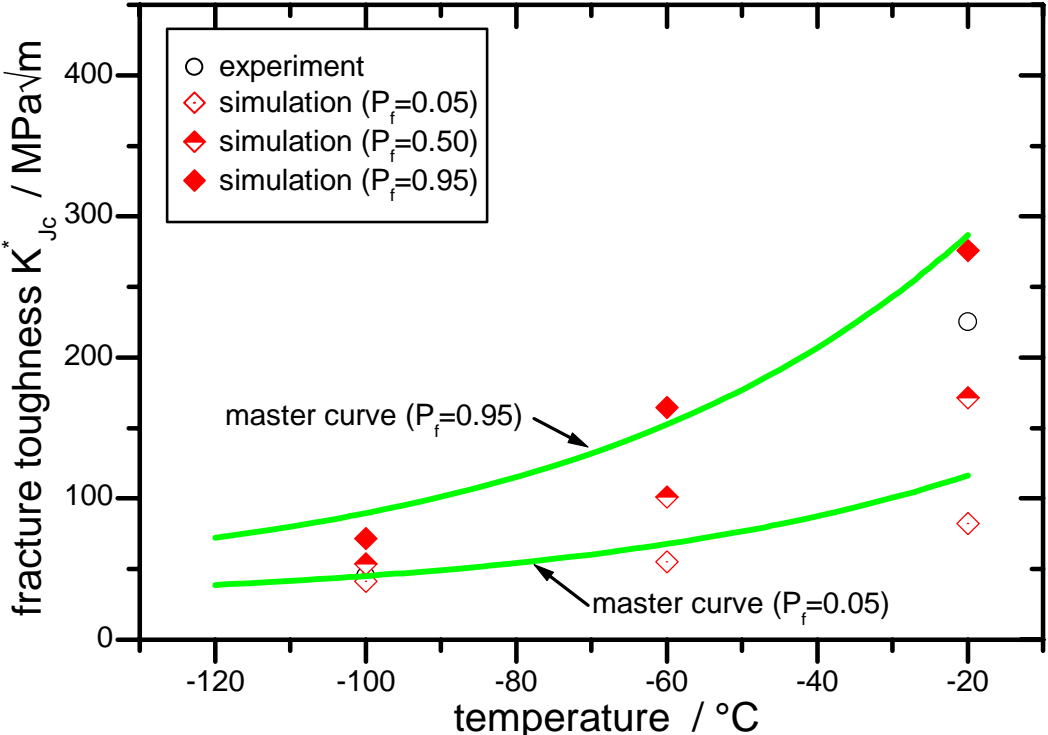


Fig. 5.29: Comparison of simulated (nonlocal damage) scatter of fracture toughness with experiment in the transition temperature region [3D analysis of 4T CT], * stands for the value of K_{JC} which is not corrected for specimen size effect

Fig. 5.28 and 5.29 compare the predicted fracture toughness (here the fracture toughness at instability has not been corrected for the specimen size and hence is denoted as K_{JC}^* instead of K_{JC} for the standard 1T CT fracture mechanics specimen) vs temperature curves (corresponding to different probabilities of failure P_f) for the 2T and 4T CT specimen respectively and it can be observed from the above figures that the predicted results are able to capture the experimental scatter satisfactorily. Master curves corresponding to 5% and 95% failure probabilities are also presented in Fig. 5.28 and 29 respectively for 2T CT and 4T CT specimens and it can be observed that the numerical simulations results compare very well with those of master curve predictions (of the fracture toughness scatter band of the specimen)

over the whole transition temperature region for both the specimens. Having compared the individual results of fracture toughness variation (with temperature for different probabilities of fracture) with experimental data, we proceed to study the effect of specimen size on the fracture toughness vs temperature curve (for different fracture probabilities) in the ductile to brittle transition temperature region.

Fig. 5.30 shows the predicted fracture toughness (corresponding to different failure probabilities P_f) vs temperature for 1T, 2T and 4T CT specimens respectively. It can be observed that fracture toughness results for the larger specimens are smaller compared to the smaller specimens over the whole transition temperature range. This may be explained from the fact that larger specimens have more constraint at the crack tip and hence they show the greater tendency towards cleavage fracture at the same value of applied stress intensity factor compared to smaller specimens.

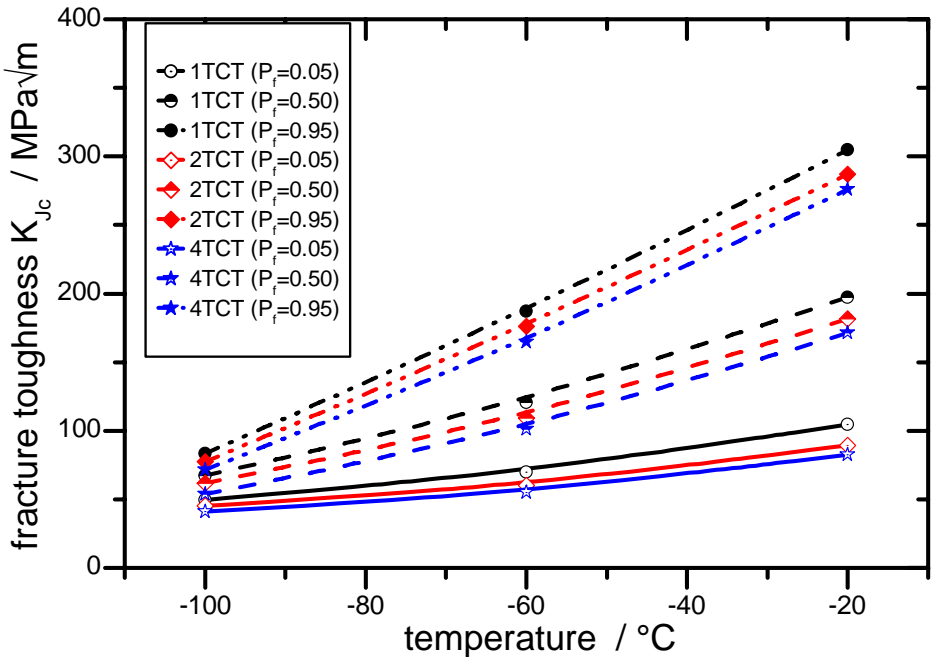


Fig. 5.30: Effect of specimen size on probability of cleavage fracture in the transition temperature region [1T vs 2T vs 4T CT, 3D analysis]

5.7 Effect of specimen thickness on prediction of probability of cleavage fracture (SEB specimens with different thicknesses)

In this section, the effect of specimen thickness on the fracture toughness vs temperature curve of the SEB specimen is studied. For this purpose, three different SEB specimens having

thickness values of 10, 25 and 50mm (common width of 50mm) have been analyzed in 3D domain. The results of standard 1T SEB specimen (25mm thickness) are already presented in section 5.3. In this section, the comparisons of simulated scatter in fracture toughness with respect to experiment for the SEB specimens with 10 and 50mm thickness are presented followed by the comparison among the same SEB specimens of different thickness values.

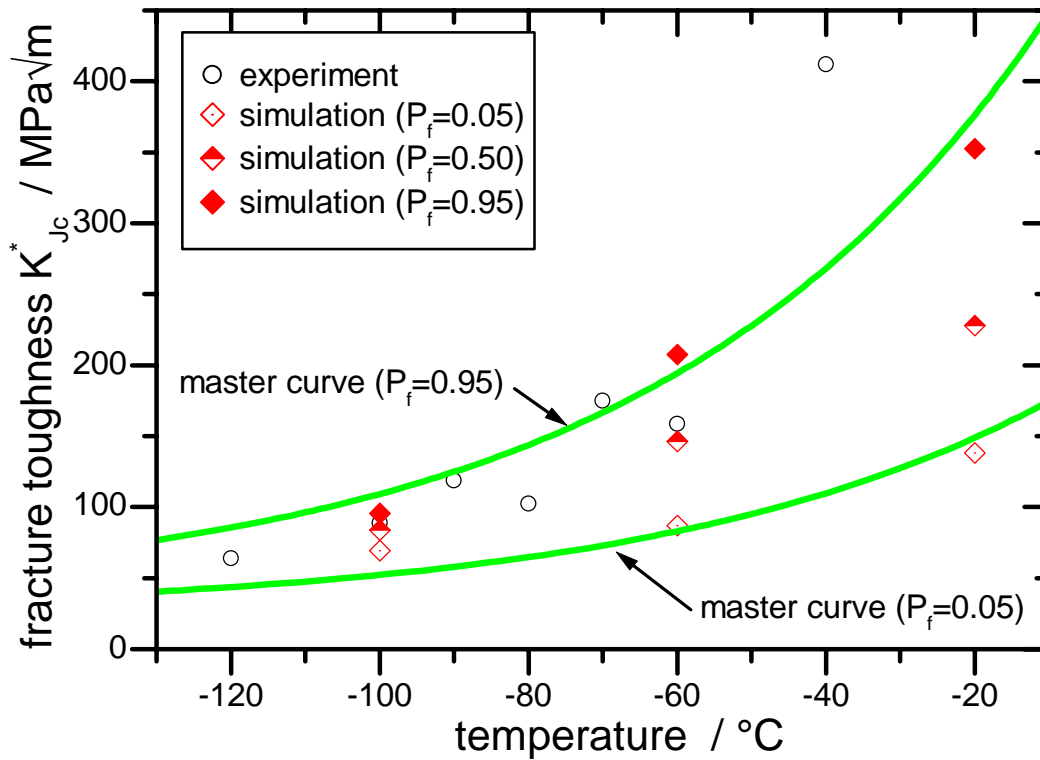


Fig. 5.31: Comparison of simulated (nonlocal damage) scatter of fracture toughness with experiment in the transition temperature region [3D analysis of SEB with 10mm thickness and 50mm width], * stands for the value of K_{Jc} which is not corrected for the specimen thickness

Fig. 5.31 and 5.32 compare the predicted fracture toughness (K_{Jc}^* represents fracture toughness at instability not corrected for specimen thickness) vs temperature curves (corresponding to different P_f) for the SEB specimens with 10 and 50mm thickness values respectively and it can be observed from the above figures that the predicted results are able to capture the experimental scatter satisfactorily. Master curves corresponding to 5% and 95% failure probabilities for both the SEB specimens are also presented in Fig. 5.31 and 5.32 respectively and it can be observed that the numerical simulations results compare very well with those of master curve predictions (of the fracture toughness scatter band of the specimen) over the whole transition temperature region for both the specimens. Having compared the individual results of fracture toughness variation with experimental data, we proceed to study

the effect of specimen thickness on the fracture toughness vs temperature curve in the transition region.

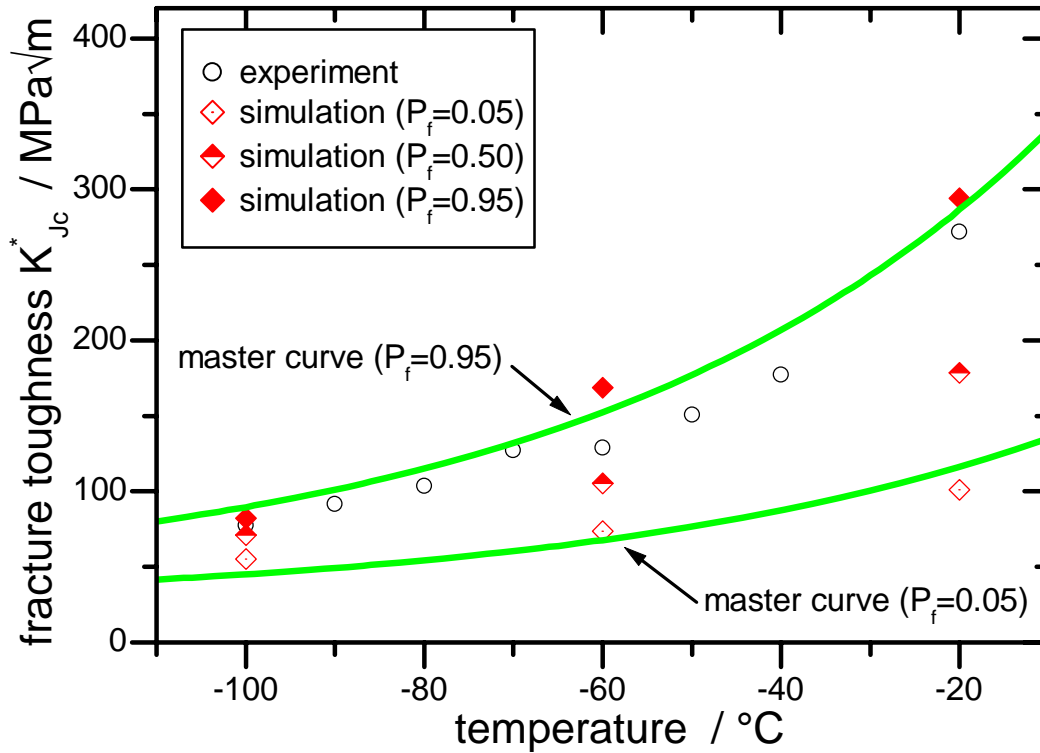


Fig. 5.32: Comparison of simulated (nonlocal damage) scatter of fracture toughness with experiment in the transition temperature region [3D analysis of SEB with 50mm thickness and 50mm width], * stands for the value of K_{JC} which is not corrected for the specimen thickness

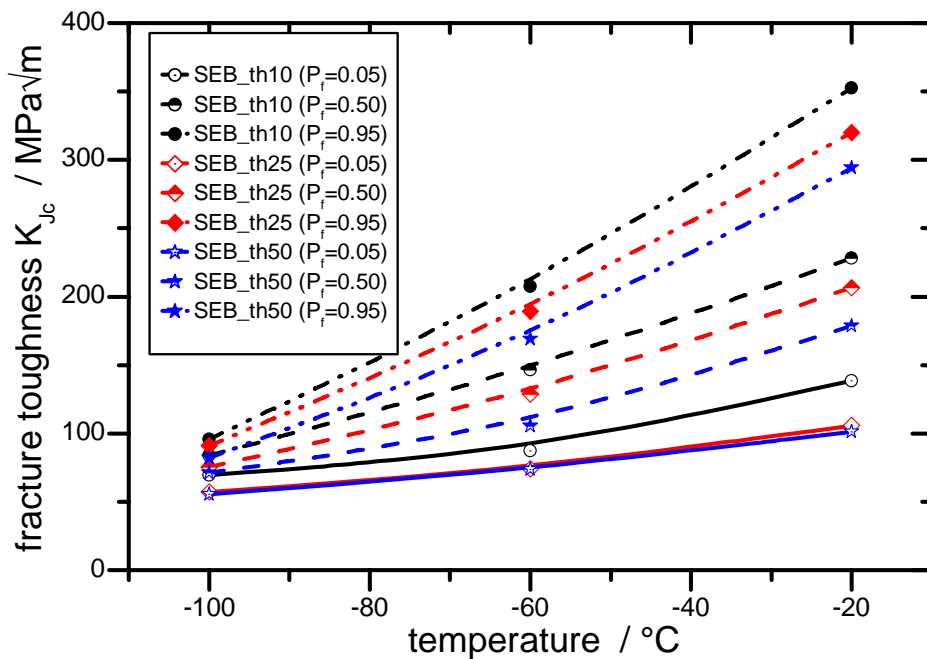


Fig. 5.33: Effect of specimen thickness on probability of cleavage fracture in the transition temperature region [SEB specimen with 10, 25 and 50mm thickness, 50mm width, 3D analysis]

Fig. 5.33 shows the predicted fracture toughness (corresponding to different failure probabilities P_f) vs temperature results for the three SEB specimens with same width, but of different thickness values. It can be observed that fracture toughness results for thicker specimens are smaller compared to thinner specimen over the whole temperature range. This may be explained from the fact that thicker specimens have more constraint at the crack tip (more plane strain condition) and hence they show the greater tendency towards cleavage fracture at same value of applied load compared to smaller specimens (plane strain region gets reduced because of free surfaces on both sides of the thickness which is small compared to other dimensions of the specimen). This effect is more pronounced towards higher end of the temperature scale in the ductile to brittle transition temperature region.

5.8 Effect of material stress-strain curve on prediction of probability of cleavage fracture

In this section, the effect of error in the extrapolated region of the material stress-strain curve on the fracture toughness vs temperature curve of the 1T CT specimen is studied. As discussed in section 4.15, we can have relative uncertainty during extrapolation of the true stress-strain curve from the experimental data points, which exist upto the ultimate tensile stress (UTS). As being discussed earlier, this error in extrapolation has a limited effect on the prediction of the fracture resistance curve of a material in the upper shelf region. However, we know that the stress-strain distribution gets modified due to the ductile damage development and this may affect the calculation of Weibull stress significantly. The aim of this study is to investigate the effect of slight change in the material stress-strain curve on the probability of cleavage fracture prediction in the transition region. Again, we know that at the lower shelf region, the plastic strains are low and they hardly exceed the strain at UTS and hence they may not affect the Weibull stress calculation for these low temperatures where there is large tendency to cleavage fracture at fairly low value of applied stress intensity factor K_I . However, the same may not be true for the higher end of temperature in the transition region.

For this purpose, the material stress-strain curves were slightly modified for their extrapolation beyond UTS for all the three temperatures (i.e., -20, -60 and -100 deg. C). The modification was done in such a way that the modified and the original stress strain curves coincide with each other upto UTS. After UTS, the true stress values of the modified curve is 10% less than

the true stress of the original curve for the same value of true plastic strain. The modified stress-strain curves along with the original curves for the material 22NiMoCr3-7 at these temperatures are shown in Fig. 5.34.

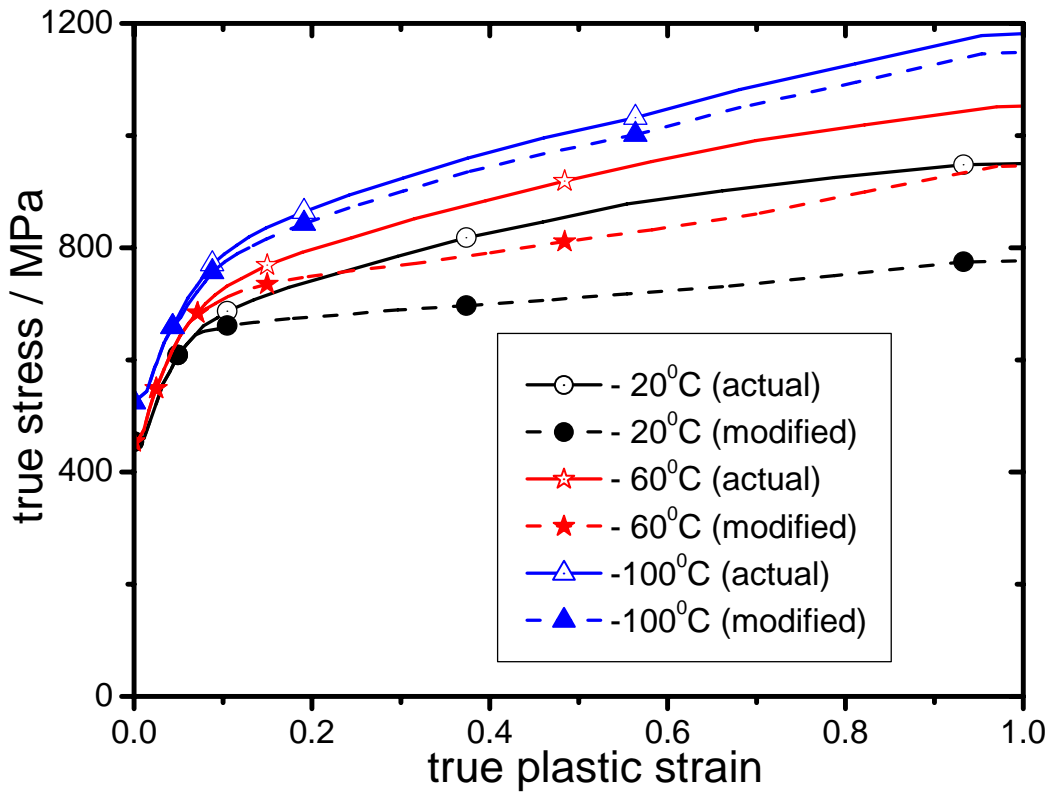


Fig. 5.34: Actual and modified true stress-strain curve of the material 22NiMoCr3-7 at three different temperatures in the transition region

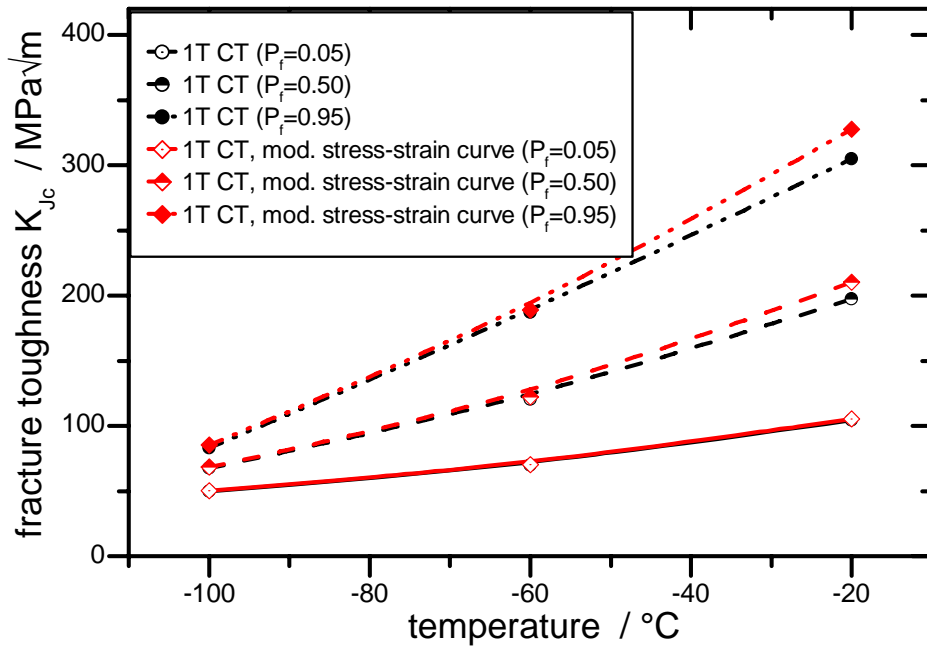


Fig. 5.35: Effect of material stress-strain curve on probability of cleavage fracture in the transition temperature region [1T CT with actual and modified stress-strain curve, 3D analysis]

Fig. 5.35 shows the predicted fracture toughness (corresponding to different failure probabilities P_f) vs temperature for the 1T CT specimen corresponding to the use of two different stress-strain curves (actual and modified). The fracture toughness results for both the stress-strain curves are almost same except those at -20 deg. C where the fracture toughness corresponding to 95% of probability of cleavage fracture shows a higher value for the analysis using modified stress-strain curve. It is because of the fact the modified stress-strain curve is slightly lower compared to the actual stress-strain curve especially for plastic strains beyond approximately 15%. Hence, the analysis using the modified stress-strain curve favours more plastic deformation and hence the probability of cleavage fracture reduces for the same value of applied fracture parameter K_I , compared to the analysis using the original stress-strain curve. This is not prominent in the lower temperatures of -100 and -60 deg. C because the extent of plastic deformation is less for these temperatures.

5.9 Effect of crack tip modelling on prediction of probability of cleavage fracture

In this section, the effect of crack tip mesh design on the fracture toughness vs temperature curve of the 1T CT specimen is studied using 2D plane strain formulation. In this analysis, we usually use the rectangular mesh near the crack tip for analysis of crack growth simulations as well as prediction of fracture probability in the transition region. The rectangular mesh near the crack tip of the CT specimen is shown in Fig. 5.36.

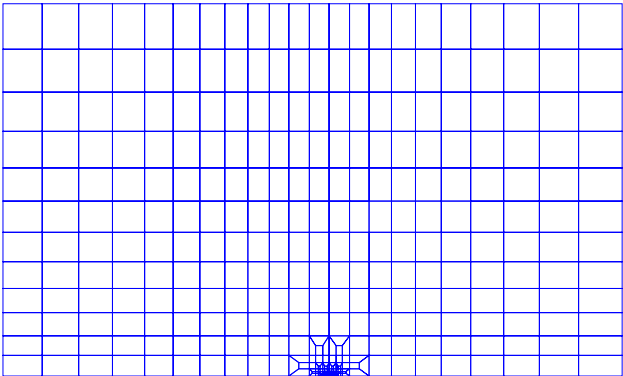


Fig. 5.36(a): Rectangular mesh near the crack tip for 1T CT specimen

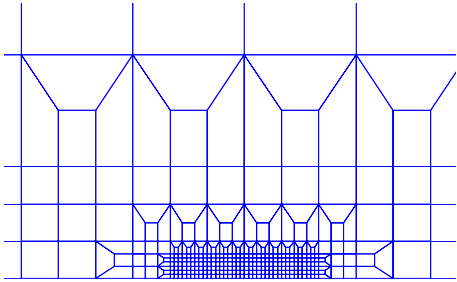


Fig. 5.36(b): Enlarged view of Fig. 5.36(a) near crack tip

In this crack tip modeling method, the crack is modeled by use of boundary conditions, i.e., by constraining some nodes along bottom line of the mesh (to prevent motion in vertical direction

only) and in this way, we can simulate an infinitely sharp crack. However, we know that cracks have always some finite tip radius and our effort here is to understand the effect of the crack tip radius on the fracture toughness variation (with respect to temperature) in the transition region. For this purpose, a spider mesh has been used for analysis as shown in Fig. 5.37 with a crack tip radius of 20 micron. The results of analysis of both the crack tip modeling methods have been compared here.

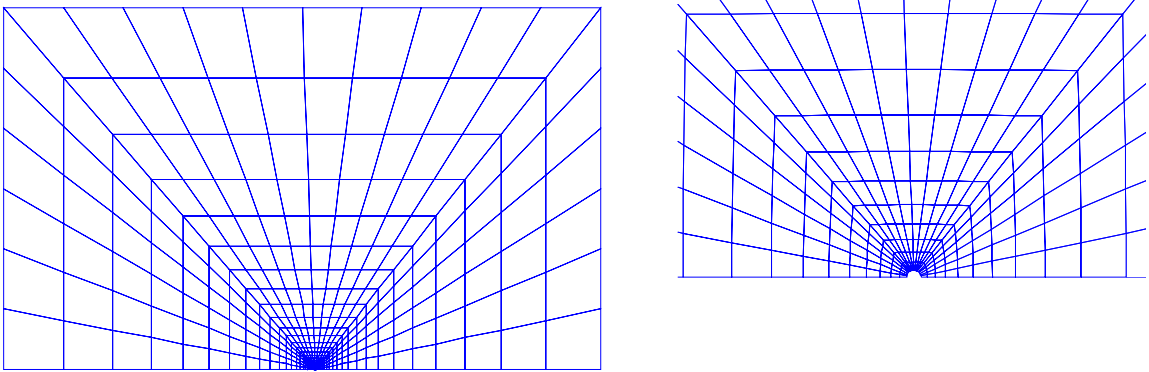


Fig. 5.37(a): Spider mesh near the crack tip for 1T CT specimen Fig. 5.37(b): Enlarged view of Fig. 5.37(a) near crack tip

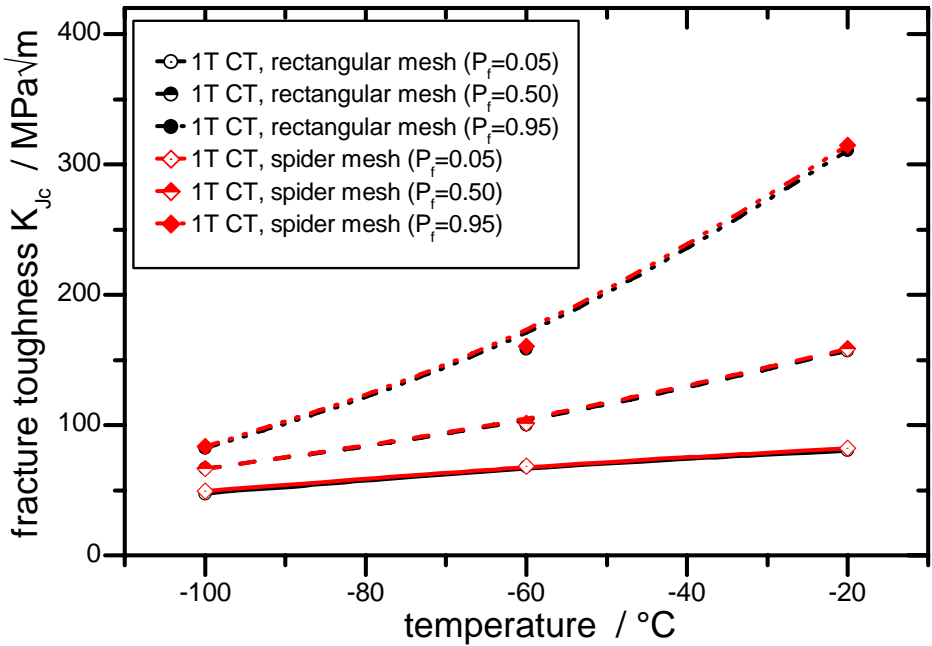


Fig. 5.38: Effect of crack tip modeling on probability of cleavage fracture in the transition temperature region [1T CT, 2D plane strain analysis]

Fig. 5.38 shows the predicted fracture toughness (corresponding to different failure probabilities P_f) vs temperature for the 1T CT specimen corresponding to the use of two different crack tip meshes (rectangular and spider). It can be observed that fracture toughness

results for both the mesh designs are almost same for the whole temperature regime (a little higher value of fracture toughness for the spider mesh compared to the rectangular mesh). It may also be noted that 2D plane strain analysis has been used here, as modeling the crack tip radius in 3D is more complicated and time consuming.

5.10 Effect of characteristics length on prediction of probability of cleavage fracture

In this section, the effect of characteristics length (of the nonlocal Rousellier’s model) on the fracture toughness vs temperature curve of the 1T CT specimen is studied. As discussed in section 4.16, the value of characteristics length parameter C_{length} of the nonlocal model is a constant for a material and is determined by comparing the simulated J -resistance curve of a fracture mechanics specimen with that of experiment. We have used the value of C_{length} as 0.05 for all the analyses. The purpose of this section is to study the effect of C_{length} on fracture toughness vs temperature curve and hence two different values of C_{length} (i.e., 0.05 and 1.0e-5) have been used here for comparison.

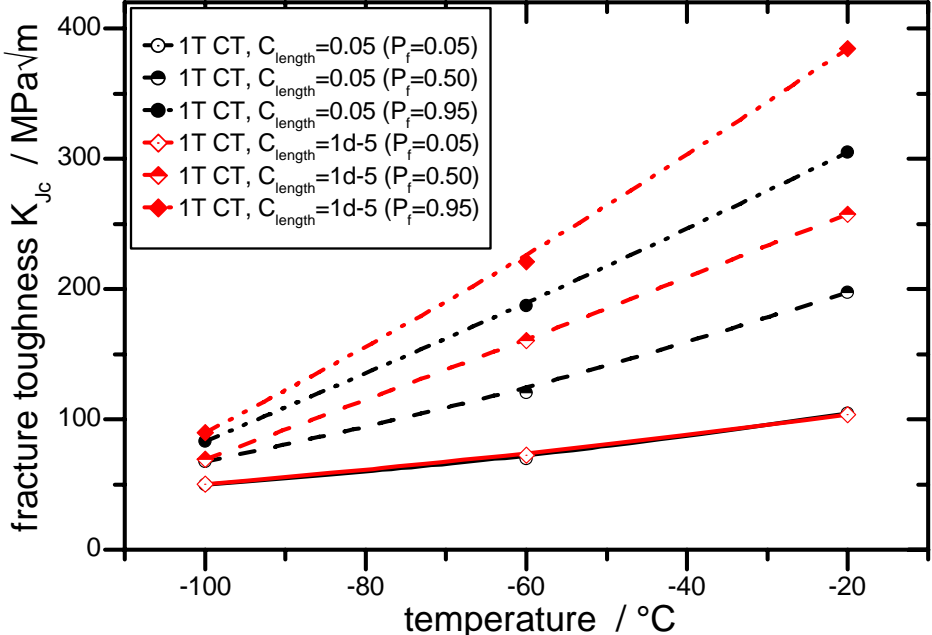


Fig. 5.39: Effect of characteristics length on probability of cleavage fracture in the transition temperature region [1T CT, 3D analysis]

Fig. 5.39 shows the predicted fracture toughness (corresponding to different failure probabilities P_f) vs temperature for the 1T CT specimen corresponding to the use of two

different values of C_{length} . It can be observed that the fracture toughness results for the analysis using C_{length} as $1.0e-5$ shows higher values for same probabilities of cleavage fracture compared to the analysis where C_{length} value of 0.05 is used. The reason for the above differences can be explained from the fact that with lower values of C_{length} , the damage zone gets localized and hence the stress-strain distributions are modified in such a way that the Weibull stress gets reduced for the same value of applied load and hence less probability of cleavage fracture for the same value of applied K_I . Hence, it may be concluded that the use of correct value of C_{length} is required for accurate predictions of probability of cleavage fracture in the transition region of the material.

In this chapter, simulations were carried out using combined nonlocal form of Rousselier's model and the Beremin's model to simulate the ductile to brittle transition curve of the material. It was observed that due to mesh independent nature of the nonlocal solutions, very small mesh sizes could be used ahead of crack tip and we were able to model small amounts of stable crack growth before the specimen fails by cleavage fracture process, which was not possible in case of local models. For this reason, the cleavage fracture probabilities in the transition region could be simulated well using a single set of Weibull parameter, which are temperature independent. Later, the effects of specimen size and geometry on the ductile to brittle transition curve were also successfully predicted. Hence, it is demonstrated that nonlocal models are very useful not only for mesh independent results in the upper shelf, but also for predicting the cleavage fracture probabilities in the transition temperature region of the material.

Chapter 6

Conclusions, recommendations and scope of future research

It is known that local damage mechanics models depend upon the use of a particular mesh size in order to predict the crack initiation and growth realistically in different specimens and hence the material parameters can be transferred to any component of the same material only if the same mesh size is used in the damage initiation and propagation zone. However, it loses the convergence property of the numerical solutions techniques (i.e., convergence of the solution with mesh refinement) because of loss of ellipticity of the governing PDEs. The purpose of the current research has been to develop a mesh independent form of the Rousselier's damage model by incorporating the characteristic length parameter into the material constitutive equation.

The above purpose has been achieved by deriving a characteristics diffusion type equation for the evolution of the nonlocal damage variable as a function of the local void volume fraction. The additional PDE has been solved along with the stress equilibrium equation of the mechanical continuum with the help of finite element discretisation. The nonlocal damage has been used as an additional degree of freedom in the FE model in addition to the three basic displacement degrees of freedom. The Neumann boundary condition has been used for the nonlocal damage degree of freedom.

The consistent tangent stiffness matrices for the coupled displacement-damage domain has been derived and implemented in a finite element program DEFINE. The above program has been used to predict the load-displacement response and fracture resistance behaviour of different kinds of specimens with different mesh sizes. The work has two broad aims, i.e., demonstration of mesh-independent nature of nonlocal solutions and predictions of ductile-to-brittle transition curve (by simulation of small amounts of crack growth realistically), which have been met with success.

6.1 Conclusions

The following broad conclusions can be drawn from the current work.

- The mesh dependency of local damage mechanics models has been removed by development of a new nonlocal formulation, which incorporates the material characteristic length parameter into the constitutive equations.
- The main feature of the new nonlocal model is that the nonlocal damage variable is used as an extra DOF in the finite element model. The evolution of nonlocal damage variable is related to the local void volume fraction through a diffusion equation. Hence, the governing partial differential equation of equilibrium of the mechanical continuum is solved alongwith the damage diffusion equation with the necessary boundary conditions.
- The new formulation has been used for numerical simulation of shear band development in a flat tensile specimen and the width of shear band is demonstrated to be independent of FE mesh size.
- In case of numerical simulation of a flat tensile specimen (with hole at the center), the normalised stress vs percentage of hole opening curve is demonstrated to be independent of mesh size. The size effect (larger specimens having lesser ductility and vice versa) is also successfully predicted.
- In case of simulation of a standard fracture mechanics specimen (e.g., 1T Compact tension specimen), the load-CMOD and J-R curves are demonstrated to be mesh independent. The ductile to brittle transition curve (for fracture toughness) is also better predicted over the transition regime with prediction of small amounts of stable (ductile) crack growth before final fracture by cleavage.
- The ductile to brittle transition curve (for fracture toughness) is also better predicted over the transition regime with prediction of small amounts of stable (ductile) crack growth before final fracture by cleavage.
- For the 1T Single edge bend (SEB) specimen, the load-CMOD and J-R curves are demonstrated to be mesh independent. The ductile to brittle transition curve (for fracture toughness) is also better predicted over the transition regime with prediction of small amounts of ductile crack growth.
- Geometry and size effect (effect of specimen type, crack depth, thickness and specimen size etc.) of the different fracture mechanics specimens on the J-resistance curve are satisfactorily modeled.

- The problem with symmetric boundary conditions could be modeled accurately by the nonlocal model whereas the local model shows different results for the symmetric model and the full model (without use of symmetric boundary conditions). This is an important advantage of nonlocal simulation.
- Geometry and size effect of the specimens on the ductile to brittle fracture toughness transition curve are satisfactorily modeled.
- For FE mesh with very fine elements (of the order of 10 to 20 micron or less), the deformation is very high and this creates convergence problem for FE simulation of large amounts of crack growth. One needs to incorporate the hyper-elastic formulation based on the multiplicative decomposition of deformation gradient or Arbitrary Lagrangian Eulerian (ALE) methods in order to proceed further.
- For simulation of ductile to brittle transition curve for fracture toughness of the materials, 3D simulation results are better than those of 2D plane strain simulation, however these are computationally expensive.
- In this work, 3D simulation of probability of cleavage fracture of CT and SEB specimens has been carried out without modeling the side groove in the specimens (which can increase the number of degrees of freedom of the FE model significantly). However, it is expected that better prediction of the ductile to brittle transition curve for fracture toughness may be achieved with the use of FE mesh with side-groove for the fracture mechanics specimens.

6.2 Recommendations

Based on the above work, the following points can be recommended for successful simulation of load response and fracture behaviour of engineering components for their safe operation in the upper shelf, lower shelf and the transition regions of temperature.

- For simulation of crack growth in components with very high stress gradients, one needs to go for fine mesh in order to simulate the stress gradients satisfactorily. If there is need to predict the load response of the components considering material damage, then one cannot use the local damage mechanics models (which require a mesh size of a particular characteristics length which can be too coarse for the steep stress gradient) and hence one should resort to nonlocal models for such cases.

- The characteristics length parameter C_{length} for the material needs to be determined (by comparing simulated results with experimental fracture resistance curve of a standard fracture mechanics specimen) before one proceeds for nonlocal simulation of an actual component.
- If computational resource is available, it is advisable to model the component in 3D with fine mesh (in all direction) in the crack propagation zone. This is especially helpful to predict the probability of cleavage fracture in the transition region. If possible, one may use the adaptive mesh refinement techniques or the Arbitrary Lagrangian Eulerian (ALE) formulation.

6.3 Scope for future research

The work carried out in this thesis can be extended in several ways as described below.

- Incorporation of hyper-elastic based formulations in the FE model to simulate very large strain.
- Development of a damage mechanics model to simulate crack growth with cyclic loading, i.e., for low cycle fatigue crack growth simulations.
- Simulation of bimetallic welded joints for studying the effects of material properties on the path of crack propagation.
- Development of mesh free methods for simulations of ductile crack growth where one can use very high order interpolation functions (to take care of crack tip singularity) and less number of nodes in the domain so that crack growth in engineering components (dimensions of several meters) can be realistically simulated with available computational resource.

References

1. Aifantis, E. C., 1984. On the microstructural origin of certain inelastic models. *Transactions of ASME Journal of Engineering Materials and Technology* 106, pp. 326-330.
2. Aifantis, E. C., 1987. The physics of plastic deformation. *International Journal of Plasticity* 3(3), pp. 211-247.
3. Aifantis, E. C., 1992. On the role of gradients in the localization of deformation and fracture *International Journal of Engineering Science* 30(10), pp. 1279-1299.
4. Aifantis, E. C., 1999. Strain gradient interpretation of size effects. *International Journal of Fracture* 95(1), pp. 299-314.
5. Andersson, T., Stienstra, D. and Dodds, R.H., 1994. A theoretical framework for addressing fracture in the ductile-brittle transition region, *Fracture Mechanics: Twenty-Fourth Volume, ASTM STP 1207*, Ed. by J. D. Landes, D. E. McCabe and J. A. Boulet, American Society for Testing and Materials, West Conshohoken, Pa., pp. 186-214.
6. Aravas, N., 1987. On the numerical integration of a class of pressure-dependent plasticity models. *International Journal for Numerical Methods in Engineering* 24, pp. 395-416.
7. Askes, H., 2000. Advanced spatial discretisation strategies for localised failure: mesh adaptivity and meshless methods. Ph.D. thesis, Delft University of Technology, The Netherlands.
8. Barenblatt, G.I., 1962. The mathematical theory of equilibrium cracks in brittle fracture. *Advances in Applied Mechanics* 7, pp. 55-129.
9. Bathe, K.J., 1995. *Finite Element Procedures*. Englewood Cliffs, NJ, Prentice-Hall.
10. Bažant, Z.P., Belytschko, T. and Chang, T.P., 1984. Continuum theory for strain softening. *Transactions of ASCE Journal of Engineering Mechanics* 110, pp. 1666-1692.
11. Bažant, Z.P. and Pijaudier-Cabot, G., 1989. Measurement of characteristic length of nonlocal continuum. *Transactions of ASCE Journal of Engineering Mechanics* 115, pp. 755-767.
12. Bažant, Z.P., 1991. Why continuum damage mechanics is nonlocal: micromechanics arguments. *Transactions of ASCE Journal of Engineering Mechanics* 117, pp. 1070-1087.
13. Beremin, F.M., 1983. A local criterion for cleavage fracture of a nuclear pressure vessel steel. *Metallurgical Transactions A*, 14A, pp. 2277-2287.

14. Betegon, C. and Hancock, J.W., 1991. Two-parameter characterization of elastic-plastic stress fields. *Transactions of ASME Journal of Applied Mechanics* 58, pp. 104-110.
15. Bilby, B. A., Howard, I. C., and Li, Z. H., 1993. Prediction of the first spinning cylinder test using ductile damage theory. *Fatigue and Fracture of Engineering Materials and Structures* 16, pp. 1-20.
16. Brekelmans, W.A.M., Schreurs, P.J.G. and de Vree, J.H.P., 1992. Continuum damage mechanics for softening of brittle materials. *Acta Mechanica* 93, pp. 33-143.
17. Brekelmans, W.A.M. and de Vree, J.H.P., 1995. Reduction of mesh sensitivity in continuum damage mechanics. *Acta Mechanica* 110, pp. 49-56.
18. Brocks, W., Klingbeil, D., Kunecke, G. and Sun, D.Z., 1995. Application of the Gurson model to ductile tearing resistance. *Constraint Effects in Fracture: Theory and applications: second volume, ASTM STP 1244*, Ed. by M. Kirk and A. Bakker, American Society for Testing and Materials, West Conshohoken, pp. 232-252.
19. Carmeliet, J., 1996. Gradient damage and size effects. *Proceedings of Engineering Mechanics, ASCE, New York*, pp. 1175-1178.
20. Chu, C.C. and Needleman, A., 1980. Void nucleation effects in biaxially stretched sheets. *Transactions of ASME Journal of Engineering Materials and Technology*, 102, pp. 249-256.
21. Clausmeyer, H., Kussmaul, K., Roos, E., 1991. Influence of stress state on the failure behaviour of cracked components made of steel. *Transactions of ASME Journal of Applied Mechanics* 44, pp. 77-92.
22. Coleman, B.D. and Hodgdon, M.L., 1985. On shear bands in ductile materials. *Archives of Rational Mechanics and Analysis* 90, pp. 219-247.
23. Curry, D.A. and Knott, J.F., 1978. Effect of microstructure on cleavage fracture stress in steel. *Metal Science* 12, pp. 511-514.
24. Curry, D.A. and Knott, J.F., 1979. Effect of microstructure on cleavage fracture toughness of quenched and tempered steels. *Metal Science* 13, pp. 341-345.
25. de Borst, R. and Mühlhaus, H.-B., 1992. Gradient-dependent plasticity: formulation and algorithmic aspects. *International Journal for Numerical Methods in Engineering* 35, pp. 521-539.
26. de Borst, R., Sluys, L.J., Mühlhaus, H.-B. and Pamin, J., 1993. Fundamental issues in finite element analysis of localization of deformation. *Engineering Computation* 10, pp. 99-121.

27. de Vree, J.H.P., Brekelmans, W.A.M. and van Gils, M.A.J., 1995. Comparison of nonlocal approaches in continuum damage mechanics. *Computers and Structures* 55, pp. 581-588.
28. Diem, H., Blind, D., Roos, E., Wachter, O., Tolksdorf, E., 1994. Failure behaviour of thick-walled, austenitic pipe bends under cyclic bending loading at constant internal pressure. *Nuclear Engineering and Design* 151, pp. 269-289.
29. Dlouhý, I., and Chlup, Z., 2000. Micromechanical aspects of constraint effects in steel for containers of spent nuclear fuel. *Proceedings of the ECF 13, San Sebastian*.
30. Dlouhý, I., Chlup, Z., and Kozák, V, 2004. Constraint effects at brittle fracture initiation in a cast ferritic steel. *Engineering Fracture Mechanics* 71, pp. 873–883.
31. Dugdale, D.S., 1960. Yielding of steel sheets containing slits. *Journal of the Mechanics and Physics of Solids* 8, pp. 100-108.
32. Eisele, U., Klein, M., Neubrech, G.E., and Roos, E., 1991. Thermal shock experiments on the HDR pressure vessel. *Nuclear Engineering and Design* 130, pp. 309-321.
33. Eisele U., and Roos, E., 1991. Evaluation of different fracture-mechanical J-integral initiation values with regard to their usability in the safety assessment of components. *Nuclear Engineering and Design* 130, pp. 237-247.
34. Eisele U. et al., 2006. Critical examination of the master curve approach regarding application in German nuclear power plants, Final Report, Reactor Safety Research - Project No. 1501 240, Materialprüfungsanstalt Universität Stuttgart, Germany.
35. Eterovic, A.L. and Bathe, K.J., 1990. A hyperelastic-based large strain elasto-plastic constitutive formulation with combined isotropic-kinematic hardening using the logarithmic stress and strain measures. *International Journal for Numerical Methods in Engineering* 30, pp.1099-1114.
36. Faleskog, J., Zaremba, K., Nilsson, F., and Öberg, H., 1991. An investigation of two-and three-dimensional elasto-plastic crack growth initiation experiments. *Defect Assessment in components -Fundamentals and Applications, ESIS/EGF9*, ed. by J. G. Blauel and K. H. Schwalbe, Mechanical Engineering Publications, London, pp. 333-344.
37. Faleskog, J., 1994. An experimental and numerical investigation of ductile crack growth characteristics in surface cracked specimens under combined loading. *International Journal of Fracture* 68, pp. 99-126.
38. Faleskog, J. and Nordlund, P., 1994. Near-tip field characterization and J-integral evaluation for nonproportional loads. *International Journal of Solids and Structures* 31, pp. 1-26.

39. Faleskog, J., 1995. Effects of local constraint along three dimensional crack fronts - A numerical and experimental investigation. *Journal of the Mechanics and Physics of Solids* 43, pp. 447-493.
40. Faleskog, J., Gao, X. and Shih, C.F., 1998. Cell model for nonlinear fracture analysis-I: Micromechanics calibration. *Journal of the Mechanics and Physics of Solids* 89, pp. 355-373.
41. Fleck, N.A. and Hutchinson, J.W., 1993. A phenomenological theory for strain gradient effects in plasticity. *Journal of the Mechanics and Physics of Solids* 41, pp. 1825-1857.
42. Gao, X., Faleskog, J., Shih, C.F. and Dodds, R.H., 1998a. Ductile tearing in part-through cracks: Experiments and cell-model predictions. *Engineering Fracture Mechanics* 59, pp. 761-777.
43. Gao, X., Ruggeri, C. and Dodds, R.H., 1998b. Calibration of Weibull stress parameters using fracture toughness data. *International Journal of Fracture* 92, pp. 175-200.
44. Gao, X., Dodds, R.H., Tregoning, R.L., Joyce, J.A. and Link, R.E., 1999. A Weibull stress model to predict cleavage fracture in plates containing surface cracks. *Fatigue and Fracture of Engineering Materials and Structures* 22, pp. 481-493.
45. Geers, M.G.D., 1997. Experimental analysis and computational modelling of damage and fracture. Ph.D. thesis, Eindhoven University of Technology, Eindhoven, The Netherlands.
46. Geers, M.G.D., de Borst, R., Brekelmans, W.A.M. and Peerlings, R.H.J., 1998. Strain-based transient-gradient damage model for failure analyses. *Computer Methods in Applied Mechanics and Engineering* 60, pp. 133-153.
47. Geers, M. G. D., De Borst, R., and Peerlings, R. H. J., 1999. Validation and internal length scale determination for a gradient damage model: application to short glass-fibre-reinforced polypropylene. *International Journal of Solids and Structures* 36(17), pp. 2557-2583.
48. Gullerud, A.S., Gao, X., Dodds Jr, R.H. and Haj-Ali, R., 2000. Simulation of ductile crack growth using computational cells: numerical aspects. *Engineering Fracture Mechanics* 66, pp. 65-92.
49. Gurson, A.L., 1975. Plastic flow and fracture behaviour of ductile materials incorporating void nucleation, growth, and interaction. Ph.D. Dissertation, Brown University, USA.

50. Gurson, A.L., 1977. Continuum theory of ductile rupture by void nucleation and growth: Part-I: Yield criteria and flow rules for porous ductile media. *Transactions of ASME Journal Engineering Materials and Technology* 99, pp. 2-15.
51. Hancock, J.W., Reuter, W.G. and Parks, D.M., 1993. Constraint and toughness parameterized by T. *Constraint Effects in Fracture*, ASTM STP 1171, American Society for Testing and Materials, West Conshohoken, pp. 21-40.
52. Hill, R., 1962. Acceleration waves in solids. *Journal of the Mechanics and Physics of Solids* 10, pp. 1-16.
53. Hillerborg, A., Modér, M. and Petersson, P.-E., 1976. Analysis of crack formation and crack growth in concrete by means of fracture mechanics and finite elements. *Cement and Concrete Research* 6, pp. 773-781.
54. Huerta, A. and Pijaudier-Cabot, G., 1994. Discretization influence on the regularization by two localization limiters. *Transactions of ASCE Journal of Engineering Mechanics* 120, pp. 1198-1218.
55. Hutchinson, J.W., 1968. Singular behaviour at the end of a tensile crack in a hardening material. *Journal of the Mechanics and Physics of Solids* 16, pp. 13-31.
56. Kaiser, S., 1983. On the relation between stable crack growth and fatigue. *Journal of Fatigue of Engineering Structures and Materials* 6, pp. 33-48.
57. Katzenmeier, G., Kussmaul, K., Roos, E., and Diem, H., 1990. Component testing at the HDR-facility for validating the calculation procedures and the transferability of test results from specimen to component. *Nuclear Engineering and Design* 119, pp. 317-327.
58. Khalili, A., Kromp, K., 1991. Statistical properties of Weibull distribution. *Journal of Material Science* 26, pp. 6741-6752.
59. Kozák, V., and Dlouhý, I., 2001. The transferability of fracture toughness characteristics from point a view of the integrity of components with defects. *Proceedings of the conference SMiRT 16*, Washington.
60. Krieg, R., Seidenfuss, M., 2003. Limit Strains for Severe Accident Conditions. Final Report of the EU-Project LISSAC, Contract No. FIKS-CT1999-00012, October 2003.
61. Kussmaul, K., Eisele, U., Roos, E., and Zirn, R., 1984. The transferability of elastic-plastic fracture mechanics parameters from CT specimens to round notched tensile specimens. *Nuclear Engineering and Design* 79, pp. 1-6.
62. Kussmaul, K., and Roos, E., 1985. Statistical evaluation of post-yield fracture mechanics properties on the basis of the notched bar impact test. *Nuclear Engineering and Design* 87, pp. 123-137.

63. Kussmaul, K., Föhl, J., and Roos, E., 1987. Some conclusions with regard to the safety assessment of cracked components drawn from the research programme “Integrity of components” (FKS II) at the present state. *Nuclear Engineering and Design* 102, pp. 397-418.
64. Kussmaul, K., Roos, E., Diem, H., Katzenmeier, G., Klein, M., Neubrech, G.E., and Wolf, L., 1990. Cyclic and transient thermal loading of the HDR reactor pressure vessel with respect to crack initiation and crack propagation. *Nuclear Engineering and Design* 124, pp. 157-170.
65. Kussmaul, K., Eisele, U., Seidenfuss, M., 1995. On the applicability of local approach models for the determination of the failure behaviour of steels with different toughness. *ASME PVP-Vol. 304: Fatigue and Fracture Mechanics in Pressure Vessel and piping*.
66. Landes, J.D., 1996. J-Q model for predicting fracture in the ductile-brittle transition. *Fatigue and Fracture of Engineering Materials and Structures* 19 (7), pp. 869–877.
67. Larsson, R. and Runesson, K., 1993. Discontinuous displacement approximation for capturing plastic localization. *International Journal for Numerical Methods in Engineering* 36, pp. 2087-2105.
68. Lasry, D. and Belytschko, T., 1988. Localization limiters in transient problems. *International Journal of Solids and Structures* 24, pp. 581-597.
69. Matsubara, M., Stumpfrock, L., Roos, E., 2001. Application of statically indeterminate fracture mechanics (SIFM) to a circumferentially cracked cylinder problem. *Nuclear Engineering and Design* 207, pp. 351-357.
70. Meftah, F., Pijaudier-Cabot, G., And Reynouard, J.M., 1998. A C^0 finite element in gradient plasticity for localized failure modes analysis. In S. Idelsohn, E. Oñate, and E. Dvorkin (eds.), *Computational Mechanics: New Trends and Application, Proceedings of the 4th World Congress on Computational Mechanics, Barcelona, Spain*.
71. Miranda, C. A. J., and Landes, J. D., 2001. An application of the J-Q model for estimating cleavage stress in the brittle-to-ductile transition. *Fatigue and Fracture of Engineering Materials and Structures* 24 (6), pp.391–404.
72. Mudry, F., 1987. A local approach to cleavage fracture. *Nuclear Engineering and Design* 105, pp. 65-76.
73. Mühlhaus, H.-B. and Aifantis, E.C., 1991. A variational principle for gradient plasticity. *International Journal of Solids and Structures* 28, pp. 845-857.

74. Narström, T. and Isacson, M., 1999. Microscopic investigation of cleavage initiation in modified A508B pressure vessel steel, *Materials Science Engineering A* 271, pp. 224-231.
75. Needleman, A. and Tvergaard, V., 1984. An analysis of ductile rupture in notched bars. *Journal of the Mechanics and Physics of Solids* 32, pp. 461-490.
76. Needleman, A., 1988. Material rate dependence and mesh sensitivity in localisation problems. *Computer Methods in Applied Mechanics and Engineering* 67, pp. 69-86.
77. Needleman, A. and Tvergaard, V., 1994. Mesh effects in the analysis of dynamic ductile crack growth. *Engineering Fracture Mechanics* 47, pp. 75-91.
78. Needleman, A. and Tvergaard, V., 1998. Dynamic crack growth in a nonlocal progressively cavitating solid. *European Journal of Mechanics A/Solids* 17, pp. 421-438.
79. Nilsson, F., 1992. Numerical investigation of J-characterization of growing crack tips. *Nuclear Engineering Design* 133, pp. 457-463.
80. Nilsson, F., Faleskog, J., Zaremba, K. and Öberg, H., 1992. Elastic-plastic fracture mechanics for pressure vessel design”, *Fatigue and Fracture of Engineering Materials and Structures* 15, pp. 73-89.
81. Nilsson, C., 1998. On nonlocal rate-independent plasticity. *International Journal of Plasticity* 14(6), pp. 551-575.
82. O’Dowd, N.P. and Shih, C.F., 1991. Family of crack-tip fields characterized by a triaxiality parameter-I. Structure of fields. *Journal of the Mechanics and Physics of Solids* 39(8), pp. 989-1015.
83. O’Dowd, N.P. and Shih, C.F., 1992. Family of crack-tip fields characterized by a triaxiality parameter-II. Fracture applications. *Journal of the Mechanics and Physics of Solids* 40, pp. 939-963.
84. O’Dowd, N.P. and Shih, C.F., 1994. Two-parameter fracture theory: theory and applications. *Fracture Mechanics: Twenty-Fourth Volume*, ASTM STP 1207, Ed. by J. D. Landes, D. E. McCabe and J. A. Boulet, American Society for Testing and Materials, West Conshohoken, Pa., pp. 21-47.
85. Oliver, J., 1996. Modelling strong discontinuities in solid mechanics via strain softening constitutive equations. Part I: Fundamentals; Part II: Numerical simulation. *International Journal for Numerical Methods in Engineering* 39, pp. 3575-3623.
86. Ortiz, M., Leroy, Y. and Needleman, A., 1987. A finite element method for localized failure analysis. *Computer Methods in Applied Mechanics and Engineering* 61, pp. 89-214.

87. Pamin, J., 1994. Gradient-dependent plasticity in numerical simulation of localization phenomena. Ph.D. thesis, Delft University of Technology, The Netherlands.
88. Pavankumar, T.V., Samal, M.K., Chattopadhyay, J, Dutta, B.K., Kushwaha, H.S., Roos, E. and Seidenfuss, M., 2005. Transferability of fracture parameters from specimens to component level. *International Journal of Pressure Vessels and Pipings* 82(5), pp. 386-399.
89. Peerlings, R. H. J., De Borst, R., Brekelmans, W. A. M., and De Vree, J. H. P., 1996. Gradient enhanced damage for quasi-brittle materials. *International Journal for Numerical Methods in Engineering* 39(19), pp. 3391-3403.
90. Peerlings, R. H. J., De Borst, R., Brekelmans, W. A. M., and Geers, M. G. D., 1998a. Gradient enhanced damage modelling of concrete fracture. *Mechanics of Cohesive-Frictional Materials* 3(4), pp. 323-342.
91. Peerlings, R. H. J., De Borst, R., Brekelmans, W. A. M., and Geers, M. G. D., 1998b. Wave propagation and localisation in non-local and gradient-enhanced damage models. *Journal de Physique IV* 8(8), pp. 293-300.
92. Peerlings, R. H. J., Geers, M. G. D., De Borst, R., and Brekelmans, W. A. M., 2001. A critical comparison of nonlocal and gradient-enhanced softening continua. *International Journal of Solids and Structures* 38(44), pp. 7723-7746.
93. Peerlings, R. H. J., De Borst, R., Brekelmans, W. A. M., and Geers, M. G. D., 2002. Localisation issues in local and nonlocal continuum approaches to fracture. *European Journal of Mechanics A-Solids* 21, pp. 175-189.
94. Pietruszczak, S. and Mróz, Z., 1981. Finite element analysis of deformation of strain softening materials. *International Journal for Numerical Methods in Engineering* 17, pp. 327-334.
95. Pijaudier-Cabot, G. and Bažant, Z.P., 1987. Nonlocal damage theory. *Transactions of ASCE Journal of Engineering Mechanics* 113, pp. 1512-1533.
96. Pijaudier-Cabot, G., Bažant, Z.P. and Tabbara, M., 1988. Comparison of various models for strain-softening. *Engineering Computations* 5, pp. 41-150.
97. Pijaudier-Cabot, G. and Huerta, A., 1991. Finite element analysis of bifurcation in nonlocal strain softening solids. *Computer Methods in Applied Mechanics and Engineering* 90, pp. 905-919.
98. Pijaudier-Cabot, G. and Benallal, A., 1993. Strain localization and bifurcation in a nonlocal continuum. *International Journal of Solids and Structures* 30, pp. 1761-1775.

99. Pijaudier-Cabot, G., 1995. Non-local damage. Mühlhaus, H.-B. (ed.), *Continuum models for materials with microstructure*, Wiley, Chichester, U.K., pp. 105-143.
100. Pitard-Bouet, J.-M., Seidenfuss, M., Bethmont, M., and Kussmaul, K., 1999. Experimental investigations on the ‘shallow crack effect’, on the 10 MnMoNi 5 5 steel, and computational analysis in the upper shelf by means of the global and local approaches. *Nuclear Engineering and Design* 190, pp. 171–190.
101. Ramaswamy, S., Aravas, N., 1998a. Finite element implementation of gradient plasticity models, Part I: Gradient-dependent yield functions. *Computer Methods in Applied Mechanics and Engineering* 163, pp. 11-32.
102. Ramaswamy, S., Aravas, N., 1998b. Finite element implementation of gradient plasticity models, Part II: Gradient-dependent evolutions equations. *Computer Methods in Applied Mechanics and Engineering* 163, pp. 33-53.
103. Reusch, F., 2003. Entwicklung und Anwendung eines nicht-lokalen Materialmodells zur Simulation duktiler Schädigung in metallischen Werkstoffen. Ph.D. thesis, Fakultät Maschinenbau, Universität Dortmund, Germany.
104. Reusch, F., Svendsen, B. and Klingbeil, D., 2003a. A non-local extension of Gurson-based ductile damage modeling. *Computational Materials Science* 26, pp. 219-229.
105. Reusch, F., Svendsen, B. and Klingbeil, D., 2003b. Local and non-local Gurson-based ductile damage and failure modelling at large deformation. *European Journal of Mechanics A/Solids* 22, pp. 779-792.
106. Rice, J. R. and Rosengren, G., 1968. Plane strain deformation near a crack tip in a power-law hardening material. *Journal of the Mechanics and Physics of Solids* 16, pp. 1-12.
107. Ritchie, R.O., Knott, J.F. and Rice, J.R., 1973. On the relationship between critical tensile stress and fracture toughness in mild steel. *Journal of the Mechanics and Physics of Solids* 21, pp. 395-410.
108. Roos, E., 1983. Transferability of post yield fracture mechanics properties from small scale specimens to large scale specimens and components. *Nuclear Engineering and Design* 76, pp. 339-346.
109. Roos, E., Kockelmann, H., and Stoppler, W., 1985. Application and evaluation of fracture mechanics failure concepts to precracked vessels. *Nuclear Engineering and Design* 84, pp. 233-240.

110. Roos, E., Eisele, U., Beyer, H., and Gillot, R., 1987a. Classification and characterization of materials by means of fracture mechanics parameters. *Nuclear Engineering and Design* 102, pp. 475-485.
111. Roos, E., Eisele, U., Silcher, H., and Spaeth, F., 1987b. The influence of the material toughness and the state of stress on fracture of large-scale specimens. *Nuclear Engineering and Design* 102, pp. 439-449.
112. Roos, E., Herter, K.-H., Julisch, P., Bartholomi G., and Senski, G., 1989. Assessment of large scale pipe tests by fracture mechanics approximation procedures with regard to leak-before-break. *Nuclear Engineering and Design* 112, pp. 183-195.
113. Roos, E., Seidenfuss, M., Krämer, D., Krolop, S., Eisele, U., and Hindenlang, U., 1991a. Application and evaluation of different numerical methods for determining crack resistance curves. *Nuclear Engineering and Design* 130, pp. 297-308.
114. Roos, E., Silcher, H., and Eisele, U., 1991b. On lower bound crack resistance curves as material law for the safety assessment of components. *Nuclear Engineering and Design* 130, pp. 249-257.
115. Roos, E., Eisele, U., and Silcher, H., 1993. Effect of stress state on the ductile fracture behavior of large-scale specimens. In: Hackett E.M., Schwalbe K.H., Dodds R., Editors. *Constraint effects in fracture*, ASTM STP 1171. Philadelphia. American Society for Testing and Materials, pp. 41-63.
116. Roos, E., Maubach, K., and Albert, N., 1996. The safety of nuclear power station components. *Nuclear Engineering and Design* 160, pp. 241-255.
117. Roos, E., and Eisele, U., 1999. Determination of fracture mechanics characteristics: initiation or instability characteristics as a basis for components assessment. *Fracture, Fatigue and Weld Residual Stress ASME PVP 393*, pp. 93-100.
118. Roos, E., and Föhl, J., 1999. Implementation of results from MPA reactor safety research in the integrity assessment of German reactor pressure vessels. *Nuclear Engineering and Design* 190, pp. 97-115.
119. Roos, E., Eisele, U., Stumpfrock, L., 2000a. Transferability of results of PTS experiments to the integrity assessment of reactor pressure vessels. *Nuclear Engineering and Design* 198, pp. 173-183.
120. Roos, E., Kockelmann, H., Herter, K.-H., Schuler, X., Zaiss, W., Bartonicek, J., 2000b. Fracture mechanics evaluation of small diameter piping considering the latest experimental results. *Nuclear Engineering and Design* 198, pp. 115-129.

121. Roos, E., Otremba, F. and Eisele, U., 2001. Fracture mechanics material characteristics for a simplified safety analysis. Proceedings of the sixteenth international conference on structural mechanics in reactor technology (SmiRT-16), Paper No. 1727, Division G, August 12–17, 2001, Washington, DC, USA.
122. Roos, E., Stumpfrock, L., Schuler, X., Eisele, U., 2005. Fracture mechanics safety analysis of components based on fracture mechanics characteristics combined with multiaxiality of the stress state. *International Journal of Pressure Vessels and Piping* 82, pp. 355-362.
123. Roos, E., Herter, K.-H., Schuler, X., 2006. Lifetime management for mechanical systems, structures and components in nuclear power plants. *International Journal of Pressure Vessels and Piping* 83, pp. 756–766.
124. Rousselier, G., 1980. Three-Dimensional Constitutive Relations and Ductile Fracture. Ed. Nemat-Nasser, Dourdan, North-Holland, pp. 331-355.
125. Rousselier, G., 1987. Ductile fracture models and their potential in local approach of fracture. *Nuclear Engineering and Design* 105, pp. 97-111.
126. Rousselier, G., 2001. The Rousselier model for porous metal plasticity and ductile fracture. *Handbook of Materials Behavior Models*. Ed. J. Lemaître, Academic Press, London, vol. 2, chapter 6.6, pp. 436-445.
127. Rudnicki, J.W. and Rice, J.R., 1975. Conditions for the localization of deformation in pressure-sensitive dilatant materials. *Journal of the Mechanics and Physics of Solids* 23, pp. 371-394.
128. Ruggieri, C. and Dodds, R.H., 1996. A transferability model for brittle fracture including constraint and ductile tearing effects: A probabilistic approach. *International Journal of Fracture* 79, pp. 309-340.
129. Ruggieri, C., Panontin, T.L. and Dodds, R.H., 1996. Numerical modeling of ductile crack growth in 3-D using computational cell elements. *International Journal of Fracture* 82, pp. 67-95.
130. Schreyer, H.L. and Chen, Z., 1986. One-dimensional softening with localization. *Transactions of ASME Journal of Applied Mechanics* 53, pp. 791-797.
131. Seebich, H.P., 2007. Doctoral Dissertation, Institut für Materialprüfung Werkstoffkunde und Festigkeitslehre, Universität Stuttgart, Germany.
132. Seidenfuss, M., 1992. Untersuchungen zur Beschreibung des Versagensverhaltens mit Hilfe von Schädigungsmodellen am Beispiel des Werkstoffes 20MnMoNi5-5, Doctoral Dissertation, Fakultät Energietechnik der Universität Stuttgart, Germany.

133. Seidenfuss, M. and Roos, E., 2004. LISSAC-size and geometry effects on the failure behaviour of notched specimens. 30th MPA Seminar, MPA, University of Stuttgart, Germany.
134. Shu, J. Y. and Barlow, C. Y., 2000. Strain gradient effects on microscopic strain field in a metal matrix composite. *International Journal of Plasticity* 16(5), pp. 563-591.
135. Simo, J.C., Oliver, J. and Armero, F., 1993. An analysis of strong discontinuities induced by strain-softening in rate-independent inelastic solids. *Computational Mechanics* 12, pp. 277-296.
136. Sluys, L.J., 1992. Wave propagation, localisation and dispersion in softening solids. Ph.D. thesis, Delft University of Technology, Delft, The Netherlands.
137. Sluys, L.J. and de Borst, R., 1994. Dispersive properties of gradient-dependent and rate dependent media. *Mechanics of Materials* 18, pp. 131-149.
138. Sluys, L.J. and Berends, A.H., 1998. Discontinuous failure analysis for mode-I and mode-II localization problems. *International Journal of Solids and Structures* 35, pp. 4257-4274.
139. Sreenivasan, P.R. and Mannan, S.L., 2000. Plastic η -factor for three-point bend specimens: Analysis of instrumented Charpy impact test results for AISI 308 weld and AISI 316 stainless steels. *International Journal of Fracture* 101, pp. 215-228.
140. Stölken, J. S. and Evans, A. G., 1998. A microbend test method for measuring the plasticity length scale. *Acta Materialia* 46(14), pp. 5109-5115.
141. Strömberg, L. and Ristinmaa, M., 1996. FE-formulation of a non-local plasticity theory. *Computer Methods in Applied Mechanics and Engineering* 136(1), pp. 127-144.
142. Stumpfrock, L., Roos, E., Huber, H., and Weber, U., 1993. Fracture mechanics investigations on cylindrical large scale specimens under thermal shock loading. *Nuclear Engineering and Design* 144, pp. 31-44.
143. Svendsen, B., 1999. On the thermodynamic of thermoelastic materials with additional scalar degrees of freedom. *Continuum Mechanics and Thermodynamics* 4, pp. 247-262.
144. Trädegård, A., Nilsson, F. and Östlund, S., 1998. J-Q characterization of propagating cracks. *International Journal of Fracture* 94, pp. 357-369.
145. Triantafyllidis, N. and Aifantis, E.C., 1986. A gradient approach to localization of deformation-I: Hyperelastic materials. *Journal of Elasticity* 16, pp.225-237.
146. Tvergaard, V., 1981. Influence of voids on shear band instabilities under plane strain conditions. *International Journal of Fracture* 17, 1981, pp. 389-407.

147. Tvergaard, V. and Needleman, A., 1984. Analysis of cup-cone fracture in a round tensile bar. *Acta Metallurgica* 32(1), pp. 157-169.
148. Tvergaard, V. and Needleman, A., 1995. Effects of non-local damage in porous plastic solids. *International Journal of Solids and Structures* 32, pp. 1063-1077.
149. Wang, Y., 1991. A two-parameter characterization of elastic-plastic crack tip fields and applications to cleavage fracture. PhD-thesis, MIT, USA.
150. Wang, W., 1997. Stationary and propagative instabilities in metals: a computational point of view. Ph.D. thesis, Delft University of Technology, The Netherlands.
151. Wallin, K., 1984. The scatter in results. *Engineering Fracture Mechanics* 19, pp. 1085-1093.
152. Williams, M., L., 1957. On the stress distribution at the base of a stationary crack. *Transactions of ASME Journal of Applied Mechanics* 24, pp. 109-114.
153. Xia, L., Shih, C.F. and Hutchinson, J.W., 1995. A computational approach to ductile crack growth under large scale yielding conditions. *Journal of the Mechanics and Physics of Solids* 43, pp. 389-413.
154. Xia, L. and Shih, C.F., 1995a. Ductile crack growth. -I: A numerical study using computational cells with microstructurally based length scales. *Journal of the Mechanics and Physics of Solids* 43, pp. 223-259.
155. Xia, L. and Shih, C.F., 1995b. Ductile crack growth. -II: Void nucleation and geometry effects on macroscopic fracture behaviour. *Journal of the Mechanics and Physics of Solids* 43, pp. 1953-1981.
156. Xia, L. and Shih, C.F., 1996. Ductile crack growth. -III: Transition to cleavage fracture incorporating statistics. *Journal of the Mechanics and Physics of Solids* 44, pp. 603-639.
157. Xia, L. and Cheng, L., 1997. Transition from ductile tearing to cleavage fracture: A cell model approach. *International Journal of Fracture* 87, pp. 289-306.
158. Zbib, H. M. and Aifantis, E. C., 1992. On the gradient-dependent theory of plasticity and shear banding. *Acta Mechanica* 92(1), pp. 209-225.
159. Zhang, Z.L. and Niemi, E., 1995. A class of generalized mid-point algorithms for the Gurson-Tvergaard material model. *International Journal for Numerical Methods in Engineering* 38, pp. 2033-2053.
160. Zimmermann, C., Demler, T., Tomoda, Y., and Roos, E., 1985. Energy transformation during dynamic crack initiation and arrest, *Nuclear Engineering and Design* 84, pp. 279-284.

Appendix A

Rousselier's model

This model for the yield potential considering the effect of porosity was developed by Rousselier (1980) using thermodynamic principles considering isotropic hardening and cavity growth inside a ductile material. There is also some damage coupling with elasticity through the density (ρ) change of the material. From the thermodynamics principle of maximum plastic dissipation in a material (plastic work is a function of stress σ_{ij} and plastic strain ε_{ij}^p fields, equivalent stress and strain of the matrix material, hardening variable r and the ductile void volume fraction f), we can write

$$\frac{1}{\rho} \sigma_{ij} \dot{\varepsilon}_{ij}^p - R\dot{r} + F\dot{f} \geq 0 \quad (\text{A.1})$$

where F is the associated thermodynamic force conjugate to f and R is the material resistance (true stress-strain curve) corresponding and conjugate to the equivalent plastic strain ε_{eq}^p or p in the material matrix. The density in the undamaged state is taken as 1 and hence after evolution of void volume fraction f , density can be calculated as $\rho = 1 - f$. Assuming additivity, one can separate the one-to-one dependence of $R = \bar{R}(r)$ and $F = h^{-1}(f)$. The existence of a plastic potential is postulated as the sum of two terms, using the first and second stress invariants (i.e., σ_{hydro} coupled with F and σ_{eq} coupled with R), hence one can write

$$\phi = \Phi_1 \left(\frac{\sigma_{eq}}{\rho}, R \right) + \Phi_2 \left(\frac{\sigma_{hydro}}{\rho}, F \right) \quad (\text{A.2})$$

Rousselier (1980) assumed the simplest forms for Φ_1 and Φ_2 as

$$\begin{aligned} \Phi_1 &= \frac{\sigma_{eq}}{\rho} - R \\ \Phi_2 &= g \left(\frac{\sigma_{hydro}}{\rho} \right) h(F) \end{aligned} \quad (\text{A.3})$$

Again, the normality conditions for plastic flow can be written as

$$\begin{aligned} \dot{\varepsilon}_{ij}^p &= \lambda \frac{\partial \Phi_1}{\partial \sigma_{ij} / \rho} \\ \dot{\varepsilon}_{hydro}^p &= \frac{1}{3} \lambda \frac{\partial \Phi_2}{\partial \sigma_{hydro} / \rho} = \frac{1}{3} \lambda g' \left(\frac{\sigma_{hydro}}{\rho} \right) h(F) \end{aligned} \quad (\text{A.4})$$

where $\dot{\varepsilon}_{ij}^{p}$ and $\dot{\varepsilon}_{hydro}^p$ are the increments in deviatoric and hydrostatic parts of plastic strain tensor respectively. λ is the proportionality constant or the plastic multiplier and it can be shown to be equal to the increment in von-Mises equivalent plastic strain, i.e., \dot{p} . Similarly, the normality rules for evolution of isotropic hardening variable r and the void volume fraction f can be written as

$$\begin{aligned} \dot{r} &= -\lambda \frac{\partial \Phi}{\partial R} = \lambda = \dot{p} \\ \dot{f} &= \lambda \frac{\partial \Phi}{\partial F} = g \left(\frac{\sigma_{hydro}}{\rho} \right) h'(F) \dot{p} \end{aligned} \quad (A.5)$$

The matrix material is postulated to be incompressible (neglecting the volumetric part of elastic strain) and hence the density can be written as (considering initial void volume fraction as f_0)

$$\rho = \frac{(1-f)}{(1-f_0)} \quad (A.6)$$

The increase in void volume fraction (due to hydrostatic part of plastic strain tensor) can be written as

$$\dot{f} = 3(1-f) \dot{\varepsilon}_{hydro}^p \quad (A.7)$$

Rousselier (1987) demonstrated that the functions g and F can be shown to be

$$\begin{aligned} g \left(\frac{\sigma_{hydro}}{\rho} \right) &= D \sigma_k \exp \left(\frac{\sigma_{hydro}}{\rho \sigma_k} \right) \\ F &= F_0 + \sigma_k \ln \left(\frac{f}{1-f} \right) \end{aligned} \quad (A.8)$$

where D , σ_k and F_0 constants of the Rousselier's model. The initial void volume fraction f_0 is also another parameter of the Rousselier's model. Using Eqs. (A.3) and (A.8), Eq. (A.2) can be written as

$$\phi = \frac{\sigma_{eq}}{1-f} + Df \sigma_k \exp \left(\frac{\sigma_{hydro}}{(1-f) \sigma_k} \right) - R(p) = 0 \quad (A.9)$$

From Eq. (A.8), the increment in deviatoric and hydrostatic part of plastic strain tensors can be written as

$$\begin{aligned}\dot{\varepsilon}_{ij}^{\prime p} &= \frac{3\sigma'_{ij}}{2\sigma_{eq}} \dot{p} \\ \dot{\varepsilon}_{hydro}^p &= \frac{1}{3} Df \exp\left(\frac{\sigma_{hydro}}{(1-f)\sigma_k}\right) \dot{p}\end{aligned}\tag{A.10}$$

where σ'_{ij} is the deviatoric part of stress tensor. It may be noted that choosing a positive value for F_0 (i.e., $F_0 = -\sigma_k \ln\left(\frac{f_0}{1-f_0}\right)$) will lead always to a positive value of F and F will also be a increasing function with respect to f . This conditions satisfies the thermodynamic condition for positive plastic dissipation. Taking into account the effect of nucleation is also possible by adding a term (i.e., $A\dot{p}$ or $A(1-f)\dot{p}$) to the increase in void volume fraction \dot{f} . This can also satisfy the condition of positive plastic dissipation. In order to describe the process of void coalescence and subsequent ductile fracture in Rousselier's model, it may be useful to accelerate the void volume fraction f when it exceeds the critical void volume fraction f_c for coalescence.

Curriculum Vitae

- Born** 3rd May 1974 in Kanpur (Jajpur district of Orissa, India)
- 1979 to 1982** Primary school education in Gopalpatana lower primary school, Orissa (India)
- 1982 to 1987** Secondary school education in Sribantapur UGME school, Orissa (India)
Passed secondary school examination with highest grade in June 1987
- 1987 to 1989** High school education in Jakhapura high school, Orissa (India)
Passed High School Certificate examination of Board of Secondary Education, Govt. of Orissa (India) with First class in June 1989
- 1989 to 1991** Higher secondary (pre-university) education in Ravenshaw college, Orissa (India). Passed Higher secondary examination of Council of Higher Secondary Education, Govt. of Orissa (India) with First class in June 1991
- 1991 to 1992** First year Bachelor of Science (Hons.) in Bhadrak College, Orissa (India)
- 1992 to 1996** Bachelor of Technology in Mechanical Engineering in Orissa University of Agriculture and Technology, Bhubaneswar, Orissa (India).
Passed the final B.Tech (Mech. Engg.) examination with first class (Honours) in July 1996
- 1996 to 1997** One year Orientation course in Nuclear Science and Engineering in Bhabha Atomic Research Centre Training School, Trombay, Mumbai (India). Received Homi Bhabha Award for ranking first among the mechanical engineers
- 2001 to 2003** Master of Technology in Mechanical Design in Indian Institute of Technology Bombay (India). Passed the final M.Tech (Mech. Design) examination with first class in April 2003. Received P.M. Natu memorial prize and Ashok Chaturvedi memorial prize for ranking first in the Mechanical Engineering department of IIT Bombay. Selected for DAAD fellowship for carrying out Masters thesis at Technische Universität Darmstadt, Germany.
- 1996 to current date** Working as scientific officer in Reactor Safety division of Bhabha Atomic Research Centre, Mumbai (India). Areas of research and teaching include finite element method, damage mechanics, online creep-fatigue monitoring and smart materials.